EFFECT OF RADIATIVE HEAT TRANSFER ON THE STRUCTURE AND PROPAGATION OF LAYERED COAL-DUST EXPLOSIONS

By

SWAGNIK GUHATHAKURTA

A DISSERTATION PRESENTED TO THE GRADUATE SCHOOL
OF THE UNIVERSITY OF FLORIDA IN PARTIAL FULFILLMENT
OF THE REQUIREMENTS FOR THE DEGREE OF
DOCTOR OF PHILOSOPHY

UNIVERSITY OF FLORIDA

2021

To Upasna, my parents and my sister

ACKNOWLEDGMENTS

I want to thank my Ph.D. advisor, Dr. Ryan Houim, for his guidance, support and patience for the entire duration of my research. I wish to thank Prof. S. Balachandar, Prof. Subrata Roy and Dr. Laura Blecha for serving as my doctoral committee members and providing me their insights. I would also like to thank Dr. Elaine Oran of Texas A&M and Marcia Harris and Dr. Mike Sapko of NIOSH for their fruitful discussions.

This research was supported in part by the US National Science Foundation (NSF) grant 1942861 and the US National Institute for Occupational Safety and Health (NIOSH) grant 200-2015-64091. I would like to express my gratitude to these founding sources, without which this research would not have been possible.

I would also like to thank all the past and present members of the Multiphase Reactive Flow Research group at UF for all their help and suggestions. If not for their help, this research would have probably taken a lot longer to finish.

This is a good opportunity to extend my gratitude to the UF Supercomputing center, HiPerGator, which I have used quite extensively throughout my research and this wouldn't be possible without their computing resources. At the same time, I would like to thank Dr. Ryan Hoium and Skyler Bagley, for setting up and maintaining our lab servers, MICS, which was absolutely essential for developing and testing our codes.

Finally, I would like to thank my family - my parents and sister back in India, and my wife, Upasna Rai, for their infinite support for and belief in my graduate career.

TABLE OF CONTENTS

page

ACKNOWLEDGMENTS . . . 4

LIST OF TABLES . . . 8

LIST OF FIGURES . . . 9

ABSTRACT . . . 15

CHAPTER

1 INTRODUCTION . . . 17

- 1.1 Motivation and Background . . . 17
  - 1.1.1 Selected Case Studies of Dust Explosions . . . 19
    - 1.1.1.1 Benxihu Colliery Mining Disaster . . . 19
    - 1.1.1.2 Westray Coal Mine Explosion . . . 20
  - 1.1.2 Granular Dust Explosions - Safety Concerns . . . 20
- 1.2 Introduction to Dust Explosions . . . 21
  - 1.2.1 Explosibility Parameters . . . 21
  - 1.2.2 Fire Triangle and Explosion Pentagon . . . 22
  - 1.2.3 Primary and Secondary Explosions . . . 23
- 1.3 Current Status of Research on Flame Propagation in Dust Clouds . . . 24
  - 1.3.1 Laminar Flames in Dust Clouds . . . 25
  - 1.3.2 Turbulent Flames in Dust Clouds . . . 27
  - 1.3.3 Experimental Facilities Used to Study Large-Scale Dust Explosions . . . 28
    - 1.3.3.1 Laboratory scale experiments . . . 28
    - 1.3.3.2 Industrial scale experiments . . . 29
  - 1.3.4 Numerical Simulations of Flame Propagation in Dust Clouds . . . 33
- 1.4 The Science of Coal Dust Explosions . . . 34
  - 1.4.1 Shock-Flame Complex . . . 36
  - 1.4.2 Devolatilization of Coal Dust Particles . . . 36
  - 1.4.3 Burning Velocity and Flame Structure of Laminar Coal Dust Flames . . . 38
  - 1.4.4 Effect of Thermal Radiation on Coal Dust Explosions . . . 42
- 1.5 Scope of this Research . . . 44

2 GOVERNING EQUATIONS AND MATHEMATICAL MODELS . . . 47

- 2.1 Governing Equations . . . 47
- 2.2 Granular Phase Governing Equation Terms . . . 51
- 2.3 The Nozzling and pDV Work Terms . . . 53
- 2.4 Interphase Mass, Momentum and Energy Transfer . . . 54
- 2.5 Chemical Reactions . . . 57
  - 2.5.1 Solid-Phase Reactions . . . 57
  - 2.5.2 Gas-Phase Reactions . . . 59

2.5.2.1 Single-step methane-air reaction 59
2.5.2.2 Two-step methane-air reaction 60
2.6 Thermodynamic and Transport Models 63
2.7 Radiation Solver 65
2.7.1 The Spherical Harmonics Approximation to the Radiation Transport Equation 65
2.7.1.1 3-D spherical harmonics approximation 68
2.7.1.2 The eigenstructure 69
2.7.2 Filtered Spherical Harmonics Expansion (FP_N) 71
2.7.3 Solid-Phase Radiative Properties 72
2.7.4 Gas-Phase Radiative Properties 74

3 NUMERICAL METHODS 78

3.1 Solving the Hyperbolic Terms 78
3.1.1 Spatial Discretization 80
3.1.2 Nozzling and pDV Work Terms 80
3.1.3 Solid Phase Fluxes 81
3.1.4 Gas Phase Fluxes 87
3.2 Integrating the Chemical Reaction Terms 89
3.2.1 Single-Step Reaction Mechanism 90
3.2.2 Two-step reaction mechanism 90
3.3 Radiation Solver 91
3.3.1 MUSCL Interpolation Scheme 92
3.3.2 Rusanov Flux Scheme 93

4 CODE VERIFICATION TESTS 95

4.1 Hydrodynamic Solver 95
4.2 Granular Multiphase Solver 97
4.2.1 Loosely Packed Two-Phase Granular Shock-Tube Problem 97
4.2.2 Densely Packed Two-Phase Granular Shock-Tube Problem 98
4.3 Integration of the Gas-Phase Chemical Reactions 102
4.3.1 Constant-Volume Reactor 102
4.3.2 Flame Speeds and Temperatures 104
4.4 Laminar Coal-Dust Flame Speed Test 106
4.5 Radiation Solver Verification Test 108

5 SINGLE STEP REACTION MECHANISM RESULTS AND DISCUSSION 116

5.1 Problem Description and Numerical Methods for the 2-D Long Channel Cases 116
5.1.1 Physical Model 116
5.1.2 Radiation Modeling 117
5.1.3 Numerical Solution Methods 118
5.1.4 Results 118
5.1.5 Shock-Flame Structure 118

5.1.5.1 Short 10-m Channel With 47% Volume Fraction in the Dust Layer . . . 119
5.1.5.2 Long 40-m Channel With 47% Volume Fraction in the Dust Layer . . . 121
5.1.5.3 Long Channel With 1% Volume Fraction . . . 123
5.1.6 Discussion . . . 124
5.1.7 Conclusions . . . 126

6 TWO-STEP REACTION MECHANISM RESULTS AND DISCUSSION . . . 127

6.1 Short 10-m Channel With the 2-Step Methane-Air Reaction Mechanism . . . 127
6.2 Long 40-m Channel With the 2-Step Methane-Air Reaction Mechanism . . . 131
6.3 Effect of Particle Size . . . 134
6.4 Effect of Reaction Mechanism . . . 139
6.5 Discussion . . . 145
6.6 Conclusions . . . 155

7 THREE-DIMENSIONAL SIMULATIONS RESULTS AND DISCUSSION . . . 157

7.1 Problem Description . . . 157
7.2 Results . . . 158
7.3 Discussion . . . 160
7.4 Conclusions . . . 164

8 OVERALL CONCLUSIONS AND FUTURE WORK . . . 168

8.1 Conclusions . . . 168
8.2 Recommendations for Future Work . . . 170

REFERENCES . . . 171

BIOGRAPHICAL SKETCH . . . 183

LIST OF TABLES

Table page

2-1 Correlation parameters for the prediction of nondimensional coal properties 74

4-1 Flame properties of the single and two-step reaction mechanisms compared for HyBurn and Cantera. 107

4-2 Number of equations needed to solve for various orders of FP$_n$ approximations . . . 110

LIST OF FIGURES

Figure page

1-1 Schematic of the Shock-flame complex for a layered coal dust explosion 18

1-2 Benxihu (Honkeiko) collier disaster of 1942 20

1-3 Destructive power of overpressures, Westray Coal Mine 21

1-4 Scanning electron microscope images of unburned and burned bituminous coal particles 22

1-5 Logic diagram for dust explosion hazard identification and risk reduction 23

1-6 Fire triangle for dusts 24

1-7 Explosion Pentagon 24

1-8 Structure of a laminar flame 26

1-9 Vertical and horizontal cross sections of PRL 20-L explosibility test chamber 29

1-10 The University of Michigan wind tunnel facility for the study of the smoldering combustion of dust 30

1-11 Jet-stirred reactor used for studying combustion of dust mixtures at the University of Michigan 30

1-12 Schematic diagram of the University of Michigan vertical detonation tube 31

1-13 Experimental mine Barbara in Poland 32

1-14 Bruceton Experimental Mine, USA 33

1-15 Structure and components of coal particles 35

1-16 Ignition delay times for Pittsburg and Black Thunder coal using the CPD and Kobayashi devolatilization models 38

1-17 Temperature and species mass fraction profiles for MP1 and BFER2 methane combustion reaction mechanisms without surface chemistry 40

1-18 Temperature and species mass fraction profiles for DRM19 and GRI-Mech 3.0 reaction mechanisms without surface chemistry 41

1-19 Temperature and species mass fraction profiles for MP1 reaction mechanism with surface chemistry 42

1-20 Comparison of flame location using continuum and discrete models for the MP1 and DRM19 reaction mechanisms 43

1-21 Burning velocity for continuum and discrete models 43

1-22 Numerical setup for the simulation of layered coal-dust explosions. 45

2-1 Side view of D-drift in the Lake Lynn experimental mine, showing instrumentation . 48

2-2 Schematic diagram of HyBurn and its components. 48

4-1 Initial conditions for the Sod's shock tube problem. 95

4-2 Approximate (using 10,000 grid points) and exact Riemann solver solutions to the Sod's shock tube problem after 16 ms 96

4-3 Solutions for the loosely packed two-phase granular shock-tube problem at 184 μs . 98

4-4 Solutions for the loosely packed two-phase granular shock-tube problem at 184 μs, comparing cases with and without particles to show the effect of the granular phase 99

4-5 Solutions for the densely packed two-phase granular shock-tube problem at 100 μs . 100

4-6 Plot of granular volume fraction and granular temperature for the densely packed two-phase granular shock-tube problem at 100 μs, showing the granular shock relaxation structure. 101

4-7 Constant-volume reactor plots comparing species mass fractions and gas temperature results from Cantera and HyBurn at 0.2 ms for the single-step reaction mechanism . 104

4-8 Constant-volume reactor plots comparing species mass fractions and gas temperature results from Cantera and HyBurn at 2 ms for the two-step reaction mechanism . . . 105

4-9 Initial temperatures and species mass fractions of participating species for the methane-air laminar flame speed test using single-step, and two-step reaction mechanisms 106

4-10 Plots of gas temperatures and major species mass fractions for single-step ($t \approx 6.5$ ms), and two-step ($t \approx 6.2$ ms) reaction mechanisms showing the structures of the gas-phase flames 107

4-11 Flame location, and flame speed for the methane-air laminar flame speed test using single-step, and two-step reaction mechanisms 108

4-12 Laminar coal-dust flame speed test initial conditions, and results showing the gas-phase and granular-phase temperatures and major species mass fraction plots using the single-step and two-step reaction mechanisms 109

4-13 Initial and boundary conditions for the 1-D radiation test problem. 110

4-14 Incident radiations for various FP$_n$ approximations compared to the exact solution for the 1-D radiation test problem. 111

4-15 Radiation heat flux for various FP$_n$ approximations compared to the exact solution for the 1-D radiation test problem (log scale). 112

4-16 Initial conditions for the 2-D lattice problem. 113

4-17 Solution of the incident radiation field after $t = 16/c$ s 114

4-18 Percentage errors for the FP_1, FP_3 and FP_5 approximations in the 2-D lattice test problem, assuming FP_{13} as the exact solution. 114

4-19 Solution of the incident radiation field in the X-Y plane, centered at Z = 3.5 cm, after 50,000 time steps. 115

5-1 Initial and boundary conditions 116

5-2 Plots of gas temperature, volume fraction, methane mass fraction, and oxygen mass fraction, showing the shock flame complex (SFC) 119

5-3 XT plot shaded by gas phase temperature for the 10-m channel with 47% layer volume fraction with and without radiation 120

5-4 Heat release rates due to chemical reactions for the cases with and without radiation, and with inert ash and reactive coal for the 10 m channel with a dust volume fraction of 47% 120

5-5 Contour plots of gas temperature for the cases with and without radiation at 45 ms for the 10-m channel the dust layer volume fraction of 47% 121

5-6 Dense (47%) case total heat release rate due to gas phase chemical reactions and shock and flame velocities 122

5-7 Dense (47%) case XT plot shaded by gas phase temperature with and without radiation 122

5-8 Dilute (1%) case total heat release rate due to gas phase chemical reactions and shock and flame velocities 123

5-9 Dilute (1%) case XT plot shaded by gas phase temperature with and without radiation 123

5-10 Plots of gas temperature, dust volume fraction, incident radiation, methane mass fraction, and coal temperature for cases with and without radiation for the 1% volume fraction dust layer in the 40-m channel at a time of 26 ms 125

6-1 X-t diagram for the 10-m long channel shaded by gas phase temperature at y = 2.5 cm with the 2-step reaction mechanism, with and without radiation 128

6-2 X-t diagram for the 10-m long channel shaded by gas phase temperature at y = 5 cm with the 2-step reaction mechanism, with and without radiation 128

6-3 Shock and flame velocities for the 10-m channel using the 2-step reaction mechanism. 129

6-4 Shock and flame positions and heat release rates due to chemical reactions for the 10-m channel using the 2-step reaction mechanism. 130

6-5 Contour plots of gas temperature for the cases, with and without radiation at 17 ms for the 10-m channel with the 2-step reaction mechanism 130

6-6 Gauge pressure plots for the 10-m channel radiative and non-radiative cases with the 2-step reaction mechanism at locations of 1 m, 6 m and 10 m in the channel, and at a height of 2.5 cm. 131

6-7 impulse plots for the 10-m channel radiative and non-radiative cases with the 2-step reaction mechanism at locations of 1 m, 6 m and 10 m in the channel, and at a height of 2.5 cm. 132

6-8 Shock and flame positions and heat release rates due to chemical reactions for the 40-m channel using the 2-step reaction mechanism. 133

6-9 Shock and flame velocities for the 40-m channel using the 2-step reaction mechanism. 134

6-10 X-t diagram for the 40-m long channel shaded by gas phase temperature at y = 2.5 cm with the 2-step reaction mechanism, with and without radiation 135

6-11 Gauge pressure plots for the 40-m channel radiative and non-radiative cases with the 2-step reaction mechanism at locations of 1 m, 10 m, 20 m and 30 m in the channel, and at a height of 2.5 cm. 136

6-12 Impulse plots for the 40-m channel radiative and non-radiative cases with the 2-step reaction mechanism at locations of 1 m, 10 m, 20 m and 30 m in the channel, and at a height of 2.5 cm. 137

6-13 Shock positions for 5, 30, 100 and 150 μm particles using the 10-m channel and the 2-step reaction mechanism. 138

6-14 Flame positions for 5, 30, 100 and 150 μm particles using the 10-m channel and the 2-step reaction mechanism. 139

6-15 Total chemical heat release rates on log plot for 5, 30, 100 and 150 μm particles using the 10-m channel and the 2-step reaction mechanism. 140

6-16 Shock velocity for 5, 30, 100 and 150 μm particles using the 10-m channel and the 2-step reaction mechanism. 141

6-17 Flame velocity for 5, 30, 100 and 150 μm particles using the 10-m channel and the 2-step reaction mechanism. 142

6-18 X-t diagram for the 5 μm particles using the 10-m long channel shaded by gas phase temperature at y = 5 cm with the 2-step reaction mechanism, with and without radiation 143

6-19 X-t diagram for the 150 μm particles using the 10-m long channel shaded by gas phase temperature at y = 5 cm with the 2-step reaction mechanism, with and without radiation 143

6-20 Radiative heat flux plots for the 5, 30, 100 and 150 μm radiative cases. 144

6-21 Gauge pressure plots for 5, 30, 100 and 150 μm particles using the 10-m channel with the 2-step reaction mechanism 145

6-22 Impulse plots for 5, 30, 100 and 150 μm particles using the 10-m channel with the 2-step reaction mechanism 146

6-23 Flame positions for 30 μm particles using the 10-m channel and the 1-step and 2-step reaction mechanisms. 147

6-24 Total chemical heat release rates for 30 μm particles using the 10-m channel and the 1-step and 2-step reaction mechanisms. 148

6-25 Shock velocity for 30 μm particles using the 10-m channel and the 1-step and 2-step reaction mechanisms. 149

6-26 Flame velocity for 30 μm particles using the 10-m channel and the 1-step and 2-step reaction mechanisms. 150

6-27 Dilute (1% volume fraction) case total heat release rate due to gas phase chemical reactions and shock and flame velocities using single-step reaction mechanism . . . 151

6-28 Dense (47% volume fraction) case X-t plots for the 1-step reaction mechanism, shaded by gas phase temperature, with and without radiation 151

6-29 Plots of gas temperature and oxygen mass fraction for the 30 μm particle 10-m channel non-radiative case at different times, highlighting the effects of the reflected shock on the thermal and chemical equilibrium. 153

6-30 Plots of CO mass fraction and particle volume fraction for the 30 μm particle 10-m channel non-radiative case at different times, highlighting the effects of the reflected shock on the thermal and chemical equilibrium. 154

7-1 Shock and flame positions and heat release rates due to chemical reactions for the 5-m channel 2-D and 3-D radiative cases using the 2-step reaction mechanism. . . . 159

7-2 Shock and flame velocities for the 5-m channel 2-D and 3-D radiative cases using the 2-step reaction mechanism. 160

7-3 Gauge pressure plots for the 5-m channel 2-D and 3-D radiative cases using the 2-step reaction mechanism at locations of 1 m, 3 m and 5 m in the channel, and at a height and depth of 2.5 cm each. 161

7-4 Impulse plots for the 5-m channel 2-D and 3-D radiative cases using the 2-step reaction mechanism at locations of 1 m, 3 m and 5 m in the channel, and at a height and depth of 2.5 cm each. 162

7-5 X-t diagram for the 5-m long channel shaded by gas phase temperature at y = 2.5 cm with the 2-step reaction mechanism for the 2-D and 3-D simulations 163

7-6 X-t diagram for the 5-m long channel shaded by gas phase temperature at y = 5 cm with the 2-step reaction mechanism for the 2-D and 3-D simulations 163

7-7 Plots of gas temperature, particle volume fraction and incident radiation for the 5-m long channel 2-D case with the 2-step reaction mechanism at t $\sim$ 35 ms. . . . 164

7-8 Plots of gas temperature, particle volume fraction and incident radiation for the 5-m long channel 3-D case with the 2-step reaction mechanism at t $\sim$ 23 ms. . . . 165

7-9 Slice plots of particle volume fraction for the 5-m long channel 3-D case with the 2-step reaction mechanism at t $\sim$ 30 ms 166

Abstract of Dissertation Presented to the Graduate School
of the University of Florida in Partial Fulfillment of the
Requirements for the Degree of Doctor of Philosophy

EFFECT OF RADIATIVE HEAT TRANSFER ON THE STRUCTURE AND PROPAGATION OF LAYERED COAL-DUST EXPLOSIONS

By

Swagnik Guhathakurta

August 2021

Chair: Ryan W. Houim
Major: Aerospace Engineering

Multidimensional unsteady numerical simulations were carried out to explore the influence of thermal radiation on the propagation and structure of layered coal dust explosions. The simulations solved the reactive compressible Navier-Stokes equations coupled to an Eulerian kinetic-theory-based granular multiphase model. The radiation heat transfer is modeled by solving the radiation transfer equation using the third-order filtered spherical harmonics approximation. The radiation was assumed to be gray and all boundaries of the domain are black at 300 K. The reaction mechanism is based on global reactions for each physical process including devolatilization, char burning, moisture vaporization, and methane combustion. The governing equations were solved using a high-order Godunov method. Several simulation configurations were considered: layer volume fractions of 47% and 1%, channel lengths of 10 m and 40 m, single and two-step reaction mechanisms, several particle sizes, and radiative and non-radiative cases. The results show that gray radiation significantly influences the propagation and structure of a layered dust explosion. However, radiation can have opposite effects on different scenarios. For example, using the single-step reaction mechanism, radiation promotes the propagation of the dust flame when the layer volume fraction was 1% and in the short-channel cases where reflected shock-flame interactions are important. However, radiation enhances quenching for the 47% volume fraction dust layer in the longer channel. When using the two-step reaction mechanism, radiation enhances flame propagation and explosion severity in almost all test cases where the particles are easy to ignite. On the other hand, it seems to

quench or slow down the flame propagation through radiative heat loss for particles that are difficult to ignite.

CHAPTER 1
INTRODUCTION

1.1 Motivation and Background

Granular media can be found in nature in a vast variety of forms, ranging from salt to sand, from landslides to asteroids. Some types of granular media can be highly reactive in the presence of an oxidizer. Such reactive particles mixed in oxiders, can be quite disastrous under certain circumstances, such as enclosed spaces in coal mines and sugar refineries. They can be a health hazard and have been the cause of multiple disasters all over the world. In other cases, highly energetic particles mixed with oxidizers are highly sought after to increase the energy output of a system, for e.g., in solid rocket motors. There are many other applications of such multiphase flows for which the understanding of granular multiphase flows is essential, including the chemical and petroleum industries, power generation industries, geology, aerospace engineering.

Granular dust explosions can occur when dispersed combustible particles are present in sufficiently high concentrations in a gaseous oxidizer, such as oxygen (or air). In such cases, large overpressures can build up, which can lead to severe structural damage as well as fatalities. Many common organic materials, such as powdered spices, sugar, coffee, etc., as well as non-organic materials such as powered metals (aluminum, magnesium and titanium) can be a cause of dust explosions. Some recent notable incidents related to dust explosions include the Imperial Sugar Explosion in Port Wentworth, Georgia, USA (February, 2008), which was caused by sugar dust and killed 6 people and caused 38 injuries, the Kunshan explosion in Kunshan, China (August, 2014), where metal powder was the source material and it killed 146 people and injured a further 114, and Benxihu Colliery explosion in Benxi, Liaoning, China (April, 1942), which is the worst coal mine accident in the world, was caused by coal dust and gas in air, which killed an unbelievable 1,549 people. Thus understanding granular dust explosions is essential in order to control them or better still, completely avoid them altogether.

On the other hand, granular metal particles are added to propellants as an extra source of energy. Since the effects of aluminum were discovered, there was significant progress. Brzustowski and Glassman (1964) found that metal combustion is similar to combustion of hydrocarbon fuel droplets which follow the D^2 law. Thus, it has been a common additive to propellants and high explosives. In the case of solid rocket motor (SRM), aluminum is used to increase the specific impulse of the propellant due to a lower molecular weight of the products, and an increase of the adiabatic flame temperature. These particles do not react in the primary flame zone of the main propellant, but instead react with the product gases, which are usually CO_2, H_2O and HCl at temperatures of around 2600-3000 K and pressures of 40-100 atm. However, the drawbacks of aluminum combustion are deposition of slag in the rocket nozzle and incomplete combustion.

In this research, we will be looking at dust explosions in coal mines and the effect that radiation heat transfer can play on such explosions. Fig. 1-1 shows a schematic diagram of how dust explosions are formed and how they propagate in coal mines. A primary explosion (discussed in details later on) causes a shock wave to pass over a layer of dust that might have settled on the floor of the mines after a long period of mining. This shock lifts the dust and mixes it with the air in the mines. Once the dust is mixed to a combustible concentration, high temperature products from the primary explosion can then ignite these dust clouds, which causes a secondary explosion. The results of these secondary explosions can be fatal.

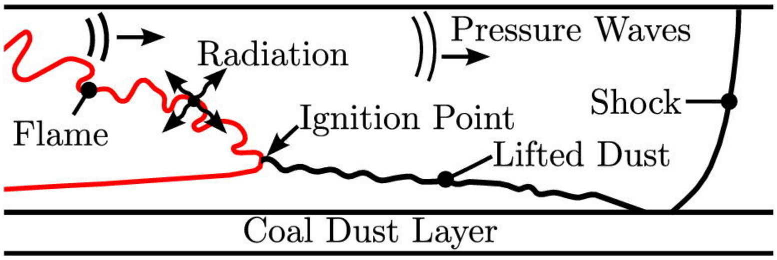

Figure 1-1. Schematic of the Shock-flame complex for a layered coal dust explosion (Houim and Oran, 2015b)

The primary focus of this research is to find out how important thermal radiation can be in such dust explosion scenarios. Generally, in numerical simulations of dust explosions, radiation is often ignored due to the their complexity and computational cost. However, if indeed radiation is found to have a significant effect on the nature and severity of these explosions, then the methods of mitigating dust explosions may need to be revised.

1.1.1 Selected Case Studies of Dust Explosions

The Turin (Italy) flour warehouse explosion in 1795 is among the very first examples of dust explosions in recorded history. Since then, there has been quite a large number of dust explosions that have occurred in coal mines all over the world. The Benxihu colliery mining disaster is the worst known mining disaster and the second worst known industrial disaster. Other than coal mine explosions, there are a variety of other materials that have been known to be the cause of dust explosions. The list includes things like wood dust, organic food grain, chemical flakes (such as acetates, pharmaceuticals, etc.), metal dust, etc. In this section, we take a slightly more detailed look at a couple of mining disasters and their causes.

1.1.1.1 Benxihu Colliery Mining Disaster

The worst known mining disaster occurred in the Benxihu (also known as Honkeiko) coal mine, located in Benxi, Liaoning province of China, which was responsible for the death of 1,549 miners. On April 26, 1942, a hybrid gas and dust explosion occurred in one of the shafts that sent out flames from the entrance of the mine shafts. In order to contain the fire, the Japanese guards shut off ventilation, thus also trapping the workers inside the underground shaft. Many relatives of the workers rushed to the site, but were held back by the Japanese using electric fences. The witnesses blamed the Japanese for not evacuating the pit before sealing it, thus unnecessarily increasing the death toll.

Many of the victims of the disaster were burnt beyond recognition and it took the workers ten days to remove all the dead bodies that were buried in the rubble, which were then buried in a mass grave nearby. It was later found during an investigation that only a few workers died directly from the gas and coal-dust explosion. The majority of deaths were due to carbon monoxide poisoning when the ventilation was cut off and the pit was sealed.

Figure 1-2. Benxihu (Honkeiko) collier disaster of 1942. Reproduced with permission from Devastating Disasters, https://devastatingdisasters.com/benxihu-honkeiko-colliery-1942/ (July 12, 2021).

1.1.1.2 Westray Coal Mine Explosion

One of the most well analyzed and studied dust explosions in recent history is that of the Westray coal mine explosion, which happened on May 9, 1992, in Plymouth, Nova Scotia, Canada. It resulted in the death of 26 mine workers. A lot of factors contributed to this explosion: the methane levels were consistently higher than the permissible level due to insufficient ventilation, there was an accumulation of coal dust due to the lack of cleanup, rock dusting - a technique to make the coal dust inert using limestone or dolomite - was entirely absent, to name a few. Ignoring safety regulations by the management was the primary cause of such dangerous working conditions.

1.1.2 Granular Dust Explosions - Safety Concerns

While industries understand gas explosions somewhat well, the same is not true for dust explosions. Dust explosions follow the same basic rules of gas explosions - the requirement of the three basic ingredients, i.e., fuel, oxidizer and source of ignition. More specifically, dust explosions occur in the presence of dust particles, suspended in air, along with an ignition source. The main difference between dust explosions and gas explosions is that dust explosions involve solid particles and thus the particle size is an important factor. Conventionally, anything

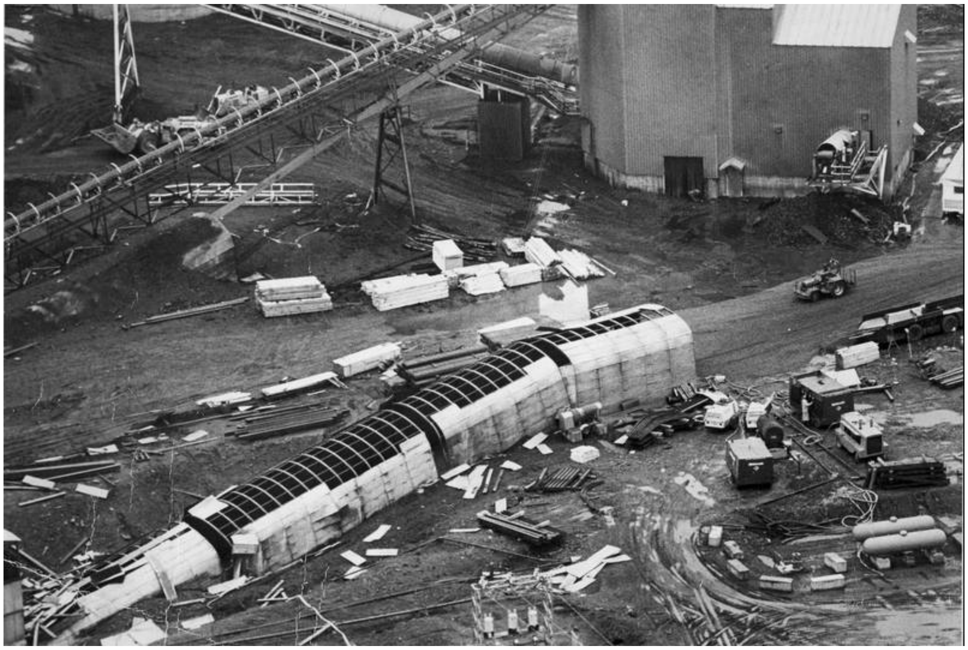

Figure 1-3. Destructive power of overpressures, Westray Coal Mine. Reproduced with permission from SaltWire https://www.saltwire.com/atlantic-canada/opinion/local-perspectives/ (July 9, 2021).

with a diameter of less than 420 μm is considered as a dust particle. However, according to Cashdollar (2000), the minimum explosible concentration (MEC) of dust particles with diameters greater than 100 μm is too high to be combustible in any practical situation. Even so, the range of particle diameters that are combustible is wide, ranging from 10-100 μm. Apart from that, the particle shape doesn't need to be spherical (Fig. 1-4) and can include flakes, fibers and flocculant forms. This is a major challenge to understanding and mitigating dust explosions.

1.2 Introduction to Dust Explosions

1.2.1 Explosibility Parameters

According to Amyotte and Eckhoff (2010), the explosivity of granular dust depends on a variety of factors, (i) whether the dust material is capable of producing explosions, (ii) how high the resulting overpressures are considering constant volume explosions, (iii) how quickly the pressure rise occurs in such a condition, (iv) the concentration of such dust particles

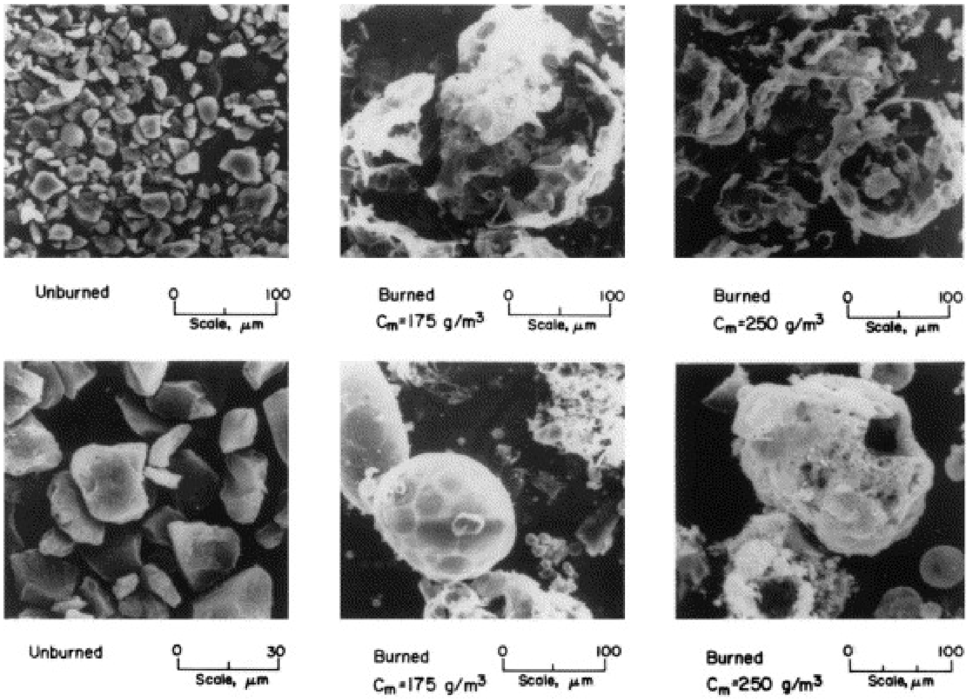

Figure 1-4. Scanning electron microscope images of unburned and burned bituminous coal particles (Cashdollar, 2000)

needed to create an explosion, (v) what kind of ignition source is required and how much energy it should have, and (vi) what percentage of oxygen in the atmosphere is required to result in a sustained flame propagation? A basic flowchart to answer these questions is shown in Fig. 1-5.

1.2.2 Fire Triangle and Explosion Pentagon

In most cases, the three necessary components for fire are (i) fuel, (ii) oxidzer and (iii) an ignition source. However, for dust explosions, there are additional fuel conditions that have to be met as well. These are: (i) the dust material must be combustible, (ii) the dust particles must be airborne, (iii) the dust particle size distribution must be capable of propagating the flame, (iv) the concentration of dust must be in the combustible range.

According to Kauffman, the fire triangle can be expanded by including the effects of mixing and confinement, to form the Explosion Pentagon. Unlike gas explosions, dust cloud explosions require the dust to be suspended in air, and thus the effect of gravity can be

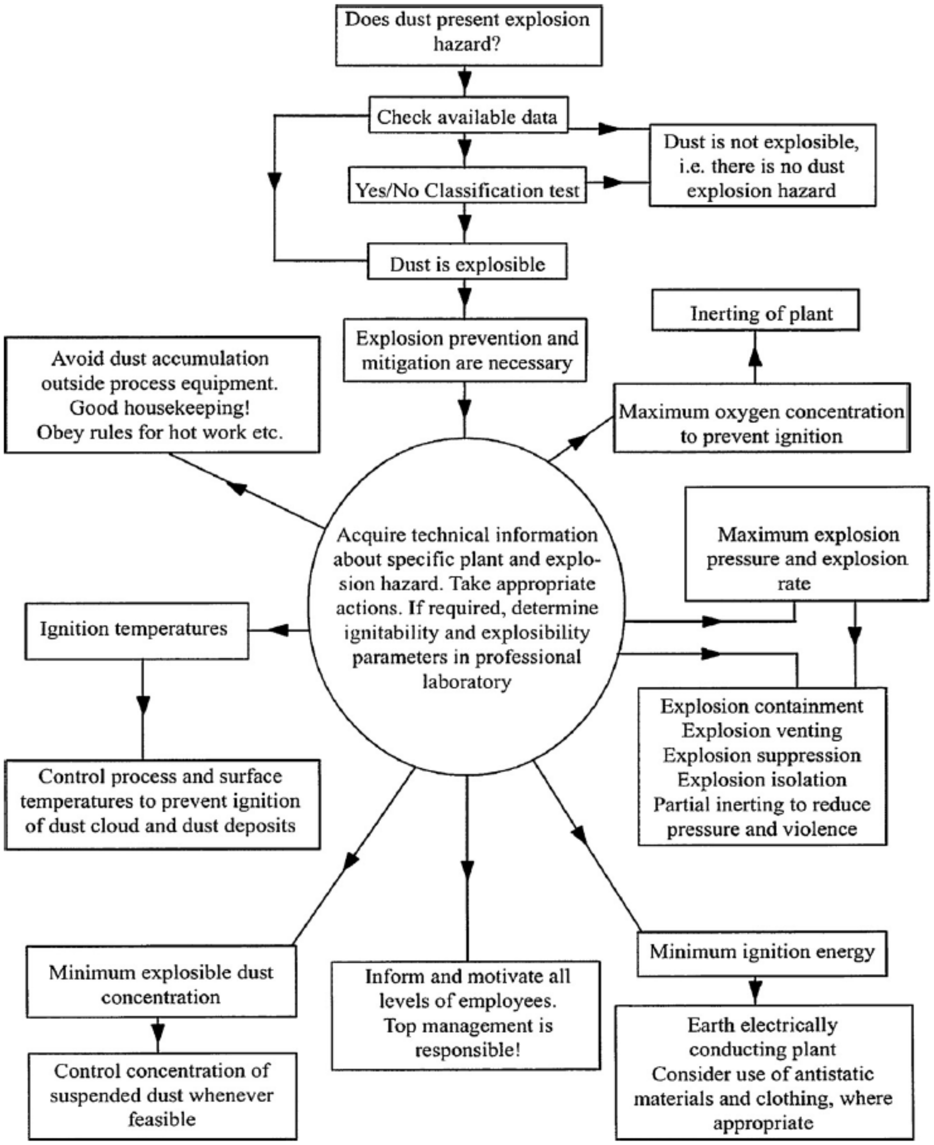

Figure 1-5. Logic diagram for dust explosion hazard identification and risk reduction (Amyotte and Eckhoff, 2010)

important. In the presence of confinement, the build up of pressure during combustion is significant enough to burn the dust flame faster, which can lead to an explosion.

1.2.3 Primary and Secondary Explosions

Industrial dust explosions usually occur inside process vessels and units such as mills, grinders and dryers, where the conditions for the explosion pentagon are satisfied. Usually the first explosion that occurs due to the ignition of suspended dust in confined spaces such as containers, rooms, etc., is referred to as a primary explosion.

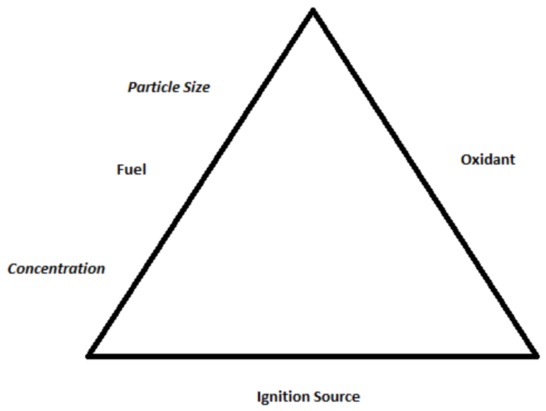

Figure 1-6. Fire triangle for dusts (Amyotte and Eckhoff, 2010)

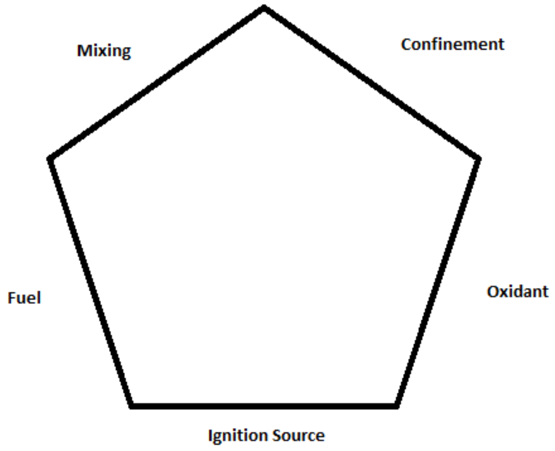

Figure 1-7. Explosion Pentagon (Amyotte and Eckhoff, 2010)

Secondary explosions can be initiated by the blast waves from primary explosions or some other form of disturbance that can disperse the dust layers that accumulate on floors or other work surfaces. In coal mines, coal dust explosions are often triggered by a preceding natural gas explosion. The dust concentration required to cause a secondary dust explosion is often overestimated by industries. Sometimes, even a few millimeters of dust accumulation into a thin layer can be explosive.

1.3 Current Status of Research on Flame Propagation in Dust Clouds

Dust explosions and gas explosions have similar properties such as flammability/explosibility limits, laminar burning velocities and quenching distances, adiabatic constant-volume explosion pressures, and minimum ignition temperatures and energies. However, there are some significant differences as well that set them apart. Two important differences are:

- The method of generation of explosible dust clouds is significantly different from that of gas/vapor clouds.
- Range of combustible fuel concentrations for dust clouds can vary greatly, as opposed to that of gas/vapor clouds which needs to be within the upper and lower flammability limits. This is because a layer of dust that has settled always has air in the gaps between particles, which can lead to sustained combustion propagation.

In contrast to gas phase explosions for which the fuel-oxidizer mixture remains fairly homogeneous due to random molecular motion, the inertial forces acting on dust particles can cause regions with significantly different dust concentrations. This is because dust particles are much larger than air molecules, and as such, their motion is affected more by forces such as gravity rather than by random molecular motion. Unlike gas molecules which undergo elastic collisions, inelastic dust particle collisions may also be responsible for particle agglomeration. Thermal radiation may also be of importance, depending on the dust material.

Lee et al. (1992) has shown that constant-pressure adiabatic flame temperatures and maximum constant-volume explosion pressures obtained from numerical codes agree well with experimental data. Ignition of dust clouds in shock tubes using incident and reflected shocks have been studied extensively by Nettleton and Stirling (1967), Kauffman et al. (1979), Boiko et al. (1984), Wolanski (1981), Breipohl et al. (1979), Sichel et al. (1985), and Wolanski (1987). Sichel et al. (1985) made detailed calculations on the particle history during the ignition process by a shock wave.

1.3.1 Laminar Flames in Dust Clouds

Before talking about laminar flames, it is important to define a few widely used terms. According to Turns et al. (1996), "a flame is a self-sustaining propagation of a localized combustion zone at subsonic velocities". The temperature profile in a flame is shown in Fig. 1-8. A laminar flame propagates into the unburned reactants section with a velocity known as the laminar flame speed, S_L.

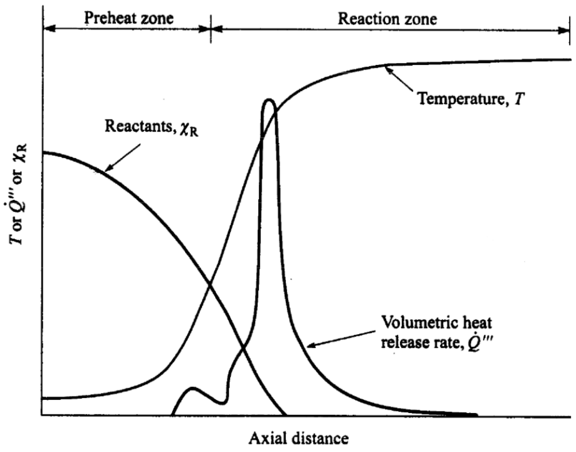

Figure 1-8. Structure of a laminar flame (Turns et al., 1996). Temperature and heat-release-rate are based on results from experiments of Friedman and Burke (1954).

Valuable work on laminar dust flames in stabilized burners has been done in the past, but some of the more recent contributions to this field was provided by Dahoe et al. (2002). In their work, they used laser Doppler anemometry (LDA) to measure the laminar burning velocities of stable cornstarch flames in air, and found that the laminar burning velocity varied with flame shape. This was accounted for by introducing the 'Markstein length' of a dust/air flame, which is the critical wavelength required for a stable flame front, and is a parameter specific to the given dust cloud. This is a measure of the sensitivity of the laminar burning velocity to changes in the flame shape.

In Cloney et al. (2018), the authors discuss in details about the laminar burning velocity of coal dust flames, as well as their structure, which were obtained from numerical simulations. From the results, the authors inferred that simplified reaction mechanisms used in the research are able to accurately predict the coal dust flame structure and burning velocities when compared to experimental observations. However, the single-step heterogeneous reaction mechanism underpredicts the amount of CO that have been reported in previous literature. They also observed that larger particles have an overall greater burning velocity, which is in line with experimental data. In addition, the effect of initial temperature on the burning velocities also match well with experiments. Finally, the authors noticed that using discrete particles instead of continuum assumption decreased the burning velocities by up to 25% depending on particle size and concentrations.

The effect of radiation on laminar flame propagation in organic dust clouds were studied by Haghiri and Bidabadi (2010), and specifically for coal-dust by Cao et al. (2014a). Cao et al. (2014b) also compared the behavior of coal-dust flame propagation from both experimental and numerical studies. In Haghiri and Bidabadi (2010), the authors analyzed the structure of flame propagation through a two-phase mixture composed of organic fuel particles and air. Their results suggest that the vaporization of the organic dust and the burning velocity were significantly enhanced by the induced thermal radiation from the flame interface into the preheat and vaporization zones. In summary, important flame parameters, such as the burning velocity, mixture temperature, mass fraction of volatile fuel particles and gaseous fuel mass fraction, were all altered substantially when considering radiation heat transfer. Similar results were obtained in the research performed by Cao et al. (2014a). They observed that the burning velocity and temperatures were increased when radiation was accounted for in coal-dust explosions. Apart from that, they also conclude that the coal-dust concentration is important to the behavior of the dust flame propagation. When the concentrations were increased, the flame propagation velocity and the fireball temperature also increased.

1.3.2 Turbulent Flames in Dust Clouds

One of the most important things to understand in the field of explosions is how a flame is accelerated by turbulence produced by an explosion. The acceleration of flames due to the presence of obstructions in the flow field has been studied by a number of resaerchers, including Moen et al. (1982); Hjertager et al. (1988); Bakke et al. (1992). Rzal-Rebière and Veyssière (1994) shows the differences between turbulent combustion of premixed gases and dust clouds. They observed that the burning rate of dust clouds react to turbulence differently than that of a premixed gas. Differences between these two types of flames have been shown to exist even on a microscopic scale. Mitgau (1996) and Mitgau et al. (1997) in their results showed that if the oxidizer can replace the reaction products at the surface of the particles efficiently due to turbulence, it can significantly enhance the rate of combustion.

1.3.3 Experimental Facilities Used to Study Large-Scale Dust Explosions

Despite the vast importance of dust combustion, this field (in contrast to hydrocarbon flames) remains quite under-developed. To some extent, this is due to the challenges of conducting experiments with laminar suspension of solid particles, which is required to measure parameters such as the burning velocity. Being heavy, dust particles settle under quiescent conditions. In order to counteract this, flow velocities, that may even exceed the flame speed, may be required. Another challenge is getting particles of uniform size and uniform concentrations.

Experimental facilities in the field of dust explosion research can be broadly categorized into two types - laboratory scale experiments and industrial scale experiments. Let us look at the kind of research performed in these types of facilities.

1.3.3.1 Laboratory scale experiments

Most laboratory scale experiments are often carried out in closed volume chambers (also known as closed bomb chambers). Cross sectional diagrams of the PRL 20-L explosibility test chamber that was used by Cashdollar (2000) is shown in Fig. 1-9. However, Kauffman et al. (1992) in their research used various other types of facilities along with closed volume chambers. For their studies on smoldering combustion of dust mixtures, they used a wind tunnel facility shown in Fig. 1-10. Studies on combustion of dust mixtures were performed using a jet-stirred reactor, shown in Fig. 1-11. In addition, they used a vertical detonation tube to investigate shock wave initiated dust combustion, which is shown in Fig. 1-12. In their paper they present the results of two decades of research on dust explosions. They explored the various forms of dust ignition processes such as ignition through smoldering combustion and turbulent combustion, as well as detonative combustion. They also studied the effects of adding combustible gas to the dust mixture and of inert particles to combustible gaseous mixtures.

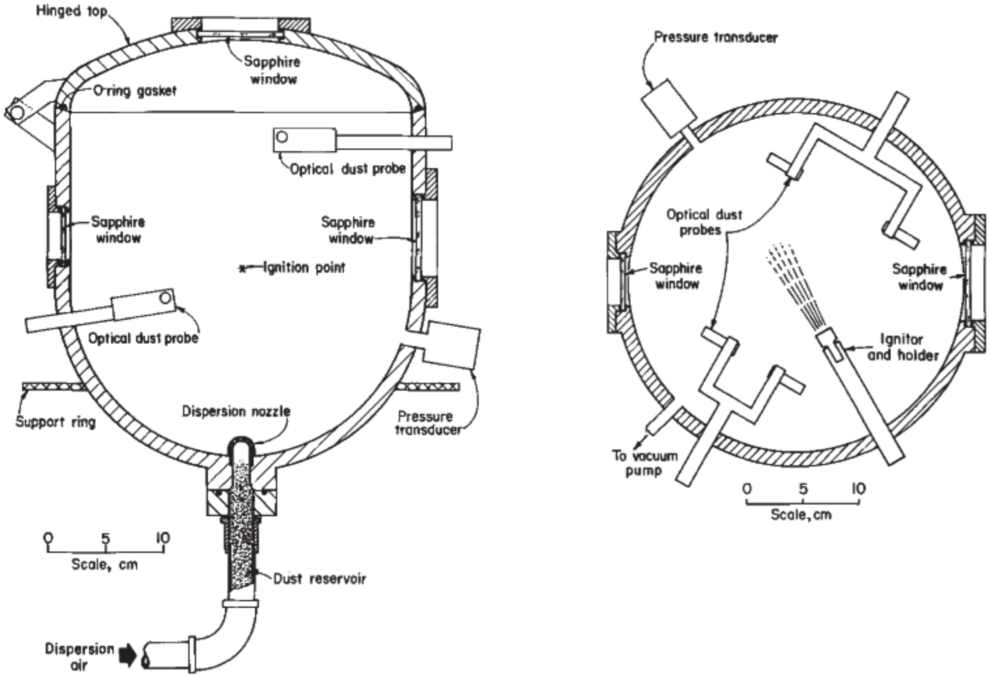

Figure 1-9. Vertical and horizontal cross sections of PRL 20-L explosibility test chamber (Cashdollar, 2000).

In their studies, they found that even a very thin layer of dust can cause explosions in tubes. The arrangement of the dust and the properties of the dust are the main factors that decide the flame acceleration in layered dust explosions. In some cases, they found that fine and reactive dusts can even transition to quasi-detonative combustion, with huge overpressures of up to 26 bars. In such quasi-detonative and detonative combustion, flame velocities have been seen to range between 1000 m/s to more than 1500 m/s.

1.3.3.2 Industrial scale experiments

One of the most prominent research facilities in the field of coal-dust explosions is the experimental mine "Barbara". It was founded in 1925 in Poland and currently perform research on gas hazard control, dust hazard control, blasting safety, explosion-proof protection, and mining. The laboratory of dust and gas explosions control in mines performs:

- research and service-related work on coal-dust explosion hazards in mines,
- tests on coal-dust explosion hazard in rock workings,
- tests on necessary protection for coal storage,

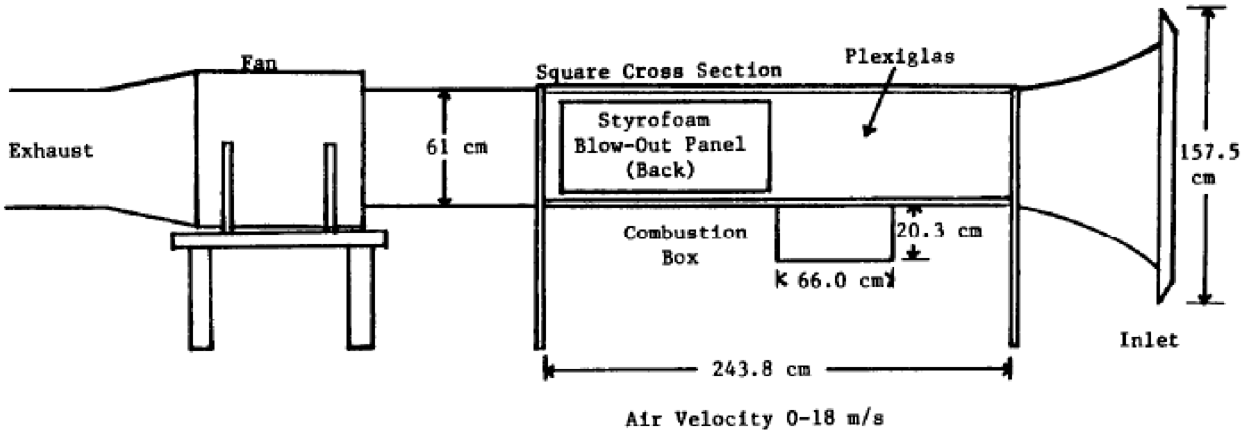

Figure 1-10. The University of Michigan wind tunnel facility for the study of the smoldering combustion of dust (Kauffman et al., 1992).

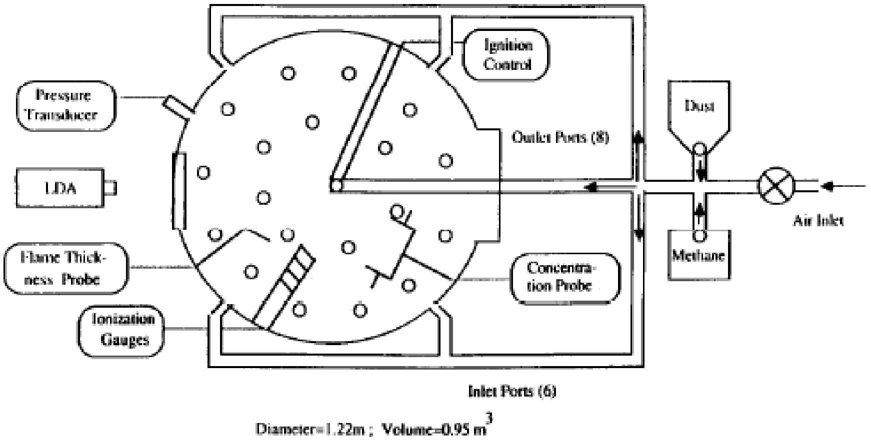

Figure 1-11. Jet-stirred reactor used for studying combustion of dust mixtures at the University of Michigan (Kauffman et al., 1992).

- assessments for the need to use explosion-proofing barriers,
- studies on the effects of limiting coal dust dispersibility using liquid and solid dampers,
- research on the effects of limiting volatility of coal-dust using calcium chloride or magnesium chloride with surface-active agent additive,

among various other things. They have several testing facilities such as the experimental 100 m tunnel, the 1 m^3 and 5 m^3 test chambers, and the underground experimental headings of 400 and 200 m.

Another experimental facility of importance is the experimental mine in Bruceton, U.S. This experimental facility demonstrated in its early days that coal dust by itself is capable of

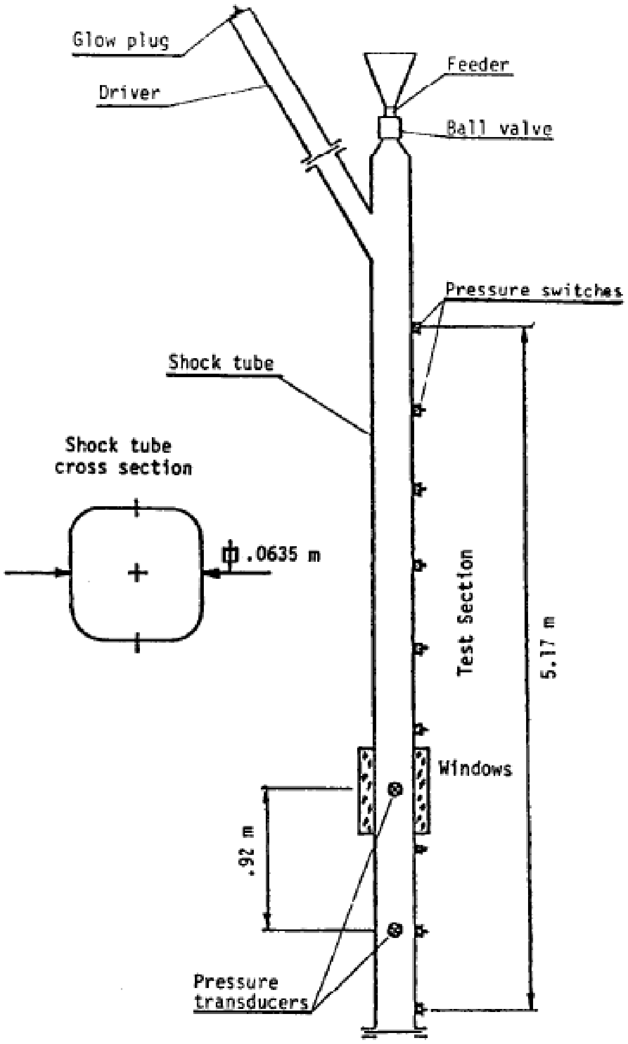

Figure 1-12. Schematic diagram of the University of Michigan vertical detonation tube (Kauffman et al., 1992).

propagating an explosion even without any presence of methane gas. At the time, this was a radically new discovery which produced regulations that prohibit using loose coal dust in mines to pack explosives in boreholes. This facility was established to by the U.S. Bureau of Mines (USBM) to perform research focused on:

- explosibility of mine gas and coal dust, and the prevention of explosions and fires,
- safety of explosives used in mines,
- electrical safety in mines,
- safety of mine lights and their use as gas detectors,

Figure 1-13. Experimental mine Barbara in Poland. Reproduced with permission from Wikimedia https://commons.wikimedia.org/wiki/ (July 12, 2021).

- emergency breathing apparatus.

Some notable highlights of the first five years of work at the Bruceton experimental mine are:

- coal dust was shown to greatly increase the severity of mine explosions as opposed to explosions involving only methane,
- tests were performed on explosives used in mines to reduce the dangers of coal mine explosions caused by them,
- safety precautions in mines were improved due to their research,
- demonstrated the use of rescue apparatus and trained miners in first aid, which led to 200 workers being rescued after mine disasters since then.

Thanks to their work, the Federal Coal Mine Safety Act was implemented in 1952. This Act brought forth improvements in roof control plans, the discontinuation of using dangerous black blasting powder, installation of ventilating fans, usage of water to suppress dust, and the banning of open flame lights, among several other things.

Despite having such experimental facilities, experiments in coal-dust explosions have their limitations. Most of the data available on dust combustion are from experiments in closed bombs without any visual access. The data from pressure monitors within the vessel are the

Figure 1-14. Bruceton Experimental Mine, USA. Reproduced with permission from Wikipedia https://en.wikipedia.org/wiki/ (July 12, 2021).

only available data. While this can provide some knowledge on the explosivity of dust clouds, any knowledge about flame propagation mechanism or flame structure is not obtained. Due to such short comings of experiments, accurate mathematical models of dust cloud combustion, along with numerical methods, are highly valuable for the advancement of this field. With massive technological and thus computational advancements being made every decade, fast numerical calculations of even highly complex systems are becoming more and more accessible and viable these days.

1.3.4 Numerical Simulations of Flame Propagation in Dust Clouds

Some of the earliest works on turbulent dust explosions using computational fluid dynamics (CFD) were performed by Kjäldman (1992). Some of the more recent research on this topic include Bielert and Sichel (2001); V.P. Korobeinikov et al. (2002); P. Kosinski et al. (2002); ROSE et al. (1999); Smirnov et al. (2000); Worsdorfer et al. (2001); S. Zhong et al. (2002). Many of the numerical dust explosion work performed by researchers are based on already existing dust explosion simulation codes such as FLACS which was originally developed by Hjertager et al. (1988). Numerical simulations of dust cloud explosions are are increasing in demand since it provides the ability to accurately predict a variety of dust explosion scenarios. However, in order to develop such codes, they will have to be rigorously tested for validation using data from full-scale dust explosion experiments, involving a variety of materials, dust cloud states and geometries.

1.4 The Science of Coal Dust Explosions

Simulations of dust explosion scenarios considering a dust layer have only recently started to appear in literature, for example, McMahon et al. (2007) and Houim and Oran (2015b) which carry out small scale tests. There are quite a few complex phenomena that occur in coal dust explosions.

The first is the interaction of the shock waves from primary explosions with the dust layers. The shock causes the dust to lift into the air and disperses it. Then the heated flow behind the shock heats the dust particles and ignites them. This forms a flame, and this whole structure is referred to as the shock-flame complex. Ugarte et al. (2017b) studied the dispersal of dust layers by a shock. They considered uniform layers of limestone dust for their simulations. The forces that act on the particles were the Archimedes force, produced by gas pressure gradients, lift and grad forces, produced due to the relative motion between particles and gas, intergranular forces, which result from particle collisions and frictional stress, and gravitational force. It was observed that the dust layer undergoes compaction first and then dispersal when the shock travels over it. An important observation was that the larger particles dispersed higher than the smaller particles. This is because even though the smaller particles experience larger upward acceleration, the drag that opposes the lifting of the particles is much greater than for the larger particles.

Secondly, the ignition of the coal dust particles is also a very interesting and complicated phenomena. Temperature, turbulence and time are the most important factors in the coal combustion process. The fuel must first reach its ignition temperature, and this temperature must be maintained for a stable flame. For coal, this is usually around 400 to 425 degrees Celsius. Once this temperature is reached, turbulence enhances the mixing of the fuel with the necessary oxygen molecules to promote rapid combustion. A certain amount of time is then required for complete combustion, which depends on the size of the particle. This time is reduced when the temperature is higher and their is substantial turbulence. Combustion itself is the rapid chemical reaction that occurs between fuel and oxygen. Coal may contain various types of combustible fuel such as carbon, sulfur and hydrogen, which when they react with oxygen, their respective oxides are formed and the reactions release heat. The particles are usually assumed to be composed of volatiles (such as methane) and char, and may in addition to that include unreactive components such as ash, as well as in some cases may also contain moisture in the solidified form (coal structure shown in Fig. 1-15). The devolatilization of the coal particles is a subject of research in itself and there exist a number of models to represent it. The third important topic is that of the actual chemical reactions that take place. Again, there are several models that exist for the chemical reactions involving burning of char and methane. The char burning may involve a kinetic or diffusion limited process (discussed in details in Chapter 2), or a combination of both, whereas the methane combustion model can be based on global reactions or detailed chemistry models.

Finally, one of the most interesting topic of study is the effect of radiative heat transfer on the structure and propagation of coal dust flames. These topics will be examined briefly, based on research that has been already performed prior to this thesis. This also gives us the opportunity to find topics that have probably not been explored before.

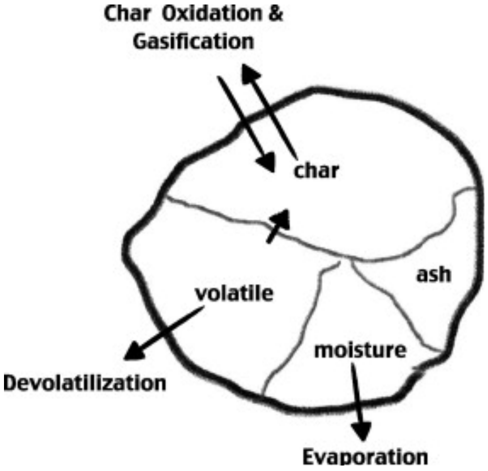

Figure 1-15. Structure and components of coal particles (Goshayeshi and Sutherland, 2014)

1.4.1 Shock-Flame Complex

Houim and Oran (2015b) used numerical simulations to study coal dust explosions of both dense and dilute layers. The authors used a high-order, compressible, multiphase fluid dynamics solver to simulate a couple of two-dimensional cases - one with a loosely packed layer of coal dust, having a volume fraction of 1%, and the other with a densely packed layer, having a volume fraction of 47%. The primary objective of this research was to study how a shock wave interacts with and affects a layer of coal dust. It was observed that a self-sustaining shock-flame complex (SFC) was formed that was also accelerated due to the pressure waves formed from the flame. For the dilute case, the SFC was accelerated from Mach 2.2 to 2.6 and for the dense case, from Mach 1.7 to 1.8. After the detonation decays to a shock, the turbulent, high temperature and high velocity flow behind the shock lifts and heats the dust. This dust cloud is then ignited by the reaction wave from the char combustion. The authors observed that the flame structure is similar to that of a turbulent nonpremixed flame. Radiative heat transfer, diffusion, and viscous stress were neglected in their calculations.

The flame structure in coal dust explosions was of main interest in their study. According to the structure of the SFC in their study (Fig. 1-1), the ignition point (IP) behaved like a reaction wave following a shock. The position of the IP is determined by a region behind the shock where the fuel (in this case carbon char) and air are premixed in stoichiometric proportions (solid volume fraction of $\approx\ 5 \times 10^{-4}$. The authors mention that the IP also depends on the ignition delay time of the char, which in turn depends on the time it takes for the dust to be lifted, the mixing of the dust with the air, the convective heating timescales and the chemical reaction time. There exist other examples of shock-flame complexes in the literature, for example the SFC in stoichiometric hydrogen-air mixture in the presence of obstacles (Gamezo et al., 2008) and reactive boundary layers (Gamezo et al., 2001).

1.4.2 Devolatilization of Coal Dust Particles

Devolatilization is the process of removal of volatile substances from a solid. According to Speight (2015), devolatilization in coal occurs when it is heated to more than 400 °C. In this scenario, the structure of coal undergoes changes, producing solid chars, tars, condensible liquids, and light gases.

As noted by Goshayeshi and Sutherland (2014), there are many models for the devolatilization of coal available in literature. Some models, such as Smith et al. (2013), provide details of the of the chemical structure of coal and how it affects the devolatilization. Other models use Arrhenius-type reaction models, for example, the single-rate model (Badzioch and Hawksley, 1970) and Kobayashi-Sarofim model (Kobayashi et al., 1977). Another model suggested the use of Gaussian distribution for the activation energy (Anthony and Howard, 1976) which posed the challenge of finding the finding the appropriate Gaussian distribution parameters (Please et al., 2003). Some of the more advanced models account for the functional groups of coal, such as the aromatic and aliphatic groups, as well as oxygen-carrying groups (Gavalas et al., 1981; Solomon et al., 1988). Grant et al. (1989), Brewster et al. (1988) and Smith et al. (2013) worked on another model called the Chemical Percolation Devolatilization (CPD) model, which considers the thermal decomposition of macromolecular network and the structural differences in different types of coal.

The Kobayashi-Sarofim model uses two first order Arrhenius-type reactions, with different weights. The overall reaction rate for this model can be written as

$$dm_v/dt = -[\alpha_1 B_1 e^{-E_1/RT_p} + \alpha_2 B_2 e^{-E_2/RT_p}]m_v, \tag{1-1}$$

where α_1 and α_2 are the weights, B_1 and B_2, the pre-exponential factors, and E_1 and E_2, the activation energies for the two reactions, and R is the universal gas constant. For their research, Goshayeshi and Sutherland (2014) uses the following reaction,

$$CH_aO_b \longrightarrow (b)\,CO + \left(\frac{a+b-1}{2}\right) H_2 + \left(\frac{1-b}{2}\right) C_2H_2, \tag{1-2}$$

where a and b can be derived from the coal's ultimate and proximate analysis.

The other devolatilization model that was used was the CPD model. One of the major benefits of the CPD model is that the devolatilization process accounts for the structural differences in the different types of coal. This model assumes coal to be "a macromolecular network of aromatic ring clusters of various sizes and types that are connected by a variety of chemical bridges (so-called 'labile bridges') of different bond strengths" (Goshayeshi and Sutherland, 2014). The devolatilization process starts with the breaking of the labile bridges (l), which form highly reactive intermediate bridges (l^*). Once these bridges react, they can form char and light gases, or side chains (δ) which ultimately convert to light gases. One of the downsides of this model is that it is numerically expensive. It requires the 18 ODEs to be solved and gives rise to a number of gas-phase species such as, CO_2, CO, CH_4, C_2H_2, HCN, NH_3, H and H_2O. However, on the plus side, this model has been shown to be extremely accurate.

The ignition delay results from Goshayeshi and Sutherland (2014) provide a comparison of the models, as shown in Fig. 1-16 for two variety of coals - Pittsburg coal and Black Thunder coal.

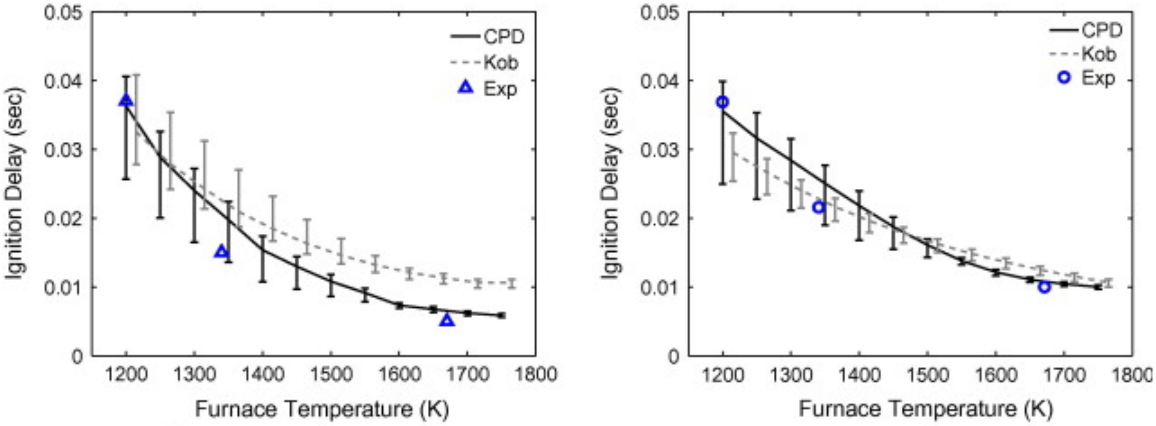

(a) Pittsburgh, cases $A.1$ & $A.2$

(b) BlackThunder, cases $A.5$ & $A.6$

Figure 1-16. Ignition delay times for Pittsburg and Black Thunder coal using the CPD and Kobayashi devolatilization models (Goshayeshi and Sutherland, 2014)

1.4.3 Burning Velocity and Flame Structure of Laminar Coal Dust Flames

According to Cloney et al. (2018), the works of Smoot and Horton (1977) and Krazinski et al. (1979) provide a summary of the experimental and numerical simulation work on laminar coal dust flames up to the 1980s. Their works segregated the literature into two types - one in which radiation is slightly important and the other in which radiation is the dominating heat transfer mechanism. The mathematical model developed by Smoot and Horton (1977) predicted that the coal dust flame burning velocities were in the range of 15 cm/s to 30 cm/s for 10 μm particles and 13 cm/s to 17 cm/s for 33 μm particles. Some of the more recent literature (Droujko et al., 2016) found that the importance of radiation depends on the dust cloud size. In the case of aluminum dust explosions, the radiative heating length is $\approx$ 25 cm (Julien et al., 2015b). Thus for scenarios that have lengths smaller than this, the radiative heating will not have an effect on the dust clouds ahead of the flame. However, for domains that are larger than 25 cm, the radiative preheating ahead of the flame may be significant. In their research, Cloney et al. (2018) neglect the radiative heating effects by using smaller domains to perform their simulations.

The authors use a single-step global reaction mechanism for the surface reaction (char combustion) and a single-step process for the coal devolatilization. However, their results for burning velocities and the flame structures match well with experimental data. Their prediction that the highest burning velocities occur at higher concentrations of dust and that the initial temperature also affects the burning velocity, agree with experimental observations in the literature. They do claim, however, that the simplified reaction mechanism is responsible for the incorrect prediction of certain species, for example, CO.

Cloney et al. (2018) also performed simulations to see the effects of different reaction mechanisms, various constant diffusion coefficients, and the continuum assumption on the flame structure of coal dust flames. Using various reactions mechanisms, including both global (one-step and two-step) and detailed chemistry models, the authors compared the results of flame thicknesses and species concentrations. The reaction mechanisms used are

- MP1 (CER, 2017a) single-step global reaction mechanism, with 5 species,
- BFER2 (Franzelli et al., 2012) two-step global reaction mechanism, with 6 species,
- DRM19 (Kazakov and Frenklach, 1994) reduced chemistry reaction mechanism, with 84 reactions and 19 species,

- GRI-Mech 3.0 (Smith et al., 1999) detailed chemistry reaction mechanism, with 325 reactions and 53 species.

For the first two models, the temperature and species mass fraction profiles are similar once steady-state is reached, however, the MP1 mechanism overpredicts the burning velocity (19.9 cm/s) by about 12% when compared to the BFER2 model (17.8 cm/s). These simulations were run with a particle concentration of 144.3 g/m^3. The temperature and species volume fraction from these calculations are shown in Fig. 1-17. The flame thickness for these cases are predicted to be around 1 mm, which according to the authors are lower than what is reported in literature.

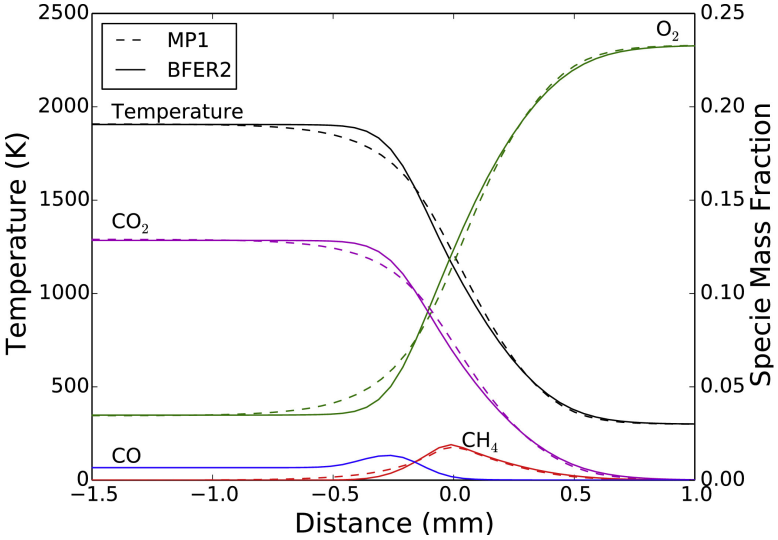

Figure 1-17. Temperature and species mass fraction profiles for MP1 and BFER2 methane combustion reaction mechanisms without surface chemistry (Cloney et al., 2018)

With the reduced (DRM19) and detailed (GRI-Mech 3.0) chemistry models, the flame thickness was predicted to be between 1 and 2 mm which is reported to agree well with previous simulations. The main difference between these two reaction models is the maximum predicted concentrations for radicals such as OH, O and H, as can be seen in Fig. 1-18. The burning velocities predicted by DRM19 and GRI-Mech 3.0 are 16.9 cm/s and 15.8 cm/s, respectively.

To see the effects of surface reactions, the authors ran simulations with constant diffusion coefficient values of 0, 100 and 500 mm^2/s at the particle surface. The surface reactions

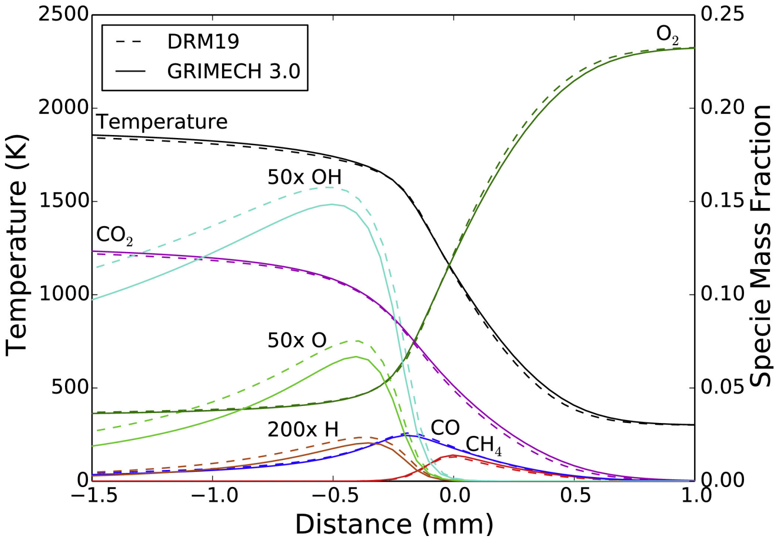

Figure 1-18. Temperature and species mass fraction profiles for DRM19 and GRI-Mech 3.0 reaction mechanisms without surface chemistry (Cloney et al., 2018)

depend on the ability of the oxygen surrounding the particles to diffuse to the surface of the particles so that the oxidizer and fuel can combine to ignite. The methane that is released from the particle surface flows in a direction away from the surface, whereas the oxygen needs to flow toward the surface against this outward flow of methane. If the diffusion coefficient is higher, the oxygen has a greater ability to reach the surface. These simulations were run with the MP1 chemistry model. One of the primary observations of this test was the significant increase in both the flame temperature and the burning velocity than the cases without surface reactions. The oxygen mass fraction behind the flame also dropped. When the diffusion coefficient was increased beyond 100 mm^2/s, 99% of the oxygen was consumed by the reactions within a millimeter of the flame front, similar to what was reported by Bradley et al. (1994). However, when the diffusion coefficient was increased to high values of 500 mm^2/s, the gas phase and heterogeneous reactions start to compete with each other for oxygen, which results in a significant amount of unreacted methane. Thus, using a nominal value for diffusion coefficient of 100 mm^2/s seems reasonable, and has been used in our research, unless otherwise noted. The temperature and species profiles for the various diffusion coefficients used are shown in Fig. 1-19.

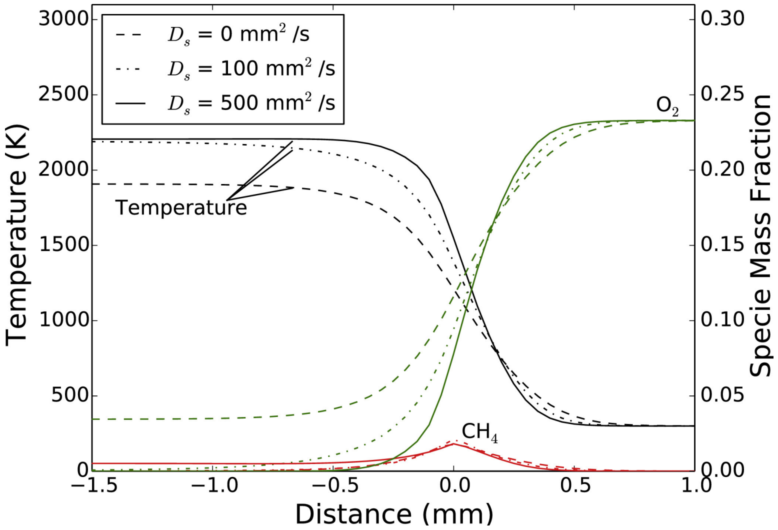

Figure 1-19. Temperature and species mass fraction profiles for MP1 reaction mechanism with surface chemistry (Cloney et al., 2018)

The use of Eulerian description for the particle phase is common among research groups that work on simulation of coal dust flames. To understand the validity of this assumption and see the effect it has on the results, the authors performed simulations with both Eulerian and Lagrangian discretizations for the particle phase. Using the MP1 and DRM19 chemistry models to run the calculations, it was observed that for both the chemistry models, the discrete representation reported lower values for the laminar burning velocity. Looking closely at the flame position data (Fig. 1-20), the authors concluded that this occurs because when using the discrete model, the devolatilization, ignition and surface reaction accelerate the flame, but once that particle has completely burned, there is a deceleration in the flame till the next particle starts burning. This trend was also observed for cases with different initial temperatures and dust concentrations for 33 μm particles (Fig. 1-21).

1.4.4 Effect of Thermal Radiation on Coal Dust Explosions

There are few research articles available in the literature about the effect of thermal radiation on dust cloud flames. Some of the recent work in this area include Cao et al. (2014a), Houim and Oran (2015a), Bidabadi and Azad (2015) and Liberman et al. (2015). While the first three concentrate on coal dust flames, the fourth article is about radiation

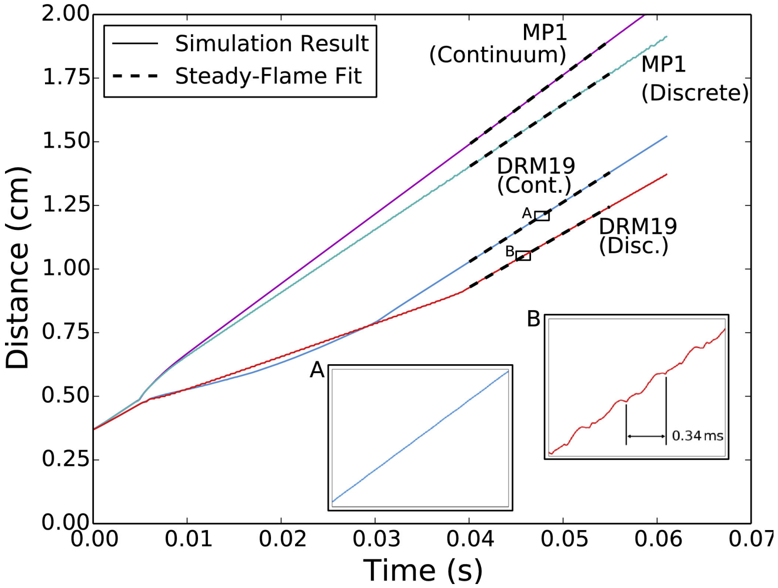

Figure 1-20. Comparison of flame location using continuum and discrete models for the MP1 and DRM19 reaction mechanisms (Cloney et al., 2018)

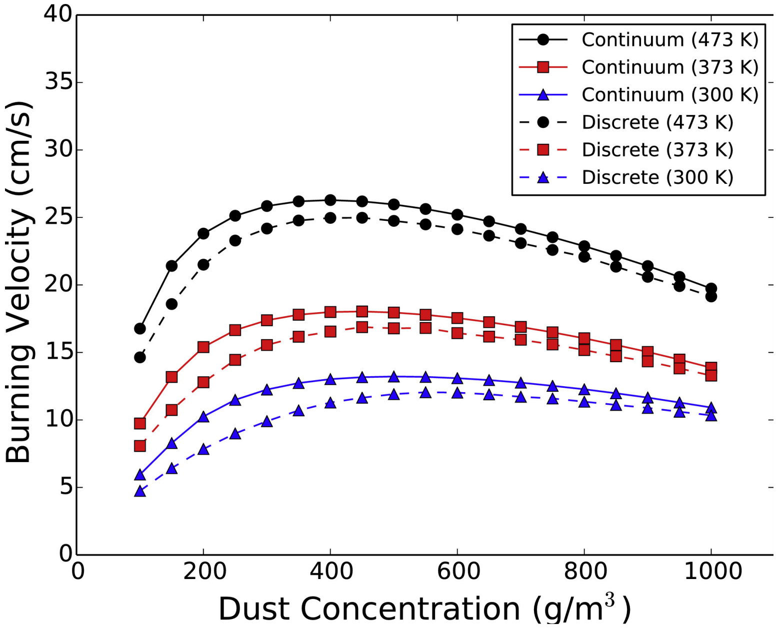

Figure 1-21. Burning velocity for continuum and discrete models (Cloney et al., 2018)

effects of particle-laden hydrogen-oxygen flames. Liberman et al. (2015) assumes that the gas phase is transparent to radiation, whereas the particles can both absorb and emit radiation. Depending on whether the particle distribution was uniform or nonuniform, the authors observed different effects. The reactants ahead of the flame was preheated due to thermal radiation which caused either the flame to accelerate or start a new deflagration or detonation ahead of the flame. Furthermore, whether the radiative preheating triggers a deflagration or a detonation ahead of the flame depends on the radiation absorption length.

In Houim and Oran (2015a), the authors used a filtered spherical harmonic (FP_3) approximation to the radiative transfer equation (RTE) to perform numerical calculations to study the effect of radiative heat transfer on coal dust cloud ignition and propagation. They looked at two configurations - the first one was the flame propagating through an open tube, and the second one was in a closed tube with two chambers, separated by a window that is transparent to radiation. The simulations were performed both with and without radiation and for equivalence ratios of 1.2 and 2.4. Assuming spectrally gray radiation, their results showed that for the case with radiation, the flame was able to jump across the barrier window to the other chamber, purely due to radiation heat transfer that was able to ignite the cold reactants, whereas without radiation, this was not observed.

1.5 Scope of this Research

The main objective behind this work is to understand the influence of thermal radiation on the structure and propagation of layered coal-dust explosions using numerical simulations. To mimic a layered coal-dust explosion in a mine, we use a numerical setup shown in Fig. 1-22. In order to solve this problem numerically, we have to first be able to accurately simulate the multiphase flow in the computational domain. Thus, thorough knowledge of the governing equations for multiphase reactive flows and their numerical methods is imperative. Furthermore, to accurately simulate radiation heat transfer, we need to numerically solve the Radiation Transfer Equation (RTE) and add it as a source term to the hydrodynamic equations.

In Chapter 2 of this dissertation, we take a detailed look at the governing equations and mathematical models for the multiphase flow. We present an overview of the Euler equations and discuss each term of the equations in details. Then we take a closer look at the chemical reactions for both the gas and solid phases. The thermodynamic and transport models being

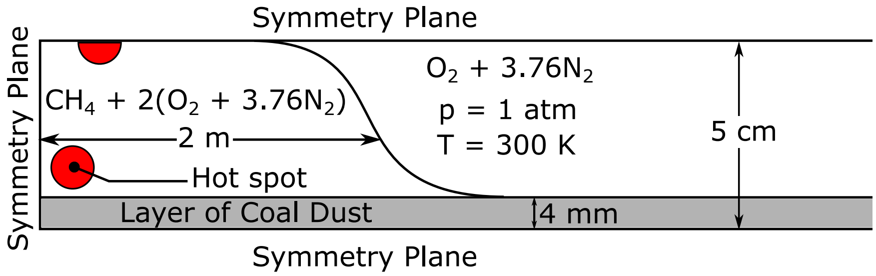

Figure 1-22. Numerical setup for the simulation of layered coal-dust explosions.

used in this research are then introduced. Finally we talk about the radiation solver theory and provide insight on the spherical harmonics (P_N) approximation to the RTE and the mathematical models used for the gas and solid phase radiative properties.

Chapter 3 is dedicated to the numerical methods used to solve the equations discussed in chapter 2. Here we talk about the flux schemes used for the solid and gas phases as well as the numerical techniques to solve the hyperbolic terms, reaction terms and the radiative heat transfer.

We present the code verification tests in Chapter 4 and present their results, comparing them to available analytical data or other established numerical codes, such as Cantera for chemical reactions. This is done to check the accuracy of the code and establish confidence in it. We do the verification tests in parts. The first tests are to check the ability of the code to accurately solve simple 1-D, single and multi-phase, compressible flow problems. Then we look at the chemical reactions and make sure that we get accurate results from the time-integration of the associated equations. This is done by running constant-volume reactor and flame speed tests for the gas-phase reactions. Finally, we test the accuracy of the radiation solver by solving the 2-D lattice problem.

Results from tests performed using the single-step reaction mechanism and their discussions are presented in Chapter 5. We perform layered coal-dust explosion problems in long, narrow channels, both with and without thermal radiation. The results from the radiative and non-radiative cases are then compared and the effects of radiation heat transfer on the results are discussed.

In Chapter 6, we will look at the effects of using a different reaction mechanism. After repeating the same tests from Chapter 5, we also explore the influence of particle size. Finally, we compare the results from the two different reaction mechanisms.

Chapter 7 presents the results from our three-dimensional calculations on the same tests, with reduced channel length and lower resolution. We also perform a 2-D version of the 3-D case to be able to properly compare the results from the 2-D and 3-D tests. This will give us an insight into the importance of considering all three dimensions.

The last chapter, Chapter 8, we summarize the conclusions of all the results. In addition, we propose the ideas for future work that that may be of interest to answer the questions that we face as a consequence of the results presented in this work. We also discuss the different scenarios that may be interesting to investigate to further our knowledge on the topic.

CHAPTER 2
GOVERNING EQUATIONS AND MATHEMATICAL MODELS

To simulate dust explosions in coal mines, we use a scaled down version (Fig. 1-22) of the experimental setup in Sapko et al. (2000), shown in Fig. 2-1. The details of the numerical setup will be explained in Chapter 5. To simulate such a complex scenario, we have to numerically solve discretized versions of the various governing equations, including the Navier-Stokes (NS) equations for the hydrodynamic part and the radiative transport equations (RTE) for the thermal radiation. The hydrodynamic solver is further composed of two phases - the granular (solid) phase and the gas phase, with their own set of governing equations and models to solve those equations, and source terms such as chemical reactions. The two phases are coupled to each other via various physical processes such as the drag, convective heat transfer and the Magnus lifting forces. The radiation solver is coupled to the hydrodynamic solver via the energy equation. To solve all these, we need a numerical code. For this research, we use the code called HyBurn, that was developed by our research group at the University of Florida.

HyBurn is a fully compressible, multidimensional, multiphase reactive flow solver that has the ability to also solve the radiative heat transfer. It uses a fully structured mesh for the discretization of the governing equations. We use Eulerian-Eulerian approach (continuum assumption) for both the granular and the gas phases. For our research, we use high order interpolation schemes. Time marching in HyBurn is performed explicitly using the Runge-Kutta (RK) 3 time integration method. We use a variable specific heats fluid model that will be explained further later on in this chapter. Details about the numerical methods used in HyBurn will also be discussed in Chapter 3. A schematic diagram of the HyBurn solver and its components is shown in Fig. 2-2.

2.1 Governing Equations

Let us now look at the various governing equations. The equations of motion for both the fluid and the particle phases described here are based on the system of equations used in

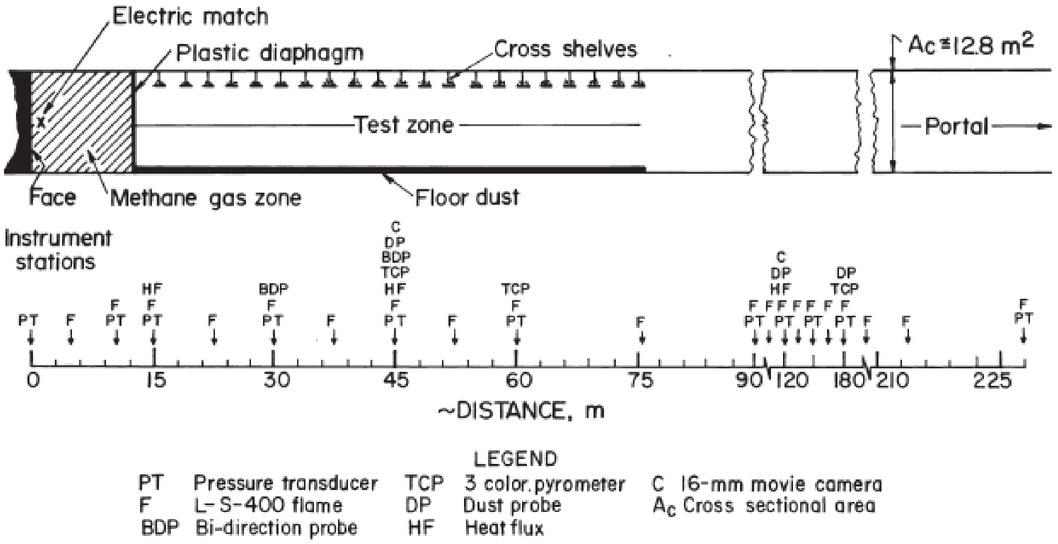

Figure 2-1. Side view of D-drift in the Lake Lynn experimental mine, showing instrumentation (Sapko et al., 2000).

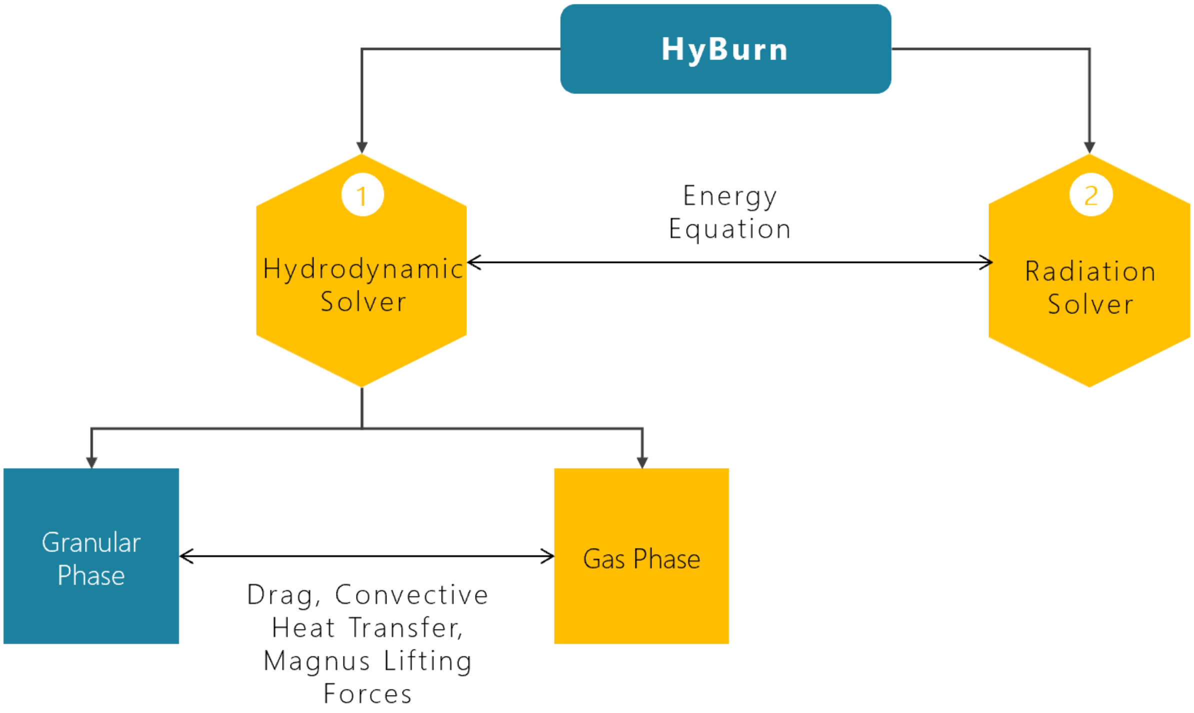

Figure 2-2. Schematic diagram of HyBurn and its components.

Houim and Oran (2016) but have been modified to include the diffusion terms to get the full Navier-Stokes form, and also include the radiation coupling source terms.

For the gas phase, the governing equations with N$_g$ chemical species are given by

$$\frac{\partial \alpha_g \rho_g}{\partial t} + \nabla \cdot (\alpha_g \rho_g \boldsymbol{v}_g) = S^M, \tag{2-1}$$

$$\frac{\partial \alpha_g \rho_g Y_{g,j}}{\partial t} + \nabla \cdot (\alpha_g \rho_g Y_{g,j} \boldsymbol{v}_g) + \alpha_g \nabla \cdot (\rho_g Y_{g,j} \boldsymbol{V}_{g,j}) = \alpha_g \dot{\boldsymbol{\omega}}_{g,j} + S^Y_{g,j}, \qquad j = 1, ..., N_g, \tag{2-2}$$

$$\frac{\partial \alpha_g \rho_g \boldsymbol{v}_g}{\partial t} + \nabla \cdot (\alpha_g \rho_g \boldsymbol{v}_g \boldsymbol{v}_g) + \nabla \alpha_g p_g = p_{int} \nabla \alpha_g + \alpha_g \rho_g \boldsymbol{g} + \nabla \alpha_g \cdot (\boldsymbol{\tau}_g) + \boldsymbol{S}^p, \tag{2-3}$$

$$\frac{\partial \alpha_g \rho_g E_g}{\partial t} + \nabla \cdot [\alpha_g \boldsymbol{v}_g (\rho_g E_g + p_g)] = -\nabla \cdot (\alpha_g \boldsymbol{q}) - p_{int} \frac{\partial \alpha_g}{\partial t} + \alpha_g \rho_g \boldsymbol{g} \cdot \boldsymbol{v}_g + \alpha_g \nabla \cdot (\boldsymbol{\tau}_g \cdot \boldsymbol{v}_g) + S^E_g + S^{\text{rad}}_g, \tag{2-4}$$

where subscript 'g' is for gas. Also,

$$\alpha_g + \alpha_s = 1 \quad \text{and} \quad \nabla \alpha_g = -\nabla \alpha_s, \tag{2-5}$$

where subscript 's' is for granular. $Y_{g,j}$, ρ_g, p_g, T_g, E_g and $\boldsymbol{v}_g$ are mass fraction of j^{th} species, density, pressure, temperature, total energy and velocity vector of the gas phase, respectively. $\dot{\boldsymbol{\omega}}_{g,j}$ denotes the homogeneous chemical reaction rates. S^M, $S^Y_{g,j}$, $\boldsymbol{S}^p$ and S^E_g are the interphase coupling terms for mass, momentum and energy transfer, and S^{rad}_g is the source term due to thermal radiation. These are discussed in details later on in this chapter. $\boldsymbol{V}_{g,j}$ is the diffusion velocity of species j. $\boldsymbol{q}$ is the diffusion heat flux vector, which is given by

$$\boldsymbol{q} = \sum_{j=1}^{N_g} (\rho_{g,j} Y_{g,j} \boldsymbol{V}_{g,j}) h_{g,j} - \lambda_g \nabla T_g, \tag{2-6}$$

Lastly, $\boldsymbol{\tau}_g$ is the viscous stress tensor.

The Navier-Stokes equations for the granular phase with N_s chemical species can be written as

$$\frac{\partial \alpha_s \rho_s}{\partial t} + \nabla \cdot (\alpha_s \rho_s \boldsymbol{v}_s) = -S^M, \tag{2-7}$$

$$\frac{\partial \alpha_s \rho_s Y_{s,j}}{\partial t} + \nabla \cdot (\alpha_s \rho_s Y_{s,j} \boldsymbol{v}_s) = \alpha_s \dot{\boldsymbol{\omega}}_{s,j} + S^Y_{s,j}, \qquad j = 1, ..., N_s, \tag{2-8}$$

$$\frac{\partial \alpha_s \rho_s \boldsymbol{v}_s}{\partial t} + \nabla \cdot (\alpha_s \rho_s \boldsymbol{v}_s \boldsymbol{v}_s) + \nabla p_s + \nabla p_{fric} = -\nabla \alpha_s p_g - p_{int} \nabla \alpha_g + \alpha_s \rho_s \boldsymbol{g} - \boldsymbol{S}^p, \tag{2-9}$$

$$\frac{\partial \alpha_s \rho_s E_s}{\partial t} + \nabla \cdot (\alpha_s \rho_s E_s \boldsymbol{v}_s) = -p_s \nabla \cdot \boldsymbol{v}_s + S^{PTE}_s, \tag{2-10}$$

$$\frac{\partial \alpha_s \rho_s e_s}{\partial t} + \nabla \cdot (\alpha_s \rho_s e_s \boldsymbol{v}_s) = S^E_s + S^{\text{rad}}_s, \tag{2-11}$$

where 'PTE' stands for pseudo-thermal energy. p_s, p_{fric}, e_s and E_s are the solids pressure, frictional-collisional pressure, internal energy and PTE respectively. $\dot{\boldsymbol{\omega}}_{s,j}$ are the homogeneous chemical reaction rates for the granular species. Similarly as before, the interphase coupling terms, $S^Y_{s,j}$, S^{PTE}_s and S^E_s, and the thermal radiation source term, S^{rad}_s are discussed in details later in this chapter.

For radiation heat transfer, the governing equation, known as the radiation transfer equation (RTE), needs to be solved to obtain the radiation field and the radiative heating and cooling rates for the particles. The RTE can be written as

$$\begin{aligned} \frac{1}{c}\frac{\partial I}{\partial t} + \Omega \cdot \nabla I + \sigma_s I = {} & \frac{1}{4\pi} \int_{4\pi} d\Omega' \sigma_s I(\boldsymbol{r}, \Omega') \\ & + \sigma_{a,\text{gas}} \left(\frac{a c T^4_{\text{gas}}}{2\sqrt{\pi}} - I \right) \\ & + \sigma_{a,\text{particles}} \left(\frac{a c T^4_{\text{particles}}}{2\sqrt{\pi}} - I \right), \end{aligned} \tag{2-12}$$

where, c is the speed of light, I is the radiation intensity, Ω is the angular variable, σ_s is the scattering coefficient, $\sigma_{a,\text{gas}}$ and $\sigma_{a,\text{particles}}$ are the absorption coefficient for the gas and particle phases respectively, a is a radiation constant (1.372×10^{13} Jm^{-3}keV^{-4}). G is the incident radiation, defined as

$$G = \int_{4\pi} I d\Omega. \tag{2-13}$$

The radiation heat sources can be written as

$$S_g^{\text{rad}} = -\nabla \cdot q_{\text{rad,gas}} = \sigma_{a,\text{gas}}(G - 4\pi I_{b,\text{gas}}), \tag{2-14}$$

and

$$S_s^{\text{rad}} = -\nabla \cdot q_{\text{rad,particles}} = \sigma_{a,\text{particles}}(G - 4\pi I_{b,\text{particles}}), \tag{2-15}$$

for the gas and particles respectively, where q_{rad} is the radiative heat flux and I_b is the blackbody intensity.

Having looked at all the relevant governing equations, now let us understand the details about the various terms in the governing equations and the models that are used to compute them.

2.2 Granular Phase Governing Equation Terms

The PTE represents the energy due to random translational motion of particles and is given by

$$E_s = \frac{3}{2}\Theta_s. \tag{2-16}$$

where Θ_s is the granular temperature, which is the mean square of the velocity fluctuations of the particles. This should not be confused with the thermodynamic temperature of the granular phase, T_s, which is obtained from the solid sensible internal energy, e_s, using the equation:

$$e_s = \sum_{j=1}^{N_s} Y_{s,j}\left(e_{fj}^0 + \int_{T_0}^{T_s} C_{V,s,j}(s)ds\right), \tag{2-17}$$

where e^0_{fj} is the internal energy of formation and $C_{V,s,j}$ is the constant-volume specific heat of the j^{th} species.

The solid phase density can be written as,

$$\rho_s = \sum_{j=1}^{N_s} Y_{s,j} \rho_{s,j}(T_s), \tag{2-18}$$

where $\rho_{s,j}$ is the density of the j^{th} species in the granular phase. Here we assume that ρ_s is constant.

The solids pressure p_s is given by

$$p_s = \alpha_s \rho_s \Theta_s [1 + 2(1+e)\alpha_s g_0], \tag{2-19}$$

which is known as equation of state for a granular gas. Here e is the coefficient of restitution and g_0 is the radial distribution function, which is given by

$$\frac{1}{g_0} = 1 - \left(\frac{\alpha_s}{\alpha_{s,max}} \right)^{1/3}, \tag{2-20}$$

where $\alpha_{s,max}$ is the granular phase packing limit (random close-packing limit of uniform spheres), which is a constant (usually set to 0.65).

Frictional-collisional pressure must also be considered in regions og high particle volume fractions. This is a pressure-like force that arises from the layers of granular particles sliding over each other. When this is included, it limits compaction when Θ_s is very small. Here, the correlation of Johnson and Jackson (1987) is used,

$$p_{fric} = \begin{cases} 0 & \text{if } \alpha_s < \alpha_{s,crit}, \\ 0.1\alpha_s \frac{(\alpha_s - \alpha_{s,crit})^2}{(\alpha_{s,max} - \alpha_s)^5} & \text{if } \alpha_s \geq \alpha_{s,crit}, \end{cases} \tag{2-21}$$

where $\alpha_{s,crit}$ is 0.5 unless otherwise noted. Thus, the total intergranular stress can now be written as,

$$p_{s,tot} = p_s + p_{fric}. \tag{2-22}$$

Since the granular phase is also compressible, just as the gas phase is, the granular-compaction wave speed can be derived as a function of α_s as,

$$c_s{}^2 = \frac{1}{\rho_s}\left[\frac{\partial p_s^{tot}}{\partial \alpha_s}\Big|_{\Theta_s} + \frac{2}{3}\frac{\Theta_s\left(\frac{\partial p_s^{tot}}{\partial \Theta_s}\Big|_{\alpha_s}\right)^2}{\rho_s \alpha_s^2}\right]. \tag{2-23}$$

Using the previously defined equations for p_s and p_{fric}, we can write

$$c_s{}^2 = \Theta_s(A + \frac{2}{3}A^2 + \alpha_s B) + c_{fric}^2, \tag{2-24}$$

where,

$$A = 1 + 2(1+e)\alpha_s g_0, \quad B = 2(1+e)(g_0 + \alpha_s g_0'), \quad g_0' = \frac{g_0^2}{3\alpha_{s,max}}\left(\frac{\alpha_{s,max}}{\alpha_s}\right)^{2/3}. \tag{2-25}$$

Also,

$$c_{fric}^2 = \begin{cases} 0 & \text{if } \alpha_s < \alpha_{s,crit}, \\ \frac{1}{\rho_s}\frac{(\alpha_s - \alpha_{s,crit})}{(\alpha_{s,max} - \alpha_s)^5}\left[\alpha_s\left(\frac{1}{5} + \frac{1}{2}\frac{\alpha_s - \alpha_{s,crit}}{\alpha_{s,max} - \alpha_s}\right) + \frac{\alpha_s - \alpha_{s,crit}}{10}\right] & \text{if } \alpha_s \geq \alpha_{s,crit}, \end{cases} \tag{2-26}$$

which is the frictional contribution to the compaction wave speed.

2.3 The Nozzling and pDV Work Terms

According to Gidaspow (1994), it is common to assume $p_{int} = p_g$. We can also assume that ρ_s is independent of pressure and intergranular stress. Then the pDV work term can be written as,

$$-p_{int}\frac{\partial \alpha_g}{\partial t} = p_g \frac{\partial \alpha_s}{\partial t} = -p_g \nabla \cdot \alpha_s \boldsymbol{v}_s - p_g \frac{S^M}{\rho_s}. \tag{2-27}$$

Using this, the momentum equations for the two phases become

$$\frac{\partial \alpha_g \rho_g \boldsymbol{v}_g}{\partial t} + \nabla \cdot (\alpha_g \rho_g \boldsymbol{v}_g \boldsymbol{v}_g) + \nabla \alpha_g p_g = p_g \nabla \alpha_g + \alpha_g \rho_g \boldsymbol{g} + \boldsymbol{S}^p, \tag{2-28}$$

$$\frac{\partial \alpha_s \rho_s \boldsymbol{v}_s}{\partial t} + \nabla \cdot (\alpha_s \rho_s \boldsymbol{v}_s \boldsymbol{v}_s) + \nabla p_s + \nabla p_{fric} = -\alpha_s \nabla p_g - p_{int} \nabla \alpha_g + \alpha_s \rho_s \boldsymbol{g} - \boldsymbol{S}^p, \tag{2-29}$$

and the gas-phase energy equation becomes

$$\frac{\partial \alpha_g \rho_g E_g}{\partial t} + \nabla \cdot [\alpha_g \boldsymbol{v}_g (\rho_g E_g + p_g)] = -p_g \nabla \cdot \alpha_s \boldsymbol{v}_s + \alpha_g \rho_g \boldsymbol{g} \cdot \boldsymbol{v}_g + S_g^E, \tag{2-30}$$

where the pDV work due to phase change is accounted for in S_g^E.

2.4 Interphase Mass, Momentum and Energy Transfer

Interphase mass, momentum and energy exchange due to drag, convective heat transfer, phase change, dissipation of PTE due to inelastic collisions, and lifting forces have to be considered. Mass exchange due to phase change is

$$S^M = \dot{M}, \tag{2-31}$$

where $\dot{M}$ is the total mass rate of phase change, and is given by

$$\dot{M} = \sum_{i=1}^{N_g} S_{g,i}^Y = -\sum_{i=1}^{N_s} S_{s,i}^Y, \tag{2-32}$$

and $S_{g,i}^Y$ and $S_{s,i}^Y$ are the mass rates of production of i^{th} specie in the gas and particle phases, respectively, due to phase change. The source terms for the momentum equations are

$$\boldsymbol{S}_p = \boldsymbol{f}_{Drag} + \boldsymbol{f}_{Lift} + \boldsymbol{v}_{int} \dot{M}. \tag{2-33}$$

Here, the correlation of Gidaspow (1994) has been used for the granular drag force,

$$\boldsymbol{f}_{Drag} = K_{sg} (\boldsymbol{v}_s - \boldsymbol{v}_g), \tag{2-34}$$

and

$$K_{sg} = \begin{cases} 0.75 C_d \frac{\rho_g \alpha_g \alpha_s |\boldsymbol{v}_s - \boldsymbol{v}_g|}{d_s \alpha_g^{2.65}} & \text{if } \alpha_g \geq 0.8, \\ 150 \frac{\alpha_s^2 \mu_g}{\alpha_g d_s^2} + 1.75 \frac{\rho_g \alpha_s |\boldsymbol{v}_g - \boldsymbol{v}_s|}{d_s} & \text{if } \alpha_g < 0.8, \end{cases} \tag{2-35}$$

with drag coefficient,

$$C_d = \begin{cases} 24(\alpha_g Re)^{-1}[1 + 0.15(\alpha_g Re)^{0.687}] & \text{if } \alpha_g Re < 1000, \\ 0.44 & \text{if } \alpha_g Re \geq 1000, \end{cases} \tag{2-36}$$

and Reynold's number given by,

$$Re = \frac{\rho_g |\boldsymbol{v}_g - \boldsymbol{v}_s| d_s}{\mu_g}. \tag{2-37}$$

The Magnus lift force is used to calculate $\boldsymbol{f}_{Lift}$,

$$\boldsymbol{f}_{Lift} = C_l \alpha_s \rho_g (\boldsymbol{v}_s - \boldsymbol{v}_g) \times (\nabla \times \boldsymbol{v}_g), \tag{2-38}$$

where the lift coefficient, C_l, is a constant value of 0.5. The Saffman lift force is neglected in this research.

The interfacial velocity depends on the velocity of the phase that loses mass. Thus,

$$\boldsymbol{v}_{int} = \begin{cases} \boldsymbol{v}_s & \text{if } \dot{M} > 0, \\ \boldsymbol{v}_g & \text{if } \dot{M} < 0. \end{cases} \tag{2-39}$$

The energy equation source terms can be written as,

$$S_g^E = -q_{conv} + \phi_{visc} - \phi_{slip} + E_{g,int}\dot{M} + (\boldsymbol{f}_{Drag} + \boldsymbol{f}_{Lift}) \cdot \boldsymbol{v}_s, \tag{2-40}$$

$$S_S^E = q_{conv} - e_{s,int}\dot{M} + \dot{\gamma}, \tag{2-41}$$

$$S_S^{PTE} = -\dot{\gamma} - \phi_{visc} + \phi_{slip} - E_{s,int}\dot{M}, \tag{2-42}$$

where $E_{g,int} = H_{g,int} - p_{int}/\rho_s$. Thus, effects of PTE dissipation through inelastic collisions ($\dot{\gamma}$), PTE dissipation through viscous effects of particles immersed in a fluid (ϕ_{visc}), and PTE production due to drag forces (ϕ_{slip}) are considered in addition to the convective heat transfer between the two phases, q_{conv}, which is given by the relation,

$$q_{conv} = 6\frac{\alpha_s \lambda_g Nu}{d_s^2}(T_g - T_s). \tag{2-43}$$

Here the Nusselt number has been calculated using the correlation of Gunn (1978),

$$Nu = (7 - 10\alpha_g + 5\alpha_g^2)(1 + 0.7Re^{0.2}Pr_g^{1/3}) + (1.33 - 2.4\alpha_g + 1.2\alpha_g^2)Re^{0.7}Pr_g^{1/3}, \tag{2-44}$$

where Pr_g is the gas-phase Prandtl number.

For the viscous damping of the PTE, the model of Gidaspow (1994) has been used,

$$\phi_{visc} = 3K_{sg}\Theta_s, \tag{2-45}$$

and the rate of rate of production of gas phase internal energy due to frictional heating of the accelerating particles is given as,

$$q_{Drag} = \Delta\boldsymbol{v} \cdot \boldsymbol{f}_{Net}, \tag{2-46}$$

where $\boldsymbol{f}_{Net} = \boldsymbol{f}_{Drag} + \boldsymbol{f}_{Lift}$ and $\Delta\boldsymbol{v} = \boldsymbol{v}_s - \boldsymbol{v}_g$. Part of this internal energy produces random translational motion of the particles, which increases the PTE. For the granular dissipation, a variant of Haff's cooling law has been used, Haff (1983); Brilliantov and Pöschel (2010),

$$\dot{\gamma} = \frac{12(1 - e^2)g_0\alpha_s^2}{\sqrt{\pi}}\frac{\rho_s\Theta_s^{3/2}}{d_s}. \tag{2-47}$$

The interfacial energy exchange terms for phase change also depend on the phase that loses mass, just as with the interfacial velocity,

$$E_{g,int} = \begin{cases} e_s + E_s + \boldsymbol{v}_s \cdot \boldsymbol{v}_s/2 & \text{if } \dot{M} > 0, \\ E_g & \text{if } \dot{M} < 0, \end{cases} \tag{2-48}$$

$$E_{s,int} = \begin{cases} E_s & \text{if } \dot{M} > 0, \\ 0 & \text{if } \dot{M} < 0, \end{cases} \tag{2-49}$$

$$e_{s,int} = \begin{cases} e_s & \text{if } \dot{M} > 0, \\ E_g - \boldsymbol{v}_g \cdot \boldsymbol{v}_g/2 & \text{if } \dot{M} < 0. \end{cases} \tag{2-50}$$

2.5 Chemical Reactions

The reactions that take place can be categorized into solid-phase and gas-phase reactions, depending on which phases are involved in the reaction. The solid-phase reactions include the devolatilization of the volatiles, sublimation of the moisture and the heterogeneous reaction involving the combustion of char. The devolatilization process releases gaseous methane $CH_{4,g}$, and solid char C_s in a single-step irreversible process based on Kobayashi et al. (1977).

In the gas phase, the combustion of methane is also based on a single-step irreversible process. The arrhenius data for the reaction is taken from CER (2017b) and will be discussed in more details later.

2.5.1 Solid-Phase Reactions

The coal particles are assumed to be composed of three parts: (a) dry ash-free (DAF) part, (b) moisture or H_2O_s, and (c) ash. The first step is the devolatilization of the DAF to produce gaseous methane $CH_{4,g}$ and solid-phase carbon or char C_s.

According to the model based on Kobayashi et al. (1977), the devolatilization takes part via two competing reactions

$$\mathrm{DAF} \xrightarrow{\mathrm{k_{DAF,1}}} \mathrm{CH_4} + \mathrm{C_s}, \tag{R1}$$

and

$$\mathrm{DAF} \xrightarrow{\mathrm{k_{DAF,2}}} \mathrm{CH_4} + \mathrm{C_s}, \tag{R2}$$

where the volatiles in this study are both assumed to be $CH_{4,g}$ and the residues are C_s. Assuming both reactions to be of arrhenius type, the rate constants can be expressed as

$$k_1 = B_1 exp(-E_1/RuT_p), \tag{2-51}$$

$$k_2 = B_2 exp(-E_2/RuT_p), \tag{2-52}$$

where the pre-exponential factors $B1$ and $B2$ are taken as 3.7×10^5 and 1.46×10^{13}, respectively, activation energies E_1 and E_2 are 7.37×10^7J and 2.51×10^8J, respectively, and T_p is the particle temperature. At lower temperatures, the first reaction is more dominant and asymptotes to a yield value of 0.37. At higher temperatures, however, the second reaction proceeds much faster than the first reaction and leads to a maximum yield value of 0.56. Together, the yield values from the two reactions are combined to give the yield value of methane. The remainder of the DAF forms the char.

The next step is the sublimation of moisture. This is also assumed to be an arrhenius type reaction

$$\mathrm{H_2O_s} \xrightarrow{\mathrm{k_{H_2O}}} \mathrm{H_2O_g}, \tag{R3}$$

and the rate constant is again given by

$$k = A_{H_2O} exp(-Ea_{H_2O}/RuT_p), \tag{2-53}$$

where $A_{H_2O} = 1.46 \times 10^{13}$ and $Ea_{H_2O} = 1.464 \times 10^8$J.

Finally, we come to the combustion of coal. There are two regimes that decide the reaction rate: (a) diffusion-limited regime, and (b) kinetic-limited regime. In the diffusion-limited regime, the reaction rate is dictated by how fast the oxygen molecules can diffuse to the surface of the carbon particles, whereas, in the kinetic-limited regime, it is dependent on the surface kinetics (meaning that the concentration of O_2 is large at the surface), and thus follows an arrhenius-type reaction. These reaction rate constants can be calculated using

$$k_{f(C),diff} = \frac{24 T_g D_s}{T_g + T_p} \tag{2-54}$$

and

$$k_{f(C),kin} = A_C exp(-Ea_C/RuT_p), \tag{2-55}$$

where, $k_{f(C),diff}$ and $k_{f(C),kin}$ are the reaction rate constants in the diffusion-limited and kinetic-limited regimes, T_g and T_p are the gas and particle-phase temperatures, D_s is the gas diffusivity at the surface of the particle and is a constant that can be varied, $A_C = 9.5 \times 10^7$ and $Ea_C/Ru = 17,977$J are the pre-exponential factor and activation energies for the kinetic-limited reaction. Then the overall reaction rate is taken as

$$k_{f(C)} = \frac{k_{f(C),diff} \times k_{f(C),kin}}{k_{f(C),diff} + k_{f(C),kin}}, \tag{2-56}$$

using the resistor circuit analogy.

Then the chemical reaction can be expressed as

$$\mathrm{C_s} + \mathrm{O_{2,g}} \xrightarrow{\mathrm{k_{f(C)}}} \mathrm{CO_2}, \tag{R4}$$

2.5.2 Gas-Phase Reactions

For the gas-phase reactions, two reaction mechanisms were considered. The first mechanism consists of a single-step irreversible methane air combustion reaction, and the second mechanism is based on a two-step methane air combustion reaction, with the first step being a irreversible reaction and the second step is a reversible reaction. Here we discuss both mechanisms in more details.

2.5.2.1 Single-step methane-air reaction

This gas-phase reaction mechanism consists of a methane combustion reaction, which is assumed to be a global, one-step, irreversible reaction based on the data from CER (2017b). The reaction can be expressed as

$$\mathrm{CH_4} + 2\,\mathrm{O_2} \xrightarrow{\mathrm{k_{CH_4}}} \mathrm{CO_2} + 2\,\mathrm{H_2O}. \tag{R5}$$

and is assumed to be of arrhenius-type. The order of the reaction with respect to CH_4 and O_2 are 1 and $1/2$ respectively. The reaction rate constant can be written as

$$k_{CH_4} = A_{CH_4} T_g^b exp(-Ea_{CH_4}/RuT), \tag{2-57}$$

where, $A_{CH_4} = 1.1 \times 10^10$ is the pre-exponential factor, $b = 0$ is the temperature dependence of the pre-exponential factor, which is zero in this case, meaning that the pre-exponential factor is independent of temperature, and $Ea_{CH_4} = 20,000$ cal/mol. The reaction is time-integrated using the YASS method (Khokhlov et al., 2012).

Since this is a mixed-order reaction, the reaction rate can be written as

$$RR = k_{CH_4}[CH_4]^1[O_2]^{1/2} \tag{2-58}$$

such that it is first order with respect to CH_4 and half order with respect to O_2. Here, $[CH_4]$ and $[O_2]$ represent the molar concentrations of methane and oxygen. If we denote the rate of consumption of CH_4 by ϵ, then

$$RR = \frac{d\epsilon}{dt}. \tag{2-59}$$

Following with the analysis leads to

$$\frac{d\epsilon}{dt} = k_{CH_4}(CH_4^0 - \epsilon)\sqrt{O_2^0 - 2\epsilon}, \tag{2-60}$$

where CH_4^0 and O_2^0 are the initial concentrations of methane and oxygen at the start of the that time step.

Integration of the chemical reactions have been discussed in details in Chapter 3.

2.5.2.2 Two-step methane-air reaction

In this mechanism, there are two reaction steps based on the data from CER (2017b). Here the first reaction is irreversible, whereas the second reaction is reversible. These reactions are

$$\mathrm{CH_4 + 1.5\,O_2 \longrightarrow CO + 2\,H_2O}, \tag{R6}$$

and

$$\mathrm{CO + 0.5\,O_2 \longleftrightarrow CO_2}. \tag{R7}$$

and are assumed to be of arrhenius-type. However, to make things easier to integrate into the HyBurn solver, we split this into three equations

$$\mathrm{CH_4 + 1.5\,O_2 \xrightarrow{k_{f,CH_4}} CO + 2\,H_2O}, \tag{R6}$$

$$\mathrm{CO + 0.5\,O_2 \xrightarrow{k_{f,CO}} CO_2}, \tag{R8}$$

$$\mathrm{CO_2 \xrightarrow{k_{b,CO}} CO + 0.5\,O_2}. \tag{R9}$$

The order of the first reaction with respect to CH_4 and O_2 are 0.5 and 0.65 respectively. The reaction rate constants can be written as

$$k_{f,CH_4} = A_{f,CH_4} T_g^{b_{f,CH_4}} exp(-Ea_{f,CH_4}/RuT), \tag{2-61}$$

for the first step,

$$k_{f,CO} = A_{f,CO} T_g^{b_{f,CO}} exp(-Ea_{f,CO}/RuT), \tag{2-62}$$

for the second step, and

$$k_{b,CO} = A_{b,CO} T_g^{b_{b,CO}} exp(-Ea_{b,CO}/RuT), \tag{2-63}$$

for the third step. Here, A, b and Ea are the pre-exponential factors, temperature dependence of the pre-exponential factors and the activation energies respectively for the steps. The values are

Reaction Step	A	b	Ea (J/kmol)
R6	1.73859×10^9 kg$^{0.15}$ s^{-1}	0	1.48532×10^8
R8	6.32456×10^6	0.7	5.0208×10^7
R9	$8.80076634 \times 10^{13}$	-0.39538219	3.37920737×10^8

The overall production/destruction rates of the participating species can then be written as

$$\begin{aligned}
\frac{\partial \epsilon_{CH_4}}{\partial t} =& - k_{f,CH_4}(CH_4^0 - \epsilon_{CH_4})^{0.5}(O_2^0 - 1.5\epsilon_{CH_4})^{0.65}, && \text{(2-64)}\\
\frac{\partial \epsilon_{O_2}}{\partial t} =& - 1.5k_{f,CH_4}(CH_4^0 - \epsilon_{CH_4})^{0.5}(O_2^0 - 1.5\epsilon_{CH_4})^{0.65} \\
& - 0.5k_{f,CO}(CO^0 - \epsilon_{CO})(O_2^0 - 0.5\epsilon_{CO})^{0.5} \\
& + 0.5k_{b,CO}(CO_2^0 - \epsilon_{CO}), && \text{(2-65)}\\
\frac{\partial \epsilon_{H_2O}}{\partial t} =& 2k_{f,CH_4}(CH_4^0 - \epsilon_{CH_4})^{0.5}(O_2^0 - 1.5\epsilon_{CH_4})^{0.65}, && \text{(2-66)}\\
\frac{\partial \epsilon_{CO_2}}{\partial t} =& - k_{b,CO}(CO_2^0 - \epsilon_{CO_2}) + k_{f,CO}(CO^0 - \epsilon_{CO})(O_2^0 - 0.5\epsilon_{CO})^{0.5}, && \text{(2-67)}\\
\frac{\partial \epsilon_{CO}}{\partial t} =& - k_{f,CO}(CO^0 - \epsilon_{CO})(O_2^0 - 0.5\epsilon_{CO})^{0.5} \\
& + k_{f,CH_4}(CH_4^0 - \epsilon_{CH_4})^{0.5}(O_2^0 - 1.5\epsilon_{CH_4})^{0.65} \\
& + k_{b,CO}(CO_2^0 - \epsilon_{CO_2}), && \text{(2-68)}
\end{aligned}$$

where CH_4^0, O_2^0, CO_2^0 and CO^0 are the initial concentrations of methane, oxygen, carbon dioxide and carbon monoxide, respectively, at the start of the time step.

For this mechanism, assuming constant temperature during the integration of the reactions can result in highly erroneous values. Thus, the gas-phase temperature also has to be solved simultaneously along with the species concentrations. The time-derivative of the temperature is given by

$$\frac{\partial T}{\partial t} = -\frac{1}{\rho c_V}\sum_{i=1}^{5} e_{\text{chem},i} MW_i \frac{\partial \epsilon_i}{\partial t}, \tag{2-69}$$

where ρ is the gas-phase density, c_V is the mixture specific heat at constant volume, $e_{\text{chem},i}$ is the enthalpy of formation of species i, MW_i is the molecular weight of species i, and $\frac{\partial \epsilon_i}{\partial t}$ is the net production/destruction rate of species i.

The integration of this reaction mechanism is more complicated than the single-step reaction mechanism and has also been elaborated in Chapter 3.

2.6 Thermodynamic and Transport Models

The fluid model being used in this research is a variable specific heats model in order to preserve a high degree of accuracy. The thermodynamic and transport data for the species have been obtained from the AramcoMech2.0 library. The temperature range for the validity of this data is $200 - 6000$ K. The data is in the form of NASA-7 polynomials and the polynomial coefficients are divided into two groups with temperature ranges of $200 - 1000$ K and $1000 - 6000$ K.

For the transport properties, the modified AramcoMech2.0 file was loaded into cantera and data was extracted for the thermal conductivity, viscosity and the binary diffusion coefficients for each of the species. Then, we made curve fits to the obtained data using fourth-order polynomials, and the coefficients of these polynomials are stored in the code and used to get an approximate value for the transport properties.

For the purposes of this research, the ideal gas law has been assumed for all the gaseous species. We also assume thermal equilibrium. The partial pressure of species i is given by

$$p_i = \rho_i \frac{Ru}{MW_i} T = [X_i] Ru T, \tag{2-70}$$

where Ru is the universal gas constant, T is the gas-phase temperature, MW_i is the molecular weight of i^{th} specie, ρ_i is the density of i^{th} specie and $[X_i]$ is the molar concentration of i^{th} specie. Then the total pressure of the gas phase can be calculated using Dalton's law of partial pressure

$$p = \sum_{i}^{N_g} p_i, \tag{2-71}$$

where N_g is the total number of gas-phase species. Thus, the ideal gas law can now be expressed as

$$p = \rho RuT \sum_{i}^{N_g} \frac{Y_i}{MW_i}, \tag{2-72}$$

where Y_i is the mass fraction of species i and is defined as

$$Y_i = \frac{\rho_i}{\rho}. \tag{2-73}$$

The mole fraction of species i is defined as

$$X_i = \frac{[X_i]}{\sum_{k=1}^{N_g}[X_k]}. \tag{2-74}$$

Then, the relation between mass and mole fractions is given by

$$X_i = Y_i \frac{MW_{mix}}{MW_i}, \tag{2-75}$$

where the mixture molecular weight, MW_{mix} is

$$MW_{mix} = \sum_{i=1}^{N_g} X_i MW_i = \frac{1}{\sum_{i=1}^{N_g} Y_i/MW_i}. \tag{2-76}$$

The mixture-average viscosity is calculated using Ern and Giovangigli (1994)

$$\mu = \left(\sum_{i=1}^{N_g} X_i \mu_i^6 \right)^{1/6}, \tag{2-77}$$

where μ_i is the viscosity of species i, that is obtained from the curve fit data mentioned earlier.

Similarly, the mixture-average thermal conductivity can be calculated by

$$\lambda = \left(\sum_{i=1}^{N_g} X_i \lambda_i^{1/4} \right)^{4}, \tag{2-78}$$

where λ_i is the thermal conductivity of species i, obtained from curve fit data.

For the binary diffusion coefficients, we use the Curtis-Hirschfelder approximation (Kee et al., 2005).

$$D_{i,mix} = \frac{1 - Y_i}{\sum_{j \neq i}^{N_g} X_j / D_{ij}} \approx \frac{\sum_{j \neq i}^{N_g} (X_j + \epsilon) MW_j}{MW_{mix} \sum_{j \neq i}^{N_g} (X_j + \epsilon) / D_{ij}}, \tag{2-79}$$

where D_{ij} are the binary diffusion coefficients of all pairs of species i and j which are also obtained from the curve fit data, and ϵ is a small number that is added to avoid division by zero errors.

2.7 Radiation Solver

The RTE is a highly complicated equation to solve due to the presence of both integral and differential terms in the equation. It is also a very non-linear equation. Analytical solutions to the RTE are extremely rare and thus they have to be solved numerically. However, numerically solving the RTE in its original form is not possible. Thus, we have to make approximations to the RTE to be able to solve them. Several approximation methods for the RTE are in existence, but we have chosen the filtered spherical harmonics (FP$_N$) approximation method. It is a widely used and relatively straightforward method that can give accurate results without a massive computational cost.

2.7.1 The Spherical Harmonics Approximation to the Radiation Transport Equation

The spherical harmonics (P_N) method is a spectral method, which is obtained by linearly expanding the radiation intensity in angle with the help spherical harmonic basis functions. This leads to a system of hyperbolic partial differential equations for the expansion coefficients. An advantage of this method is that it preserves the rotational invariance property, unlike the discrete ordinates method. Due to the hyperbolic nature of the equations, the solution to the P_N equations yields wave-like propagation of the radiation field. The wave speed is limited by the speed of light and thus makes physical sense. Flux-limited diffusion methods, on the other hand, allow photons to travel faster than that.

One of the major downfalls of this method is the occurrence of numerical oscillations in scenarios where there is a lack of interaction with the material. This can result in negative values for the radiation energy density, which in turn causes material temperatures to become negative. This is a general problem of the system and does not go away by changing the order of accuracy of the system (McClarren et al., 2008).

The spherical harmonics approximation is derived by expanding the angular flux $\psi(\boldsymbol{\Omega})$ in terms of spherical harmonic functions $Y_l^m(\boldsymbol{\Omega})$. Following the work of Brunner and Holloway (2005), let us consider only the absorption and isotropic scattering coefficients.

Spherical harmonic functions, $Y_l^m(\mu, \varphi)$, can be defined as (Bell and Glasstone, 1970):

$$Y_l^m(\mu, \varphi) = (-1)^m \sqrt{\frac{2l+1}{4\pi}\frac{(l-m)!}{(l+m)!}} \frac{(1-\mu^2)^{m/2}}{2^l l!} e^{\mathrm{i}m\varphi} \frac{\mathrm{d}^{l+m}}{\mathrm{d}\mu^{l+m}} (\mu^2 - 1)^l, \tag{2-80}$$

where $l \geq 0$ and $0 \leq m \leq l$. This equation can be written in a modified form for $m < 0$, however, for our purpose, these terms are not necessary since the angular flux is always real. Now, the angular flux can expanded in terms of the complete set of orthonormal basis functions provided by the spherical harmonics,

$$\psi(\boldsymbol{x}, \boldsymbol{\Omega}) = \sum_{l=0}^{\infty} \sum_{m=-l}^{l} \psi_l^m(\boldsymbol{x}) Y_l^m(\boldsymbol{\Omega}), \tag{2-81}$$

where

$$\psi_l^m(\boldsymbol{x}) = \int\limits_{4\pi} \bar{Y}_l^m \psi(\boldsymbol{x}, \boldsymbol{\Omega}) d\boldsymbol{\Omega}. \tag{2-82}$$

Up to this point, no approximations have been made, however in order to use this expansion, the series has to be truncated. We can choose a value of N, for which $\psi_l^m = 0$ for $l > N$. This is then known as P_N approximation. The spherical harmonic moments of ψ represent physical quantities. The ψ_0^0 moment represents the scalar flux of density times the velocity. ψ_1^m terms are related to the particle momentum. ψ_2^m terms are related to the pressure.

The three-dimensional Boltzmann transport equation can be expanded as

$$\begin{aligned}\frac{\partial}{\partial t}\psi_l^m + \frac{1}{2}\frac{\partial}{\partial x}&\left(-C_{l-1}^{m-1}\psi_{l-1}^{m-1} + D_{l+1}^{m-1}\psi_{l+1}^{m-1} + E_{l-1}^{m+1}\psi_{l-1}^{m+1} - F_{l+1}^{m+1}\psi_{l+1}^{m+1}\right)\\ &+\frac{1}{2}i\frac{\partial}{\partial y}\left(C_{l-1}^{m-1}\psi_{l-1}^{m-1} - D_{l+1}^{m-1}\psi_{l+1}^{m-1} + E_{l-1}^{m+1}\psi_{l-1}^{m+1} - F_{l+1}^{m+1}\psi_{l+1}^{m+1}\right)\\ &+\frac{\partial}{\partial z}\left(A_{l-1}^{m}\psi_{l-1}^{m} + B_{l+1}^{m}\psi_{l+1}^{m}\right) + \sum_t \psi_l^m = \sum_s \psi_0^0\delta_{l0}\delta_{m0},\end{aligned} \tag{2-83}$$

for $0 \le l < \infty$ and $-l \le m \le l$. The coefficients A, B, C and D are given by

$$\begin{aligned} A_l^m &= \sqrt{\frac{(l-m+1)(l+m+1)}{(2l+3)(2l+1)}}, & B_l^m &= \sqrt{\frac{(l-m)(l+m)}{(2l+1)(2l-1)}},\\ C_l^m &= \sqrt{\frac{(l+m+1)(l+m+2)}{(2l+3)(2l+1)}}, & D_l^m &= \sqrt{\frac{(l-m)(l-m-1)}{(2l+1)(2l-1)}},\\ E_l^m &= \sqrt{\frac{(l-m+1)(l-m+2)}{(2l+3)(2l+1)}}, & F_l^m &= \sqrt{\frac{(l+m)(l+m-1)}{(2l+1)(2l-1)}}.\end{aligned} \tag{2-84}$$

For our applications, we assume that ψ is real and thus we can write

$$\begin{aligned}&\bar{Y}_l^m = (-1)^m Y_l^{-m}, \qquad \text{and}\\ &\bar{\psi}_l^m(\boldsymbol{x}) = (-1)^m \psi_l^{-m},\end{aligned} \tag{2-85}$$

thus reducing the number of unkowns by eliminating terms with $m < 0$.

For two-dimensional problems, one of the directions in Eq. 2-83 can be dropped. For convenience, we choose to eliminate the y-direction, which helps us decouple the real and imaginary parts of the equation. Thus we have to solve only for the real parts. Eq. 2-83 then becomes

$$\begin{aligned}\frac{\partial}{\partial t}\psi_l^m + \frac{1}{2}\frac{\partial}{\partial x}&\left(-C_{l-1}^{m-1}\psi_{l-1}^{m-1} + D_{l+1}^{m-1}\psi_{l+1}^{m-1} + E_{l-1}^{m+1}\psi_{l-1}^{m+1} - F_{l+1}^{m+1}\psi_{l+1}^{m+1}\right)\\ &+\frac{\partial}{\partial z}\left(A_{l-1}^{m}\psi_{l-1}^{m} + B_{l+1}^{m}\psi_{l+1}^{m}\right) + \sum_t \psi_l^m = 0,\end{aligned} \tag{2-86}$$

when $m \neq 0$. If $m = 0$,

$$\frac{\partial}{\partial t}\psi_l^0 + \frac{1}{2}\frac{\partial}{\partial x}\left(E_{l-1}^1\psi_{l-1}^1 - F_{l+1}^1\psi_{l+1}^1\right) + \frac{\partial}{\partial z}\left(A_{l-1}^0\psi_{l-1}^0 + B_{l+1}^0\psi_{l+1}^0\right) + \sum_t \psi_l^0 = \sum_s \psi_0^0\delta_{l0}. \tag{2-87}$$

Here we used the relations $C_l^{-1} = E_l^1$ and $D_l^{-1} = F_l^1$ to eliminate terms with $m = -1$ for the case when $m = 0$.

2.7.1.1 3-D spherical harmonics approximation

For the two-dimensional case, as seen in the previous section, we were able to eliminate the third direction which contained the imaginary term. In order to use the full 3-D Boltzmann transport equations with spherical harmonics approximation, we have to use the real-valued spherical harmonics. To convert the complex-valued spherical harmonics to real-valued spherical harmonics, we use the inverse transforms given by

$$\tilde{\psi}_l^m = \begin{cases} \frac{1}{\sqrt{2}}\left(-\psi_l^m i + \psi_l^{-m}\right) & \text{if } m < 0, \\ \psi_l^m & \text{if } m = 0, \\ \frac{(-1)^m}{\sqrt{2}}\left(\psi_l^m + i\psi_l^{-m}\right) & \text{if } m > 0, \end{cases} \tag{2-88}$$

where $\tilde{\psi}_l^m$ represents the complex-valued spherical harmonics and the same without the tilde symbol are the real-valued versions.

Starting with eq. 2-83 and substituting the real-valued spherical harmonics for their respective complex-valued functions, we get (Frank et al., 2016)

$$\begin{aligned} \frac{\partial}{\partial t}\psi_l^m + \frac{1}{2}\frac{\partial}{\partial x}\Big[(1-\delta_{k,-1})\left(\tilde{C}_{l-1}^{|m|-1}\psi_{l-1}^{m^-} - \tilde{D}_{l+1}^{|m|-1}\psi_{l+1}^{m^-}\right) - \tilde{E}_{l-1}^{|m|+1}\psi_{l-1}^{m^+} + \tilde{F}_{l+1}^{|m|+1}\psi_{l+1}^{m^+}\Big] \\ +\frac{1}{2}\frac{\partial}{\partial y}\Big[\text{sgn}(k)(1-\delta_{k,1})\left(-\tilde{C}_{l-1}^{|m|-1}\psi_{l-1}^{-m^-} + \tilde{D}_{l+1}^{|m|-1}\psi_{l+1}^{-m^-}\right) - \tilde{E}_{l-1}^{|m|+1}\psi_{l-1}^{-m^+} + \tilde{F}_{l+1}^{|m|+1}\psi_{l+1}^{-m^+}\Big] \\ +\frac{\partial}{\partial z}\left(A_{l-1}^m\psi_{l-1}^m + B_{l+1}^m\psi_{l+1}^m\right) + \sum_t \psi_l^m = \sum_s \psi_0^0\delta_{l0}\delta_{m0}, \end{aligned} \tag{2-89}$$

where $\delta_{i,j}$ is the Kronecker delta which is defined as

$$\delta_{i,j} = \begin{cases} 1 & \text{if } i = j, \\ 0 & \text{if } i \neq j, \end{cases} \tag{2-90}$$

and sgn(k) is the sign function, which gives -1 if m $<$ 0, and 1 otherwise. The coefficients are given by

$$m^{+} = m + \text{sgn}(m), \text{and } m^{-} = m - \text{sgn}(m), \tag{2-91}$$

$$\tilde{C}_l^m = \begin{cases} 0, & m < 0 \\ \sqrt{2}\tilde{C}_l^m, & m = 0 \\ \tilde{C}_l^m, & m > 0 \end{cases}, \qquad \tilde{D}_l^m = \begin{cases} 0, & m < 0 \\ \sqrt{2}\tilde{D}_l^m, & m = 0 \\ \tilde{D}_l^m, & m > 0 \end{cases}, \tag{2-92}$$

$$\tilde{E}_l^m = \begin{cases} \sqrt{2}\tilde{E}_l^m, & m = 1 \\ \tilde{E}_l^m, & m > 1 \end{cases}, \qquad \tilde{F}_l^m = \begin{cases} \sqrt{2}\tilde{F}_l^m, & m = 1 \\ \tilde{F}_l^m, & m > 1 \end{cases}. \tag{2-93}$$

This reduces exactly to the 2-D case when the y-direction is neglected.

2.7.1.2 The eigenstructure

The P_N approximation is used with a Riemann solver, for example a Roe-type Riemann solver. The knowledge of the eigenstructure of the system is thus necessary. Due to the linear nature of the spherical harmonics, the Jacobian meets all the properties of the linearized Roe matrix.

The z-Jacobian is a block diagonal matrix if we group the equations with the same values of m. Each of block has an eigenstructure that is independent of the others. An example of a block of the z-Jacobian looks like

$$\boldsymbol{A}_z^m = \begin{bmatrix} 0 & B_{m+1}^m & 0 & \dots & & & \\ & & & \vdots & & & \\ \dots & 0 & A_{l-1}^m & 0 & B_{l+1}^m & 0 & \dots \\ & & & \vdots & & & \\ & & & \dots & 0 & A_{N-1}^m & 0 \end{bmatrix}. \tag{2-94}$$

Here each block contains $m+1 \leq l \leq N-1$ modes. When we multiply a vector of Y_l^m's by the Jacobian, we get

$$\begin{bmatrix} 0 & B_{m+1}^m & 0 & \dots & & & \\ & & & \vdots & & & \\ \dots & 0 & A_{l-1}^m & 0 & B_{l+1}^m & 0 & \dots \\ & & & \vdots & & & \\ & & & \dots & 0 & A_{N-1}^m & 0 \end{bmatrix} \begin{bmatrix} Y_m^m \\ \vdots \\ Y_l^m \\ \vdots \\ Y_N^m \end{bmatrix} = \begin{bmatrix} B_{m+1}^m Y_{m+1}^m \\ \vdots \\ A_{l-1}^m Y_{l-1}^m + B_{l+1}^m Y_{l+1}^m \\ \vdots \\ A_{N-1}^m Y_{N-1}^m \end{bmatrix}, \tag{2-95}$$

which is equivalent to the recursion relation $Y_l^m cos\theta = A_l^m Y_{l+1}^m + B_l^m Y_{l-1}^m$, which can also be expressed as

$$\begin{bmatrix} B_{m+1}^m Y_{m+1}^m \\ \vdots \\ A_{l-1}^m Y_{l-1}^m + B_{l+1}^m Y_{l+1}^m \\ \vdots \\ A_{N-1}^m Y_{N-1}^m \end{bmatrix} = \begin{bmatrix} A_m^m Y_{m+1}^m \\ \vdots \\ B_l^m Y_{l-1}^m + A_l^m Y_{l+1}^m \\ \vdots \\ B_N^m Y_{N-1}^m \end{bmatrix} = \mu \begin{bmatrix} Y_m^m \\ \vdots \\ Y_l^m \\ \vdots \\ Y_N^m \end{bmatrix}, \tag{2-96}$$

where $\mu = cos\theta$. In order to ensure this, we need

$$Y_{N+1}^m(\mu, \varphi) = 0. \tag{2-97}$$

When Eq. 2-97 is solved, the μ's give the eigenvalues for each $0 \leq m \leq N$. For each of the m blocks, the spherical harmonics evaluated at these μ_k's are the eigenvectors. The Jacobian is symmetric since $A_{l-1}^m = B_m^l$. Thus the left and right eigenvectors are exactly the same, and are normalized such that $\boldsymbol{r}_k \cdot \boldsymbol{r}_k = 1$. When $m = 0$, the A_z^0 block of the Jacobian corresponds to the one-dimensional Legendre polynomial expansion of the RTE (Brunner] and Holloway], 2001; Brunner, 2000).

All eigenvalues are real and bounded, $-1 < \mu < 1$, as well as unique. The only exception is that multiple eigenvalues can be zero. When N is odd, the eigenvalues are zeros only for $m > 0$.

2.7.2 Filtered Spherical Harmonics Expansion (FP_N)

In order to get rid of the inherent oscillations in spherical harmonics approximation, we use the technique of filtering the spherical harmonics expansions. This includes multiplying each term of the spherical harmonics expansion by a factor which is order-dependent. The resulting modification is referred to as *filtered* spherical harmonics expansion (FP_N) since this acts like a high-frequency filter.

The kind of filter used can vary. In McClarren and Hauck (2010), the authors use a spherical-spline filter. Using this filter and following the procedure in Radice et al. (2013), we get

$$[\mathcal{F}(F)](\varphi, \theta) = \sum_{l=0}^{N} \sum_{m=-l}^{l} \left\{ \frac{1}{1 + \alpha l^2 (1 + l^2)} \right\} F^{lm} Y_{lm}(\varphi, \theta), \tag{2-98}$$

where

$$\alpha \equiv \frac{c\Delta t}{\Delta x} \frac{1}{N^2} \frac{1}{(\sigma_t L + N)^2}. \tag{2-99}$$

Here L is a characteristic length scale which is used to nondimensionalize α and σ_t is chosen such that its order of magnitude matches that of the total extinction coefficient, κ ($\kappa = \kappa_a$(absorption coefficient) $+ \kappa_s$(scattering coefficient)). F is a distribution function, which can be related to the intensity by

$$I = \frac{h^4 \nu^3}{c^2} F, \tag{2-100}$$

where h is the Planck's constatnt, ν is the frequency and c s the speed of light.

One shortcoming of this method as reported by McClarren and Hauck (2010) is the lack of a clear continuum limit as Δx, $\Delta t \to 0$. The implication of this is that the FP_N cannot be interpreted as a system of partial differential equations. Thus the quality of the solution is dependent on grid resolution. This makes it impossible to achieve spatial convergence.

Radice et al. (2013) suggested a modification to the aforementioned FP_N method by introducing a strength parameter, $s \geq 0$. This modification is applied to Eq. 2-98 to give

$$[\mathcal{F}(F)](\varphi, \theta) = \sum_{l=0}^{N} \sum_{m=-l}^{l} \left\{ \sigma \left(\frac{l}{N+1} \right) \right\}^{s} F^{lm} Y_{lm}(\varphi, \theta), \tag{2-101}$$

where $\sigma(\eta)$ is called a *filter function* of order p, that is, $\sigma \in C^{p}(\mathbb{R}^{+}; [0,1])$, such that

$$\sigma(0) = 1, \qquad \sigma^{(k)}(0) = 0, \qquad \text{for } k = 1, 2, \ldots p-1. \tag{2-102}$$

The rotational invariance is maintained since the strength of the filter only depends on l. Another advantage of this method is that as N increases, the filter strength decreases, thus ensuring convergence as $N \to \infty$. The order of convergence is $\sim p-1$ for a filter of order p (Vandeven, 1991; Hesthaven and Kirby, 2008).

In this study, we use the modified Lanczos second-order filter of Radice et al. (2013), which is given by

$$\sigma_{\text{Lanczos}}(\eta) = \frac{sin\eta}{\eta}. \tag{2-103}$$

Using an even-order filter ensures that the truncation error of these filters, which can be interpreted as a numerical viscosity, is 2nd order or higher, whereas for odd-order filters the truncation error is similar to dispersion type error (Meister et al., 2009).

2.7.3 Solid-Phase Radiative Properties

In order to determine the radiative properties of coal and ash particles, it is necessary to know how their complex refraction indexes vary with wavelength and temperature. Generally, it has been observed that the real part of the refractive index, n, does not vary much between different coal types, especially in the infrared range. However, this is not true for the complex part of the index, k, which is interpreted as the absorptive index (Foster and Howarth, 1968; Blokh, 1974; Blokh and Burak, 1973). The optical properties of the coal depend on its fly ash content and thus vary quite a lot between different types of coal. Most of the literature available report $n \approx 1.5$ but there is no consensus on the value of absorptive index. Wall et al. (1981) reported k values between 0.008 and 0.020 based on their work with Australian coals with varying fly ash content. On the other hand, the temperature dependence of the refractive index still remains unexplored.

Buckius and Hwang (1980) used Lorenz-Mie method to calculate the complex refraction indices of a large variety of particle distribution functions. It was observed that by normalizing the absorption coefficient, extinction coefficient and the symmetry factor with the Rayleigh small-particle limit, these parameters are independent of the particle size distribution function, but are only a function of the particle diameter. They developed correlations for several nondimensional radiative properties by studying their numerical data for different types of coals - the absorption coefficient κ, extinction coefficient β, and the asymmetry factor. Nondimensional forms of κ and β are given by

$$\kappa^*(\lambda, m) = \frac{\kappa(\lambda, m, N_T)}{f_A}, \tag{2-104}$$

$$\beta^*(\lambda, m) = \frac{\beta(\lambda, m, N_T)}{f_A}, \tag{2-105}$$

where f_A is the total projected area of particles per unit volume and is expressed as

$$f_A = \int_0^\infty \pi a^2 n(a) da. \tag{2-106}$$

The nondimensional Planck-mean and Rosseland-mean absorption and extinction coefficients are also defined in a similar way, all normalized by f_A. The correlations obey the same basic equation

$$\frac{1}{y^z} = \frac{1}{y_0^z} + \frac{1}{y_\infty^z}, \tag{2-107}$$

Table 2-1. Correlation parameters for the prediction of nondimensional coal properties from $y^{-z} = y_0^{-z} + y_\infty^{-z}$ (Buckius and Hwang, 1980)

y	y_0	y_∞	z
$\beta^*(\lambda, m)$	$\beta_0^*(1 + 6.78\beta_0^{*2})$	$3.09/\beta_0^{*0.1}$	1.2
$\kappa^*(\lambda, m)$	$\beta_0^*(1 + 2.30\beta_0^{*2})$	$1.66/\beta_0^{*0.16}$	1.6
$g(\lambda, m)$	g_0	0.9	1.0
β_p^*	$0.0032\phi[1 + (\phi/355)^{1.9}]$	$10.99/\phi^{0.02}$	1.2
β_R^*	$0.0032\phi[1 + (\phi/458)^{1.75}]$	$10.99/\phi^{0.02}$	1.2
κ_p^*	$0.0032\phi[1 + (\phi/725)^{1.65}]$	$13.75/\phi^{0.13}$	1.5
κ_R^*	$0.0032\phi[1 + (\phi/650)^{2.3}]$	$15.65/\phi^{0.143}$	1.15

where y represents one of the above nondimensional properties, y_0 is the same property for small average particle sizes and y_∞ is for large average particle sizes. The correlation parameters y_0, y_∞ and z for various properties ares summarized in Table 2-1. Here, $\phi = \bar{r}T$ μm^{-1} K^{-1}, $\bar{r}$ is the average particle size in μm, and T is the particle temperature in K. Thus the final form of κ and β can be written as

$$\beta = \frac{f_A(\beta_0^{-z} + \beta_\infty^{-z})^{-\frac{1}{z}}}{1 - \alpha_s}, \qquad \kappa = \frac{f_A(\kappa_0^{-z} + \kappa_\infty^{-z})^{-\frac{1}{z}}}{1 - \alpha_s}, \tag{2-108}$$

where α_s is the particle volume fraction.

For our calculations, we use

$$\beta_0 = 0.0032\phi\left[1 + \frac{\phi}{355}^{1.9}\right], \qquad \beta_\infty = 10.99/\phi^{0.02}, \qquad \text{and} \qquad z = 1.2. \tag{2-109}$$

We also calculate f_A using the relation

$$f_A = 1.5 \times \frac{\alpha_s}{d_s}, \tag{2-110}$$

where d_s is the particle diameter.

2.7.4 Gas-Phase Radiative Properties

Strongly radiating flames cannot describe most of the recent turbulent nonpremixed flames (TNF). Except for the most highly diluted hydrogen jet flames, thermal radiation from all other sources reduces the local temperatures enough to affect the production rate of NO. It is computationally very expensive to have a detailed treatment of radiative transfer in a turbulent flame. To deal with this issue, it is important to have a highly simplified model for radiative heat loss. This uses an optically thin radiation model with radiative properties based on the RADCAL model by Grosshandler of NIST (Grosshandler, 1993). There is some evidence however, that the optically thin assumption significantly over predicts radiative losses from methane flames due to the strong absorption by the 4.3-micron band of CO_2.

Assuming optically thin flames essentially means assuming that each radiating point source has an unimpeded isotropic view of the cold surroundings. In this case, the radiative loss rate per unit volume is calculated using the relation

$$Q(T, \text{species}) = 4 \sum p_i a_{p,i} \times (T^4 - T_b^4), \tag{2-111}$$

where the summation is over all the species included in the radiation calculation, p_i is the partial pressure of species i in atmospheres (mole fraction times local pressure), $a_{p,i}$ is the Planck-mean absorption coefficient of species i, T is the local flame temperature in kelvin, and T_b is the background temperature (300 K unless otherwise specified in the data).

The most important radiating species for hydrocarbon flames are CO_2 and H_2O. For example, Jay Gore observed that the peak temperature in a strained laminar flame calculation decreased by 50 K when radiation by CO_2 and H_2O was included. When CH_4 and CO were also included, the peak temperature dropped by a further 5 K. When the mixture was rich, including CH_4 and CO radiation resulted in 8 K reduction in temperature.

Curve fits for the Planck-mean absorption coefficients for H_2O, CO_2, CH_4 and CO are given below as functions of temperature. These fits were derived from results of the RADCAL program.

For curve fits, the absorption coefficients for H_2O and CO_2 can be calculated using

$$a_p = c_0 + c_1 \left(\frac{1000}{T}\right) + c_2 \left(\frac{1000}{T}\right)^2 + c_3 \left(\frac{1000}{T}\right)^3 + c_4 \left(\frac{1000}{T}\right)^4 + c_5 \left(\frac{1000}{T}\right)^5 . \tag{2-112}$$

The coefficients c_0, c_1, ..., c_5 for CO_2 and H_2O are given as

	H_2O	CO_2
c_0	-0.23093	18.741
c_1	-1.12390	-121.310
c_2	9.41530	273.500
c_3	-2.99880	-194.050
c_4	0.51382	56.310
c_5	-1.8684×10^{-5}	-5.8169

For CH_4, the following fourth-order polynomial in temperature is used

$$a_{p,CH_4} = 6.6334 - 0.0035686T + 1.6682 \times 10^{-8}T^2 + 2.5611 \times 10^{-10}T^3 - 2.6558 \times 10^{-14}T^4. \tag{2-113}$$

Two temperature ranges are used to find the fit for CO using (in Horner form)

$$a_{p,CO} = c_0 + T(c_1 + T(c_2 + T(c_3 + Tc_4))), \tag{2-114}$$

and the coefficients c_0, c_1, ..., c_4 are given by

$$\begin{aligned} c_0 &= 4.7869, \\ c_1 &= -0.06953, \\ c_2 &= 2.95775 \times 10^{-4}, \\ c_3 &= -4.25732 \times 10^{-7}, \\ c_4 &= 2.02894 \times 10^{-10}, \end{aligned} \tag{2-115}$$

if $T < 750$, and

$$\begin{aligned} c_0 &= 10.09, \\ c_1 &= -0.01183, \\ c_2 &= 4.7753 \times 10^{-6}, \\ c_3 &= -5.87209 \times 10^{-10}, \\ c_4 &= -2.5334 \times 10^{-14}, \end{aligned} \tag{2-116}$$

otherwise.

We also assume that the gas-phase medium is nonscattering. Thus, the extinction coefficient β is equal to the linear absorption coefficient κ (since the scattering coefficient $\sigma = 0$).

CHAPTER 3
NUMERICAL METHODS

In this chapter we will look at the various numerical methods used to solve the various terms of the governing equations. First, we will look at the hyperbolic equations, then the chemical reaction terms and finally the radiation solver.

3.1 Solving the Hyperbolic Terms

Due to the coupled nature of the hyperbolic equations, they can be quite challenging to solve. The choice of appropriate models for both the gas and granular phases is difficult and has to depend on the particular situation. Some models may be highly accurate for a certain scenario, but quite the opposite for another. Thus there is no universally correct model. Besides choosing the right model, there are a host of computational challenges as well.

In this research, we use the method of Strang operator splitting, which can be written as,

$$\boldsymbol{U}^{t+2\Delta t} = \mathcal{H}_{xyz}^{\Delta t}(\mathcal{S}^{2\Delta t}(\mathcal{H}_{xyz}^{\Delta t}(\boldsymbol{U}^{t}))), \tag{3-1}$$

where $\boldsymbol{U}$ is the vector of conserved variables and this solution is for time $t + 2\Delta t$ with t as the starting time. The integration of the directionally unsplit advection and wave propagation terms is represented by $\mathcal{H}_{xyz}$ for a time step of Δt, and the integration of the inhomogeneous source terms are represented by $\mathcal{S}^{2\Delta t}$ for a time step of $2\Delta t$. When radiation source terms are considered, this expression can be further expressed as,

$$\boldsymbol{U}^{t+2\Delta t} = \mathcal{H}_{xyz}^{\Delta t}(\mathcal{S}^{R,\Delta t}(\mathcal{S}^{\Delta t}(\mathcal{S}^{R,\Delta t}(\mathcal{H}_{xyz}^{\Delta t}(\boldsymbol{U}^{t}))))), \tag{3-2}$$

where $\mathcal{S}^{R,\Delta t}$ is the radiative source term. This term is achieved by solving the ordinary differential equation (ODE),

$$\frac{d(\rho E)}{dt} = S^{\text{rad}}, \tag{3-3}$$

where S^{rad} is the radiation source term in the energy equations for the gas and solid phases that were discussed in Chapter 2 radiation governing equations.

The hyperbolic terms for the gas-phase can be written as,

$$\frac{\partial \alpha_g \rho_g Y_{g,j}}{\partial t} + \nabla \cdot (\alpha_g \rho_g Y_{g,j} \boldsymbol{v}_g) = 0, \tag{3-4}$$

$$\frac{\partial \alpha_g \rho_g \boldsymbol{v}_g}{\partial t} + \nabla \cdot (\alpha_g \rho_g \boldsymbol{v}_g \boldsymbol{v}_g) + \nabla \alpha_g p_g = p_g \nabla \alpha_g + \boldsymbol{f}_{Lift} + \alpha_g \rho_g \boldsymbol{g}, \tag{3-5}$$

$$\frac{\partial \alpha_g \rho_g E_g}{\partial t} + \nabla \cdot [\alpha_g \boldsymbol{v}_g (\rho_g E_g + p_g)] = -p_g \nabla \cdot \alpha_s \boldsymbol{v}_s + \boldsymbol{f}_{Lift} \cdot \boldsymbol{v}_s + \alpha_g \rho_g \boldsymbol{g} \cdot \boldsymbol{v}_g, \tag{3-6}$$

and for the granular-phase as,

$$\frac{\partial \alpha_s \rho_s}{\partial t} + \nabla \cdot (\alpha_s \rho_s \boldsymbol{v}_s) = 0, \tag{3-7}$$

$$\frac{\partial \alpha_s \rho_s Y_{s,j}}{\partial t} + \nabla \cdot (\alpha_s \rho_s Y_{s,j} \boldsymbol{v}_s) = 0, \tag{3-8}$$

$$\frac{\partial \alpha_s \rho_s \boldsymbol{v}_s}{\partial t} + \nabla \cdot (\alpha_s \rho_s \boldsymbol{v}_s \boldsymbol{v}_s) + \nabla p_s + \nabla p_{fric} = -\alpha_s \nabla p_g - \boldsymbol{f}_{Lift} + \alpha_s \rho_s \boldsymbol{g}, \tag{3-9}$$

$$\frac{\partial \alpha_s \rho_s E_s}{\partial t} + \nabla \cdot (\alpha_s \rho_s E_s \boldsymbol{v}_s) = -p_s \nabla \cdot \boldsymbol{v}_s, \tag{3-10}$$

$$\frac{\partial \alpha_s \rho_s e_s}{\partial t} + \nabla \cdot (\alpha_s \rho_s e_s \boldsymbol{v}_s) = 0. \tag{3-11}$$

A standard second-order difference scheme is used to discretize the lift force where the lowest granular volume fraction is greater than $\alpha_{s,min}$, which is set at 10^{-10}. For spatial discretization, a variety of schemes have been used, which will be discussed later.

3.1.1 Spatial Discretization

The hyperbolic terms of the gas-phase governing equations can be spatially dicretized as

$$\begin{aligned}
\frac{d(\alpha_g \rho_g Y_{g,j})_i}{dt} &= -\frac{\alpha_{g,i+1/2}\rho_{g,i+1/2}u_{g,i+1/2}Y_{g,j,i+1/2} - \alpha_{g,i-1/2}\rho_{g,i-1/2}u_{g,i-1/2}Y_{g,j,i-1/2}}{\Delta x}, \\
\frac{d(\alpha_g \rho_g u_g)_i}{dt} &= -\frac{\alpha_{g,i+1/2}\rho_{g,i+1/2}u_{g,i+1/2}u_{g,i+1/2} - \alpha_{g,i-1/2}\rho_{g,i-1/2}u_{g,i-1/2}u_{g,i-1/2}}{\Delta x} \\
&\quad -\alpha_{g,i}\frac{p_{g,i+1/2} - p_{g,i-1/2}}{\Delta x} + \alpha_{g,i}\rho_{g,i}g_x, \\
\frac{d(\alpha_g \rho_g E_g)_i}{dt} &= -\frac{\alpha_{g,i+1/2}\rho_{g,i+1/2}u_{g,i+1/2}H_{g,i+1/2} - \alpha_{g,i-1/2}\rho_{g,i-1/2}u_{g,i-1/2}H_{g,i-1/2}}{\Delta x} - p_{g,i} \\
&\quad \frac{\alpha_{s,i+1/2}u_{s,i+1/2} - \alpha_{s,i-1/2}u_{s,i-1/2}}{\Delta x} + \alpha_{g,i}\rho_{g,i}u_{g,i}g_x,
\end{aligned}$$

and for the solid-phase as

$$\begin{aligned}
\frac{d(\alpha_s \rho_s)_i}{dt} &= -\frac{\dot{m}_{s,i+1/2} - \dot{m}_{s,i-1/2}}{\Delta x}, \\
\frac{d(\alpha_s \rho_s Y_{s,j})_i}{dt} &= -\frac{\dot{m}_{s,i+1/2}Y_{s,j,i+1/2} - \dot{m}_{s,i-1/2}Y_{s,j,i-1/2}}{\Delta x}, \\
\frac{d(\alpha_s \rho_s u_s)_i}{dt} &= -\frac{\dot{m}_{s,i+1/2}u_{s,i+1/2} + p_{s,tot,i+1/2} - \dot{m}_{s,i-1/2}u_{s,i-1/2} + p_{s,tot,i-1/2}}{\Delta x} \\
&\quad -\alpha_{s,i}\frac{p_{g,i+1/2} - p_{g,i-1/2}}{\Delta x} + \alpha_{s,i}\rho_{s,i}g_x, \\
\frac{d(\alpha_s \rho_s E_s)_i}{dt} &= -\frac{\dot{m}_{s,i+1/2}E_{s,i+1/2} - \dot{m}_{s,i-1/2}E_{s,i-1/2}}{\Delta x} - p_{s,i}\frac{u_{s,i+1/2} - u_{s,i-1/2}}{\Delta x}, \\
\frac{d(\alpha_s \rho_s e_s)_i}{dt} &= -\frac{\dot{m}_{s,i+1/2}e_{s,i+1/2} - \dot{m}_{s,i-1/2}e_{s,i-1/2}}{\Delta x}.
\end{aligned}$$

In these equations, j is used to represent species, u_g and u_s are the gas-phase and solid-phase velocities respectively, $\dot{m}_s$ represents solid phase mass flux, and g_x is the x-component of gravitational acceleration.

3.1.2 Nozzling and pDV Work Terms

The left-hand side of these equations can be easily solved using existing numerical algorithms (e.g., Godunov-style methods). However, they have to be solved independently for each phase. The nozzling term ($p_g \nabla \alpha_g$) in the momentum equation and the pDV work term ($p_g \nabla \cdot \alpha_s \boldsymbol{v}_s$) in the energy equation have to be treated as source terms. As long as the granular interfaces vary smoothly, these do not pose a challenge, but places where there are steep interfaces, getting a well behaved solution may be quite difficult. In such regions, it is not uncommon to see numerical pressure oscillations.

The stratified-flow idea, proposed by Chang and Liou (2007), has been proven to work well for such cases. Their work used compressible liquids and gases as their phases and each phase has separate control volumes. They solve the hyperbolic fluxes for each of the phases independently. This same idea can be used for gas and granular media as the two phases and is further simplified if the granular phase is assumed to be incompressible. In that case, the volume fraction does not depend on the gas-phase state and is only influenced by the motion of the particles. Thus the pressure gradient term ($\nabla \alpha_g p_g$) can be simplified and the the momentum equation can be written as,

$$\frac{\partial \alpha_g \rho_g \boldsymbol{v}_g}{\partial t} + \nabla \cdot (\alpha_g \rho_g \boldsymbol{v}_g \boldsymbol{v}_g) = -\alpha_g \nabla p_g + \boldsymbol{f}_{Lift} + \alpha_g \rho_g \boldsymbol{g}. \tag{3-12}$$

However, now Godunov-style methods cannot be used for the gas-phase hyperbolic terms since this equation doesn't resemble Euler's equations any more. Even so, the solution for the gas-gas part of the control volume is still valid. The pressures at the cell edges are obtained from this solution and are used to find $\alpha_g \nabla p_g$, which for the x-direction can be written as

$$\alpha_g \frac{\partial p_g}{\partial x} \approx \alpha_{g,i} \frac{p_{g,i+1/2} - p_{g,i-1/2}}{\Delta x}, \tag{3-13}$$

and Δx is the length of the grid cell in the x-direction. One caveat is that the pressure now has to be explicitly solved for. This demands a modification to the HLLC and AUSM flux schemes (Houim and Oran, 2016).

3.1.3 Solid Phase Fluxes

In order to maintain the robustness of the code, the accuracy is reduced from fifth (or seventh) order to first order when the volume fraction is close to the packing limit. In such scenarios, the compaction wave speeds and the frictional-collisional pressures approach infinity and thus the reduction of the order of accuracy in such cases is required. Another issue that occurs when the granular temperature is zero, is that the compaction wave speed and the granular pressure become zero. One way to deal with this problem is to use a pressureless dust model based on Collins et al. (1994) and thus the fluxes can be written as

$$\boldsymbol{F}_{s,i+1/2} = \begin{cases} \boldsymbol{F}_s(\boldsymbol{U}_s^L) & \text{if } u_s^L \geq 0 \text{ and } u_s^R > 0, \\ \boldsymbol{F}_s(\boldsymbol{U}_s^R) & \text{if } u_s^L < 0 \text{ and } u_s^R \leq 0, \\ \boldsymbol{F}_s(\boldsymbol{U}_s^L) + \boldsymbol{F}_s(\boldsymbol{U}_s^R) \text{if } u_s^L > 0 \text{ and } u_s^R < 0, \\ 0 & \text{if } u_s^L < 0 and u_s^R > 0, \end{cases} \tag{3-14}$$

where $\boldsymbol{F}_s$ is the solid-phase flux vector and $\boldsymbol{U}_s^L$ and $\boldsymbol{U}_s^R$ are the left and right reconstructed vector of conserved solid-phase variables respectively. This flux form is only used in locations where the solid pressure become zero and in other locations, the usual Riemann solver is used. The AUSM$^+$-up solver by Liou (2006) can deal with such situations without the need to switch between two different flux schemes. Slight modifications are needed to obtain $u_{s,i+1/2}$ which is required to calculate $p_s \nabla \cdot \boldsymbol{v}_s$, along with $\alpha_{s,i+1/2} u_{s,i+1/2}$ needed for pDV work term, and $\alpha_{g,i+1/2}$ for the gas phase flux. α_g at the cell edge can be calculated using

$$\alpha_{g,i+1/2} = \begin{cases} \alpha_{g,i+1/2}^L & \text{if } \dot{m}_{s,i+1/2} > 0, \\ \alpha_{g,i+1/2}^R & \text{if } \dot{m}_{s,i+1/2} \leq 0, \end{cases} \tag{3-15}$$

where $\dot{m}_{s,i+1/2}$ is the mass flux of the solid phase which is obtained from the AUSM$^+$-up solver.

For the solid phase, we have

$$\alpha_{s,i+1/2} u_{s,i+1/2} = \begin{cases} \frac{\dot{m}_{s,i+1/2}}{\rho_{s,i+1/2}^L} & \text{if } \dot{m}_{s,i+1/2} > 0, \\ \frac{\dot{m}_{s,i+1/2}}{\rho_{s,i+1/2}^R} & \text{if } \dot{m}_{s,i+1/2} \leq 0, \end{cases} \quad u_{s,i+1/2} = \begin{cases} \frac{\dot{m}_{s,i+1/2}}{\rho_{s,i+1/2}^L \alpha_{s,i+1/2}^L} & \text{if } \dot{m}_{s,i+1/2} > 0, \\ \frac{\dot{m}_{s,i+1/2}}{\rho_{s,i+1/2}^R \alpha_{s,i+1/2}^R} & \text{if } \dot{m}_{s,i+1/2} \leq 0. \end{cases} \tag{3-16}$$

while the pressure term can be written as

$$p_s \frac{\partial u_s}{\partial x} \approx p_{s,i} \frac{u_{s,i+1/2} - u_{s,i-1/2}}{\Delta x} \tag{3-17}$$

and the pDV work term as

$$p_g \frac{\partial \alpha_s u_s}{\partial x} \approx p_{g,i} \frac{\alpha_{s,i+1/2} u_{s,i+1/2} - \alpha_{s,i-1/2} u_{s,i-1/2}}{\Delta x}. \tag{3-18}$$

For the solid phase, we use the AUSM$^+$-up flux scheme based on Liou (2006). At the cell edge $i+1/2$, the flux vector can be written as

$$\boldsymbol{F}_{s,i+1/2} = \boldsymbol{p}_{i+1/2} + \dot{m}_{s,i+1/2} \begin{cases} \boldsymbol{\psi}^L, & \text{if } \dot{m}_{s,i+1/2} > 0, \\ \boldsymbol{\psi}^R, & \text{if } \dot{m}_{s,i+1/2} \leq 0. \end{cases} \tag{3-19}$$

Here, the pressure flux vector, $\boldsymbol{p}_{i+1/2}$ is defined as

$$\boldsymbol{p}_{i+1/2} = [0, 0, p_{s,tot,i+1/2}, 0, 0]^T \tag{3-20}$$

and is zero for all except the momentum equation.

The vector of passively advected scalars, $\boldsymbol{\psi}$ is defined as

$$\boldsymbol{\psi} = [1, Y_{s,j}, u_s, E_s, e_s]^T \tag{3-21}$$

The mass flux needs to be slightly modified to protect against hyperbolic degeneracy. Extra dissipation needs to be added as the volume fraction nears the packing limit,

$$\dot{m}_{s,i+1/2} = \mathcal{F} + c_{1/2} M_{1/2} \begin{cases} \alpha_s^L \rho_s^L, & \text{if } M_{1/2} > 0, \\ \alpha_s^R \rho_s^R, & \text{if } M_{1/2} \leq 0, \end{cases} \tag{3-22}$$

where $M_{1/2}$ is the solid phase Mach number, which is based on the compaction wave speed at the cell edge; and $\mathcal{F}$ is the extra dissipation term defined as

$$\mathcal{F} = \frac{(c_{1/2} - \epsilon)[1 + |M_{1/2}|(1 - \mathcal{G}/2)]}{2} \frac{max(\alpha_s^L, \alpha_s^R)}{\alpha_{s,max}} (\alpha_s^L \rho_s^L - \alpha_s^R \rho_s^R). \tag{3-23}$$

$\alpha_{s,max}$ is the packing limit as discussed before, and $\mathcal{G}$ is the parameter that decides the amount of dissipation. This is used when the primitive variables,

$$[\alpha_s, Y_{s,i}, \boldsymbol{v}_s, \Theta_s, T_s]^T \tag{3-24}$$

are interpolated at the cell edges. ϵ (a constant, usually $= 10^{-10}$) is used to avoid division by zero when the compaction wave speed is zero. The function, $\mathcal{F}$, has a form that is similar to the Rusanov flux (Toro (2013)) dissipation term, and is used to reduce any numerical oscillations (Houim and Oran, 2016).

The solid phase primitive variables are interpolated using a fifth-order Weighted Essentially Non-Oscillatory (WENO) scheme based on Shu (1999), which are then passed through a TVD slope limiter, ϕ_{TVD}. Thus the solid phase primitive variable Q can be written as

$$Q^L_{1+1/2} = Q_i + 0.5(Q_i - Q_{i-1})\phi_{TVD}. \tag{3-25}$$

In this research, the slope limiter used us based on Houim and Kuo (2011) and Kim and Kim (2005),

$$\phi_{TVD} = max\left[0, min\left(\mathcal{G}, \mathcal{G}\frac{Q_{i+1} - Q_i}{Q_i - Q_{i-1}}, 2\frac{\hat{Q}^L_{i+1/2} - Q_i}{Q_i - Q_{i-1}}\right)\right], \tag{3-26}$$

where $\hat{Q}^L_{i+1/2}$ is the left-biased variable interpolated using WENO and

$$\mathcal{G} = max[2(1 - \mathcal{D}\zeta^2), 0]. \tag{3-27}$$

$\mathcal{D} \geq 0$ is an input parameter than can be changed by the user and is usually set to 1. The maximum solid volume fraction in the whole domain, α_s^M, is used by WENO for the interpolation, Also, ζ is given by

$$\zeta = \begin{cases} \frac{\alpha_s^M - \alpha_{s,crit}}{\alpha_{s,max} - \alpha_{s,crit}}, & \text{if } \alpha_s^M > \alpha_{s,crit}, \\ 0, & \text{if } \alpha_s^M < \alpha_{s,crit}, \end{cases} \tag{3-28}$$

where $\alpha_{s,crit}$ is the critical volume fraction. As far as the dissipation term and slope limiters are concerned, they do not affect the solutions when the solid volume fraction is low. They reduce oscillations only in regions that have high solid volume fractions. The factor $\mathcal{D}$ has two benefits. It reduces the edge interpolation scheme to first-order in regions of high solid volume fraction, and it increases the dissipation of the AUSM$^+$-up flux scheme. The value of $\mathcal{G}$ becomes 2 in the dilute regions and 0 in dense regions. This allows for a smooth transition between the two states. $\mathcal{G}$ is usually set to 1, unless otherwise noted.

For the average compaction wave speed, we use

$$c_{1/2} = \sqrt{\frac{\alpha_s^L \rho_s^L (c_s^L)^2 + \alpha_s^R \rho_s^R (c_s^R)^2}{\alpha_s^L \rho_s^L + \alpha_s^R \rho_s^R}} + \epsilon, \tag{3-29}$$

and the average velocity is given by

$$u_{1/2} = c_{1/2} M_{1/2}. \tag{3-30}$$

The solid phase Mach number at the cell edge is caculated by

$$M_{1/2} = \mathcal{M}_4^+(M^L) + \mathcal{M}_4^-(M^R) - 2\frac{K_p}{f_a} max(1 - \sigma \bar{M}^2, 0) \frac{p_{s,tot}^R - p_{s,tot}^L}{(\alpha_s^L \rho_s^L + \alpha_s^R \rho_s^R + \epsilon) c_{1/2}^2}, \tag{3-31}$$

where $f_a = 1$, K_p and σ are AUSM dissipation parameters, given by

$$K_p = 0.25 + 0.75(1 - \frac{\mathcal{G}}{2}), \qquad \sigma = 0.75\frac{\mathcal{G}}{2}, \tag{3-32}$$

and

$$M^L = \frac{u_s^L}{c_{1/2}}, \qquad M^R = \frac{u_s^R}{c_{1/2}}, \qquad \bar{M}^2 = \frac{(u_s^L)^2 + (u_s^R)^2}{2c_{1/2}^2}. \tag{3-33}$$

At the cell edges, the pressure is calculated using

$$\begin{aligned} p_{s,tot,i+1/2} = &-K_u f_a (c_{1/2} - \epsilon) \mathcal{P}_5^+(M^L) \mathcal{P}_5^-(M^R) (\alpha_s^L \rho_s^L + \alpha_s^R \rho_s^R)(u_s^R - u_s^L) \\ &+ \mathcal{P}_5^+(M^L) p_{s,tot}^L + \mathcal{P}_5^-(M^R) p_{s,tot}^R, \end{aligned} \tag{3-34}$$

and K_u, an AUSM dissipation parameter is given as

$$K_u = 0.75 + 0.25(1 - \frac{\mathcal{G}}{2}). \tag{3-35}$$

The way to calculate $\mathcal{M}_4^+$ and $\mathcal{M}_4^-$ is to first define $\mathcal{M}_1^\pm$ and $\mathcal{M}_2^\pm$ as

$$\mathcal{M}_1^\pm(M) = \frac{1}{2}(M \pm |M|), \mathcal{M}_2^\pm(M) = \pm\frac{1}{4}(M \pm 1)^2, \tag{3-36}$$

and then

$$\mathcal{M}_4^\pm(M) = \begin{cases} \mathcal{M}_1^\pm(M), & \text{if } |M| \geq 1, \\ \mathcal{M}_2^\pm(M)[1 \mp 16\beta\mathcal{M}_2^\mp(M)], & \text{if } |M| < 1, \end{cases} \tag{3-37}$$

Similarly, the pressure splitting polynomials, $\mathcal{P}_5^+$ and $\mathcal{P}_5^-$ can be calculated using

$$\mathcal{P}_5^\pm(M) = \begin{cases} \mathcal{M}_1^\pm(M)/M, & \text{if } |M| \geq 1, \\ \mathcal{M}_2^\pm(M)[(\pm 2 - M) \mp 16\xi M\mathcal{M}_2^\mp(M)], & \text{if } |M| < 1, \end{cases} \tag{3-38}$$

with, $\beta = 0.125$ and

$$\xi = (3/16)(-4 + 5f_a^2). \tag{3-39}$$

For the gas-phase volume fraction, we use

$$\alpha_{g,i+1/2} = \begin{cases} \alpha_{g,i+1/2}^L, & \text{if } \dot{m}_{s,i+1/2} > 0, \\ \alpha_{g,i+1/2}^R, & \text{if } \dot{m}_{s,i+1/2} \leq 0. \end{cases} \tag{3-40}$$

Also, the non-conservative terms, $\alpha_{s,i+1/2}u_{s,i+1/2}$ and $u_{s,i+1/2}$ can be calculated as

$$\alpha_{s,i+1/2}u_{s,i+1/2} = \begin{cases} \frac{\dot{m}_{s,i+1/2}}{\rho_{s,i+1/2}^L}, & \text{if } \dot{m}_{s,i+1/2} > 0, \\ \frac{\dot{m}_{s,i+1/2}}{\rho_{s,i+1/2}^R}, & \text{if } \dot{m}_{s,i+1/2} \leq 0, \end{cases} \tag{3-41}$$

and

$$u_{s,i+1/2} = \begin{cases} \frac{\dot{m}_{s,i+1/2}}{\alpha^L_{s,i+1/2}\rho^L_{s,i+1/2}}, & \text{if } \dot{m}_{s,i+1/2} > 0, \\ \frac{\dot{m}_{s,i+1/2}}{\alpha^R_{s,i+1/2}\rho^R_{s,i+1/2}}, & \text{if } \dot{m}_{s,i+1/2} \leq 0. \end{cases} \tag{3-42}$$

If the parameters $\mathcal{F} = 0$, $\mathcal{G} = 2$ and $\epsilon = 0$, this behaves exactly as the original unmodified AUSM$^+$-up scheme. When the inter-granular stress is zero,

$$c_{1/2}M_{1/2} = \begin{cases} u^L_s, & \text{if } u^L_s \geq 0 \text{ and } u^R_s > 0, \\ u^R_s, & \text{if } u^L_s < 0 \text{ and } u^R_s \leq 0, \\ u^L_s + u^R_s, & \text{if } u^L_s > 0 \text{ and } u^R_s < 0, \\ 0, & \text{if } u^L_s < 0 \text{ and } u^R_s > 0. \end{cases} \tag{3-43}$$

3.1.4 Gas Phase Fluxes

Usually, the HLLC flux scheme returns the flux vector. However, in this case, we had to modify the HLLC solver to return the solution vector for the Riemann problem instead of the flux vector. This was done in order to obtain the gas-phase pressure so that we can calculate the $\alpha_g \nabla p_g$ term, for which we need the pressure. Thus at any cell edge, $i + 1/2$, the solution vector can be written as

$$\boldsymbol{R}_{g,i+1/2} = \begin{cases} \boldsymbol{R}^L_{g,i+1/2} & \text{if } 0 \leq S^L, \\ \boldsymbol{R}^L_g* & \text{if } S^L \leq 0 \leq S^*, \\ \boldsymbol{R}^R_g* & \text{if } S^* \leq 0 \leq S^R, \\ \boldsymbol{R}^R_{g,i+1/2} & \text{if } S^R \leq 0. \end{cases} \tag{3-44}$$

The solution vectors for the left and right interpolated states and the middle (or star) states are given by

$$\boldsymbol{R}_g^M = \begin{bmatrix} \rho_g^M \\ Y_{g,j}^M \\ u_g^M \\ p_g^M \\ E_g^M \end{bmatrix}, \qquad \boldsymbol{R}_g^{M*} = \begin{bmatrix} \rho_g^{M*} \\ Y_{g,j}^M \\ S^* \\ p^* \\ E_g^{M*} \end{bmatrix}. \tag{3-45}$$

Here M represents L or R depending on whether it is the left or right interpolated state.

For the star states,

$$\rho_g^{M*} = \rho_g^M \frac{S^M - u_g^M}{S^M - S^*}, \qquad E_g^{M*} = E_g^M + \frac{p^* S^* - p_g^M u_g^M}{\rho_g^M (S^M - u_g^M)}, \tag{3-46}$$

which are the density and total energy respectively.

The contact surface velocity S^*, and pressure p^* are given by

$$S^* = \frac{p_g^R - p_g^L + \rho_g^L u_g^L (S^L - u_g^L) - \rho_g^R u_g^R (S^R - u_g^R)}{\rho_g^L (S^L - u_g^L) - \rho_g^R (S^R - u_g^R)}, \tag{3-47}$$

$$p^* = p_g^L + \rho_g^L (S^L - u_g^L)(S^* - u_g^L). \tag{3-48}$$

For the wave speed estimates, S^L and S^R, we use a Roe-averaged method based on Einfeldt et al. (1991), written as

$$S^L = min(u_g^L - c_g^L, \tilde{u}_g - \tilde{c}_g), \tag{3-49}$$

$$S^R = max(u_g^R + c_g^R, \tilde{u}_g + \tilde{c}_g), \tag{3-50}$$

where,

$$\tilde{\boldsymbol{v}}_g = \frac{\sqrt{\rho_g^L}\boldsymbol{v}_g^L + \sqrt{\rho_g^R}\boldsymbol{v}_g^R}{\sqrt{\rho_g^L} + \sqrt{\rho_g^R}}, \tag{3-51}$$

$$\tilde{H}_g = \frac{\sqrt{\rho_g^L} H_g^L + \sqrt{\rho_g^R} H_g^R}{\sqrt{\rho_g^L} + \sqrt{\rho_g^R}}, \tag{3-52}$$

$$\tilde{c}_g = [(\gamma - 1)(\tilde{H}_g - \frac{1}{2}\tilde{\boldsymbol{v}}_g \cdot \tilde{\boldsymbol{v}}_g)]^{1/2}. \tag{3-53}$$

The vector of primitive variables, $\boldsymbol{R}^L_{g,i+1/2}$ and $\boldsymbol{R}^R_{g,i+1/2}$ are interpolated using a fifth-order accurate method (Houim and Kuo, 2011).

3.2 Integrating the Chemical Reaction Terms

The mass rate of change of chemical species are time-integrated using the yet another stiff solver (YASS) method (Khokhlov et al., 2012). The YASS solver is a stiff ODE solver, used to integrate equations of the type

$$\frac{d\boldsymbol{Y}}{dt} = \boldsymbol{F}(Y) \tag{3-54}$$

with $\boldsymbol{Y} = \epsilon$ in this case and $\boldsymbol{F}(Y) = k_{CH_4}(CH_4^0 - \epsilon)\sqrt{O_2^0 - 2\epsilon}$. The time evolution of $\boldsymbol{F}$ can be written as

$$\frac{d\boldsymbol{F}}{dt} = \hat{J} \cdot \boldsymbol{F}, \tag{3-55}$$

where

$$\hat{J}(t) = \frac{\partial \boldsymbol{F}}{\partial \boldsymbol{Y}} \tag{3-56}$$

is the Jacobian matrix of $\boldsymbol{F}$. The YASS time step can then be written as

$$(\hat{I} - \Delta t \hat{J}^0)(\boldsymbol{Y}^n - \boldsymbol{Y}^0) = \Delta t \boldsymbol{F}^0, \tag{3-57}$$

where the superscript 0 denotes the value of the variables at the beginning of the time step and superscript n denotes the value of the variables at the end of the time step, and Δt is the time step size. This equation can then be rearranged to obtain $\boldsymbol{Y}^n$ as

$$\boldsymbol{Y}^n = \frac{\Delta t \boldsymbol{F}^0}{\hat{I} - \Delta t \hat{J}^0} + \boldsymbol{Y}^0. \tag{3-58}$$

3.2.1 Single-Step Reaction Mechanism

For this case, $\hat{J}^0$ can be calculated by taking the partial derivative of $\boldsymbol{F}(Y)$ with respect to $\boldsymbol{Y}$, which can be calculated as

$$\hat{J}^0 = \frac{\partial \boldsymbol{F}}{\partial \mathbf{Y}} = \frac{\partial}{\partial \epsilon}\left[k_{CH_4}(CH_4^0 - \epsilon)\sqrt{O_2^0 - 2\epsilon}\right]. \tag{3-59}$$

Thus

$$\hat{J}^0 = -k_{CH_4}\left(\frac{CH_4^0 + O_2^0 - 3\epsilon}{\sqrt{O_2^0 - 2\epsilon}}\right). \tag{3-60}$$

Now we can write $\boldsymbol{Y}^n = \epsilon^n$ as

$$\epsilon^n = \frac{\Delta t k_{CH_4}(CH_4^0 - \epsilon^0)\sqrt{O_2^0 - 2\epsilon^0}}{1 - \Delta t\left[-k_{CH_4}\left(\frac{CH_4^0 + O_2^0 - 3\epsilon^0}{\sqrt{O_2^0 - 2\epsilon^0}}\right)\right]} + \epsilon^0. \tag{3-61}$$

This equation is used to get the production/destruction rates of methane and can then be used along with the stoichiometric ratios to calculate the production/destruction rates of the oxidizer and products. Once those are calculated, the total energy deposited to the system due to the gas-phase reactions can also be found out from using the enthalpy of formation of the various species.

One assumption that we make during the integration of the chemical reaction is that the gas-phase temperature remains constant during the integration.

3.2.2 Two-step reaction mechanism

As mentioned in the previous section, here also we use the YASS (Khokhlov et al., 2012) method to time-integrate the reactions. However, here the complexity of the method is much more. There are five participating species, as well as gas-phase temperature, that need to be solved simultaneously. Thus it requires a proper 6×6 Jacobian matrix, that has to be constructed and then the equations have to solved. The equations Eq. 3-54 to Eq. 3-58 are still applicable, but the vectors $\boldsymbol{Y}$ and $\boldsymbol{F}$, as well as the matrix $\hat{J}$ are different. These are

$$\boldsymbol{Y} = \begin{bmatrix} \epsilon_{CH_4} \\ \epsilon_{O_2} \\ \epsilon_{H_2O} \\ \epsilon_{CO_2} \\ \epsilon_{CO} \\ T \end{bmatrix}, \qquad \boldsymbol{F} = \begin{bmatrix} \text{RHS of Eq. 2-64} \\ \text{RHS of Eq. 2-65} \\ \text{RHS of Eq. 2-66} \\ \text{RHS of Eq. 2-67} \\ \text{RHS of Eq. 2-68} \\ \text{RHS of Eq. 2-69} \end{bmatrix},$$

and

$$\hat{J} = \begin{bmatrix} \frac{\partial F_1}{\partial Y_1} & \frac{\partial F_1}{\partial Y_2} & \frac{\partial F_1}{\partial Y_3} & \frac{\partial F_1}{\partial Y_4} & \frac{\partial F_1}{\partial Y_5} & \frac{\partial F_1}{\partial Y_6} \\ \frac{\partial F_2}{\partial Y_1} & \frac{\partial F_2}{\partial Y_2} & \frac{\partial F_2}{\partial Y_3} & \frac{\partial F_2}{\partial Y_4} & \frac{\partial F_2}{\partial Y_5} & \frac{\partial F_2}{\partial Y_6} \\ \frac{\partial F_3}{\partial Y_1} & \frac{\partial F_3}{\partial Y_2} & \frac{\partial F_3}{\partial Y_3} & \frac{\partial F_3}{\partial Y_4} & \frac{\partial F_3}{\partial Y_5} & \frac{\partial F_3}{\partial Y_6} \\ \frac{\partial F_4}{\partial Y_1} & \frac{\partial F_4}{\partial Y_2} & \frac{\partial F_4}{\partial Y_3} & \frac{\partial F_4}{\partial Y_4} & \frac{\partial F_4}{\partial Y_5} & \frac{\partial F_4}{\partial Y_6} \\ \frac{\partial F_5}{\partial Y_1} & \frac{\partial F_5}{\partial Y_2} & \frac{\partial F_5}{\partial Y_3} & \frac{\partial F_5}{\partial Y_4} & \frac{\partial F_5}{\partial Y_5} & \frac{\partial F_5}{\partial Y_6} \\ \frac{\partial F_6}{\partial Y_1} & \frac{\partial F_6}{\partial Y_2} & \frac{\partial F_6}{\partial Y_3} & \frac{\partial F_6}{\partial Y_4} & \frac{\partial F_6}{\partial Y_5} & \frac{\partial F_6}{\partial Y_6} \end{bmatrix}. \tag{3-62}$$

We can now solve Eq. 3-58 for the new time-step n, which requires inverting the matrix $\hat{I} - \Delta t \hat{J}^0$. In our solver, we use the classic L-U decomposition method to invert the matrix and solve the set of simultaneous equations. This equation is used to get the production/destruction rates of all participating species and the total energy deposited to the system due to the gas-phase reactions can also be found out from using the enthalpy of formation of the various species.

3.3 Radiation Solver

After we make the FP$_N$ approximation to the RTE, we still have to solve the resulting equations. To do this, we use the MUSCL (Monotone Upwind Schemes for scalar Conservation Laws) along with Rusanov flux method. This is then time-integrated to a pseudo-steady state. Let us briefly discuss the MUSCL scheme and the Rusanov fluxes.

3.3.1 MUSCL Interpolation Scheme

MUSCL is a highly accurate method for solving finite volume problems. Despite the presence of discontinuities, shocks and large gradients, MUSCL is able to retain its accuracy. The term MUSCL was first introduced by Bram van Leer in van Leer (1979). In this paper, he constructed the first high-order, total variation diminishing (TVD) scheme and he was able to achieve second order spatial accuracy. MUSCL based numerical schemes extend the idea of using a linear piecewise approximation to each cell by using slope limited left and right extrapolated states. MUSCL schemes in their most general form interpolate a variable u to cell edge $i+1/2$ from the left using,

$$u_{L,i+1/2} = u_i + 0.5(u_i - u_{i-1})\phi(r_i, \alpha, \beta), \tag{3-63}$$

where ϕ is a slope limiter, $u_{L,i+1/2}$ is the left interpolated variable at the right edge of cell i, which is represented by $i+1/2$, and the slope ratio, r_i is given by,

$$r_i = \frac{u_{i+1} - u_i}{u_i - u_{i-1}}. \tag{3-64}$$

This method reduced the order of the interpolation from a higher order to a first order scheme if the function sees in discontinuities or oscillations. Various forms of slope limiters exist, such as,

$$\text{minmod:} \quad \phi(r_i, \alpha, \beta) = \text{max}(0, min(r_i, 1)), \tag{3-65}$$

$$\text{van Leer:} \quad \phi(r_i, \alpha, \beta) = \text{max}\left[0, \text{min}\left(\alpha, \alpha r_i, \frac{2r_i}{1+r_i}\right)\right], \tag{3-66}$$

$$\text{superbee:} \quad \phi(r_i, \alpha, \beta) = \text{max}[0, \text{min}(\alpha r_i, 1), \text{min}(r_i, \alpha)], \tag{3-67}$$

among others. In one dimension, α is ~ 2. In two dimensions, it is defined as,

$$\alpha = \text{max}\left[1, \text{min}\left(2, \frac{2\ \text{max}(1, r_j)(1 + \text{max}(0, r_{i+1}\text{tan}\ \theta_{i+1}))}{1 + \text{tan}\ \theta_i}\right)\right], \tag{3-68}$$

where

$$\tan\,\theta_i = \left|\frac{u_{i,j+1} - u_{i,j-1}}{u_{i+1,j} - u_{i-1,j}}\right|. \tag{3-69}$$

3.3.2 Rusanov Flux Scheme

With the evaluation of the flux function only involving pairs of selected conserved quantities on the edge from the local and adjacent cells, it can be interpreted as a Riemann problem, which can be handled by updating the flux. Riemann solvers computing flux updates are typically used for higher-order methods. They rely on flux update computations directly involving the flux term. Even if no conserved quantity is exchanged, a flux computation still leads to a flux generation. The local Lax-Friedrichs flux, also known as the Rusanv flux is one of the most widely known and used flux solver.

Consider flux computations which are based on the one-dimensional representation in edge space and a constant state representation of the solution on each side of the edge with U_i^L and U_i^R. Thus the Riemann problem in edge space is given as,

$$U(z) = \begin{cases} U^L & \text{if } z \leq 0 \\ U^R & \text{if } z > 0, \end{cases} \tag{3-70}$$

with the function

$$\mathcal{F}(U_i^L(t), U_i^R(t)) \tag{3-71}$$

computing the change of conserved quantities for this one-dimensional Riemann problem. Averaging both points, we get

$$\mathcal{F}(U_i^L(t), U_i^R(t)) = \frac{1}{2}(F(U_i^L) + F(U_i^R)), \tag{3-72}$$

where F evaluates the flux inside the cell and $\mathcal{F}$ evaluates the Riemann problem at the cell edge. Using this average value as the flux over the edges would result in a numerically unstable simulation. Therefore, an artificial numerical damping is frequently introduced to overcome these instabilities. This damping is often referred to as numerical diffusion or artificial viscosity.

One example of such fluxes involving a numerical diffusion is the Rusanov flux. This flux function introduces a diffusion term with its magnitude depending on the speed of the information propagation. This propagation speed is given by the eigenvalues of the Jacobian matrix of the flux. For the two-dimensional Lax-Friedrichs flux function for Riemann problem given by U_j^L, U_j^R and $F(U)$, we use the flux function

$$\hat{\mathcal{F}} = \frac{1}{2}(F(U_j^L) + F(U_j^R)) \cdot \overrightarrow{n}_e^+ - \frac{1}{2}\nu(U_j^R - U_j^L), \tag{3-73}$$

where the first term of the right hand side of the equation represents the average of the flux and the second term is the numerical flux viscosity. The numerical Lax-Friedrichs viscosity component is given by,

$$\nu = \mathsf{max}(|J_F(U^R)|, |J_F(U^L)|). \tag{3-74}$$

Here, $J_F(U)$ is the Jacobian of the function F with respect to the conserved quantities U.

CHAPTER 4
CODE VERIFICATION TESTS

The first step to checking the validity of results obtained from a code is to verify it against experimental or analytical data. These tests need to be performed in multiple steps in order to test the validity of the data for each part of the solver. This includes the hydrodynamic solver, the granular multiphase solver, the chemical reaction mechanism solver and the radiation solver.

4.1 Hydrodynamic Solver

A simple verification test for the hydrodynamic solver is the Sod's shocktube problem. This simple 1-D test consists of a tube with two equal length sections, initially separated by a diaphragm, and closed at both ends. The left half of the tube is filled with air at an initial pressure of 100,000 Pa and density of 1 kg/m^3. The other half is also filled with air but at a pressure of 10,000 Pa and density of 0.125 kg/m^3. The initial velocity of air in both sections is zero. The high pressure region is referred to as the driver section and the other region is called the driven section. The initial conditions are represented in Fig. 4-1.

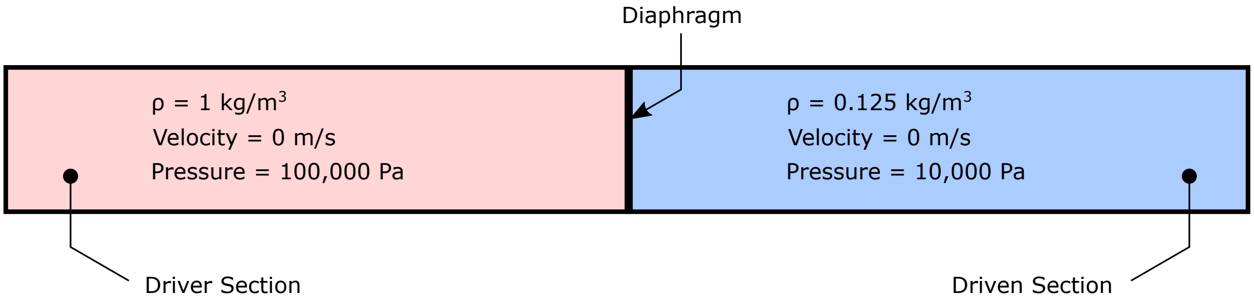

Figure 4-1. Initial conditions for the Sod's shock tube problem.

The calculation is started at the moment the diaphragm breaks. At this moment, a shock wave propagates into the driven section and an expansion wave into the driver section. The expanded gas is separated from the compressed gas by a contact surface, which moves right at a constant velocity.

Here, the approximate Riemann solver uses the MUSCL interpolation scheme (van Leer, 1979) along with the Rusanov flux method (Rusanov, 1961). It also uses the minmod slope limiter based on Roe (1986). The solution after 16 ms using 10,000 grid points is shown in Fig. 4-2, along with the exact solution from an exact Riemann solver.

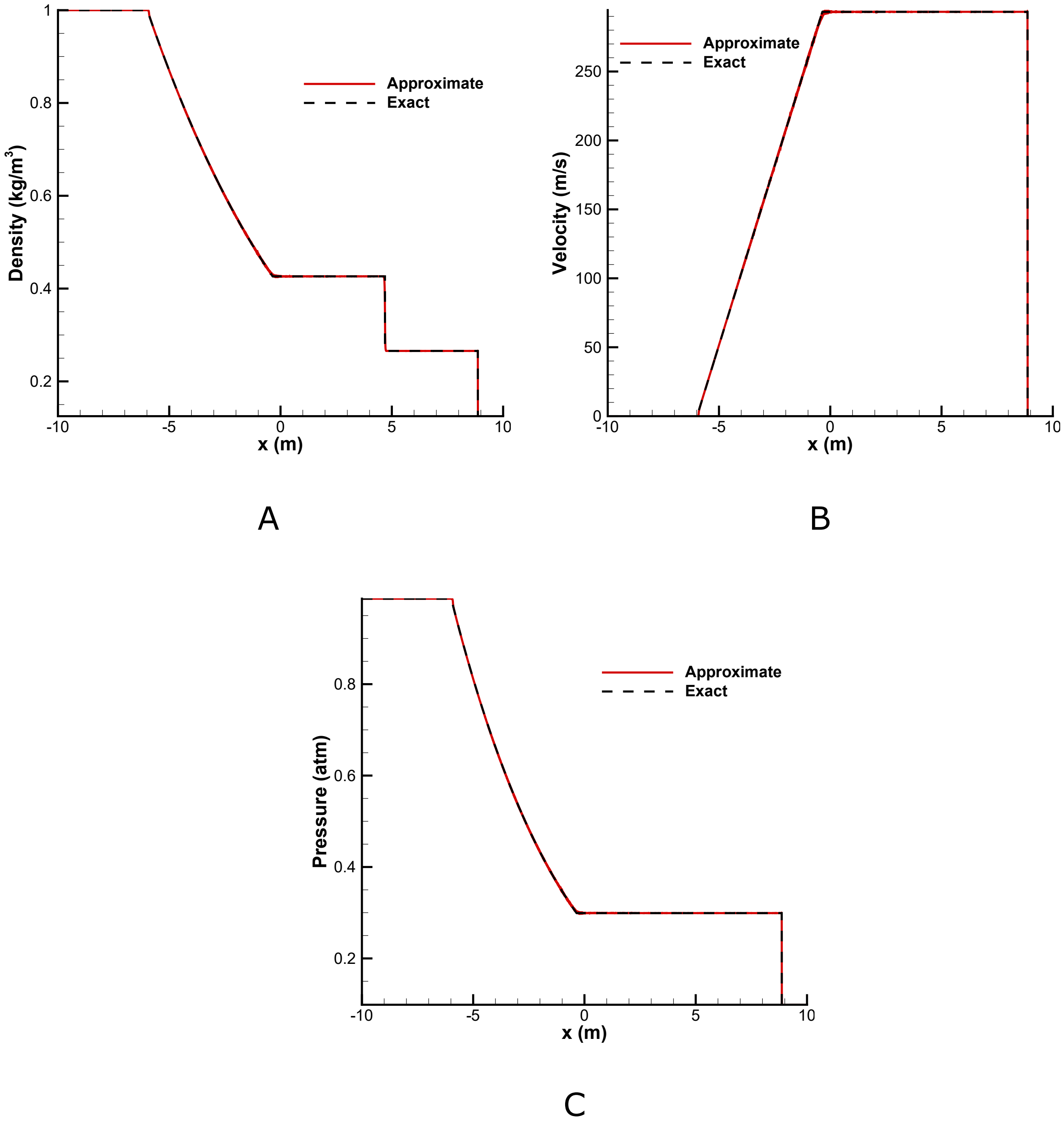

A

B

C

Figure 4-2. Approximate (using 10,000 grid points) and exact Riemann solver solutions to the Sod's shock tube problem after 16 ms. A) Density B) Velocity C) Pressure for both solutions are shown.

4.2 Granular Multiphase Solver

To test the accuracy and robustness of the solver, we ran a couple of one-dimensional, two-phase granular shock-tube problems (Houim and Oran, 2016). The first test was for a low particle volume fraction and the second was with a densely packed particle phase.

4.2.1 Loosely Packed Two-Phase Granular Shock-Tube Problem

In this case, the solids and frictional-collisional pressures are negligible due to the loose packing of the particles. Standard Riemann solvers are incapable of solving such problems due to the hyperbolic degeneracy caused by the low volume fraction. The initial conditions used in this test are based on Saito et al. (2003) and Fedorov et al. (2007):

$$\begin{aligned} p_g^L &= 10 \text{ atm}, & p_g^R &= 1 \text{ atm}, \\ T^L &= 270 \text{ K}, & T^R &= 270 \text{ K}, \\ Y_{g,air}^L &= 1, & Y_{g,air}^R &= 1, \\ \alpha_s^L &= 0, & \alpha_s^R &= 5.172 \times 10^{-4}, \\ \Theta_s^L &= 0, & \Theta_s^R &= 0. \end{aligned} \tag{4-1}$$

Here, the particle density, ρ_s = 2500 kg/m^3, particle diameter, d_s = 10 μm, and specific heat, $C_{V,s}$ = 718 J/(kg.K). The entire shock tube is 0.257798 m long and the diaphragm is at 0.129 m. The simulation was run till 184 μs after the diaphragm is ruptured, using two grid spacings of 1000 points and 100 points. These results are shown in Fig. 4-3.

Exact solutions for such granular shock-tube problems do not exist. Therefore the solution can be only verified by comparing them to the reference solutions in Fedorov et al. (2007) and Saito et al. (2003). These comparisons reveal that the modified AUSM$^+$-up scheme that is used for the granular-phase flux works well for nearly pressureless dust.

After the diaphragm is ruptured, a shock wave propagates from the left half of the domain to the right half, and a rarefaction wave propagates in the opposite direction. We can also see the presence of a contact surface. The particles in the region behind the shock interact with the gas and slow it down via drag force. This causes a localized increase in the gas pressure.

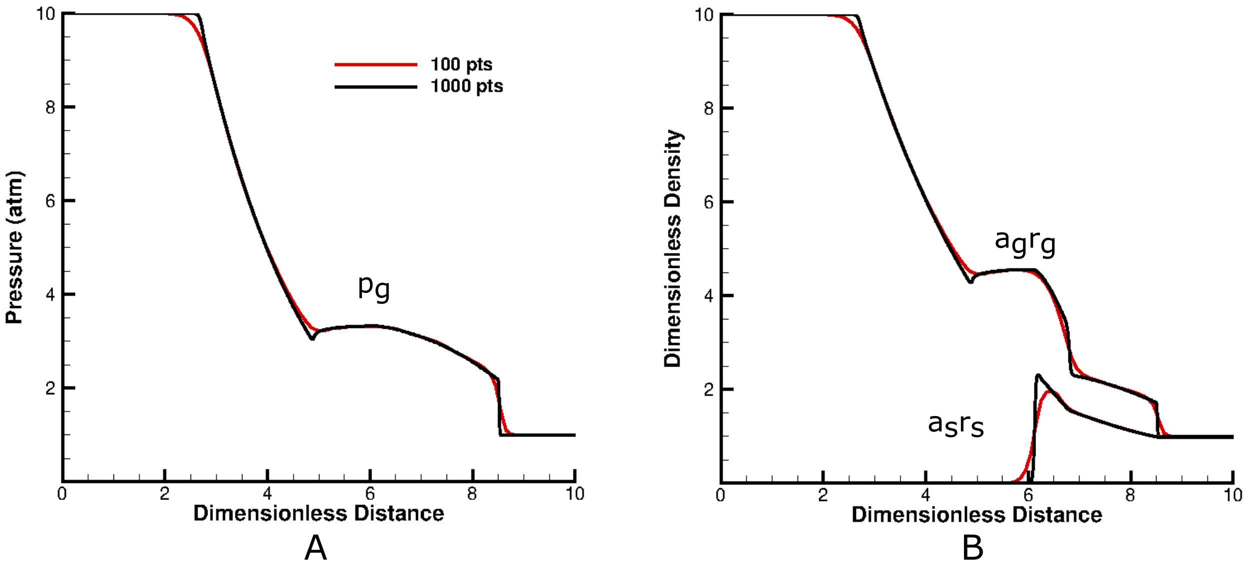

Figure 4-3. Solutions for the loosely packed two-phase granular shock-tube problem at 184 μs. A) Gas-phase pressure. B) Gas and solid-phase bulk densities. The densities are nondimensionalized by dividing the actual densities by the initial gas density in the right half of the domain. The x-distance has been nondimensionalized such that the range is from 0 to 10. This is done to make the results comparable to Fedorov et al. (2007).

Acoustic waves are produced due to this pressure rise, which travel towards the rarefaction wave and produce a hook-like structure near x = 5. The effect of the granular phase can be observed well in Fig. 4-4.

4.2.2 Densely Packed Two-Phase Granular Shock-Tube Problem

This test was performed to check the ability of the solver to predict the relaxation structures of granular shocks (Kamenetsky et al., 2000). This is also a stress test for the solver since it produces scenarios where the high-pressure gas has to interact with the high volume granular fraction regions, close to the packing limit and has steep granular interfaces. Here the particle volume fraction is initially at 40% and the initial driving section pressure is at 100 atm. The initial conditions are:

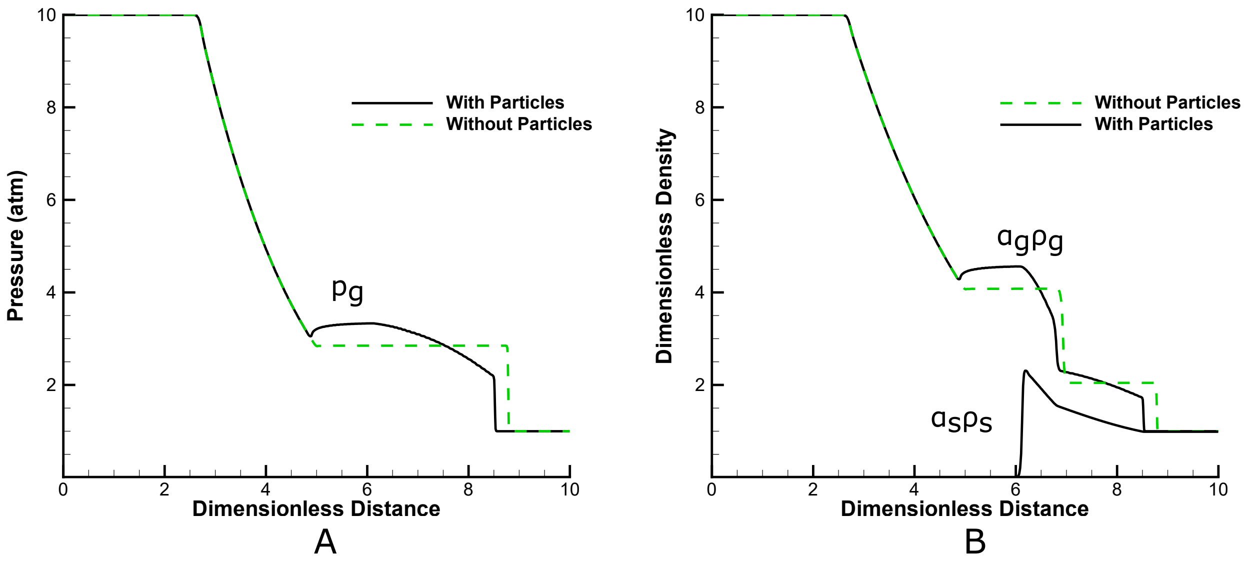

Figure 4-4. Solutions for the loosely packed two-phase granular shock-tube problem at 184 μs, comparing cases with and without particles to show the effect of the granular phase. A) Gas-phase pressure. B) Gas and solid-phase bulk densities. Both cases are using 1000 grid points. The densities are nondimensionalized by dividing the actual densities by the initial gas density in the right half of the domain. The x-distance has been nondimensionalized such that the range is from 0 to 10.

$$
\begin{aligned}
p_g^L &= 100 \text{ atm}, & p_g^R &= 1 \text{ atm},\\
T^L &= 300 \text{ K}, & T^R &= 300 \text{ K},\\
Y_{g,air}^L &= 1, & Y_{g,air}^R &= 1,\\
\alpha_s^L &= 0, & \alpha_s^R &= 0.4,\\
\Theta_s^L &= 0, & \Theta_s^R &= 0.
\end{aligned}
\tag{4-2}
$$

The shock-tube is 6 cm in length, with the diaphragm placed at the center of the tube. The calculation was run on 1200 grid points for 100 μs after the rupture of the diaphragm. Particle diameter is 5 μm, density is 1470 kg/m^3 and specific heat is 987 J/(kg.K). The coefficient of restitution is maintained at 0.999. Due to the granular volume fraction being close to the packing limit, additional dissipation had to be added by keeping the hyperbolic dissipation factor ($\mathcal{D}$) at 1. The solution at 100 μs is shown in Fig. 4-5.

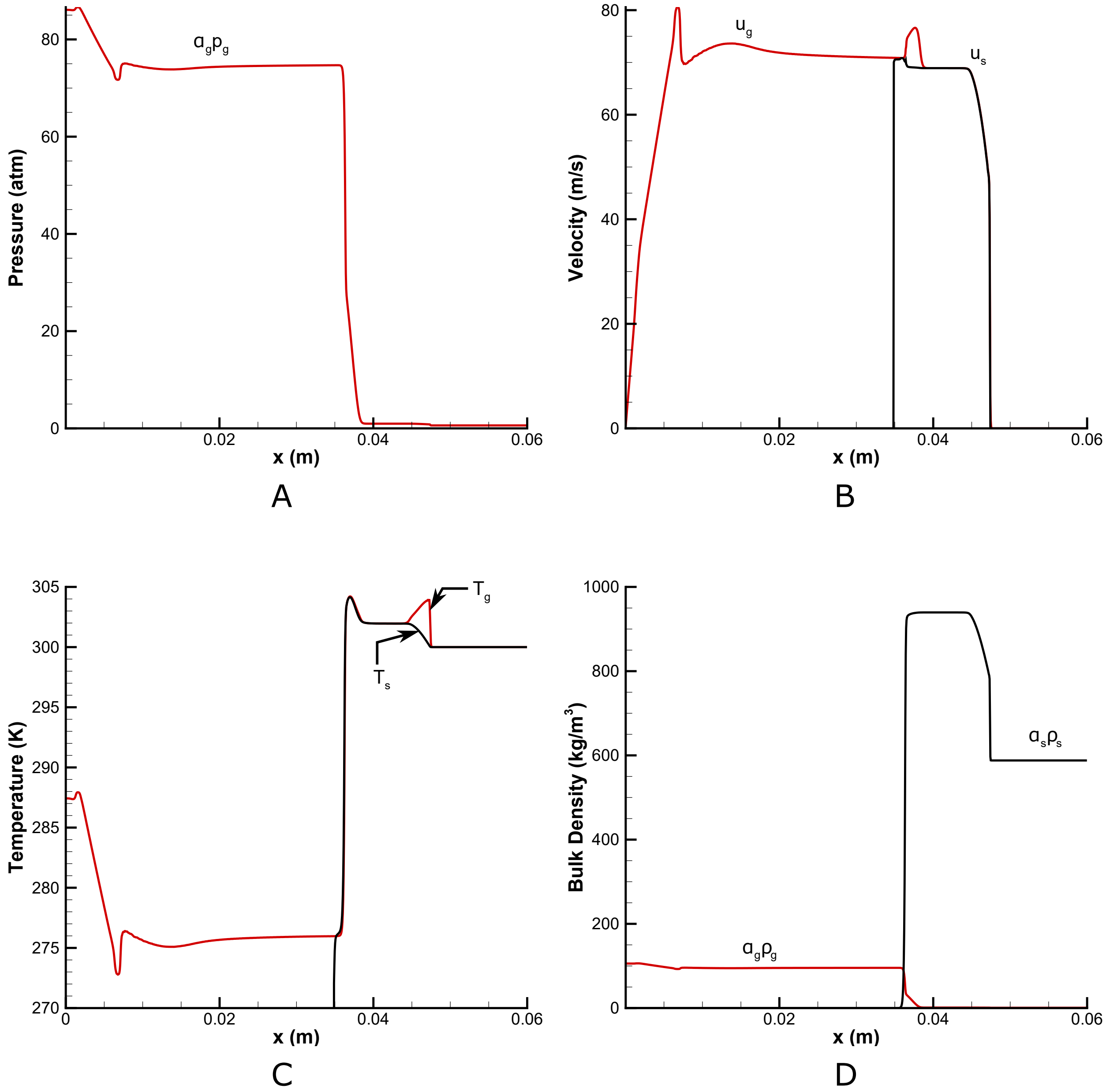

Figure 4-5. Solutions for the densely packed two-phase granular shock-tube problem at 100 μs. A) Gas-phase pressure. B) Gas and solid-phase velocities. C) Gas and solid-phase temperatures. D) Gas and solid-phase bulk densities. The coefficient of restitution e $=$ 0.999 and hyperbolic dissipation parameter $\mathcal{D} = 1$.

In this case, the interactions between the particles become important, which was negligible for the previous case. Once the calculation begins, a granular shock propagates in the solid phase. The Archimedes force ($\alpha_s \nabla p_g$) and the drag force on the particles interacting with the high-pressure gas together cause this granular shock. The granular shock relaxation structure is comparable to that in Kamenetsky et al. (2000). The temperature in both phases increase by ~ 2.5 K close to the contact surface. This is caused by the frictional heating from the interaction of the two phases. Away from the granular shock, the granular temperature, Θ_s, and the solids pressure, p_s, falls off almost linearly to zero due to the lack of sources for granular energy, E_s. In order to maintain the mechanical equilibrium, the particles pack closer in this region, thus increasing the granular volume fraction and the friction pressure, as shown in Fig. 4-6.

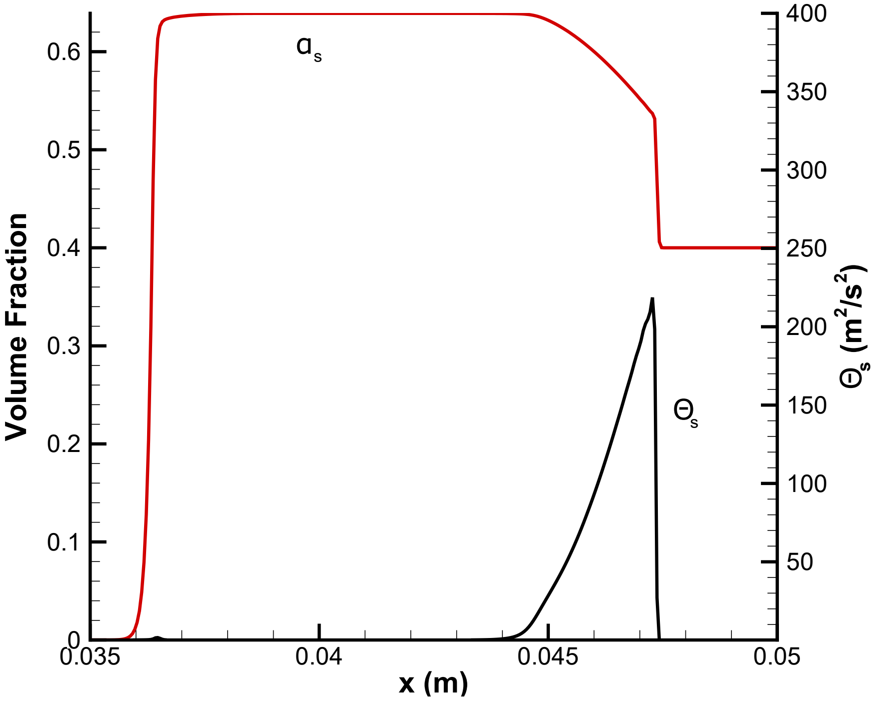

Figure 4-6. Plot of granular volume fraction and granular temperature for the densely packed two-phase granular shock-tube problem at 100 μs, showing the granular shock relaxation structure.

In this region of granular shock, the dense packing of the particles also compresses the gas, thus causing the gas-phase temperature and pressure to rise. This increase resembles a weak gas-phase shock and is representative of the Type II two-phase granular shock structure in Khmel' and Fedorov (2014a,b).

4.3 Integration of the Gas-Phase Chemical Reactions

In this section, we verify the results of HyBurn gas-phase chemical reaction integration step against the results obtained from Cantera with the same reaction mechanism. Two reaction mechanisms were used in this research and the tests are further segregated into two sections. The first section is a constant-volume reactor problem and the second is a flame speed and temperature test. The details of both these reaction mechanisms have been provided in the previous chapter.

For both the mechanisms, the test process was the same. We wrote a small python code using Cantera to solve for the equilibrium conditions of a constant-volume reactor. The same scenario was then replicated in HyBurn and the results were compared after equilibrium was achieved.

Another simple test was performed to compare the flame speeds and flame temperatures achieved from HyBurn and Cantera (Goodwin et al., 2017).

4.3.1 Constant-Volume Reactor

The constant-volume reactor belongs to the batch (or static) reactor category of ideal reactors. It also commonly referred to as a "bomb" reactor. As the name suggests, in this reactor, the volume of the reactor is always constant. No external work is done on the system, but heat can be exchanged with the surrounding via Newton's law of cooling,

$$\frac{dQ}{dt} = \hat{h}A(T_\infty - T), \tag{4-3}$$

where $\hat{h}$ is the coefficient of heat transfer (W/m^{2}K), T_∞ is the temperature of the surrounding, and A is the surface area of heat transfer.

Species mass conservation is given by,

$$\frac{dm_k}{dt} = \dot{\omega}_k W_k V \tag{4-4}$$

where m_k is the mass of species k (kg), $\dot{\omega}_k$ is the molar rate of production of species k due to chemical reaction (mole/m^{3}s), W_k is the molecular mass of species k (kg/mol), and V is the volume of the system (m^3). The species mass fraction can then be written as,

$$\frac{dY_k}{dt} = \frac{\dot{\omega}_k W_k}{\rho}, \tag{4-5}$$

where $m = \sum m_k$ is the total mass of the fluid in the system and $\rho = m/V$.

The energy equation is given by,

$$\rho c_v \frac{dT}{dt} = -\sum_{k=1}^{K_g} e_k \dot{\omega}_k W_k + \frac{\hat{h}A}{V}(T_\infty - T), \tag{4-6}$$

where c_v is the mixture-averaged constant-volume specific heat, K_g is the number of gas species, and e_k is the species internal energy. Assuming ideal gas, the mixture-average constant-volume specific heat can be written as,

$$c_v = \sum_{k=1}^{K_g} Y_k c_{v,k}, \tag{4-7}$$

where $c_{v,k}$ is the constant-volume specific heat of species k, and is related to the species internal energy by,

$$c_{v,k} = \left(\frac{\partial e_k}{\partial T}\right)\bigg|_v . \tag{4-8}$$

The results for the constant-volume reactor test after 0.2 ms for the single-step reaction mechanism are shown in Fig. 4-7. Here, we compared the flame temperatures as well as the species mass fractions. It is clear that the results from HyBurn and Cantera (Goodwin et al., 2017) match quite well, indicating that integration of the gas-phase reaction step occurs as expected. Here the exact same transport properties, thermodynamic properties and chemical reaction data were used in both softwares.

The same test was performed for the 2-step reaction mechanism as well, and the results after 2 ms are shown in Fig. 4-8. Here also, the results from the two codes agree well. The slight difference in the temperature plot here is most likely because the Arrhenius parameters for the reverse reaction rate for the second reaction was not obtained directly from the reaction data file, but is instead based on curve fits to the data from Cantera. When obtaining

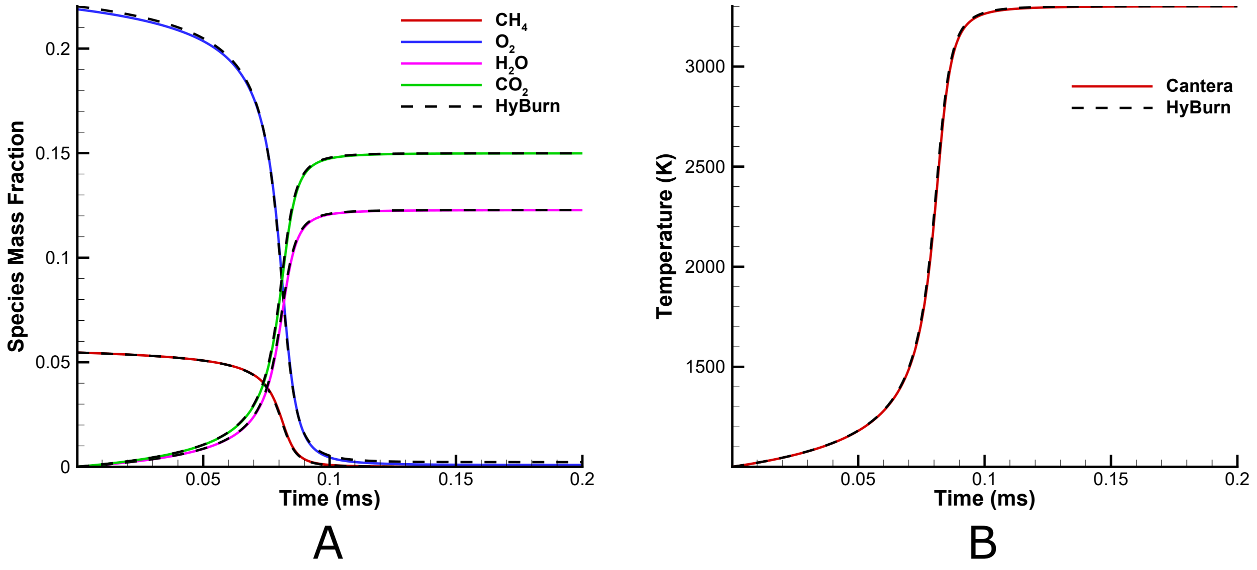

Figure 4-7. Constant-volume reactor plots comparing species mass fractions and gas temperature results from Cantera and HyBurn at 0.2 ms for the single-step reaction mechanism. A) Species mass fractions. B) Gas temperature.

this data, the parameters were chosen in such a way that they are biased towards higher temperatures. When the curve fit was not biased and taken over the entire temperature range of 300-6000 K, the constant-volume reactor data did not agree very well with the results from Cantera, especially for the species mass fractions. The temperature range was biased towards higher temperatures since it makes sense for the dissociation reactions to occur only at high temperatures and have no effect on the lower temperatures. This bias made the results a lot better. However, some accuracy is lost, and in this reaction model, the equilibrium is reached very slightly earlier than that in Cantera. It must be noted that this difference is minute and is not expected to influence the overall results of complex problems.

4.3.2 Flame Speeds and Temperatures

For this test, a short narrow 1-D tube was considered. This tube has an open left end and closed right end. The left half of the tube is filled with products at their flame temperatures, and the right half is filled with stoichiometric mixture of reactants at room temperature. The initial mass fractions and flame temperatures were based on the results from Cantera. The two reaction mechanisms have different flame temperatures and product species mass

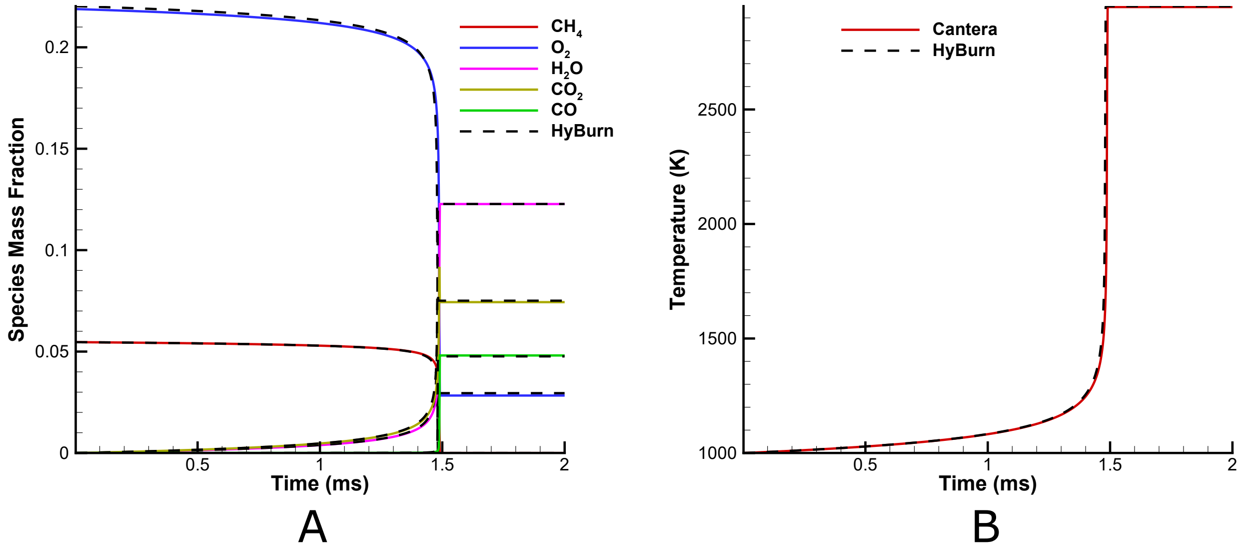

Figure 4-8. Constant-volume reactor plots comparing species mass fractions and gas temperature results from Cantera and HyBurn at 2 ms for the two-step reaction mechanism. A) Species mass fractions. B) Gas temperature.

fractions and thus these were defined individually for the mechanisms. The initial conditions for both reaction mechanisms are shown in Fig. 4-9. The initial pressures throughout the domain was 1 atm. and the initial velocities in both x and y directions are zero. The tube is 8 mm long and 1 mm high. A CFL number of 0.9 was used for both the hyperbolic and parabolic terms. This simulation used four levels of adaptive mesh refinement (AMR) using the AMReX library (Zhang et al., 2019). The base grid has 256 cells in the x-direction and 16 cells in the y-direction. The AMR refinement ratio is 2 for each level. Thus, at the finest refinement, $\Delta x = 1.9\mu m$ and $\Delta y = 3.91\mu m$. This is more than enough to resolve the flame.

After testing various settings and configurations, this configuration was chosen because it resulted in the most stable flame propagation. After the initial few milliseconds, the flames for both the reaction mechanisms propagate steadily. This can be seen in Fig. 4-11. The flame speed and temperature data were taken after the flame propagation became steady.

The flame structures for both of the reaction mechanisms are shown, along with the results from Cantera, in Fig. 4-10. These structures are identical to those of a classic diffusion

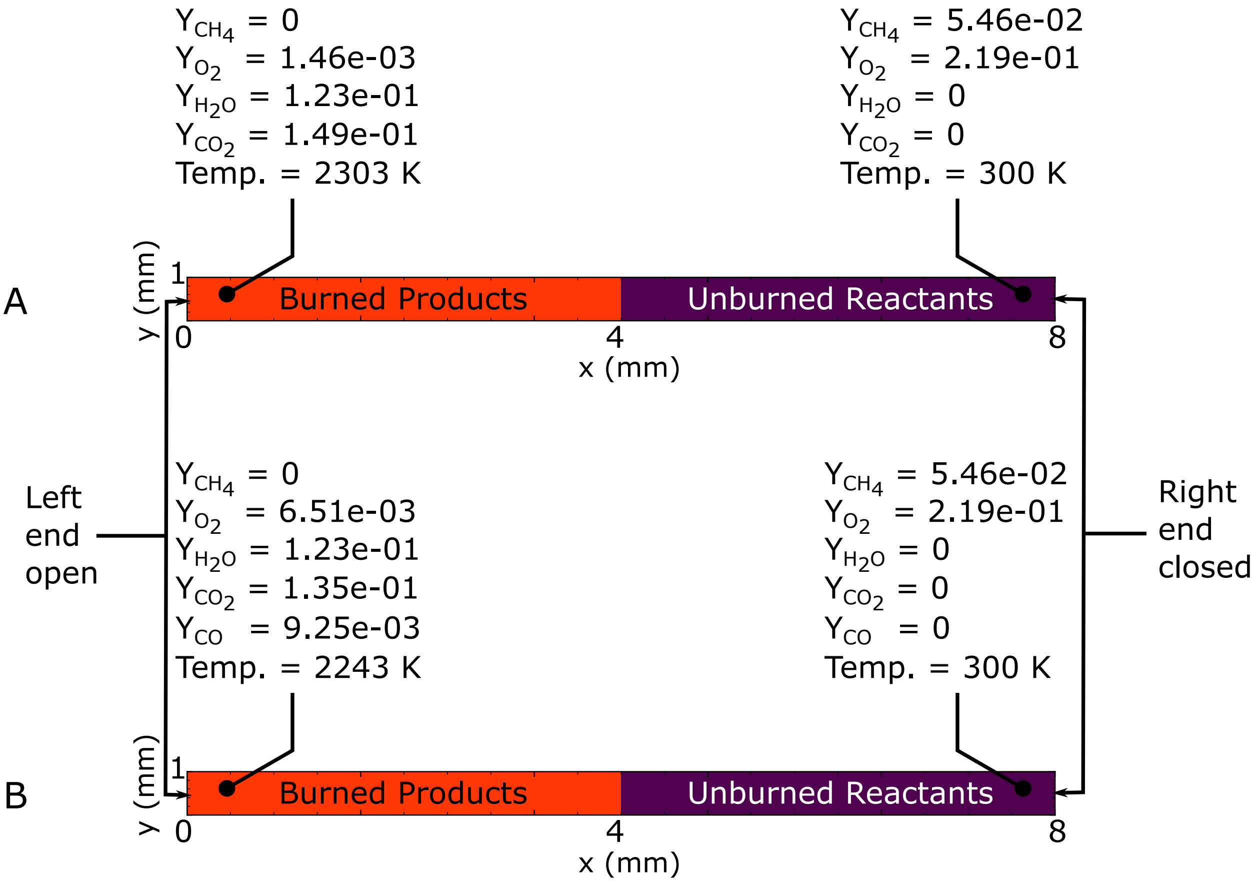

Figure 4-9. Initial temperatures and species mass fractions of participating species for the methane-air laminar flame speed test using single-step, and two-step reaction mechanisms. A) Single-step reaction mechanism. B) Two-step reaction mechanism.

flame. The plots for the singles-step mechanism was taken at $t \approx 6.5\ ms$ and for the double-step mechanism at $t \approx 6.2\ ms$.

The results from this test are summarized in Table 2-1. Flame parameters from both Cantera and HyBurn are quite close to each other, which indicate that the reaction mechanism integration step works well.

4.4 Laminar Coal-Dust Flame Speed Test

Here we will talk briefly about the laminar coal-dust flame speed test since it gives us a good comprehensive idea of the overall performance of the code (except the radiation solver). Fig. 4-12 (a) shows the initial conditions for the test. A long, narrow channel is divided equally into two halves along the length. The right half is filled with a stoichiometric mixture of 4 μm

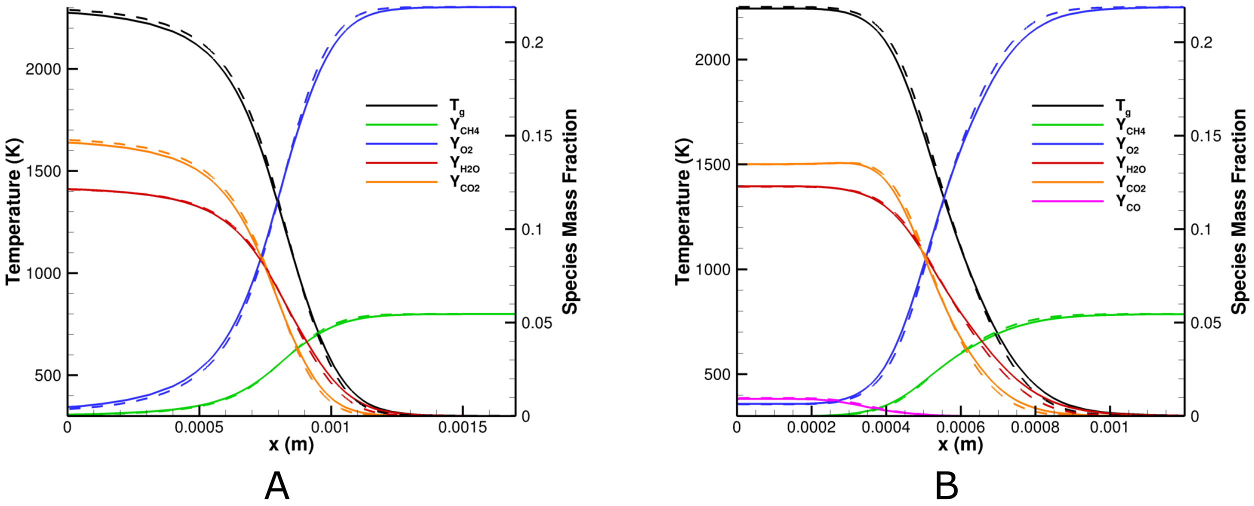

Figure 4-10. Plots of gas temperatures and major species mass fractions for the single-step ($t \approx 6.5\ ms$), and the two-step ($t \approx 6.2\ ms$) reaction mechanisms showing the structures of the gas-phase flames. A) Single-step reaction mechanism. B) Two-step reaction mechanism. The results from Cantera are in solid lines and those from HyBurn are in dashed lines.

Table 4-1. Flame properties of the single and two-step reaction mechanisms compared for HyBurn and Cantera.

Parameter	**Reaction Mechanism**	**Cantera**	**HyBurn**
Flame Speed	Single-step	37.53 cm/s	37.62 cm/s
	Two-step	40.11 cm/s	40.06 cm/s
Flame Temperature	Single-step	2303 K	2305 K
	Two-step	2243 K	2248 K
Flame Thickness	Single-step	0.34 mm	0.325 mm
	Two-step	0.445 mm	0.414 mm

diameter coal-dust and air at room temperature, with a dust concentration of ~144 g/m^3. The left half is the ignition region and has high-temperature products. When the simulation is started, the flame propagates into the right half of the channel at a stable velocity of ~28 cm/s, which is known as the laminar flame speed, S_L. This compares well to the numerical and experimental results from Cloney et al. (2018). The gas-phase and granular-phase temperatures, along with the major species mass fractions at ~11 ms for the single-step reaction mechanism and at ~10.5 ms for the two-step reaction mechanism are shown in Fig. 4-12 (b) and (c) respectively, which gives us an idea of the overall flame structure.

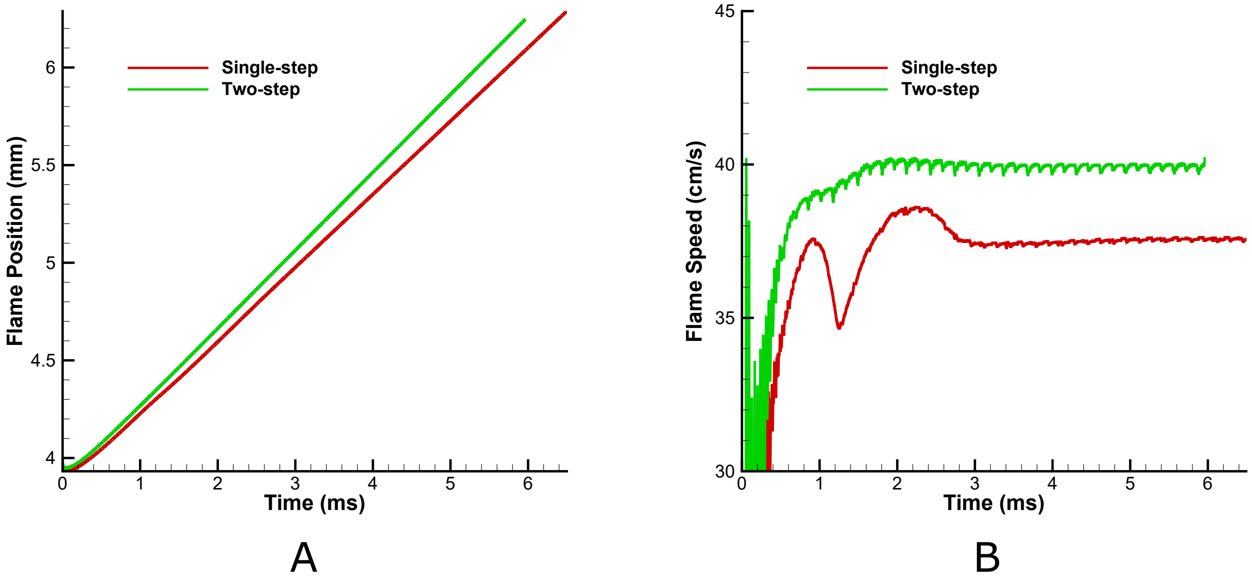

Figure 4-11. Flame location, and flame speed for the methane-air laminar flame speed test using single-step, and two-step reaction mechanisms. A) Flame location. B) Flame speed.

4.5 Radiation Solver Verification Test

For the radiation solver verification test, we performed two tests. The first is a one-dimensional radiation problem which is one of the very few cases that has an exact solution. This test lets us not only verify the radiation solver, but also helps us compare the various approximation orders for the filtered spherical harmonics method. The initial and boundary conditions for the test problem is shown in Fig. 4-13. Here, β is the extinction coefficient, which is equal to κ, the absorption coefficient. c is a constant factor that determines whether the medium is optically thick or thin. When c is set to 1, the medium is optically thin and $c = 10$ corresponds to an optically thick medium. Both the absorption coefficient and the blackbody incident radiation are chosen to be simple functions of x so that the exact solution is easier to derive. In order to get the exact solution, we use the equation Eq. 14.34 from Modest (2013), which is given by

$$G(\tau) = 2\pi \left[I_{b1} E_2(\tau) + I_{b2} E_2(\tau_L - \tau) + \int_0^{\tau} I_b(\tau') E_1(\tau - \tau') d\tau' + \int_{\tau}^{\tau_L} I_b(\tau') E_1(\tau' - \tau) d\tau' \right]. \tag{4-9}$$

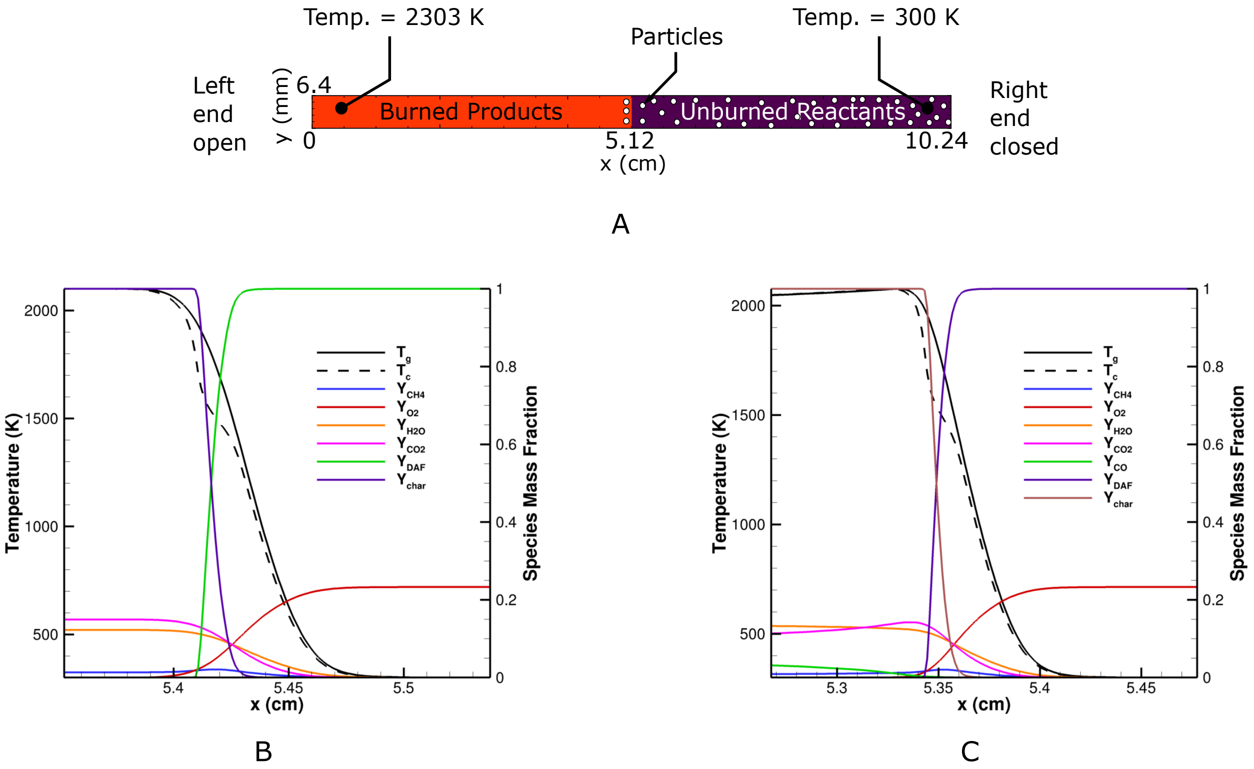

Figure 4-12. Laminar coal-dust flame speed test initial conditions, and results showing the gas-phase and granular-phase temperatures and major species mass fraction plots using the single-step and two-step reaction mechanisms. A) Initial conditions and configuration. B) Flame structure for the single-step reaction mechanism. C) Flame structure for the two-step reaction mechanism.

Fig. 4-14 shows the incident radiation from the different filtered spherical harmonics approximations compared to the exact solution, and Fig. 4-15 (on a log scale) shows the comparisons of the radiative heat fluxes. It is observed that for FP$_1$, the solutions are the furthest off from the exact solution (especially for the optically thin media), however, if we only go to FP$_3$, there is huge improvement. The errors keep reducing as we go higher up in the FP$_n$ order, but the computational costs also increase massively. Table 4-2 shows the number of equations that are needed to solve for the FP$_n$ orders of 1, 3, 5, 7, 13 and 21 in both 2-D and 3-D. Going from third to fifth order more than doubles the number of equations that have to be solved. Another thing to notice is when we compare the radiation heat fluxes, except for the 1st order approximation, all other approximation orders produce results that are very close to the exact solution, for both optically thick and thin media. This is crucial because the

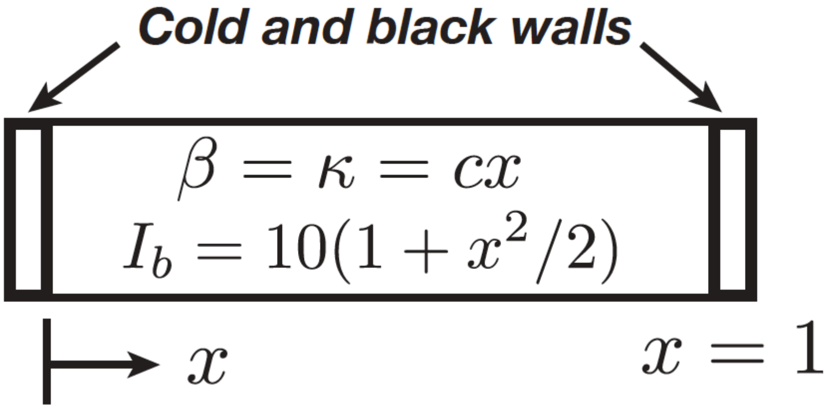

Figure 4-13. Initial and boundary conditions for the 1-D radiation test problem.

Table 4-2. Number of equations needed to solve for various orders of FP$_n$ approximations

FP$_n$ Order	**Number of equations**	
	2-D	**3-D**
FP$_1$	3	4
FP$_3$	10	16
FP$_5$	21	36
FP$_7$	36	64
FP$_{13}$	105	196
FP$_{21}$	253	484

radiation heat flux is the parameter of importance when we see how the radiation couples to the hydrodynamic solver via the energy equations.

Next, we perform a 2-D lattice test problem which has no exact solution to compare to, but is a widely used standard radiation solver test problem. This test consists of a checkerboard of multiple materials and thus provides a challenging scenario to simulate. The checkerboard pattern consists of a central radiating source, shown in red in Fig. 4-16, surrounded by purely absorbing (shown in purple) and purely scattering (shown in light yellow) regions. The central box is also purely scattering. In this problem, only radiation transport is accounted for and all the other hydrodynamic terms are turned off. The domain is 7 cm × 7 cm in size. The purely absorbing regions have an absorption coefficient of $\kappa = 10$ cm^{-1}., whereas the regions which are purely scattering have a scattering coefficient of $\sigma = 1$ cm^{-1}. The boundaries of the domain are cold and black and absorb all radiation coming towards

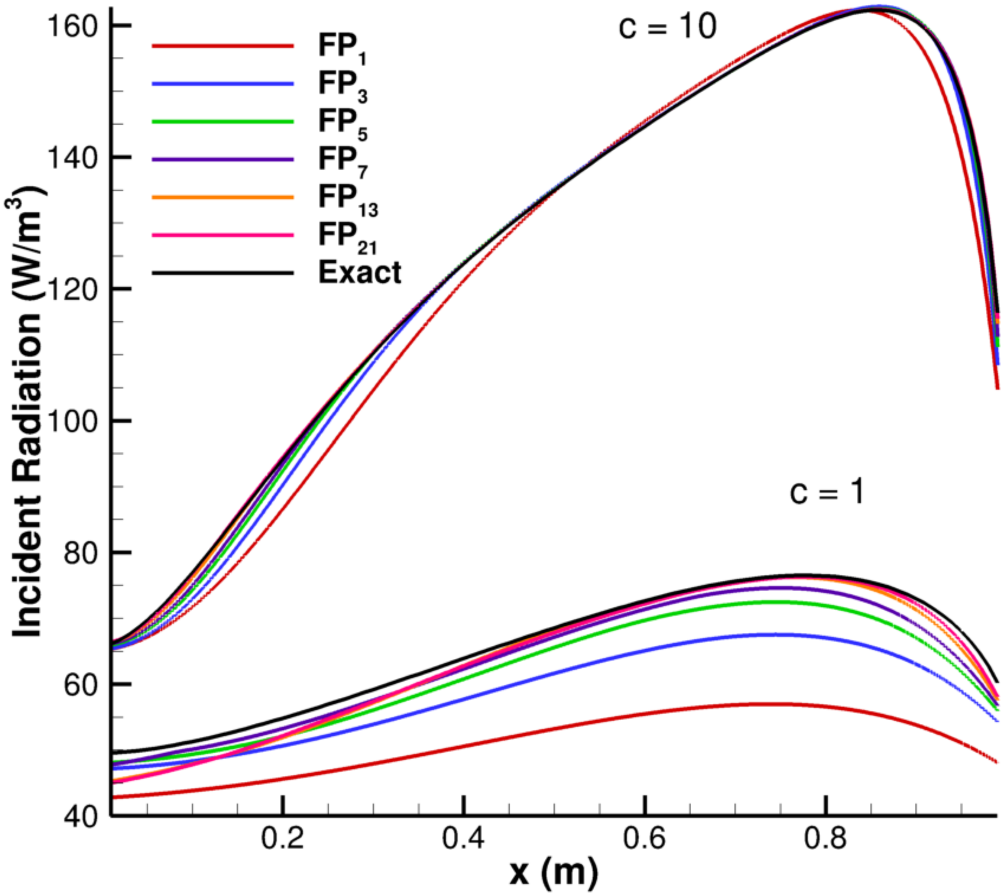

Figure 4-14. Incident radiations for various FP$_n$ approximations compared to the exact solution for the 1-D radiation test problem.

them, while themselves not radiating at all. The central radiation source has a radiation strength of $I_b = 1$ cm^{-3}s^{-1}. There are two phases in this test - granular and gas. The granular volume fraction is 50%. The gas phase extinction coefficient is set to zero, and only the granular phase is scattering and absorbing.

The domain is divided into 200 points in the x and y directions, with $\Delta x = \Delta y = 0.035$ cm. The Lanczos filter strength was 0.1. A CFL number of 0.5 was used. The number of iterations was set to 91,429, in order to get to a time of 53.33 ns (or 16/c ns) so that we can compare the results from Radice et al. (2013). At this time, the solution has reached steady state, shown in Fig. 4-17.

The results agree well with the FP$_3$ solution in Radice et al. (2013). The minor differences are possibly due to the use of slightly different colormaps. We also performed the same test

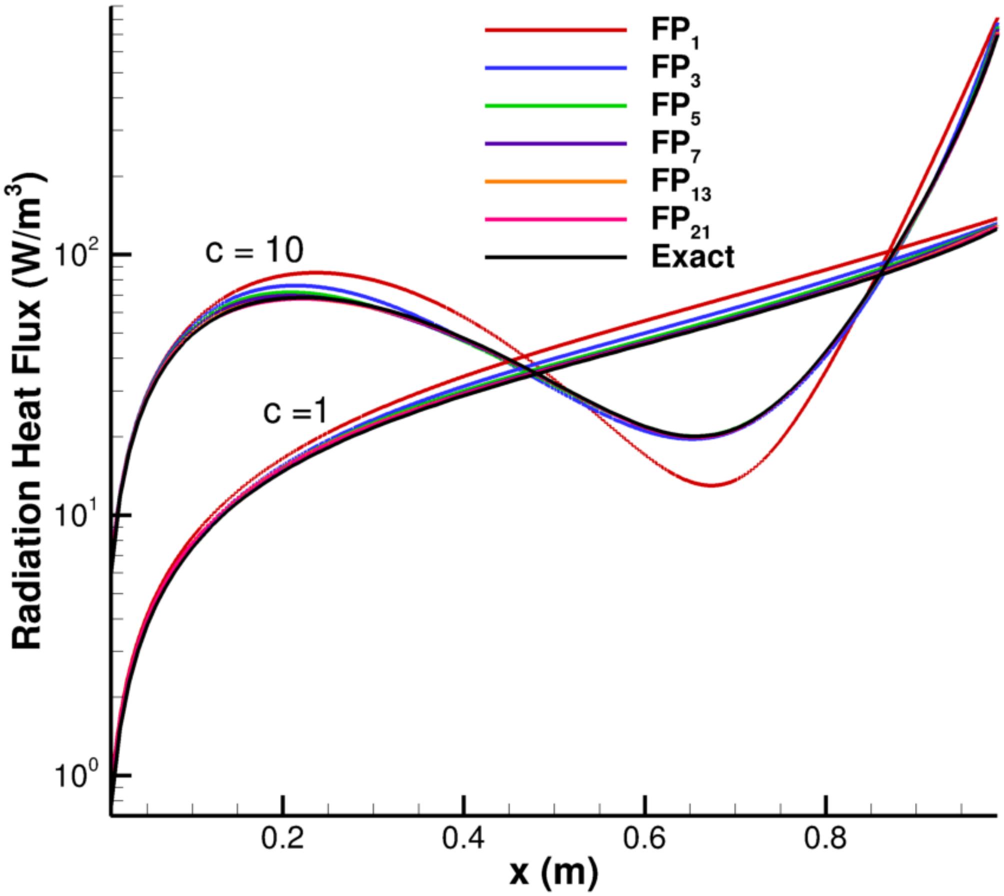

Figure 4-15. Radiation heat flux for various FP$_n$ approximations compared to the exact solution for the 1-D radiation test problem (log scale).

with FP$_1$ and FP$_5$ and FP$_{13}$ approximations and compared the errors for the 1st, 3rd and 5th order approximations assuming FP$_{13}$ as the exact solution. The errors were computed along a line parallel to the x-axis at y = 3.5 cm. These comparisons are shown in Fig. 4-18.

For the three-dimensional version of the lattice test problem, we keep the same configuration as before, except that the purely absorbing sections are extended along the full length of the z-direction, and the central source is made into a cube of 1 cm in each direction. This was done to make sure that there is a noticeable difference between the two-dimensional and three-dimensional versions of the test. If the source was also extended in the z-direction along the full length, then the solution would look identical to the two-dimensional case. Additionally, this time the radiation solver CFL number had to be reduced to 0.25 to account for the third direction. The test was run for 50,000 time steps (these tests take a massive

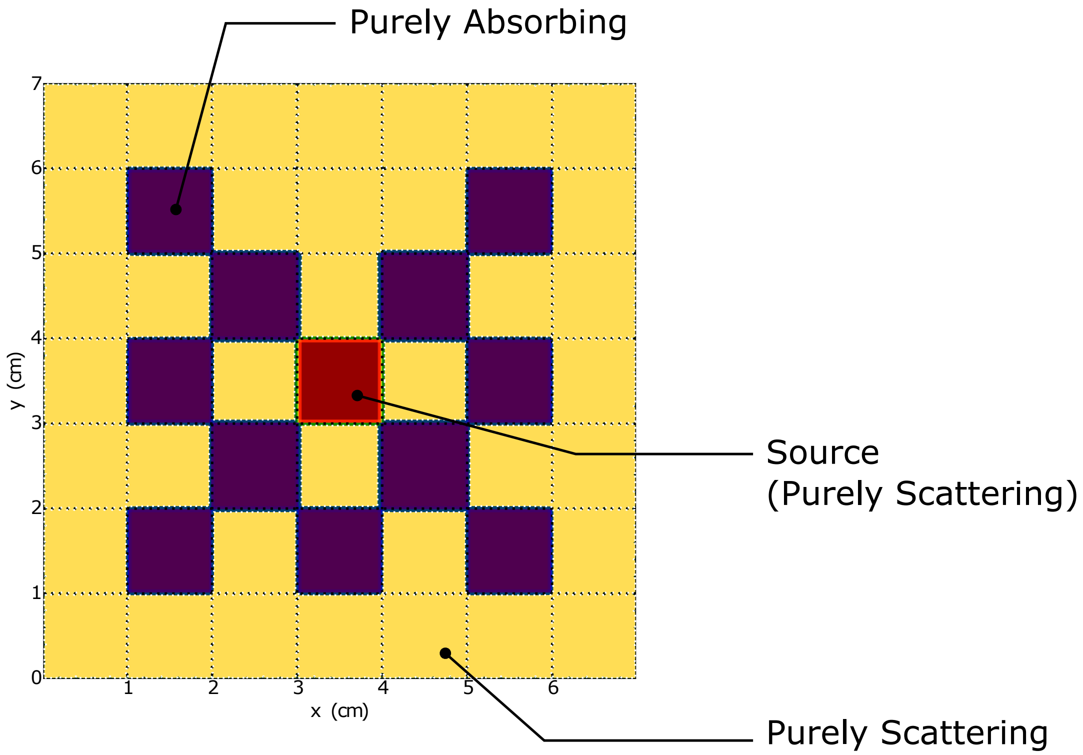

Figure 4-16. Initial conditions for the 2-D lattice problem.

amount of time to finish), which is not as much as the two-dimensional case, but it already reaches steady-state by that time. Fig. 4-19 shows the results. Notice that compared to the two-dimensional version, larger parts of the domain has lower incident radiation values. This is because the central source is much smaller than the two-dimensional case since the source is a cube and not an extended bar. Thus the amount of incident radiation reaching point in the computational domain is relatively smaller.

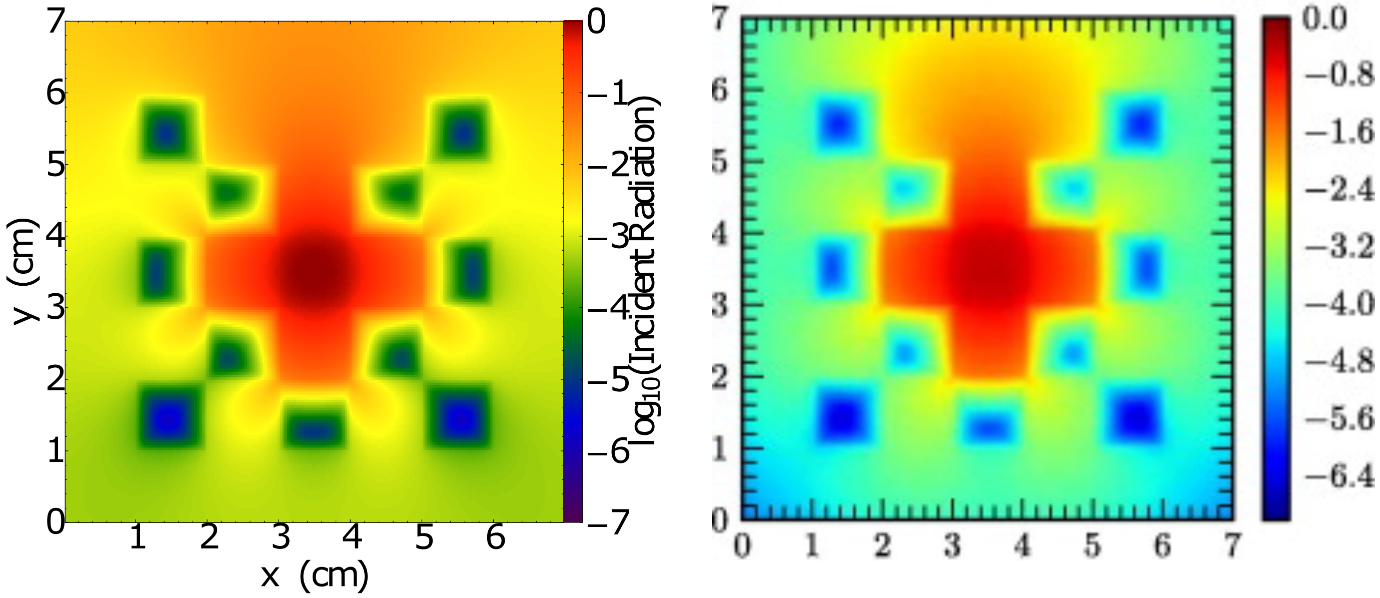

A

B

Figure 4-17. Solution of the incident radiation field after $t = 16/c$ s. A) HyBurn. B) Radice et al. (2013).

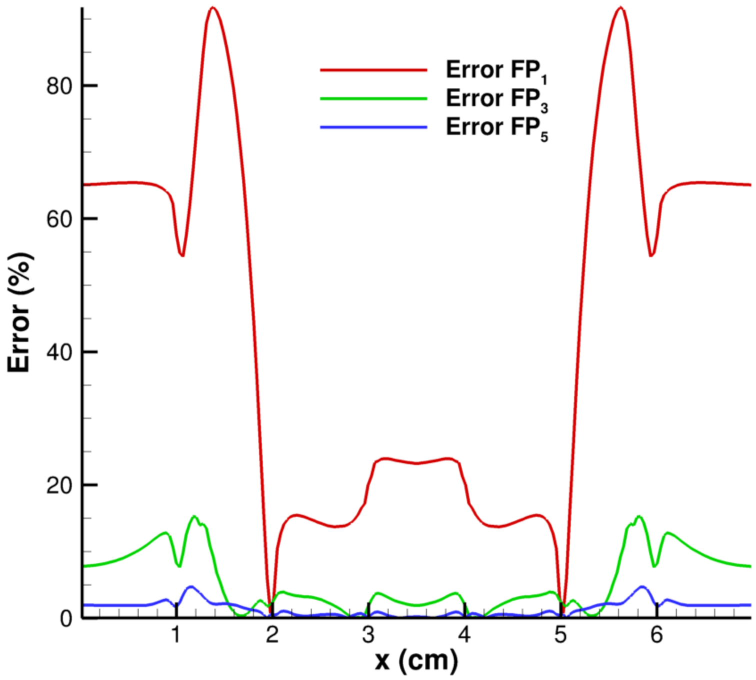

Figure 4-18. Percentage errors for the FP$_1$, FP$_3$ and FP$_5$ approximations in the 2-D lattice test problem, assuming FP$_{13}$ as the exact solution.

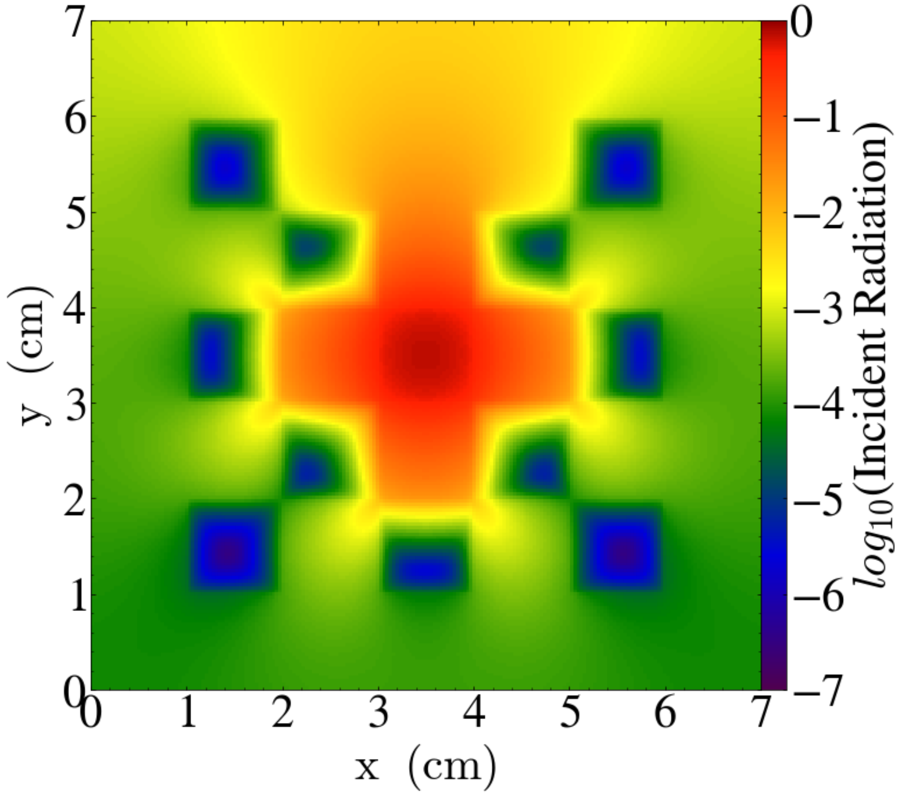

Figure 4-19. Solution of the incident radiation field in the X-Y plane, centered at Z = 3.5 cm, after 50,000 time steps.

CHAPTER 5
SINGLE STEP REACTION MECHANISM RESULTS AND DISCUSSION

5.1 Problem Description and Numerical Methods for the 2-D Long Channel Cases

5.1.1 Physical Model

The initial and boundary conditions for the simulations are shown in Fig. 5-1. The domain consists of a long two-dimensional channel 5 cm in height, with a 4-mm thick layer of coal placed on the bottom. Channel lengths of 10 m and 40 m were considered. All boundaries of the domain are assumed to be symmetry planes. The diameter of the coal particles is 30 μm, which is in the middle of the explosive range for coal dust (Cashdollar, 2000). Volume fractions of 47% and 1% of particles in the dust layer were considered to explore the influence of particle packing. The volume fraction of the dense cases is based on empirical data for densely-packed coal dust layer (Edwards and Ford, 1988) and the dilute cases are based on data from Semenov et al. (2013). The domain contains a stoichiometric mixture of methane and air from the left boundary up to 2 m. After 2 m, the rest of the domain is transitioned to pure air gradually, over a distance of about 1 m, using a hyperbolic tangent function. The dust explosion is initiated by igniting a methane-air detonation on the left portion of the domain. The detonation is triggered near the left boundary using two hot pockets of unreacted methane and air at 100 atm and 1000 K.

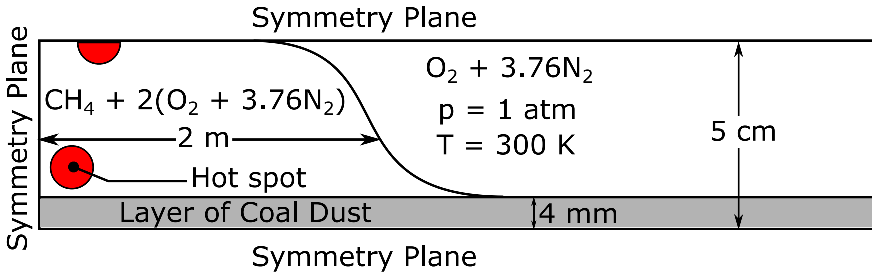

Figure 5-1. Initial and boundary conditions

The two-dimensional simulations are computed using an in-house code, HyBurn, which solves the full set of coupled, multiphase, compressible, unsteady, partial differential equations (Houim and Oran, 2016). Kinetic theory-based solid phase reactive multiphase equations are solved. Drag, convective heat transfer, particle-particle interactions and inelastic collisions are modeled (Houim and Oran, 2016).

Magnus force is used to model the lift force. The lift coefficient was not varied in these simulations, since generally the shock-lifting of dust layers is insensitive to changes in it (Zydak and Klemens, 2007). Viscous stress, molecular diffusion, heat conduction and radiation are all considered. The ideal gas model with variable specific heat is used to relate pressure, chemical composition, temperature and density of the gas phase. The gas phase is composed of $CH_{4,g}$, O_2, N_2, H_2O_g and CO_2. Global, irreversible reactions were used to model methane combustion in high speed flows from Cloney et al. (2018), which is based on the MP1 model of CERFACS.

The dust particles are composed of dry ash-free coal (DAF), moisture (H_2O_s), char (C_s), and inert ash. The DAF is first assumed to devolatilize in a process based on Kobayashi et al. (1977), releasing gaseous methane and solid carbon C_s (or char). The char can then react with air in a single-step process (Baek et al., 1990). The moisture is allowed to vaporize based on an Arrhenius reaction (Bradley et al., 2006).

The particles are assumed to be spherical and monodisperse, with a diameter of 30 μm, a constant specific heat of 987 J/kg.K, and material density, ρ_s, of 1200 kg/m^3 (Houim and Oran, 2015b). The coefficient of restitution used in these simulations is 0.99. The initial mass fractions of coal are 0.93 for DAF, 0.06 for ash, and 0.01 for moisture.

Here, we use the single-step reaction mechanism which was discussed in details in 2. The thermodynamic and transport models were also talked about in the same chapter.

5.1.2 Radiation Modeling

In this work we solve the radiation transfer equation (RTE) to compute the radiation field and the radiative heating and cooling rates for the particles. The third-order filtered spherical harmonics (FP_3) approximation to simplify the radiation transfer equation (Radice et al., 2013). The radiation is assumed to be spectrally gray with isotropic scattering. The Buckius and Hwang correlation is used to compute the Planck-mean extinction and scattering coefficients for the coal dust (Buckius and Hwang, 1980). The gray Plank-mean absorption coefficients for CH_4, O_2, CO_2 and H_2O were based on curve fits to the data from the RADCAL program (Grosshandler, 1993).

5.1.3 Numerical Solution Methods

An operator splitting method is used to solve the governing equations with separate solution methods for hydrodynamic terms, source terms arsing from chemical reactions, drag, etc., and thermal radiation. The hydrodynamic terms are solved using a Godunov-based method and a third-order Runge-Kutta method is used for time integration (Houim and Kuo, 2011; Houim and Oran, 2016). The FP_3 equations are marched in pseudo-time until steady-state is achieved using an approximate Riemann solver (McClarren and Hauck, 2010). The gas-phase reaction terms are integrated in time using the yet-another-stiff-solver (YASS) method (Khokhlov et al., 2012).

Adaptive mesh refinement was used to achieve the required amount of resolution, which is based on the AMReX library (Zhang et al., 2019). Four levels of refinement were used with finest resolution of $\Delta x_{\text{max}} = 0.2$ mm, which is roughly 6.7 particle diameters in size. This computational cell size is comparable to the resolution used in our earlier work (Houim and Oran, 2015b).

5.1.4 Results

5.1.5 Shock-Flame Structure

Fig. 5-2 shows the structure of the shock-flame (SF) interaction at 43.6 ms for the dense case of a long channel layered dust explosion. As the leading shock passes through the channel, the turbulent flow behind the shock lifts the dust. This lifting of the dust causes a dust concentration gradient to form. The shock also causes the temperature to rise behind the shock, which heats the particles to the point where ignition occurs. The SF structure observed here is similar to those reported in Houim and Oran (2015c,b). In most of the cases (excluding those in which the flame propagation stops), the overall SF structure consists of the shock and flame coupled into what is referred to as a shock-flame complex (SFC) and they always move together, with the flame following the shock.

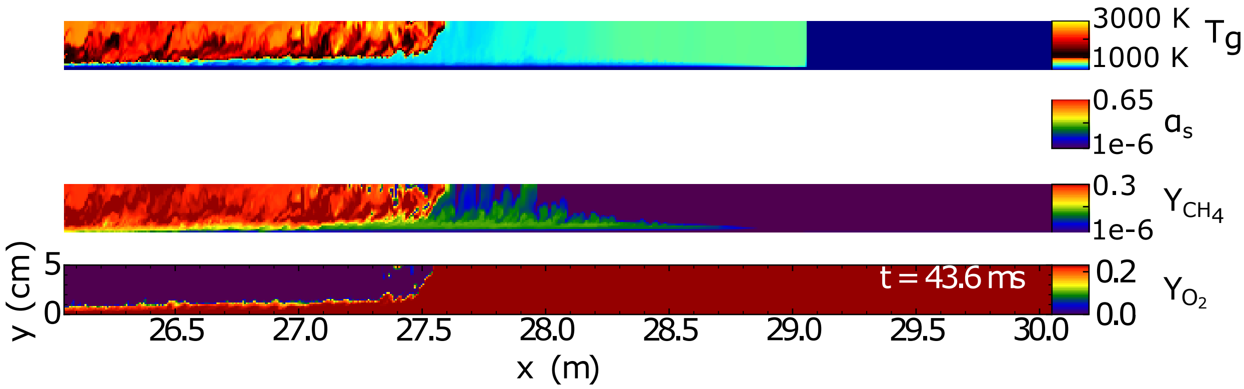

Figure 5-2. Plots of gas temperature, volume fraction, methane mass fraction, and oxygen mass fraction, showing the shock flame complex (SFC). Note that the plots have been stretched in the y-direction by 4 times for better visualization.

5.1.5.1 Short 10-m Channel With 47% Volume Fraction in the Dust Layer

Figure 5-3 shows position-time diagrams for the short channel cases. These plots show the propagation of the detonation, its subsequent failure, propagation of the dust flame, and the reflection of the incident shock. The methane-air detonation fails at ∼1.5 ms. The resulting shock remnant and the dust flame propagate separately. The incident shock propagates to the right and reflects from the end wall at ∼14 ms and propagates towards the flame. After failure of the detonation, the flame decelerates until the reflected shock reaches the flame front at ∼22 ms. In the case with radiation, the dust flame accelerates to the right after the shock-flame interaction. The dust flame in the non-radiative case is much more unstable and does not accelerate to the right.

Fig. 5-4 (a) shows the heat release rates due to gas-phase chemical reactions for the cases with and without radiation. The heat release rate is ∼2 GW/m for the first 1.5 ms which is due to the propagating detonation. The heat release rate then sharply falls after the detonation fails at 1.5 ms due to lack of pre-suspended CH_4 in the air for the first two meters in the channel. After failure of the detonation, the heat release rate sharply decreases, but shortly afterwards rises continuously until ∼12 ms for both cases due to the propagating dust flame. A case with pure inert dust in the layer, does not show the continuous rise in the heat release after detonation failure as shown in Fig. 5-4 (b). The heat release rate increases substantially

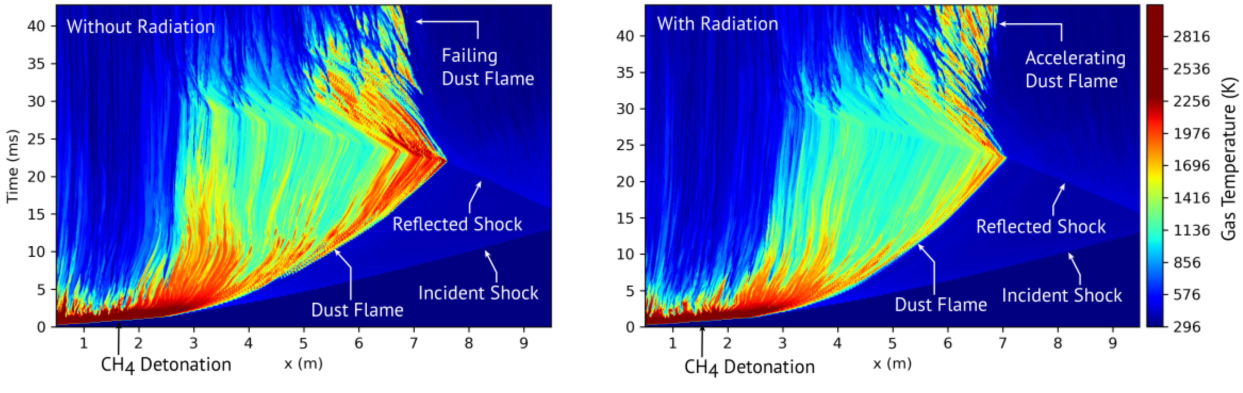

A B

Figure 5-3. XT plot shaded by gas phase temperature for the 10-m channel with 47% layer volume fraction with and without radiation. A) Without radiation. B) With radiation.

at ∼30 ms, which is likely due to effects from the shock-flame interactions enhancing mixing. After ∼36 ms, the heat release rate for the case without radiation decreases sharply until the end of the simulation while the case with radiation decreases more gradually and appears to be plateauing.

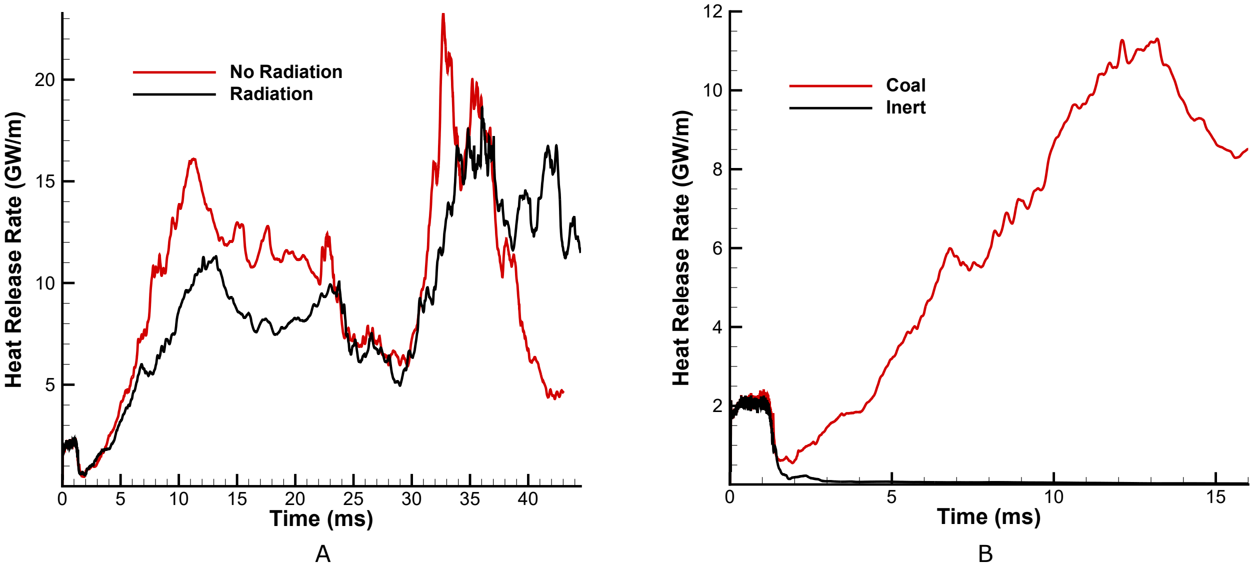

A B

Figure 5-4. Heat release rates due to chemical reactions for the cases with and without radiation, and with inert ash and reactive coal for the 10 m channel with a dust volume fraction of 47%. A) Heat release rates for coal-dust particles with and without radiation. B) Heat release rates comparing inert ash and reactive coal-dust particles.

Fig. 5-5 shows a snapshot of the structure of the coal-dust flames for both cases at 45 ms. The radiative flame, at this instance, has a much broader structure and a lower peak temperature. The flame temperature predicted by the case without radiation at $\sim$ 20 ms is $\sim$2250 K, whereas for the case with radiation, it is $\sim$2050 K. This is consistent with results studying radiation on gas-phase flames (Julien et al., 2015a).

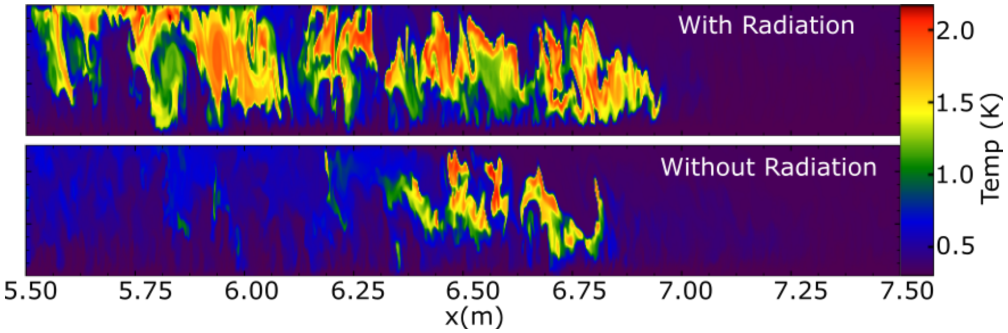

Figure 5-5. Contour plots of gas temperature for the cases with and without radiation at 45 ms for the 10-m channel the dust layer volume fraction of 47%. Note that the plots have been stretched in the y-direction by 4 times for better visualization.

5.1.5.2 Long 40-m Channel With 47% Volume Fraction in the Dust Layer

Reflected shocks interacted with the flame in the shorter 10-m channel cases. Longer 40-m long channels were simulated to eliminate the effect of these shock-flame interactions. Here we present the results for the long-channel cases with a dust layer volume fraction of 47% volume fraction, with and without radiation. This case is nearly identical to setups discussed in Houim and Oran (2015c,b); Shimura and Matsuo (2019), but with a different reaction mechanism, different coal parameters, and a much longer simulation time.

The total heat release rates due to gas phase chemical reactions and the flame and shock velocities for these cases are shown in Fig. 5-6. Figure 6-28 shows position-time of the temperature field at $y = 2.5$ cm. Toward the end of the simulations, at $\sim$80 ms, both cases show that heat release is substantially decreasing. In addition, the flame velocity, shown in Fig. 5-6(b), continuously decreases and eventually approaches zero. However, the flame locations and velocities are different for the two cases. At the end of the calculation ($t \sim 80$ ms) the flame is at 11.0 m, and 9.9 m for for non-radiative and radiative cases, respectively.

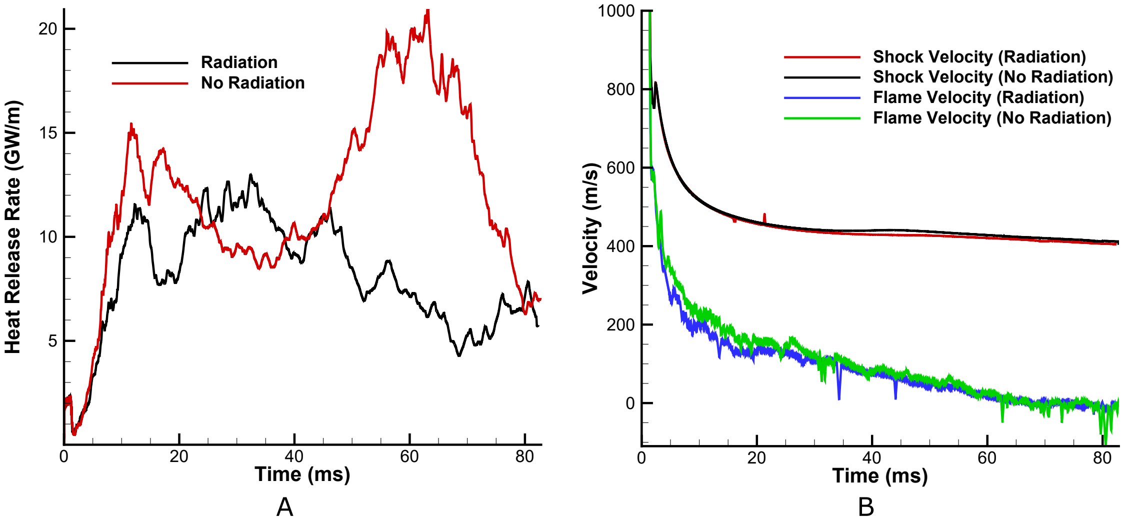

Figure 5-6. Dense (47%) case total heat release rate due to gas phase chemical reactions and shock and flame velocities. A) Total heat release rate due to gas phase chemical reactions. B) Shock and flame velocities.

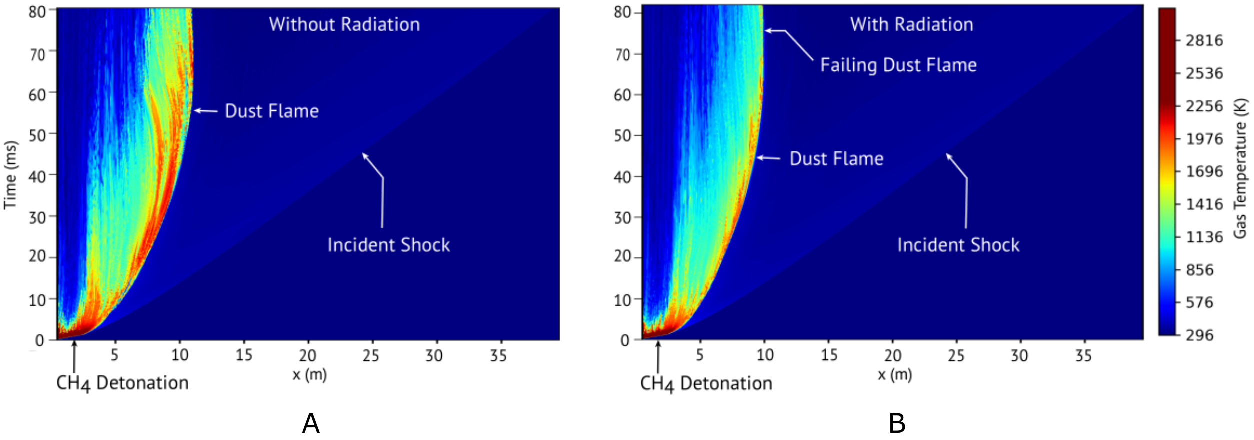

Figure 5-7. Dense (47%) case XT plot shaded by gas phase temperature. A) Without radiation. B) With radiation.

The XT diagrams shown in Fig. 6-28 indicate that the peak coal dust flame temperature is around 200 K lower when radiation is considered. The dust flame starts to quench for the radiative case when the peak temperature drops to ∼1200 K after 70 ms. The non-radiative flame shown in Fig. 6-28 (a) propagates unstably after 30 ms, with intermittent regions of high flame temperature followed by substantially lower temperatures.

5.1.5.3 Long Channel With 1% Volume Fraction

The 40-m long channel was simulated with a volume fraction of 1% to explore the influence of dust layer packing on the simulation results. Total heat release rate due to gas-phase chemical reactions and the shock and flame velocities are shown in Fig. 6-27(a) and (b), respectively. The heat release rate continually increases and the flame velocity propagates stably at roughly 400 m/s for much of the calculation for these dilute cases. This is in contrast to the dense cases where the flames eventually quenched or propagating unstably.

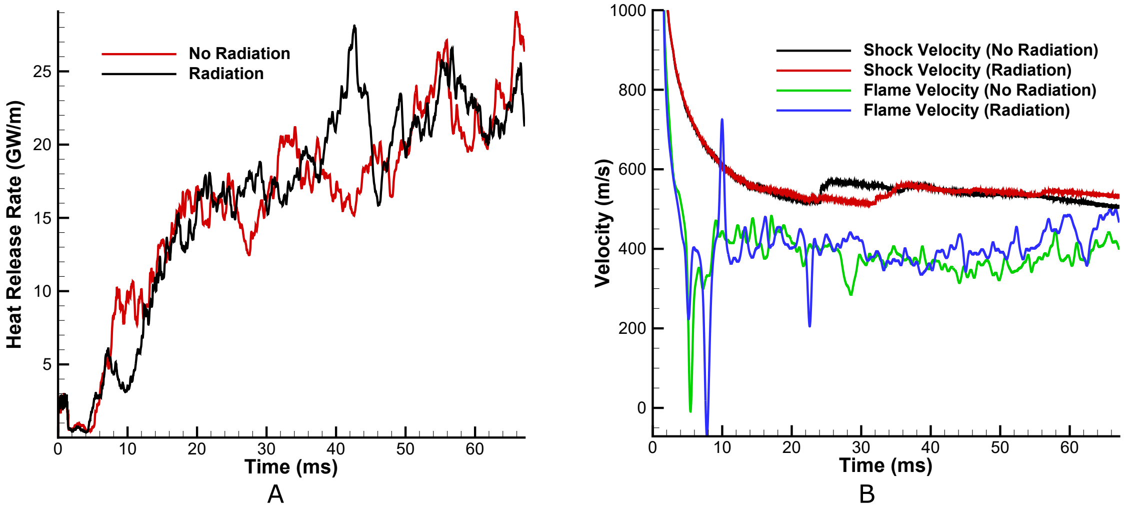

Figure 5-8. Dilute (1%) case total heat release rate due to gas phase chemical reactions and shock and flame velocities. A) Total heat release rate due to gas phase chemical reactions. B) Shock and flame velocities.

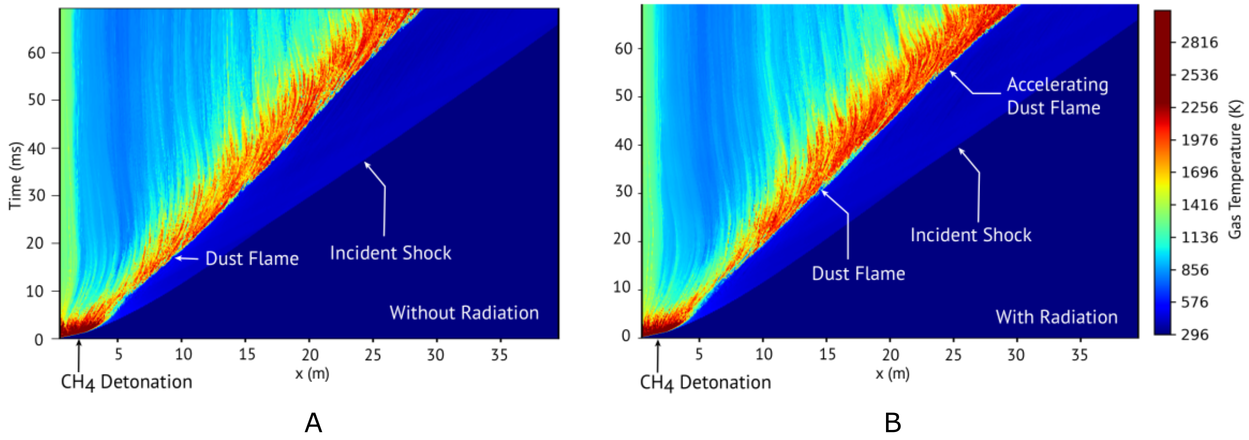

Figure 5-9. Dilute (1%) case XT plot shaded by gas phase temperature. A) Without radiation. B) With radiation.

The XT diagram in Fig. 5-9 shows that thermal radiation is accelerating the flame, which is indicated by the slight kink in the flame position in Fig. 5-9(b), at ∼50 ms. This corresponds to the time in Fig. 6-27(b) where the flame with radiation begins to accelerate relative to the case without radiation. It is interesting to note that the radiative flame produces higher peak flame temperatures relative to the non-radiative flame after 40 ms, which is opposite to the previous cases.

Fig. 5-10 shows the flame structure for (a) radiative case and (b) non-radiative case for the dilute dust layer. It is clear that radiation has an influence on the flame structure and temperature. In particular, the radiative case shows devolatilization over a longer distance ahead of the flame, which is indicative of radiative pre-heating.

5.1.6 Discussion

The simulation results show that the influence of radiation on the bulk dust flame parameters such as velocity and peak temperatures are quite different for the scenarios presented in the paper and can even have opposite effects. For example, radiation hinders flame propagation in some cases, and assists propagation in other cases. The chemical energy release rate shown in Figs. 5-4, 5-6, and 6-27 show that for majority of the time in most cases the total rate of heat release is reduced by radiation. This trend can be explained by radiation losses from the flame region dominating over radiation absorption in the cold reactants. These radiation losses near the flame reduce the peak temperature relative to the non-radiative simulations. A notable exception is the dilute cases where the opposite trend was observed. The radiative case with a layer volume fraction of 1% had peak flame temperatures that were ~ 20 K higher than the corresponding non-radiative case. This can be explain by the faster shock Mach 1.4 shock raising the air temperature by ~ 20 K for the radiative case compared to the Mach 1.33 shock for the non-radiative case. Another notable influence of radiation is that it produced a stably propagating flame for the shorter 10-m channel after the shock-flame interaction, while, simulations neglecting radiation produced a very unstable flame that is

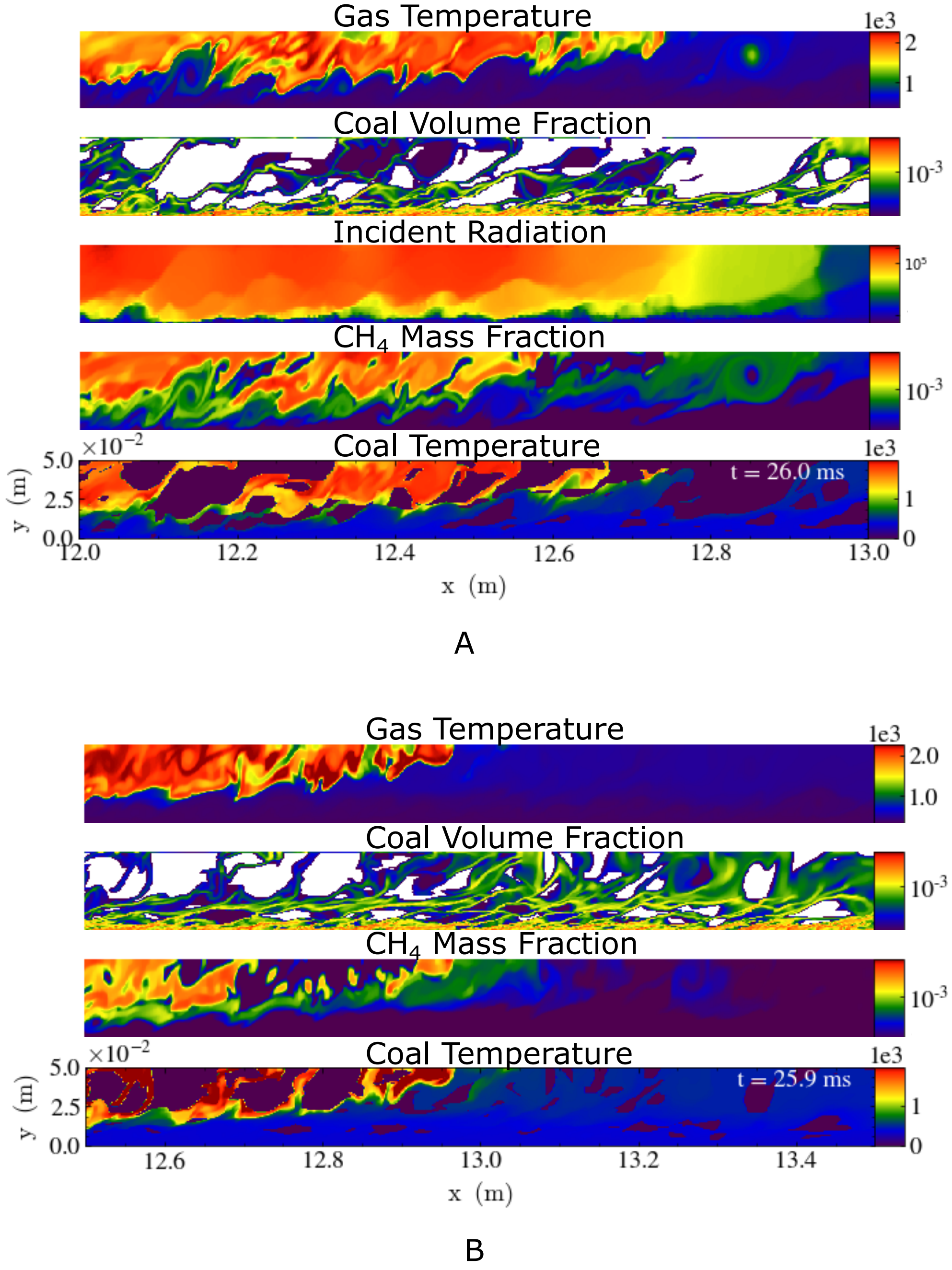

Gas Temperature

Coal Volume Fraction

Incident Radiation

CH_4 Mass Fraction

Coal Temperature

A

Gas Temperature

Coal Volume Fraction

CH_4 Mass Fraction

Coal Temperature

B

Figure 5-10. Plots of gas temperature, dust volume fraction, incident radiation, methane mass fraction, and coal temperature for cases with and without radiation for the 1% volume fraction dust layer in the 40-m channel at a time of 26 ms. A) With radiation. B) Without radiation. Note that the plots have been stretched in the y-direction by 4 times for better visualization.

likely in process of quenching. This is shown most clearly in Figs. 5-3 and 5-5 which indicate a healthy flame for the radiative case and an unstable flame for the non-radiative case.

The flame is predicted to quench for both the radiative and non-radiative cases for the 40-m channel when a realistic layer volume fraction of 47% is used. Nevertheless, radiation has a significant influence on the quenching process. The radiative flame quenches much earlier than the non-radiative case due to radiation losses from flame overwhelming the radiative and conductive heating of the reactants. Quenching of the flame was an unexpected result that has not been reported in earlier literature (Houim and Oran, 2015c; Shimura and Matsuo, 2019). However, these earlier simulations considered much shorter simulation times, used different reaction mechanisms for CH_4 and coal, and used different initial mass fractions for DAF, ash, and moisture. The sensitivity of the results to the choice in reaction mechanism and other model parameters is discussed in Chapter 6.

5.1.7 Conclusions

Numerical simulations of layered coal dust explosions were performed both with and without radiation for 10 m and 40 m long channels to explore the influence of thermal radiation on the propagation of a layered dust explosion. Two particle volume fractions in the dust layer were considered. A loosely packed case with an 1% initial volume fraction and a densely packed case where the layer volume fraction was initially 47%. The results from the different cases were examined to understand the effect of radiation heat transfer on the structure and propagation of coal dust layered explosions.

Results from each of the simulations show that key dust flame parameters, such as flame temperature, velocity, and overall structure can be quite different between the radiative and non-radiative cases. However, the influence of radiation can have opposite effects for different scenarios. In some cases, radiation can lead to enhanced quenching of the explosion, while in others it can accelerate the flame and increase the severity of the explosion. For example, radiation promotes flame propagation after the reflected shock-flame interaction in the 10-m channel, and for the dilute dust layer.

CHAPTER 6
TWO-STEP REACTION MECHANISM RESULTS AND DISCUSSION

In this chapter, we will look at how the reaction mechanism affects the structure and propagation of the coal-dust flames. We will also look at how the particle size changes the overall dynamics of the dust flame. The initial and boundary conditions for the two-step reaction mechanism simulations are nearly identical to the single-step reaction mechanism setup (Fig. 5-1), with the exception that the initial temperature in the hotspots was raised to 2000 K instead of 1000 K. This was done to ensure that the detonation occurs. The 1000 K initial temperature wasn't able to initiate a detonation for the two-step reaction mechanism.

6.1 Short 10-m Channel With the 2-Step Methane-Air Reaction Mechanism

Fig. 6-1 and Fig. 6-2 show position-time (X-t) diagrams for the short channel case with the two-step reaction mechanism at $y = 2.5$ cm and $y = 5$ cm heights respectively. We can see the detonation fail at $\sim$0.5 ms after which the flame and shock fronts separate. The shock keeps traveling right, reaches the right boundary and gets reflected. The flame follows the shock, initially decelerating and then accelerating after $\sim$8 ms. This can also be seen in the shock and flame velocity plots, Fig. 6-3. The shock and flame velocities for the radiative case are higher than the non-radiative case for most of the simulations. After the shock reflects, it starts to interact with the flame at $\sim$ 22-23 ms. Then the flame propagation to the right stops due to the reversal of the flow. Looking at the X-t diagrams, we can tell that once the reflected shock reaches the left boundary, there is a reignition of the leftover particles in both the radiative and non-radiative cases. However, the reignition in the radiative case is stronger than in the non-radiative case. This is more clearly visible in Fig. 6-2. In the non-radiative case, on the other hand, there is a stronger reignition near 8 m.

The shock and flame positions, along with the total chemical heat release rates are shown in Fig. 6-4. Both the shock and the flame for the radiative case are ahead of the non-radiative case. The heat release rate is also higher than that of the non-radiative case after $\sim$15 ms. During the detonation, the heat release rate is $\sim$0.5 GW/m for both cases, after which it drops

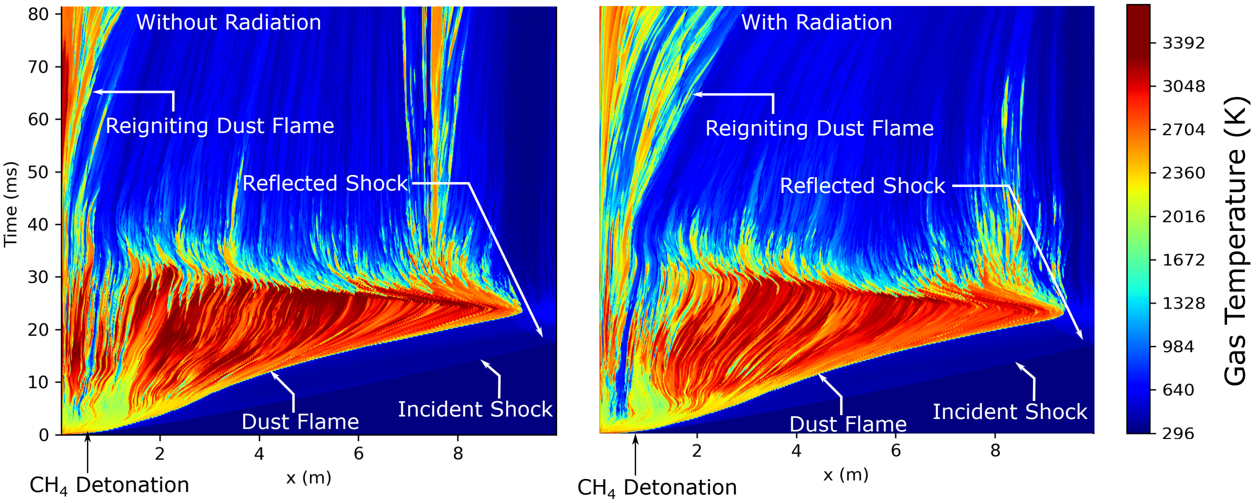

A B

Figure 6-1. X-t diagram for the 10-m long channel shaded by gas phase temperature at y = 2.5 cm with the 2-step reaction mechanism. A) Without radiation. B) With radiation.

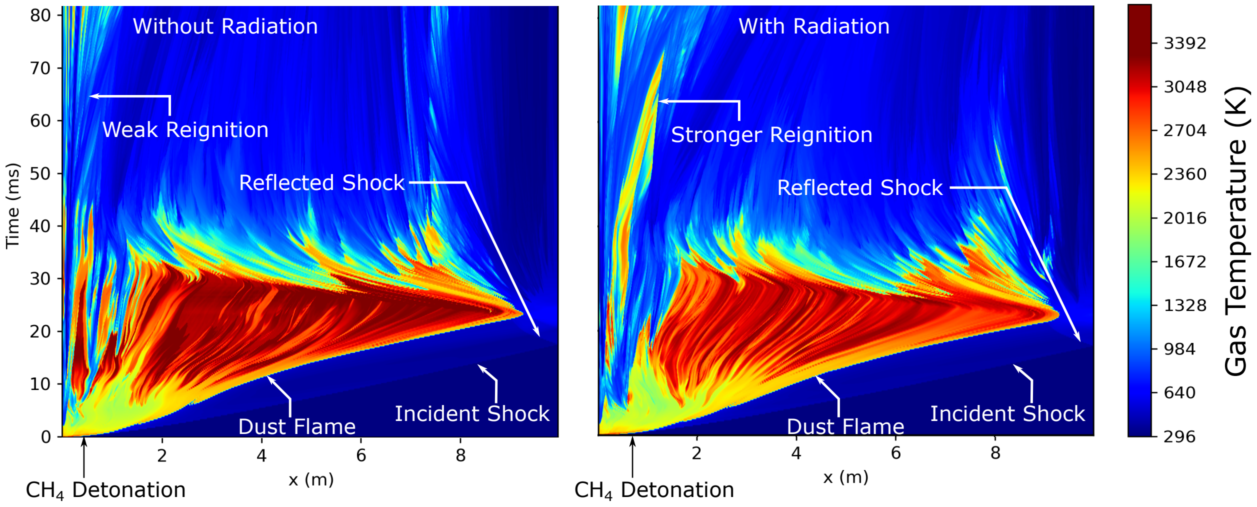

(a) **(b)**

Figure 6-2. X-t diagram for the 10-m long channel shaded by gas phase temperature at y = 5 cm with the 2-step reaction mechanism. A) Without radiation. B) With radiation.

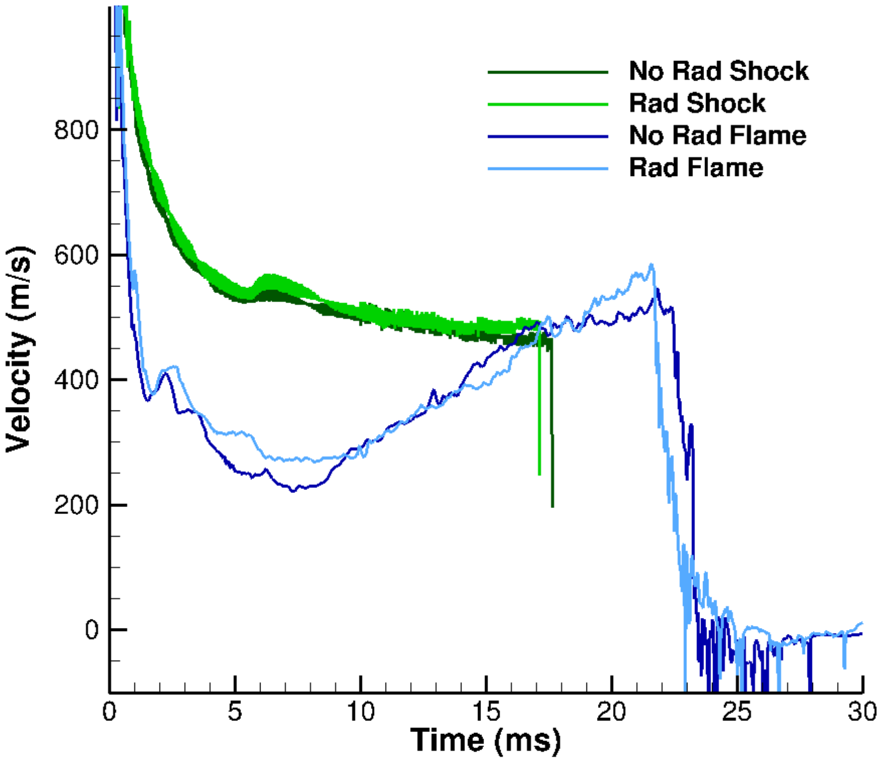

Figure 6-3. Shock and flame velocities for the 10-m channel using the 2-step reaction mechanism.

sharply as the detonation fails. Soon after, it starts to climb steadily and keeps rising up to ∼25 ms, which is when the reflected shock reverses the flow and prevents further propagation of the flame.

A snapshot of the structure of the coal-dust flames is shown in Fig. 6-5. The peak gas-phase temperature for the radiative case is observed to be more ∼150 K lower than that of the non-radiative case at ∼17 ms. This difference in temperatures can be attributed to the local heat loss due to radiation heat transfer.

In dust explosion safety, it is important to look at parameters such as the overpressure and the impulse, which gives us an idea of the damage that is caused due to these explosions, which the X-t and other plots are not able to convey. Fig. 6-6 and Fig. 6-7 compare the gauge pressure and the impulse, respectively, between the radiative and non-radiative cases for three gauges that are placed at 1 m, 6 m, and 10 m in the channel, at a height of 2.5 cm. If we look at the gauge pressure plots, we can observe that the gauge pressures for the radiative case for

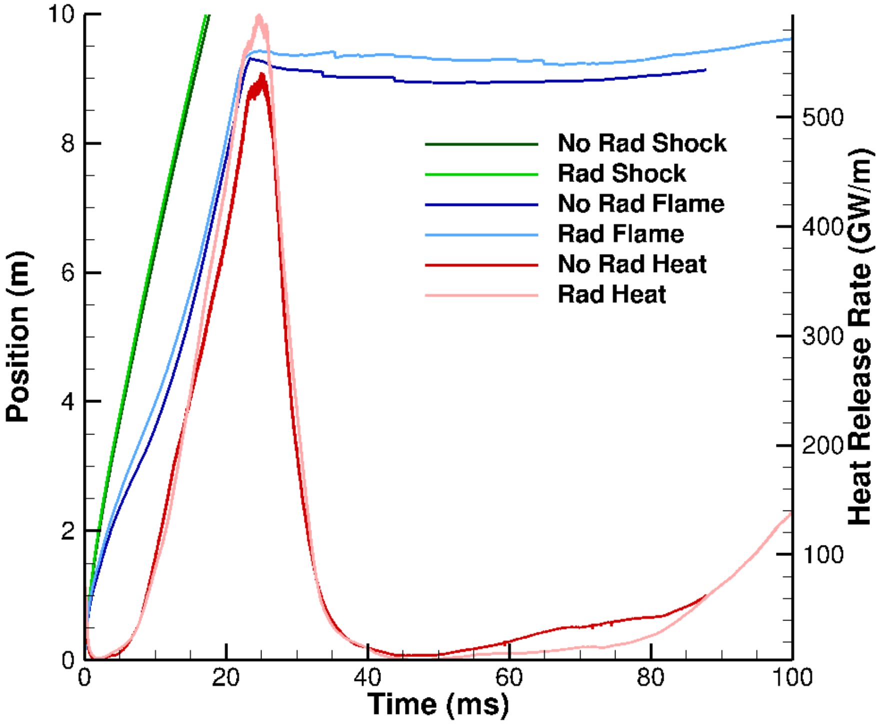

Figure 6-4. Shock and flame positions and heat release rates due to chemical reactions for the 10-m channel using the 2-step reaction mechanism.

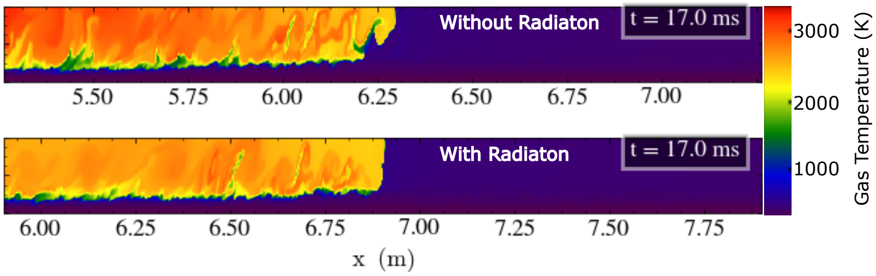

Figure 6-5. Contour plots of gas temperature for the cases with and without radiation at 17 ms for the 10-m channel with the 2-step reaction mechanism. Note that the plots have been stretched in the y-direction by 4 times for better visualization.

all three locations are significantly higher than those for the non-radiative case. As the shock travels through these locations, there is a step-change in the pressure. This higher post-shock pressure then falls sharply, till the dust flame reaches the location, at which point it starts increasing again. The peak pressures at these locations often reach values that are higher than the post-shock pressure, indicating that the flame themselves can be more damaging than the shock. A similar situation is revealed by the impulse plots in Fig. 6-7. The radiative case impulse is observed to be more than 10 kN.s higher than the non-radiative case towards the end of the simulation.

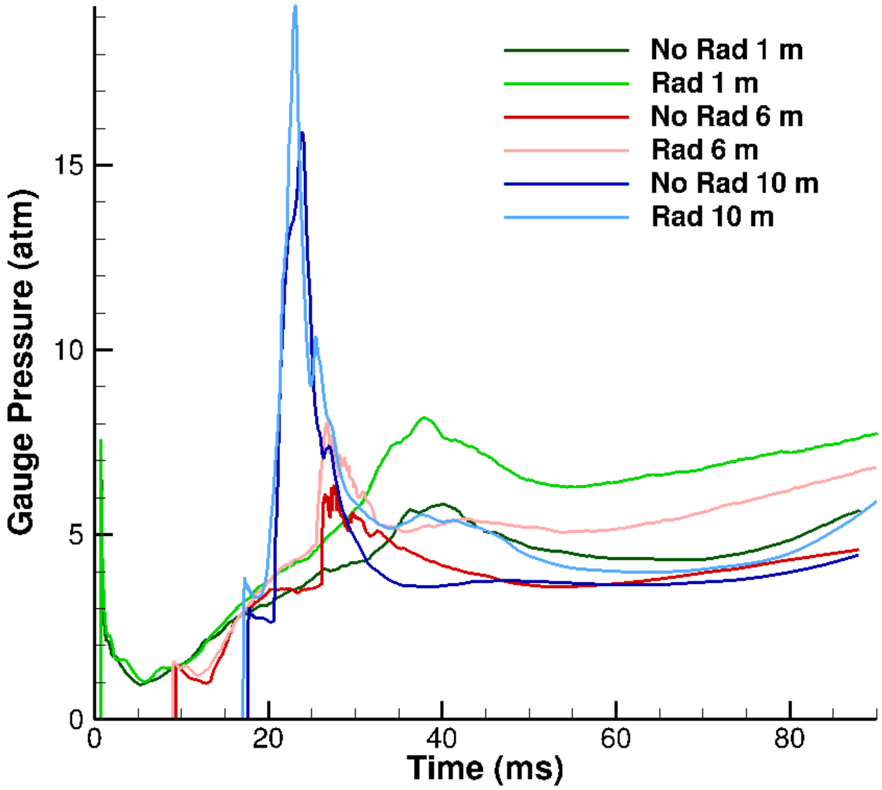

Figure 6-6. Gauge pressure plots for the 10-m channel radiative and non-radiative cases with the 2-step reaction mechanism at locations of 1 m, 6 m and 10 m in the channel, and at a height of 2.5 cm.

6.2 Long 40-m Channel With the 2-Step Methane-Air Reaction Mechanism

In the shorter 10-m channel cases, the reflected shock interacts with the flame and prevents further flame propagation by reversing the flow, but also produces a huge spike in the gauge pressure after reflection. We wanted to see what happens if we let the flame keep propagating unhindered. For this, we simulated a 40-m long channel, with a nearly identical setup to Houim and Oran (2015c,b); Shimura and Matsuo (2019), except that our simulations are using a different reaction mechanism, different coal parameters, and a much longer simulation time.

The flame and shock positions, along with the total heat release rates are shown in Fig. 6-8, and the flame and shock velocities in Fig. 6-9. These plots tell us a story that the

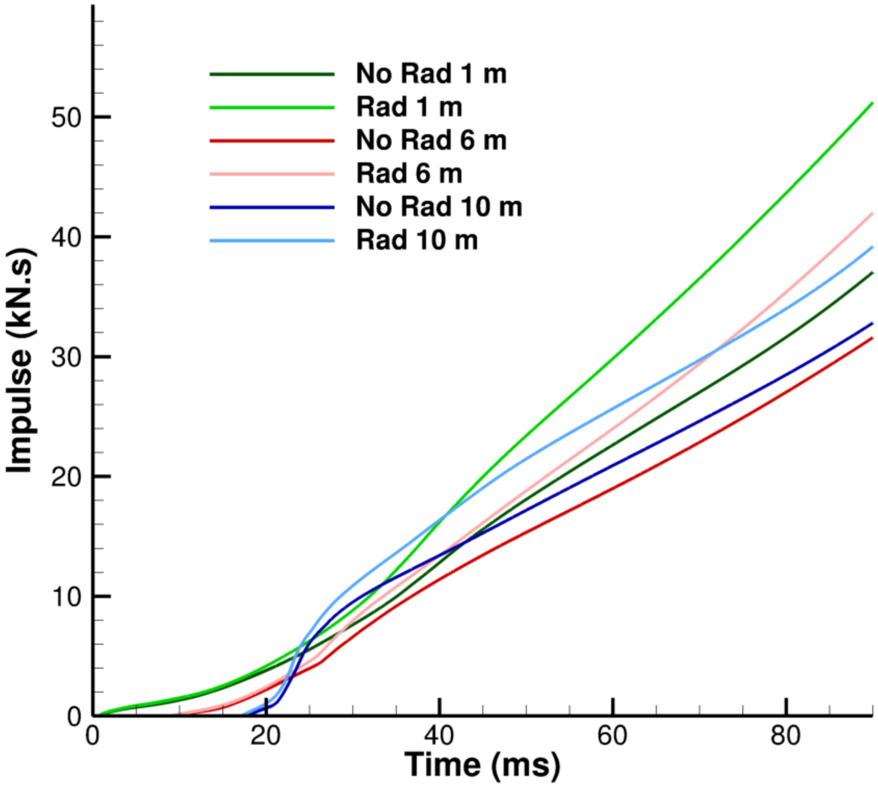

Figure 6-7. impulse plots for the 10-m channel radiative and non-radiative cases with the 2-step reaction mechanism at locations of 1 m, 6 m and 10 m in the channel, and at a height of 2.5 cm.

previous case could not. The heat release rate for the radiative case increases by a significant amount till ∼35 ms, and at the peak, it is more than 60 GW/m higher than the non-radiative case. The subsequent drop in the heat release rates for both cases is possibly due to the lack of oxidizer in the first 15 m of the channel since these cases are highly fuel-rich. We can see the flames in this section reducing in intensity from the X-t plots (y = 2.5 cm) shown in Fig. 6-10 (note that here we have only shown the X-t plot at y = 2.5 cm because the one at y = 5 cm was quite similar and did not give us any more details). Towards the end of the simulation, the flame fronts in both cases almost catch up with the leading shocks, which leaves little time for the shock-heated particles to release the volatile methane. This could also be a contributing factor to the reduction in heat release rates. In the non-radiative case, however, the heat release rate again starts to increase after ∼45 ms. In general, we observe

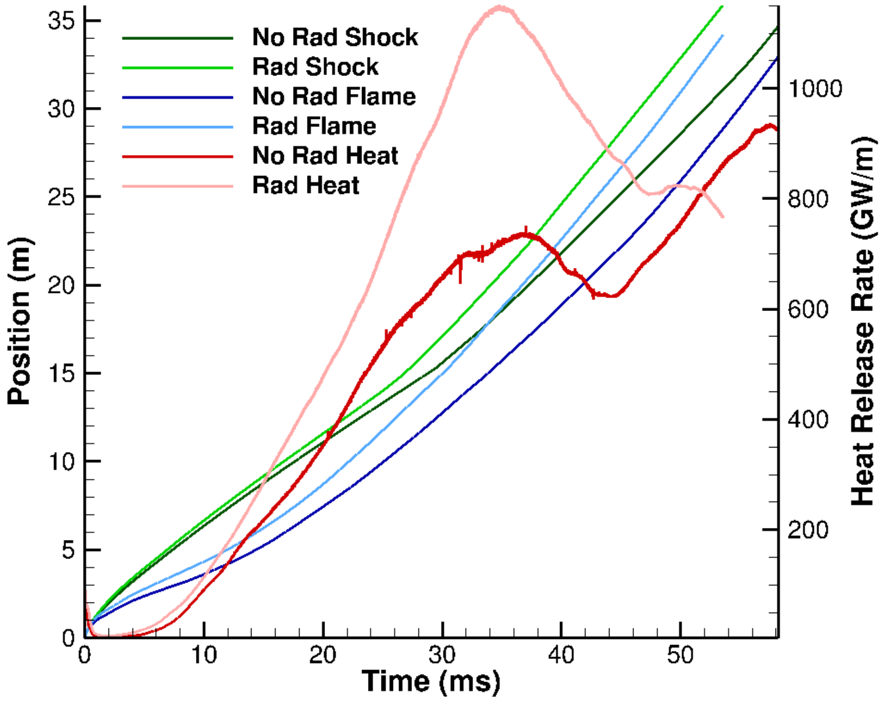

Figure 6-8. Shock and flame positions and heat release rates due to chemical reactions for the 40-m channel using the 2-step reaction mechanism.

that the flame and shock velocities for the radiative case are significantly higher than the non-radiative case.

Now, let us look at the gauge pressures and impulse for the two cases, shown in Fig. 6-11 and Fig. 6-12 respectively. The stationary gauges are placed at 1 m, 10 m, 20 m, and 30 m, at a height of 2.5 cm in the channel. Even without the reflected shock, the gauge pressures are still relatively high. Once again, we see that the radiative case has significantly higher pressures than the non-radiative case. For the gauge at 1 m, we can see the pressure jump from the detonation, after which it falls and then rises steadily once the dust flame propagation starts. For the gauges in the right half of the domain, there is no such fall in the pressure after the initial jump, also indicating that the flame and shock fronts are very close together. Just as in the previous case, the pressures due to the flame propagation are higher than the initial increase due to the shock. From both Fig. 6-11 and Fig. 6-12 we can tell that the radiative flame and shock are ahead of the non-radiative case, especially for the latter part of the

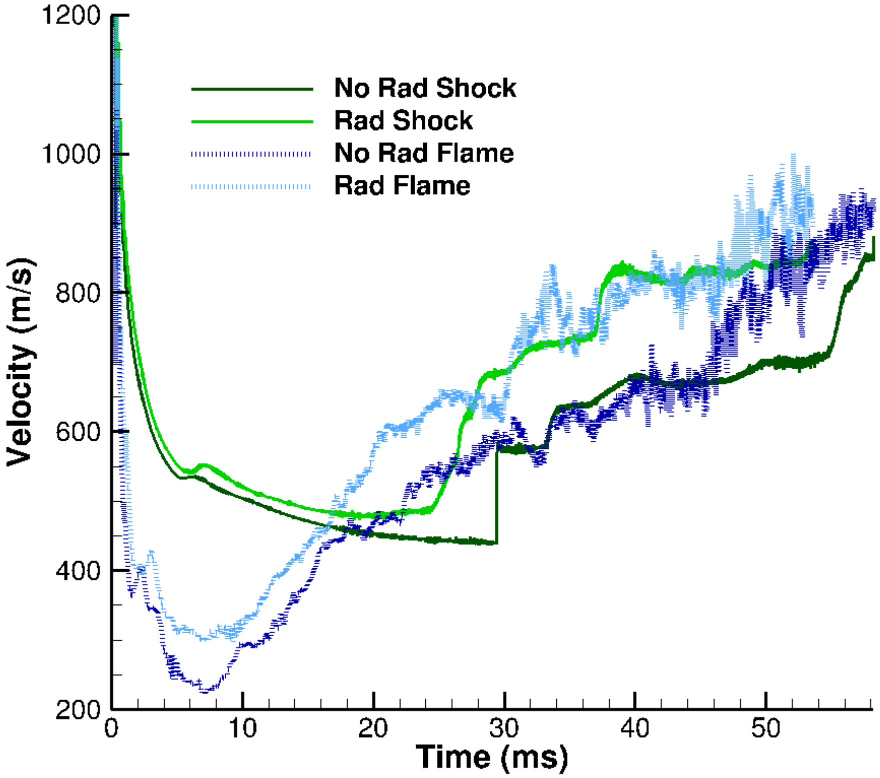

Figure 6-9. Shock and flame velocities for the 40-m channel using the 2-step reaction mechanism.

simulation. At ∼53 ms, the impulse for the radiative case (1-m gauge) is ∼10 kN.s higher than the non-radiative case.

6.3 Effect of Particle Size

According to Cashdollar (2000), the coal particle size range between 10-100 μm has the highest explosibility. For sizes less than 10 μm and greater than 100 μm, the minimum explosible concentration (MEC) increases significantly. Particles larger than 150 μm are very difficult to ignite. For our general test cases, we used a particle diameter of 30 μm, since it has one of the lowest MEC values. Nevertheless, we also wanted to explore how the size of particles can change the behavior of the flame propagation. In this section, we present the results of these tests. The particle diameters we used are 5 μm, 100 μm, and 150 μm, besides the original 30 μm particles. All these tests were run using the 10-m long channel.

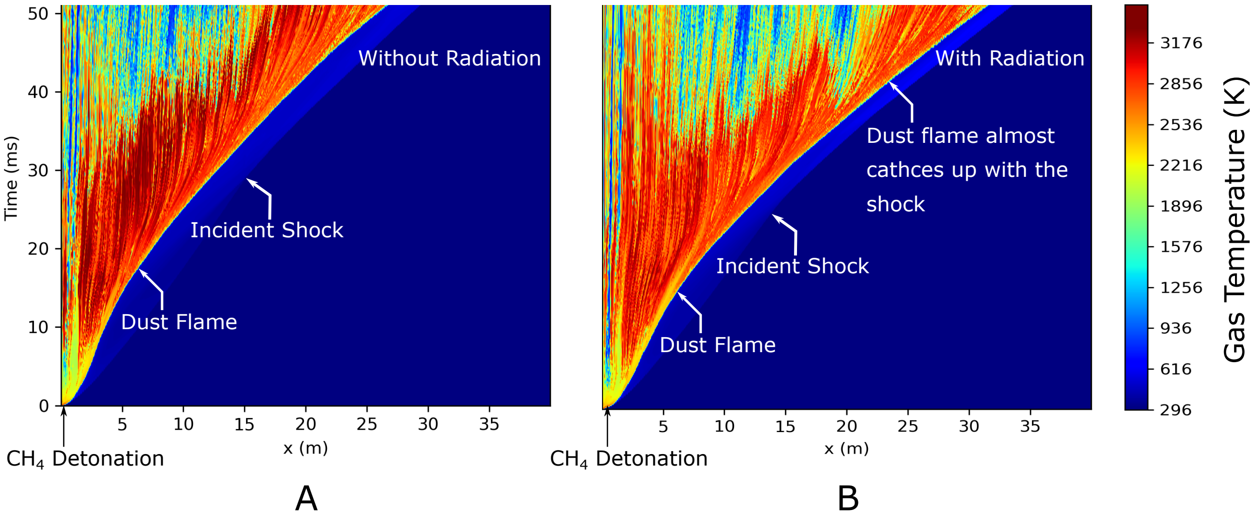

Figure 6-10. X-t diagram for the 40-m long channel shaded by gas phase temperature at y = 2.5 cm with the 2-step reaction mechanism. A) Without radiation. B) With radiation.

Once again, we start by looking at the shock positions, flame positions, total heat release rates, shock velocities and the flame velocities, shown in Fig. 6-13, Fig. 6-14, Fig. 6-15, Fig. 6-16 and Fig. 6-17, respectively. The shock velocity for the 5 μm particles is the highest, followed by the 30 μm particles, and then the velocities for the rest of the particle sizes are in the same range. This is because the 5 μm particles stay closer to the floor of the domain and do not get lifted as far as the other cases. The much smaller Stokes number of the small particles cause them to become trapped in the shear layer (dust layer). The 100 μm and 150 μm particles get lifted the most. As the shock passes over the layer, the particles almost instantly rise to the top of the domain. The reason why smaller particles stay close to the floor and larger particles get lifted higher has been explained in detail in Ugarte et al. (2017a,b). To summarize their observations, even though the smaller particles experience larger upward acceleration, the drag that opposes the lifting of the particles is much greater than that of the larger particles. The energy lost by the shock to lift the particles causes the shocks for these cases to have the lowest velocities. The 30 μm particles are somewhere in between.

The flame position and velocity plots show the differences between the radiative and non-radiative cases more prominently. The most significant differences show up for the extreme

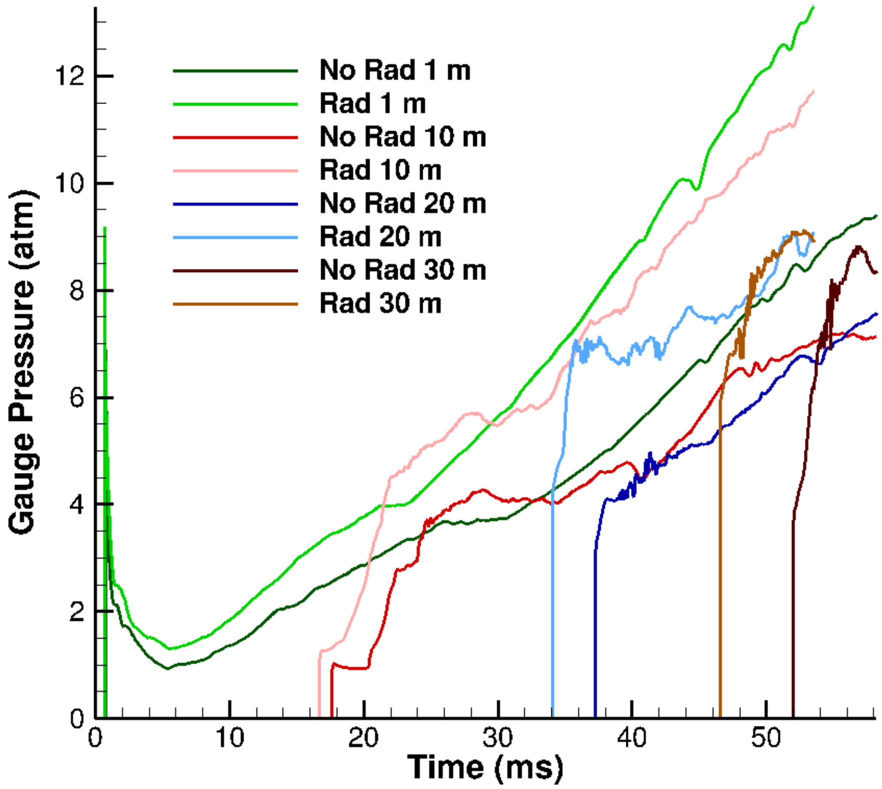

Figure 6-11. Gauge pressure plots for the 40-m channel radiative and non-radiative cases with the 2-step reaction mechanism at locations of 1 m, 10 m, 20 m and 30 m in the channel, and at a height of 2.5 cm.

cases - the 5 μm and 150 μm particle diameters. First, let us discuss the similarities. For both of these particle sizes, the flame propagation is slow and unstable. If the domain was longer and the reflected shock wasn't allowed to interact with the flame, the flames would probably stagnate and/or quench. Fig. 6-15 attests to that. They are significantly lower than the 30 and 100 μm particles. Some of the cases show a slight increase in the heat release rates after the shock reflection enhances mixing and thus the burning, but without the reflection, they would likely not survive.

The differences between the radiative and non-radiative cases for the 5 and 150 μm particles are interesting. On the one hand, the flame velocity for the 5 μm radiative case is lower than the non-radiative case, whereas for the 150 μm particles, the radiative case flame velocity is higher than the non-radiative case. A simple explanation is again linked to the lifting of the particles and the size of the particles. The 5 μm particles stay closer to the floor, and

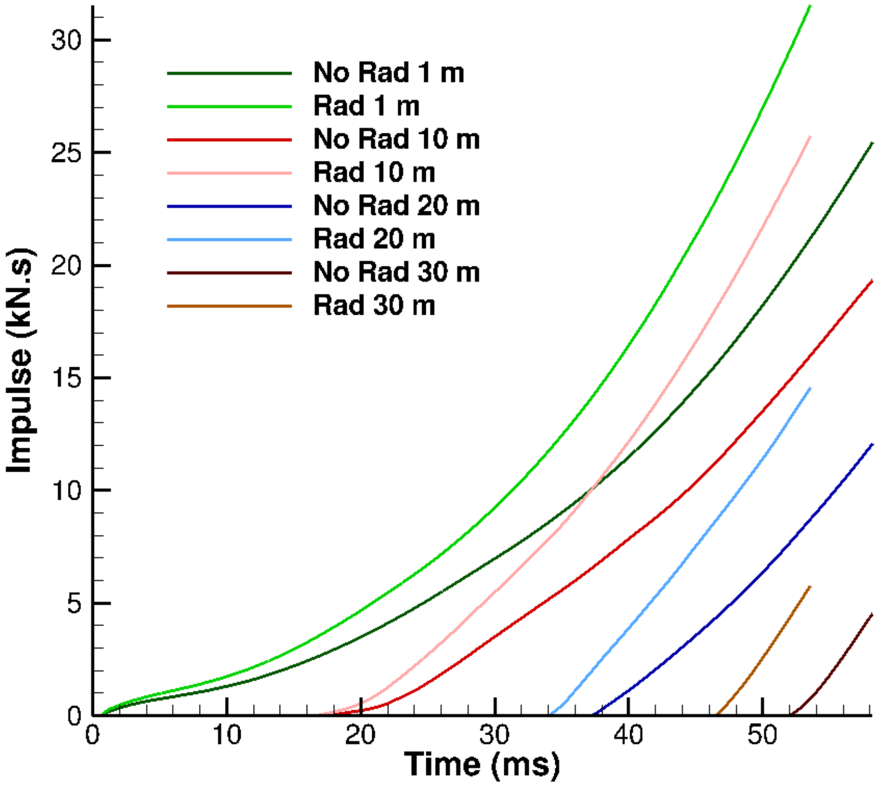

Figure 6-12. Impulse plots for the 40-m channel radiative and non-radiative cases with the 2-step reaction mechanism at locations of 1 m, 10 m, 20 m and 30 m in the channel, and at a height of 2.5 cm.

thus do not receive the majority of the radiative heat flux. On top of that, the amount of radiative energy that the particles can absorb is also lower due to the smaller surface area of the particles. Thus, the particles lose more heat due to radiation than they can absorb. This leads to a stagnating flame for the radiative case, shown in Fig. 6-18. The non-radiative case doesn't lose as much energy and thus the flame is seen to start accelerating after ~17 ms.

For the 150 μm particles, the argument is exactly the opposite. They absorb more radiative energy due to the greater surface area, as well as being more highly dispersed. This results in a considerably higher flame speed and total chemical heat release rate compared to the non-radiative case. The flame propagation for the non-radiative case is unsteady and the flames are highly intermittent. In fact, there is hardly any combustion occurring. The radiative case has a comparatively higher amount of combustion and re-ignition. The visual differences can be seen in the X-t plots in Fig. 6-19. The amount of heat energy lost and gained due to radiation can be seen in the radiative heat flux plots for all four particle sizes shown in Fig. 6-20. In this figure, we can see that the heat loss due to radiation for the 5 μm particles is the highest. The small bright red regions in these plots have a positive radiative heat flux - thus they absorb more energy than they lose due to radiation. It is evident that the regions with positive radiative heat flux are much smaller for the 5 μm particles compared to the rest of the cases. Therefore the radiative pre-heating experienced by the particles is also the lowest for the 5 μm particles and the radiative heat losses dominate. These losses are not accounted for by the non-radiative cases and thus the flame and shock velocities are much larger.

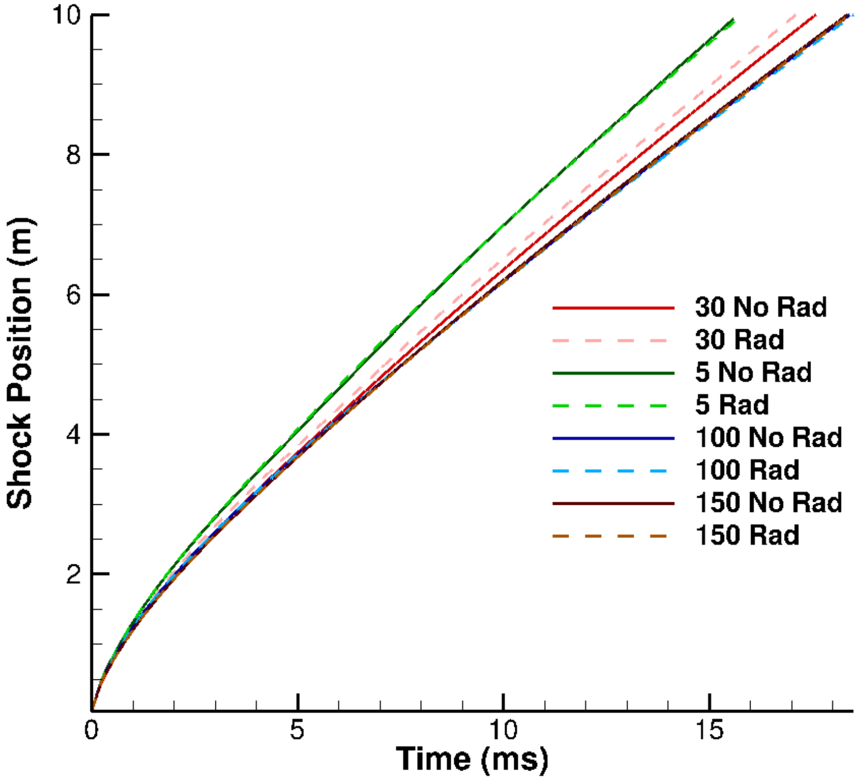

Figure 6-13. Shock positions for 5, 30, 100 and 150 μm particles using the 10-m channel and the 2-step reaction mechanism.

We can see the physical impact of these differences in the gauge pressure and impulse plots for a stationary gauge placed at 8 m, shown in Fig. 6-21 and Fig. 6-22, respectively. For all particle sizes except the 5 μm particles, both gauge pressure and impulse values for the radiative cases are higher than the non-radiative cases. It is interesting that the gauge

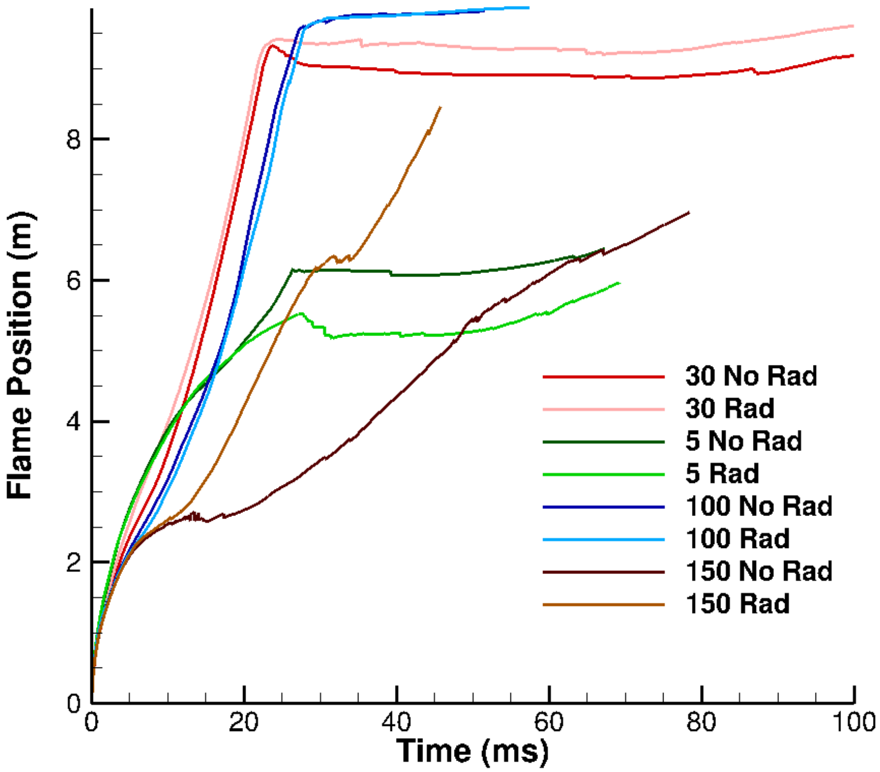

Figure 6-14. Flame positions for 5, 30, 100 and 150 μm particles using the 10-m channel and the 2-step reaction mechanism.

pressures for the 150 μm radiative case, after the shock reflection, were considerably higher than the non-radiative case and in the later stages even higher than the 30 μm particles. This shows how much of an influence the reflected shock has on the propagation of the flame, and its damaging effects. However, the non-radiative case does not show this increase in pressure and stays relatively flat.

For the 5 μm particles we observe that the gauge pressure and impulse values are higher for the non-radiative case than the radiative case. However, the pressure values themselves are pretty low as the flames never reach the 8 m location. These values are higher for the radiative case for the stationary gauges placed at 1 m and 4 m since these are the locations where the flames exist.

6.4 Effect of Reaction Mechanism

In this section, we compare the results of the simulations carried out using both the 1-step and 2-step reaction mechanisms. Recall that the results previously showed that for the 1-step

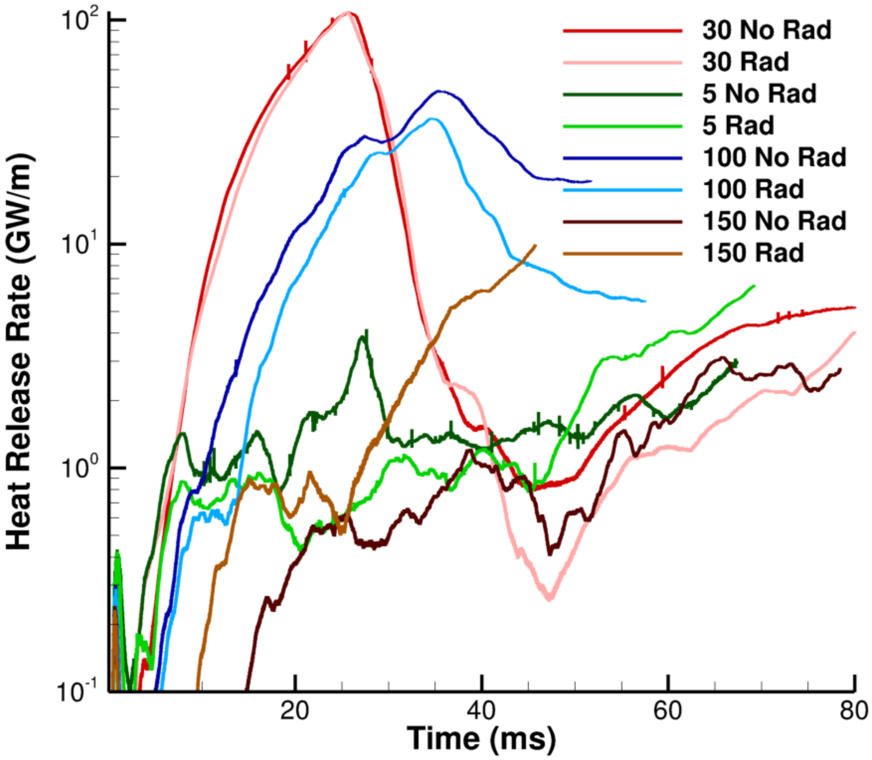

Figure 6-15. Total chemical heat release rates on log plot for 5, 30, 100 and 150 μm particles using the 10-m channel and the 2-step reaction mechanism.

reaction mechanism simulations, the flames were getting quenched, which we had not seen mentioned in earlier literature. We suspected that the reaction mechanism could be responsible for it and thus carried out the same simulations with the 2-step reaction mechanism. The initial conditions are almost identical to the 40 m-long 2-step simulations, except that the initial temperature in the hot spots for the 1-step tests was at 1000 K instead of the 2000 K in the 2-step tests. This is done so that the detonations are comparable to each other. For the 2-step tests, the 1000 K initial temperature wasn't enough to produce a detonation. Even with 2000 K initial temperature, the detonations in the 2-step tests are not stable and failed pretty quickly compared to the 1-step tests. However, it is enough to propagate the dust flame. The reason for this is probably because the reversible CO_2-dissociation reaction reduces the energy output and increases the ignition delay time. This is not accounted for in the 1-step reaction mechanism and thus the 1-step mechanism may ignite too readily. Also note that the detonation cell size for methane-air reactions, λ_{CH_4-air} is $\sim$ 17 cm. Thus for stable

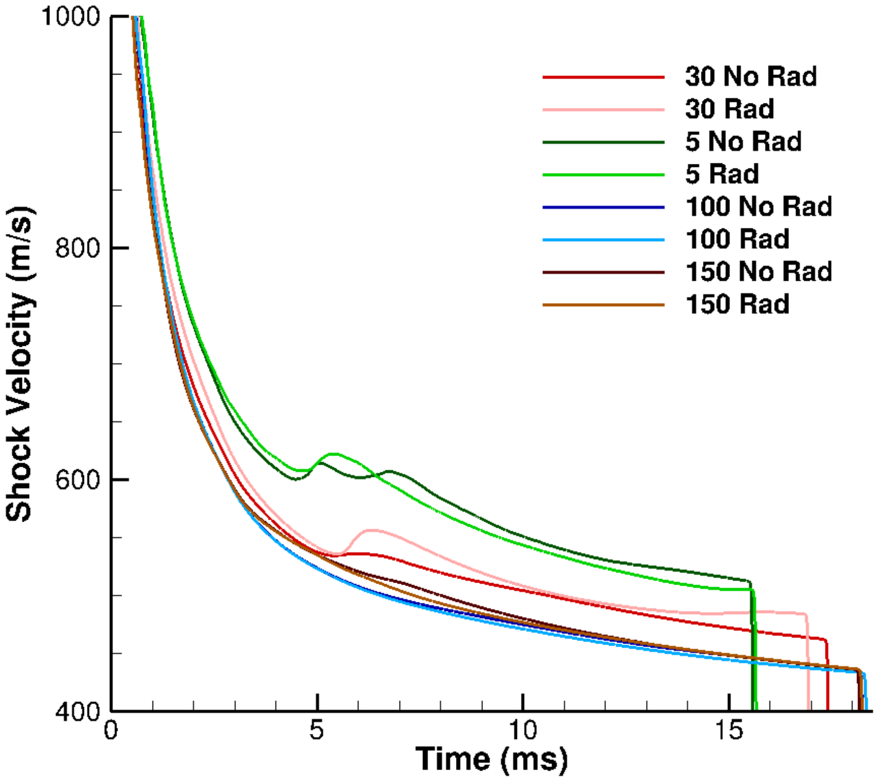

Figure 6-16. Shock velocity for 5, 30, 100 and 150 μm particles using the 10-m channel and the 2-step reaction mechanism.

detonation, the channel height should be greater than 17 cm. However, in our simulations the channel height is only 5 cm, and thus stable detonations are likely not possible. For this test also, we consider 30 μm particles.

Fig. 6-23, Fig. 6-24, Fig. 6-25, and Fig. 6-26 show the flame velocity, total heat release rate, shock velocity and flame velocity plots, respectively, for both reaction mechanisms and compare the cases with and without radiation. Fig. 6-28 shows the X-t plots for the 1-step cases with and without radiation. These can be compared to the X-t plots for the 2-step mechanism in Fig. 6-10. After the detonation fails, the flame in 1-step simulations starts decelerating and eventually stagnate. As discussed previously, Houim and Oran (2015c) and Shimura and Matsuo (2019) do not observe quenching or stagnation of the flames, though these earlier simulations were run for much shorter simulation times and used different coal parameters. For the 2-step cases, the flame does initially decelerate as well, but then they

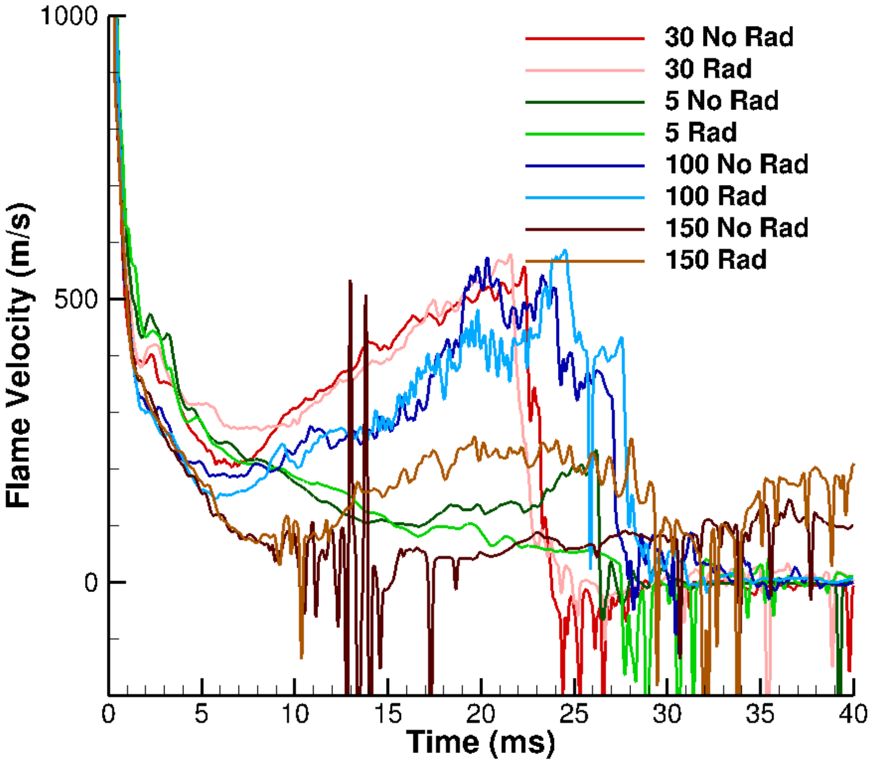

Figure 6-17. Flame velocity for 5, 30, 100 and 150 μm particles using the 10-m channel and the 2-step reaction mechanism.

start accelerating almost at the same time as the heat release rates start to climb. Once this happens, the flame propagation shows no sign of stopping or even slowing down. Instead, the flame velocity plots suggest that they will continue propagating as long as a fuel source (dust layer) is present (Kauffman et al., 1992).

The difference between the radiative and non-radiative cases is also the opposite. For the 1-step cases, radiation seems to be hurting the flame propagation. The heat release rate, for the most part, the flame velocity, and the shock velocity all appear to be lower than the non-radiative case. The flame also doesn't propagate as far as the non-radiative case. The energy lost due to radiation causes the peak flame temperatures to be about 200 K lower than the non-radiative case. On the other hand, for the 2-step cases, radiation seems to accelerate the flame propagation. All three parameters - the heat release rates, flame velocity, and shock velocity - are significantly higher than the non-radiative case.

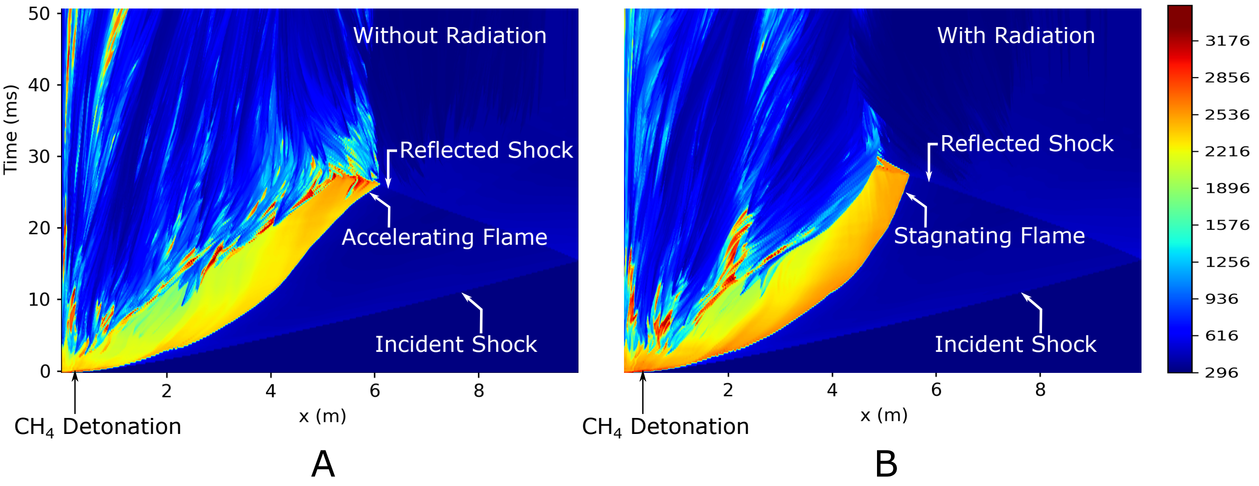

Figure 6-18. X-t diagram for the 5 μm particles using the 10-m long channel shaded by gas phase temperature at y = 5 cm with the 2-step reaction mechanism. A) Without radiation. B) With radiation.

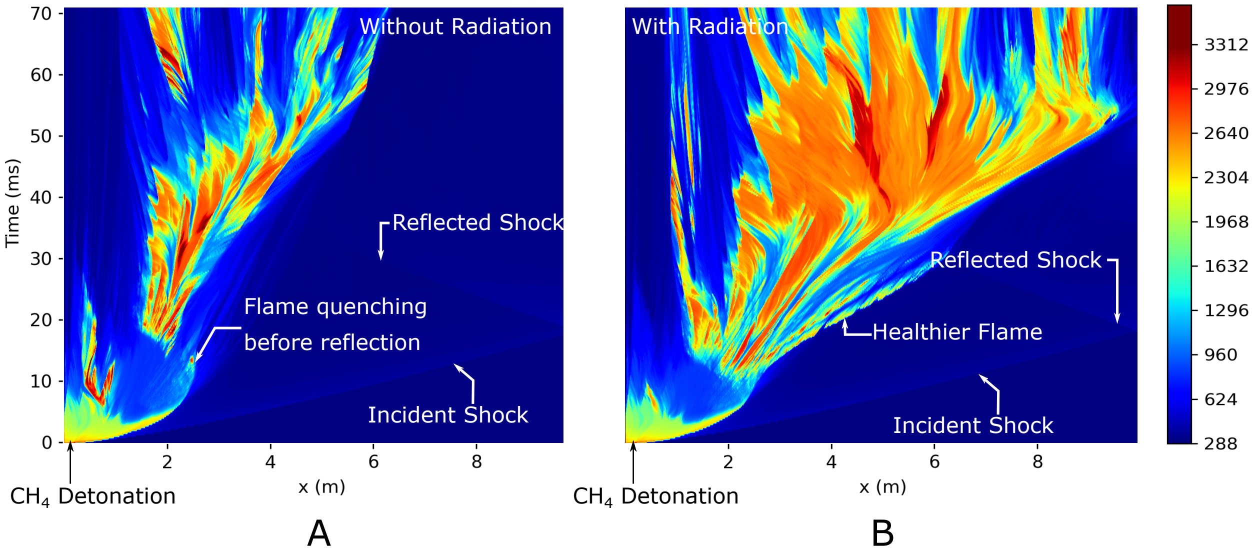

Figure 6-19. X-t diagram for the 150 μm particles using the 10-m long channel shaded by gas phase temperature at y = 5 cm with the 2-step reaction mechanism. A) Without radiation. B) With radiation.

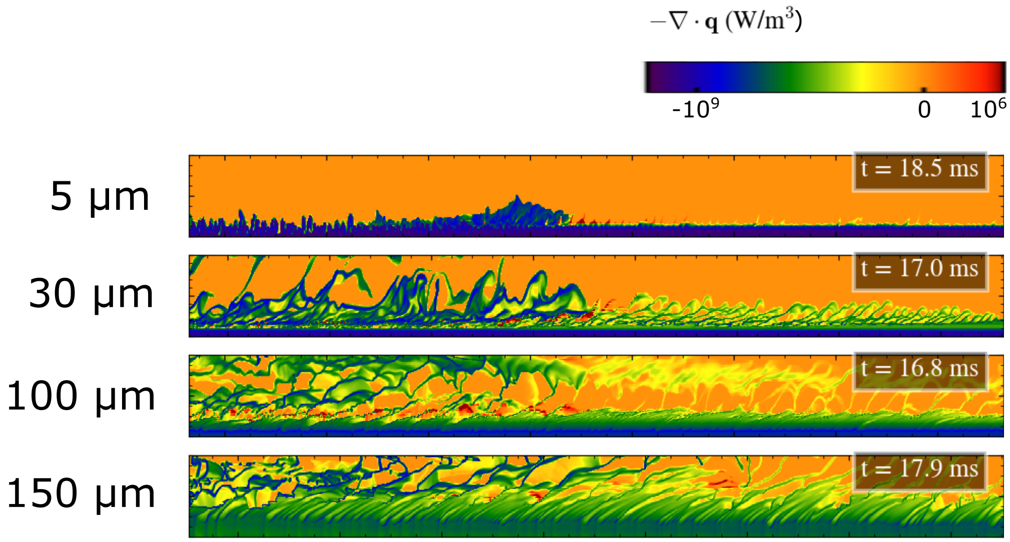

Figure 6-20. Radiative heat flux plots for the 5, 30, 100 and 150 μm radiative cases.

Another interesting phenomenon that we observed was the effect of the reflected shock on the thermal and chemical equilibrium. If we look at the X-t plots for the short channel 2-step reaction mechanism 30 μm cases in Fig. 6-1 and 6-2, we notice that there is a reignition event occurring near the left end of the channel. This is also reflected in the heat release rate plots in Fig. 6-4. After $\sim$60 ms, the heat release rates start steadily increasing again. We also observe that once the reflected shock travels through the regions where combustion was occurring, it almost completely extinguishes the flames in those locations. If we look at Fig. 6-1, we notice that there is another region of reignition that occurs between 7.5-8 m at t $\sim$ 40 ms in the channel. In this region, the reignition for the non-radiative case is stronger than that for the radiative case. On the other hand, looking at Fig. 6-2, we see that the reignition is stronger in the radiative case than the non-radiative case near the left end of the channel. Interestingly, these reignition events are not observed for the single-step mechanism cases, which indicates that the reaction mechanism may be responsible for their occurrence.

For purely theoretical reasons, we also performed the same 1-step test case, but with a 1% coal volume fraction. Note that these situations are not practical in coal mines, but we wanted to see how the flame propagation would change under these conditions, and especially how radiation would affect it. Fig. 6-27 shows the (a) total heat release rates and (b) the shock

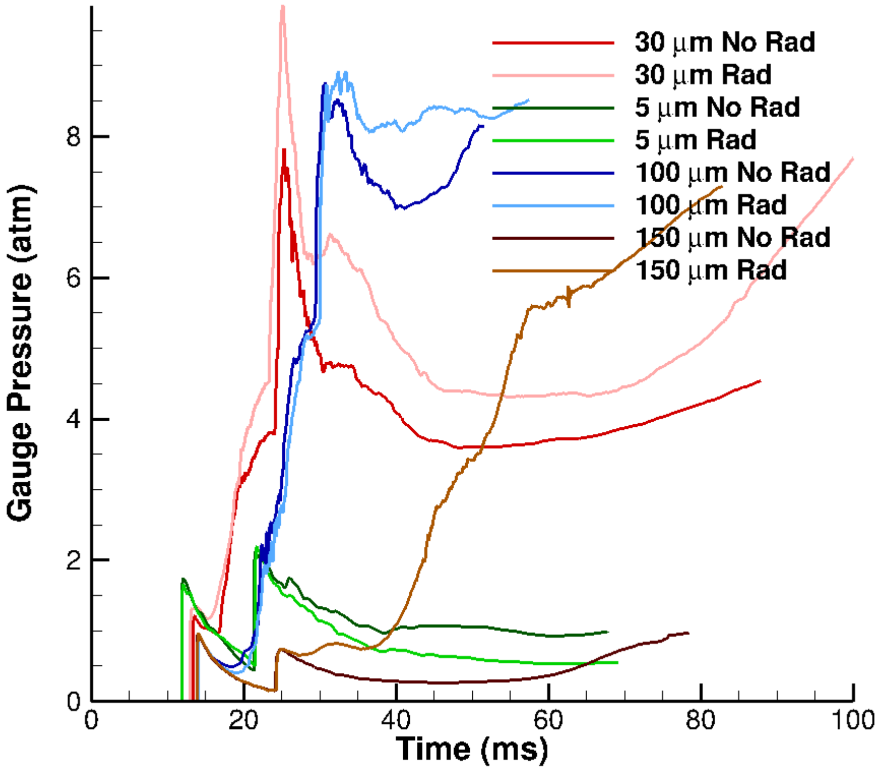

Figure 6-21. Gauge pressure plots for 5, 30, 100 and 150 μm particles using the 10-m channel with the 2-step reaction mechanism. The stationary gauge is located at 8 m in the channel, and at a height of 2.5 cm.

and flame velocities for these cases. As expected, the flame propagation continues unhindered. The flame velocities are relatively stable at ∼400 m/s. Once again, radiation causes the flame and the shock to accelerate more than in the non-radiative case. The total heat release rates are still much lower than the 2-step cases since there are much fewer particles to burn.

6.5 Discussion

From the simulation results, we observe that important bulk flame parameters such as velocity and peak temperatures are considerably different for cases that include radiation. Furthermore, radiation can often have opposite effects depending on the scenario. In most cases, radiation promotes flame propagation. The only exceptions are the 10 m-channel cases with the two-step reaction mechanism and 5 μm particles, and the 40 m-channel cases with the single-step reaction mechanism and 30 μm particles. For these cases, radiation seems to reduce the chemical energy release rates and thus hinder flame propagation. It is difficult to

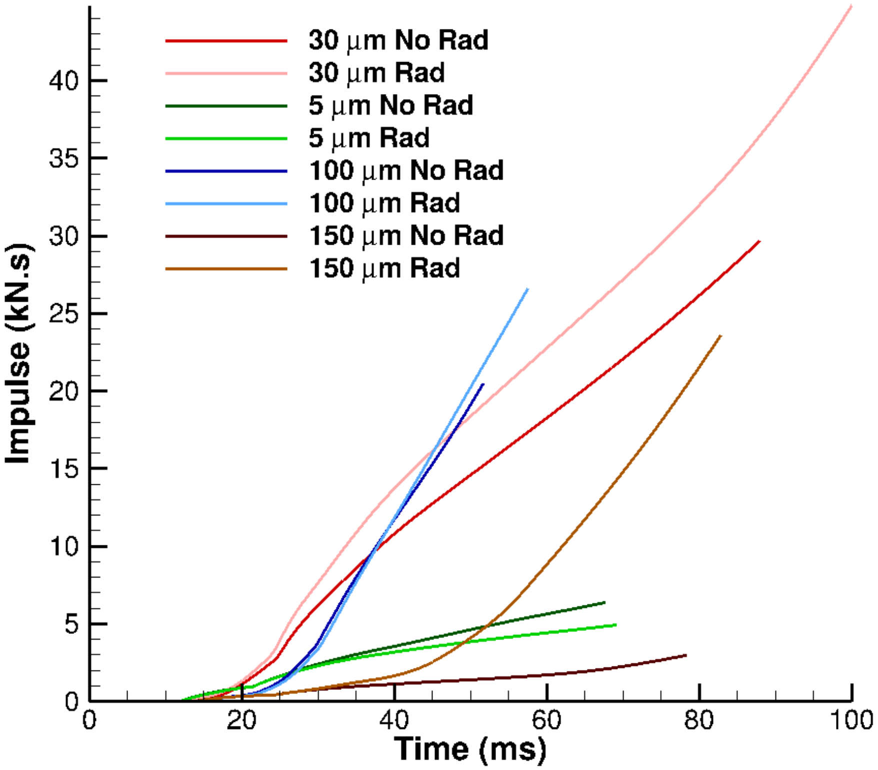

Figure 6-22. Impulse plots for 5, 30, 100 and 150 μm particles using the 10-m channel with the 2-step reaction mechanism. The stationary gauge is located at 8 m in the channel, and at a height of 2.5 cm.

generalize whether radiation helps or hurts flame propagation due to the highly non-linear nature of this phenomenon. On the one hand, heat energy lost due to radiation reduces peak flame temperatures. The chemical heat release rates are then decreased which reduces the capability for the flame to progress. On the other hand, the radiated heat energy can be absorbed by the particles ahead of the flame front, which pre-heats the particles and increases their combustibility. However, which of these dominates depends on the ability of the particles to absorb the incident radiation, and on time. If more heat is lost due to radiation than is absorbed by the particles, then thermal radiation slows the flame down and can even quench it. Also, radiation usually takes some time to show its effects. In the initial stages of all these simulations, the radiative and non-radiative cases almost overlap each other for all flame parameters (shock position and velocity, flame position and velocity, and total heat release rate). They only start to separate after a few milliseconds.

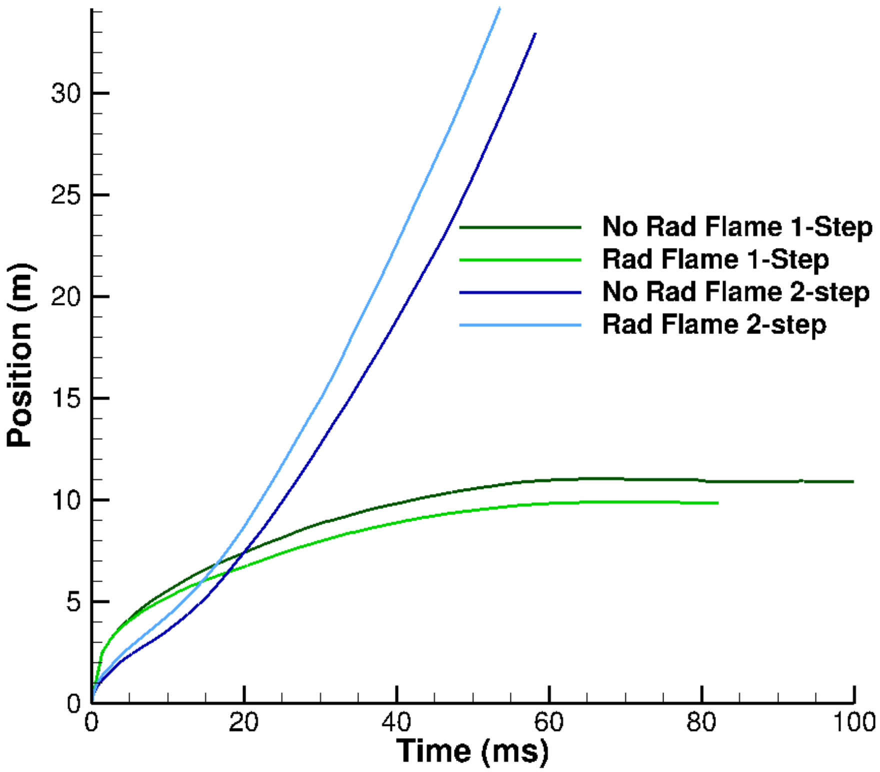

Figure 6-23. Flame positions for 30 μm particles using the 10-m channel and the 1-step and 2-step reaction mechanisms.

To assess the amount of physical damage these explosions can cause, we also looked at the gauge pressure and impulse at several locations in the channel. Again, in all the tests except the 5 μm particles, the gauge pressure and impulse for the radiative cases were substantially higher than their non-radiative counterparts. Furthermore, the difference between the cases grows as time progresses. The initial spike in the pressures is due to the shock, after which they fall till the flame reaches that stationary gauge location. Thus, the difference in the initial spikes is only due to the variation in the shock strengths. The more significant differences start showing once the flames pass through these locations. The shocks cause but a fraction of the overpressures. The flame itself appears to cause the bulk of the damage. The impulse data gives us an idea of how destructive these explosions can be over prolonged periods of exposure. Here also we see that the values diverge more with time. Therefore, neglecting radiation grossly underestimates the amount of damage such explosions can cause.

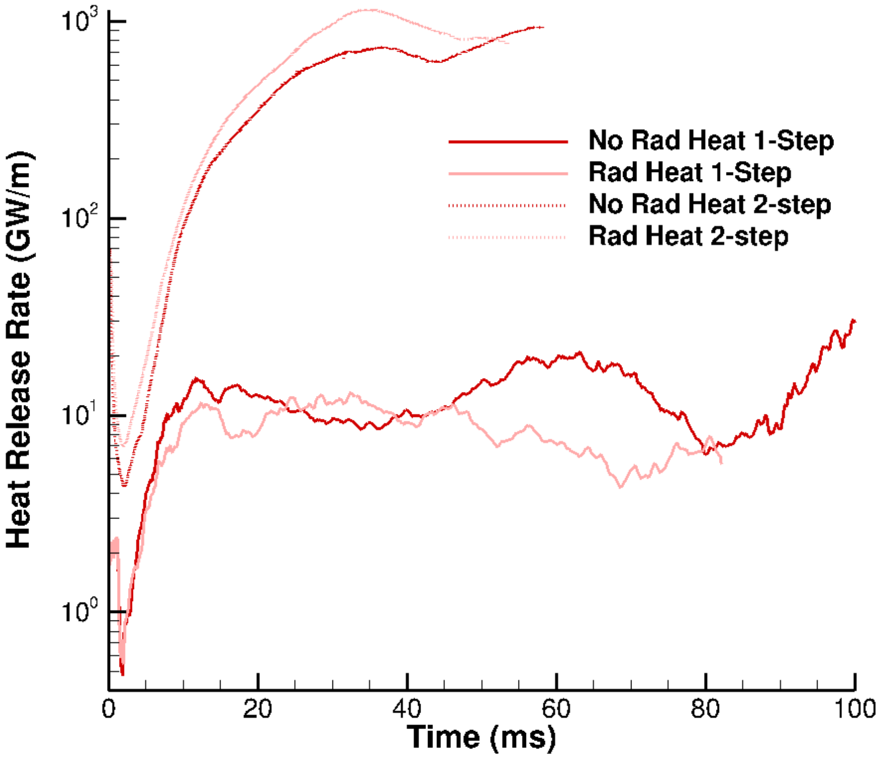

Figure 6-24. Total chemical heat release rates for 30 μm particles using the 10-m channel and the 1-step and 2-step reaction mechanisms.

Different particle sizes have varied effects on the propagation of the flame. Consistent with Cashdollar (2000), we find that particles between 10-100 μm diameter have the highest combustibility. 5 μm and 150 μm particles are much more challenging to ignite and in most simulations, they looked like they would either get quenched or stagnate or both. The only exception is the 150 μm radiative case, in which radiation has a significant effect on the flame propagation by enhancing the combustion of the particles. The 5 μm tests are the only ones using the 2-step reaction mechanism where radiation seems to inhibit the flame propagation. A simple explanation is that due to the small particle size, most of these particles stay closer to the floor of the channel, thus missing out on most of the incident radiation field. The surface area of the particles is also much smaller than the others and consequently, the particles absorb much lower radiation. For both the radiative and non-radiative cases, failure to produce a stable dust flame can also be attributed to the fact that the particles are not efficiently mixed by the shock passing over the dust layer.

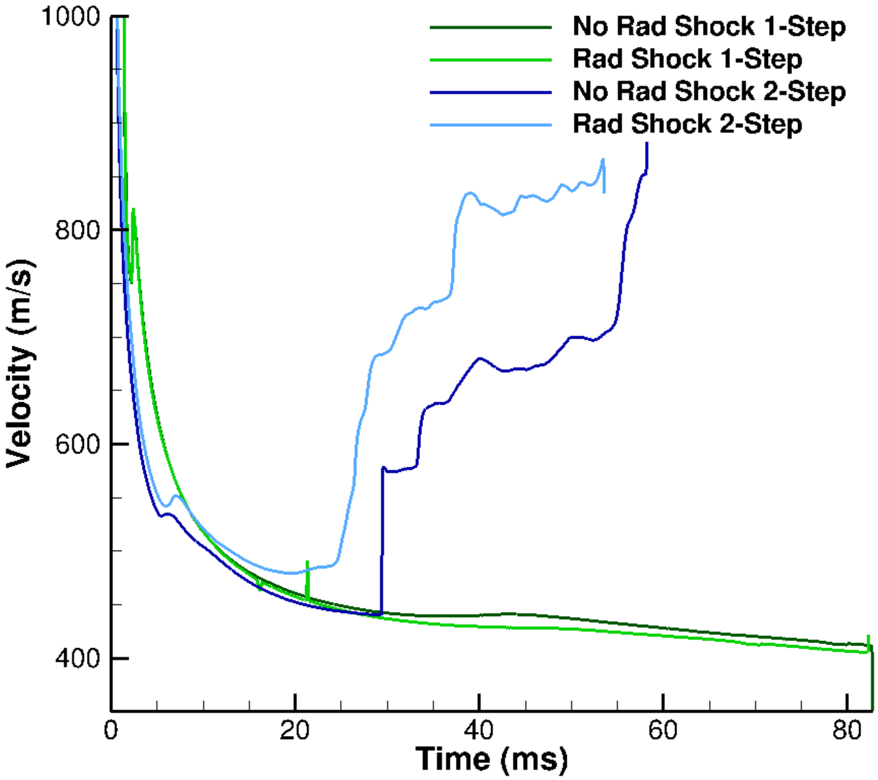

Figure 6-25. Shock velocity for 30 μm particles using the 10-m channel and the 1-step and 2-step reaction mechanisms.

The 100 μm particles are most similar to the 30 μm in terms of flame propagation. They both produce stably propagating dust flames, and the overall behaviors are quite comparable. However, due to the lower combustibility of the particles, the overall heat release rates are lower than the 30 μm particles. Interestingly, this is one situation where radiation seems to both enhance and retard the flame propagation depending on which plots and sections you look at. Plots of the various flame parameters (Fig. 6-13, Fig. 6-14, Fig. 6-15, Fig. 6-16 and Fig. 6-17) for the radiative and non-radiative cases show that the values are more similar to each other than dissimilar, with one case being ahead in certain sections and behind in others. However, the gauge pressure and impulse plots (Fig. 6-21 and Fig. 6-22) show that towards the end of the simulation, the radiative case is slightly higher in these values than the non-radiative case.

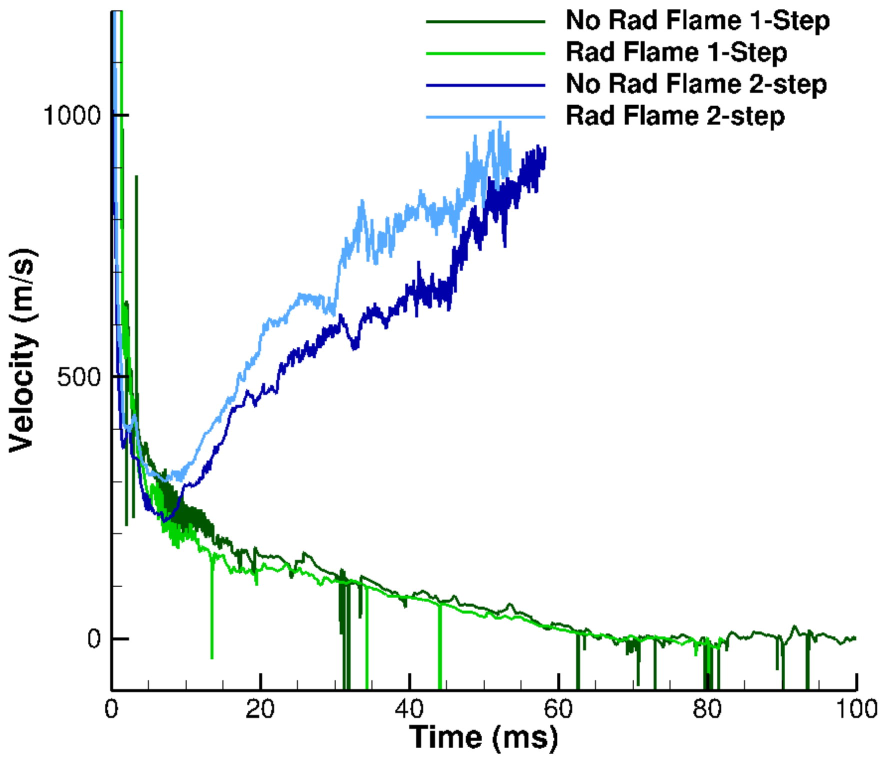

Figure 6-26. Flame velocity for 30 μm particles using the 10-m channel and the 1-step and 2-step reaction mechanisms.

The influence of the reaction mechanism also proved to be important. The 1-step reaction mechanism predicted that the flames in the 40-m channels would eventually stagnate under these conditions. However, the same tests performed with the 2-step reaction mechanism disagree and keep accelerating till the end of the simulations. We have no way of knowing which one is the correct prediction until actual experiments are performed under similar conditions (which this work can hopefully motivate). Individually, both reaction mechanisms were put through extensive code verification tests and the results were consistent with the literature on methane-air flames and coal-dust flames. This gives us sufficient confidence in both mechanisms and gives us no reason to favor one over the other. Detailed reaction mechanisms can clear this discrepancy which is a topic of future work.

The reignition events that were observed for the two-step reaction mechanism 10-m channel cases can be explained by the effect the reflected shock has on the thermal and chemical equilibrium throughout the channel. When the initial combustion events occur,

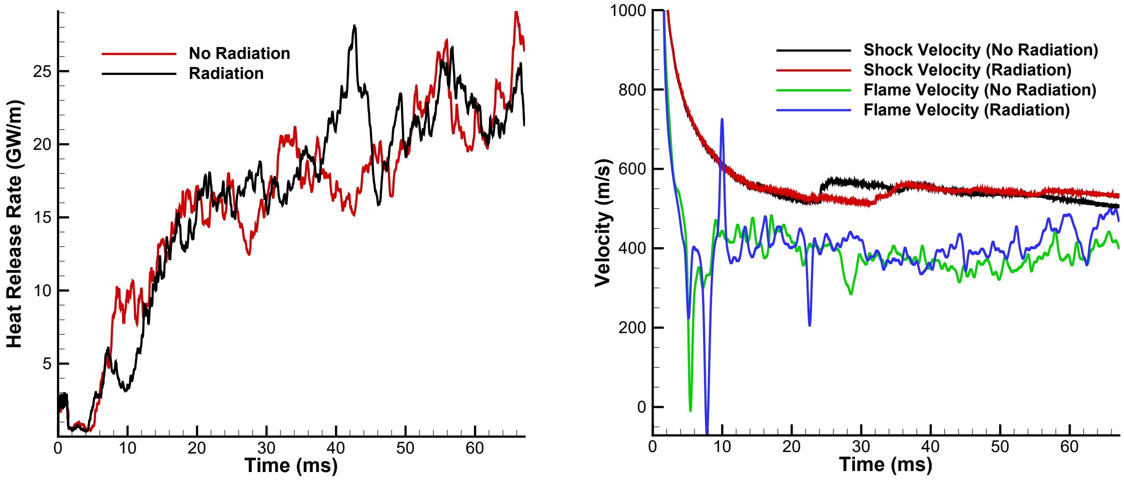

A B

Figure 6-27. Dilute (1% volume fraction) case total heat release rate due to gas phase chemical reactions and shock and flame velocities using single-step reaction mechanism. A) Total heat release rate due to gas phase chemical reactions. B) Shock and flame velocities.

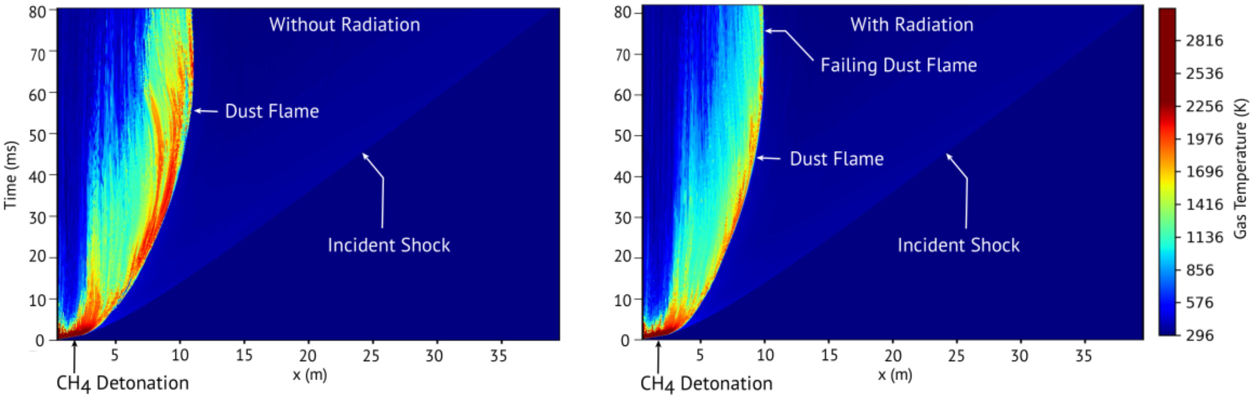

A B

Figure 6-28. Dense (47% volume fraction) case X-t plots for the 1-step reaction mechanism, shaded by gas phase temperature. A) Without radiation. B) With radiation.

thermal and chemical equilibrium is gradually reached. Once this equilibrium is reached, the reactions proceed until they are deficient of reactants (oxygen in this case). In the short channel cases, the reflected shock interacts with the flames before all the oxygen is consumed. For the longer channel (40-m) cases, looking at the X-t diagrams Fig. 6-10, we can see that without the reflected shock interaction, the flames would eventually extinguish once they ran out of oxidizer. The chemical equilibrium in these cases is ensured by the reversible reaction, R7. However, when the reflected shock reaches the regions where combustion was occurring, the little amount of oxygen that was remaining in these regions is pushed away from the reacting zones by the reverse flow. This removes the oxidizer from the high-temperature regions and the combustion halts almost immediately, which in turn reduces the temperatures. This is also reflected in the heat release rate plots in Fig. 6-4. After ∼25 ms, we see a sharp fall in the heat release rates for both the radiative and non-radiative cases. The reversed flow also removes other reaction products such as CO and CO_2 from the reaction zones thus severely affecting the chemical equilibrium. However, most regions of the channel don't have enough heat energy for reignition to occur. One notable exception is near the left boundary. Fig. 6-29 and 6-30 show time sequence plots of various parameters such as the gas temperatures, oxygen, and CO mass fractions and the particle volume fractions at different times in the simulation. The detonation fails just before the the first plot which is at 7.1 ms. At 26.1 ms, there is stable flame propagation to the right. As seen in these plots at 36 ms and 50.2 ms, after the reflected shock reaches the left boundary, the oxygen and CO mass fractions along with the gas temperature fall drastically. However, there are remnant regions of high temperature right next to the left wall. Even though the oxygen has almost entirely gone from this region (with the exception of some trapped oxygen in the coal layer), the CO_2 mass fractions are high. Given the high temperature and low oxygen and CO concentrations at the left boundary, the reaction progress variable is shifted heavily to the product side. This triggers the reverse reaction. The CO_2 in this relatively small high-temperature region starts to dissociate into CO and O_2. The region is already saturated with CH_4 due to the highly fuel-rich initial conditions. The higher temperatures close to the left boundary wall now once again ignite the highly fuel-rich mixture and the flame starts to propagate to the right, albeit much more slowly than before. Fascinatingly, the oxygen mass fraction is seen to start rising again ($t = 69.6$ ms onward) even though the combustion consumes oxygen. The oxygen mass fraction reaches the equilibrium value that was observed before the reflected shock interaction, which even though is a very small number, is greater than ∼0 which was observed just before the reignition started.

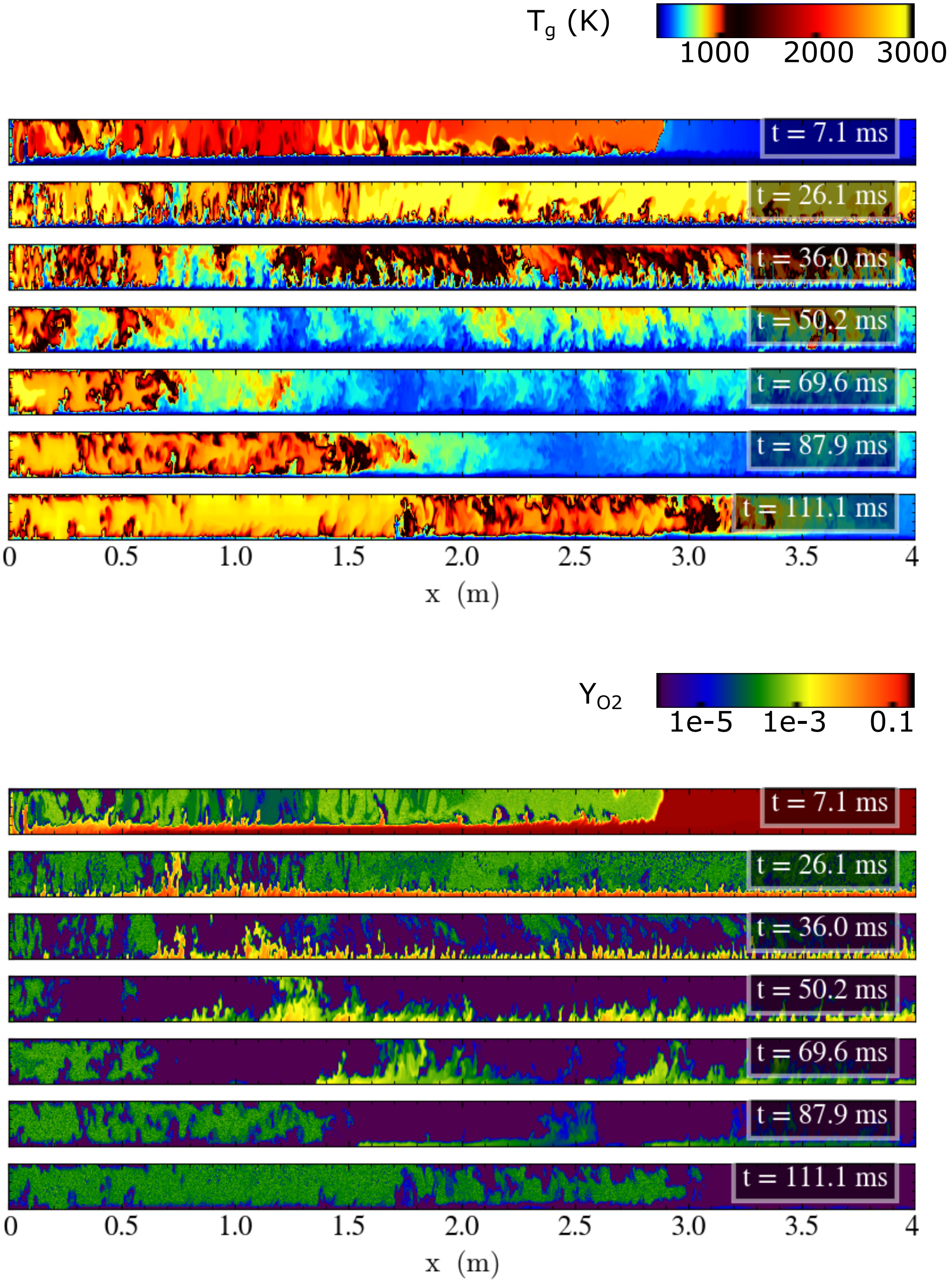

Figure 6-29. Plots of gas temperature and oxygen mass fraction for the 30 μm particle 10-m channel non-radiative case at different times, highlighting the effects of the reflected shock on the thermal and chemical equilibrium.

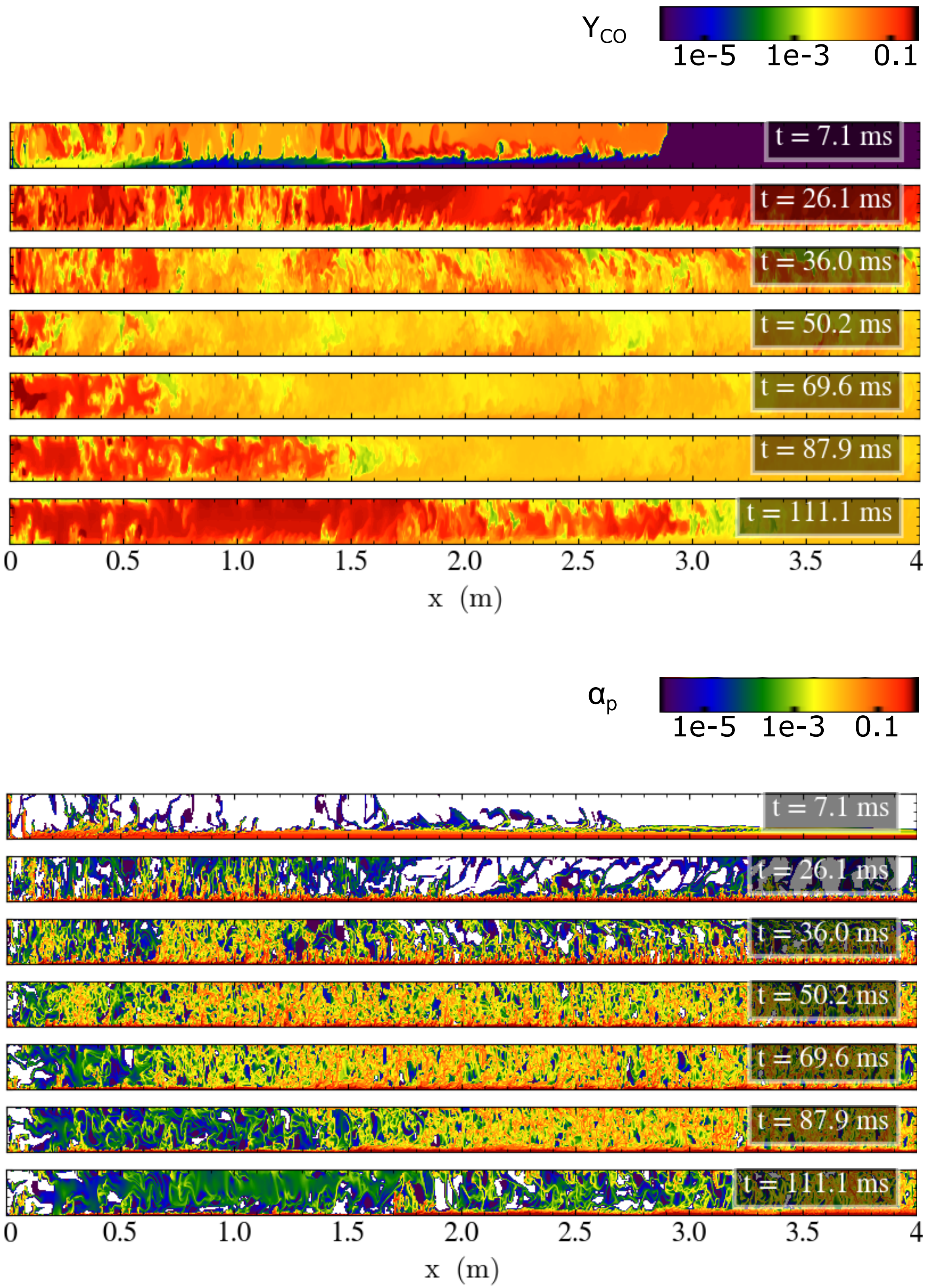

Figure 6-30. Plots of CO mass fraction and particle volume fraction for the 30 μm particle 10-m channel non-radiative case at different times, highlighting the effects of the reflected shock on the thermal and chemical equilibrium.

This reignition is observed only in small patches where the high-temperature pockets remain after the reflected shock passes through them. Nevertheless, the only two regions which show significant reignitions are the left boundary and the 8-m mark in the channel. Reignitions are also observed in the cases with different particle sizes, although the 30 μm and 100 μm particle cases showed the most significant effect of this. In these simulations, we can see from Fig. 6-29 and 6-30 that a large amount of carbon monoxide is produced and left after the combustion and very little oxygen remains. As mentioned earlier in Chapter 1, many miners in coal mines die not necessarily from the blast, but from carbon monoxide poisoning and also asphyxiation due to lack of ventilation.

In these simulations, the range of flame velocities was quite varied but generally fall in the 400-900 m/s range, which is consistent with Sapko et al. (2000).

6.6 Conclusions

Layered coal-dust explosions were simulated using computational methods. Several scenarios were investigated both with and without radiation heat transfer. Two different channel lengths of 10 m and 40 m were considered - the first one to see how the reflected shock affects the flame propagation, and the second to check how the flame progresses unhindered. These two-dimensional simulations also considered multiple particle diameters which gave us an idea of the combustibility of particles of different sizes and how radiation affects it. We also compared two reaction mechanisms - one with a 1-step reaction, and the other with a 2-step reaction. For the 1-step reaction mechanism, we studied a loosely packed case with a 1% initial volume fraction. The rest of the simulations used an initial particle volume fraction of 47%, which is typically found in coal mines.

The simulation results show that vital flame parameters, such as flame temperature, velocity, and structure, are often substantially different for the cases considering radiation compared to those that neglect radiation. Due to the complex and non-linear behavior of radiation, the influence it has on these parameters can however be opposite, and it is almost impossible to predict whether it will enhance or inhibit the flame propagation. In some cases, radiation causes the flame to stagnate/quench, whereas, in most of the other cases, radiation increased the combustion rate and accelerated the flames by the process of pre-heating the particles. This in turn increases the severity of the explosion. As seen with most of the radiative cases, the gauge pressure and impulse values are considerably higher than the non-radiative cases which shows how much more destructive these cases can be.

In general, we can conclude that in cases where there is sufficient combustion occurring, radiation almost always promotes flame propagation. On the contrary, for cases in which the particles are more difficult to ignite, radiation seems to inhibit flame propagation. This was also seen to be true for the 1-step reaction mechanism tests. However, the ability of the particles to absorb radiation is also important. As seen with the 150 μm particles, radiation prominently enhanced the burning of the particles and thus the flame propagation, even though these particles were particularly difficult to ignite.

The effect the reflected shock has on the thermal and chemical equilibrium of the system suggests that there is a significant difference between the two chemical reaction mechanisms. The single-step reaction mechanism cases all showed signs of either quenching (except the dilute cases). The two-step mechanism cases showed no quenching (except for particles that are difficult to ignite). In addition, the single-step reaction mechanism cases showed no signs of reignition either since CO_2 dissociation is not accounted for. However, with the two-step reaction mechanism, most of the short channel cases exhibited the reignition phenomena, albeit with varying intensities depending on the particle size. It would be interesting to see how different the results would be when using detailed chemistry models.

CHAPTER 7
THREE-DIMENSIONAL SIMULATIONS RESULTS AND DISCUSSION

From the two-dimensional simulation results, many key differences between radiative and non-radiative cases became apparent. However, one of the major limitations of 2-D simulations is their inability to properly demonstrate the effect of turbulence. Turbulence is a key factor in the mixing of the particles with air and this mixing is essential for the combustion of the particles. Without mixing, the particle concentrations are too high to be combustible. To explore the effects actual 3-D turbulence can have on the propagation of these coal-dust flames, we performed full 3-D simulations with radiation.

7.1 Problem Description

All 3-D simulations were run using the two-step reaction mechanism. The initial and boundary conditions are almost identical to the 2-D two-step reaction mechanism simulations (Fig. 5-1) with some minor exceptions. Due to the gigantic number of computational cells, and thus computational time, the full 3-D version of the 2-D cases would require, we had to shorten the channel length to 5 m instead of the 10 m which was used for the shorter channel 2-D cases. We also reduced the refinement levels to 2 from the original 3 that were used for the 2-D cases. Thus at the most refined level, the $\Delta x \sim 781\ \mu m$. The depth of the channel in the z-direction is 5 cm, which is the same as the channel height. Both boundary conditions in the z-direction were made periodic, which applies to both the hydrodynamic and the radiation solvers. We also performed a 2-D version of the same case to be able to compare exactly the differences between the 2-D and 3-D versions of the same test. The only major difference between this 2-D (de-refined and shorter channel) case and the 3-D case is that the initial hotspots for the 3-D version were spherical instead of the cylindrical shape which would be the exact 3-D version of 2-D case. The reason for the spherical shape for the hotspots is to generate perturbations in the z-direction from the very beginning, which could otherwise be symmetric for a long time before the randomness of turbulence could influence the z-direction variations. The downside of this is that the initial energy generated by the detonation of the hotspots is much lower than it would be for the cylindrical hotspots. However, as we will see in the results section, this does not have a major impact on the propagation of the dust flame.

The only differences with the simulation parameters for the 3-D case are the radiation CFL number and number of iterations. The radiation CFL was reduced to 0.25 from the original 0.5 used in the 2-D cases. This is to account for the inclusion of the third direction. The number of iterations required to reach the steady-state should also increase proportionally. Therefore, the number of iterations was increased to 200 from the original 100. Everything else was kept the same. The computational cost of these 3-D simulations is about 82,944 CPU hours to reach a simulation time of ∼38 ms (∼ 108,000 time steps with a CFL number of 0.7 for the parabolic and hyperbolic terms).

7.2 Results

Fig. 7-1 shows the shock and flame positions along with the total chemical heat release rates for the 2-D and 3-D radiative cases. The heat release rates for the 3-D case were divided by 0.05 m (the channel width) which gives the heat release rate per unit length in the z-direction. This enables us to compare the heat release rates for the two cases properly and with the correct units. It is immediately obvious how much energy is lost due to the spherical shape of the hotspots. The initial peak energy release for the 2-D case is ∼105 GW/m and for the 3-D case, it is ∼28 GW/m. If we look at the energy density per unit volume of the hotspots, the two cases are exactly equal. The initial hotspot volume for a 3-D equivalent of the 2-D case is

$$\pi R^2 h + \frac{\pi R^2 h}{2} = 23.56 \times 10^{-6}\ \text{m}^3, \tag{7-1}$$

and for the spherical hotspots in the actual 3-D case is

$$\frac{4}{3}\pi R^2 h + \frac{4}{3}\frac{\pi R^2 h}{2} = 6.28 \times 10^{-6}\ \text{m}^3, \tag{7-2}$$

where R is the hotspot radius = 1 cm and h is the depth in the z-direction = 5 cm. The volume ratio between the two is then ∼3.75:1, which is also exactly the ratio between the initial peak heat release rates for the 2-D and 3-D cases. As a result, it is understandable that the shock and flame speeds are lower for the 3-D cases (Fig. 7-2). However, the flame lags behind the shock by almost the same distance of ∼1 m (at t = 5 ms) for both cases.

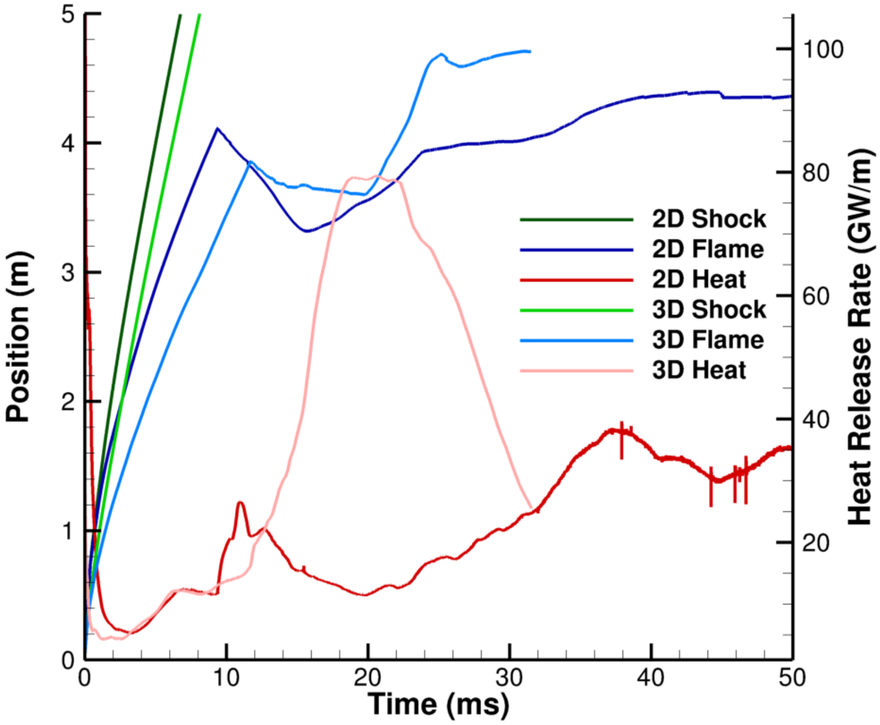

Figure 7-1. Shock and flame positions and heat release rates due to chemical reactions for the 5-m channel 2-D and 3-D radiative cases using the 2-step reaction mechanism.

The flame propagation behaves in almost the same way for both cases before the reflected shock starts to interact with the flame. In the 2-D simulation, the heat release rate remains relatively steady once the reflected shock passes over the flames. There is a steady increase in the heat release rate after an initial dip. On the other hand, for the 3-D case, there is a sharp increase in the heat release rate right after the reflected shock reaches the flame front (∼12 ms). The heat release rate keeps rising till ∼20 ms to ∼80 GW/m, remains flat for a while, and then decreases sharply. The flame front is seen to move ahead in this time almost right up to the right boundary, which is further than in the 2-D case.

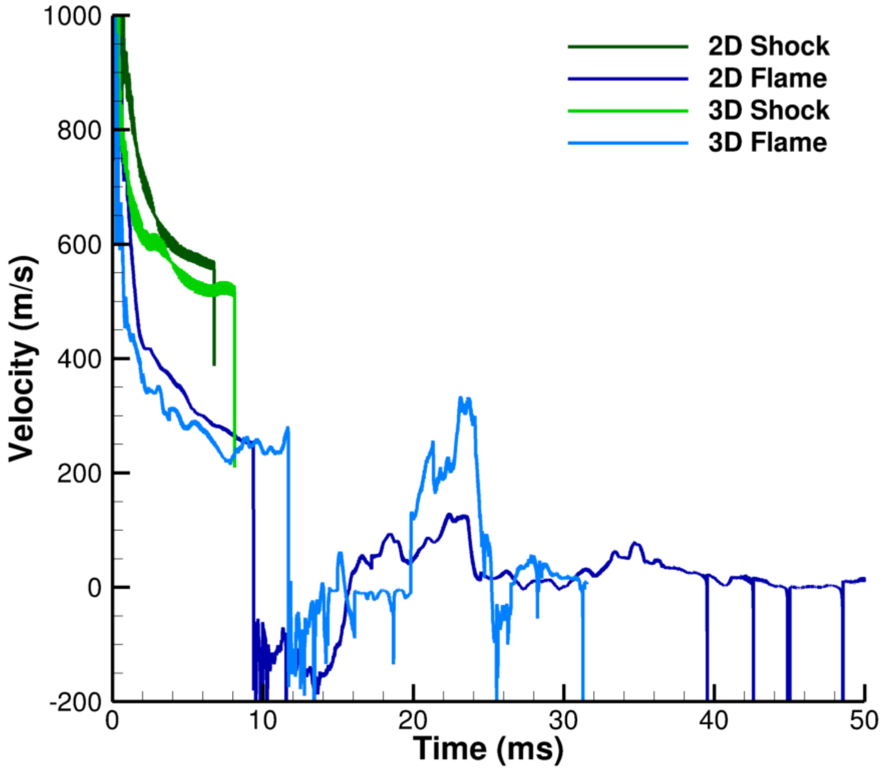

Figure 7-2. Shock and flame velocities for the 5-m channel 2-D and 3-D radiative cases using the 2-step reaction mechanism.

The gauge pressure (Fig. 7-3) and impulse (Fig. 7-4) plots show how different the practical effects of this increase in heat release rate for the 3-D case can be. As soon as the heat release rate starts to climb (∼12 ms), we see that the gauge pressures for the 3-D case also start rising. The gauge pressures for the 2-D cases are relatively more flat after the reflected shock interaction with the flames. Toward the end of the simulation, the gauge pressures for the 3-D case are significantly higher (more than 2 atm) than the same for the 2-D case. A similar trend can be noticed in the impulse plots as well. The 3-D case has impulse values more than 2 kN.s higher than the 2-D case.

7.3 Discussion

It is evident from the comparison of the 2-D and 3-D cases that there is a significant difference between them. Though the initial hotspot energy for the 3-D case is much smaller than the 2-D case, the heat release rate, gauge pressure, and impulse plots suggest that 2-D cases underestimate the destructive power of these dust explosions. The X-t plots in Fig. 7-5

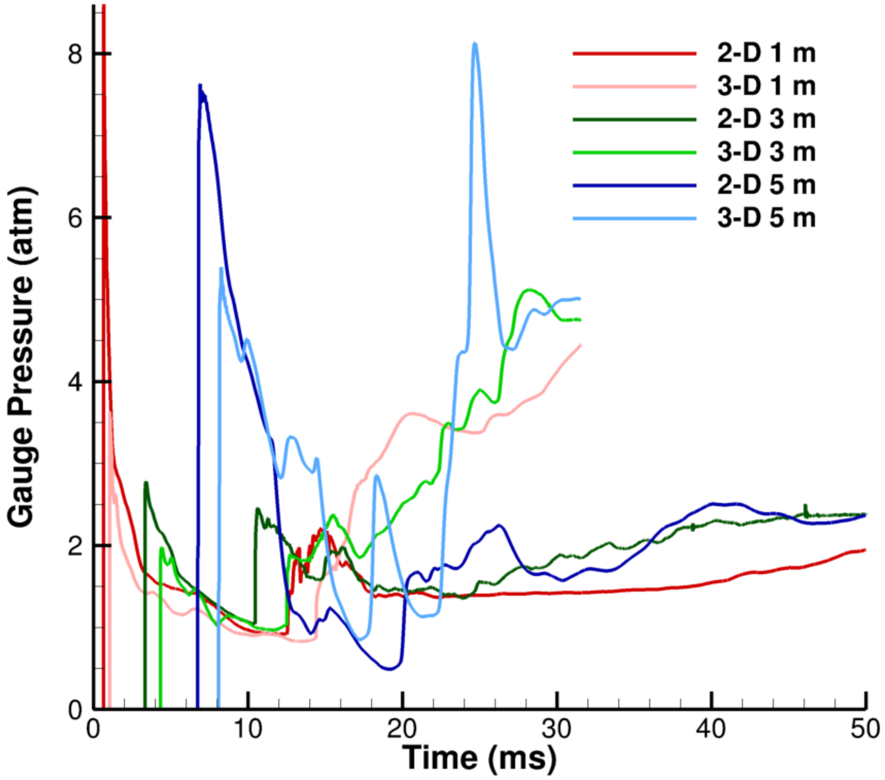

Figure 7-3. Gauge pressure plots for the 5-m channel 2-D and 3-D radiative cases using the 2-step reaction mechanism at locations of 1 m, 3 m and 5 m in the channel, and at a height and depth of 2.5 cm each.

and 7-6 also show that a higher amount of combustion takes place in the 3-D simulations, especially after the reflected shock interacts with the flame. It is also interesting to note that after the reflected shock passes over the flames, these regions burn at a higher temperature in the 3-D case compared to the 2-D case.

Fig. 7-7 and 7-8 show the plots of gas temperatures, particle volume fractions and incident radiation for the 2-D and 3-D cases respectively. In the 2-D case, the columns of particle streamers, which are lines of locally higher particle volume fraction (Houim and Oran, 2016), attenuate the radiation and practically block it. These structures have been observed in both experiments as well as computations (Agrawal et al., 2001; Helland et al., 2000; Horio and Kuroki, 1994; Igci et al., 2008). Just a couple of centimeters ahead of the flame, the radiation becomes too weak to heat particles ahead of the flame. However, in 3-D, despite the presence of particle streamers, the radiation can propagate much further to almost half

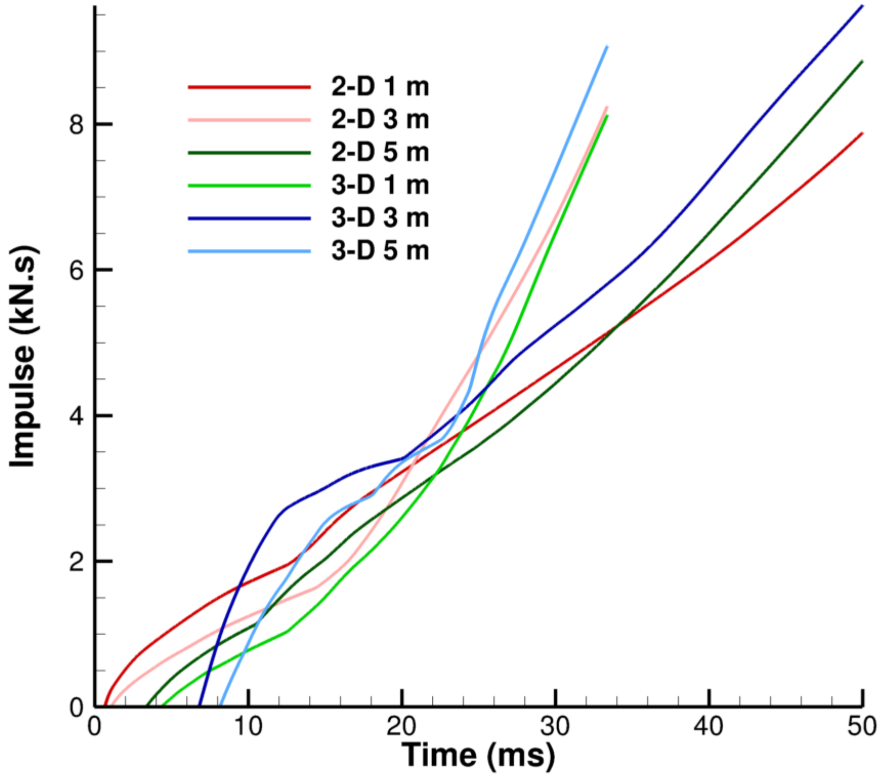

Figure 7-4. Impulse plots for the 5-m channel 2-D and 3-D radiative cases using the 2-step reaction mechanism at locations of 1 m, 3 m and 5 m in the channel, and at a height and depth of 2.5 cm each.

a meter ahead of the flame front. This happens because in 2-D, a stream of particles are sheets that cover the entire width of the channel. It forms like a wall or curtain and acts as an almost opaque object. In 3-D however, these particle streamers are thin line structures and not sheets(due to the variation in the z-direction). These produced gaps where radiation is able to pass through. This radiation in turn heats the particles ahead of the flame and prepares them for combustion. This is also an important reason why the 3-D flame travels further ahead than the 2-D flame. Fig. 7-9 shows the slice plots of the particle volume fractions for the 3-D case at ∼30 ms. Fig. 7-9(a) shows the a slice of the y-z plane at x = 4.6 m, and (b) shows a slice of the x-y plane at z = 2.5 cm. In these plots the particle streamers are clearly visible, but we can also see the gaps in the volume fractions where radiation can pass through.

Another reason for the enhanced combustion in the 3-D case can be attributed to the enhanced mixing of the particles and air by turbulence induced by the reflected shock. In 3-D,

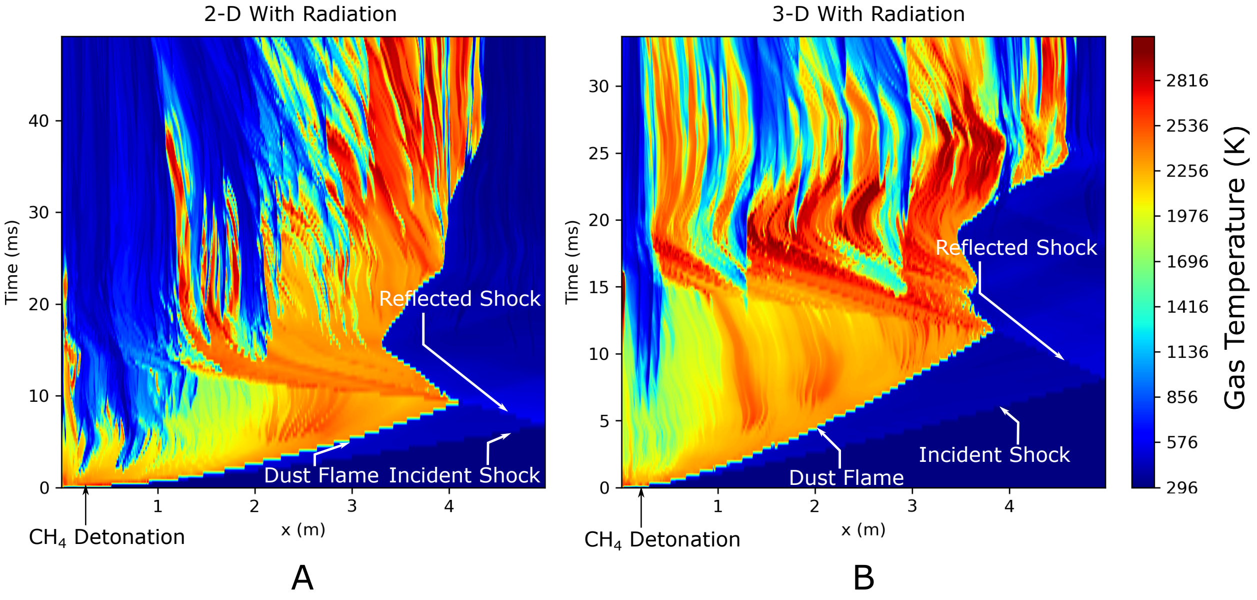

Figure 7-5. X-t diagram for the 5-m long channel shaded by gas phase temperature at y = 2.5 cm with the 2-step reaction mechanism for the 2-D and 3-D simulations. A) 2-D. B) 3-D.

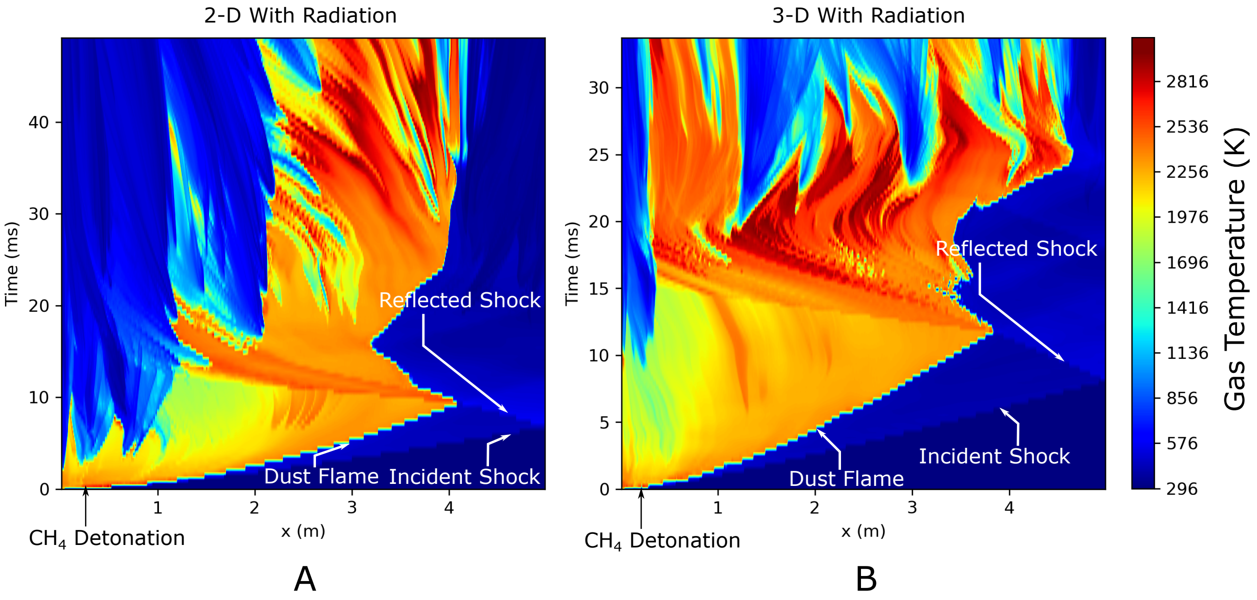

Figure 7-6. X-t diagram for the 5-m long channel shaded by gas phase temperature at y = 5 cm with the 2-step reaction mechanism for the 2-D and 3-D simulations. A) 2-D. B) 3-D.

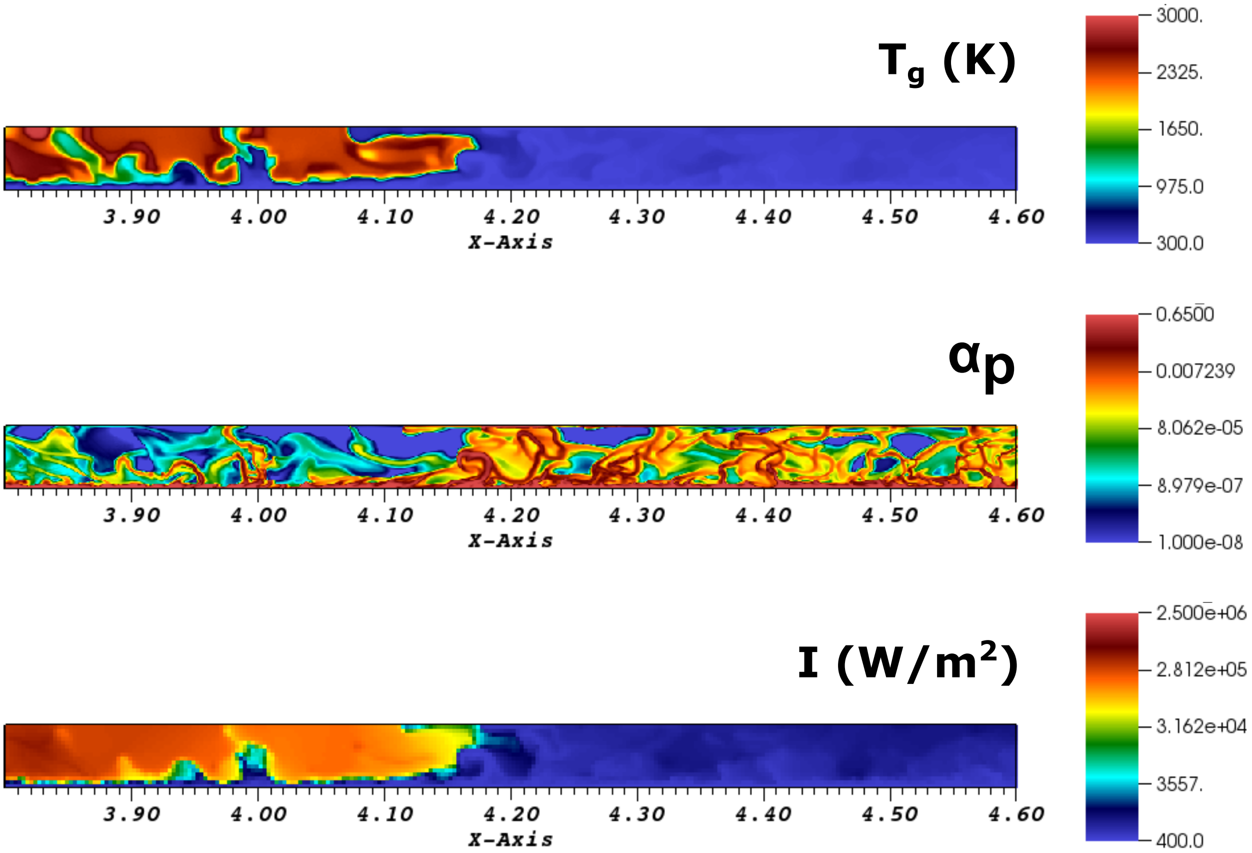

Figure 7-7. Plots of gas temperature, particle volume fraction and incident radiation for the 5-m long channel 2-D case with the 2-step reaction mechanism at t $\sim$ 35 ms.

turbulence is much more effective in mixing the particles with the air. Also, the reflected shock does not lose as much energy from drag as in the 2-D case, due to the presence of gaps in the particle clouds. This results in the higher temperatures observed in the combustion zones after the reflected shock passes through them.

7.4 Conclusions

Multidimensional layered coal-dust explosions were simulated using computational methods to compare the differences between 2-D and 3-D versions of the same test case. Channel lengths of 5 m were considered for both the 2-D and the 3-D tests, along with the two-step reaction mechanism for the homogeneous reactions (gas phase), and a particle diameter of 30 μm. A particle volume fraction of 47% was considered for these simulations.

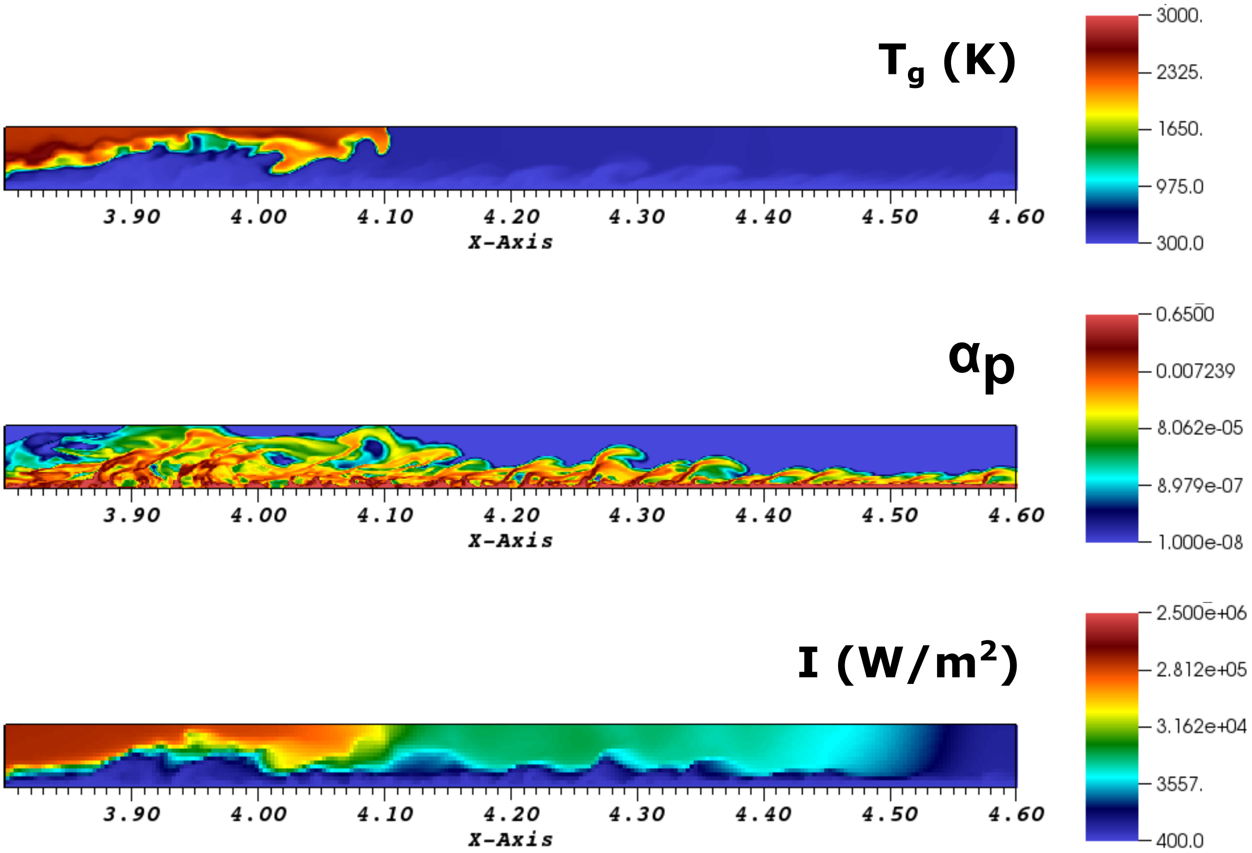

Figure 7-8. Plots of gas temperature, particle volume fraction and incident radiation for the 5-m long channel 3-D case with the 2-step reaction mechanism at t ∼ 23 ms.

The results indicate that there can be several differences between the 2-D and 3-D versions of the same case, though the overall flame propagation characteristics are similar. Most of the differences become obvious only after the reflected shock interacts with the flame. Before that, the general flame characteristics are quite similar (with the exception that the 3-D case has much lower initial energy due to the smaller size of the detonating hotspots, which causes the shock and the flame to propagate slower than in the 2-D case). After the reflected shock interacts with the flame, however, the scenarios are more different than alike. The combusting regions in the 3-D case burn at a higher temperature than those in the 2-D case. The reflected shock also enhances the mixing and loses less energy from drag with the particles, which both contribute to the increase in the flame temperatures. Just ahead of the flame front, the radiation is able to propagate much further, which causes pre-heating

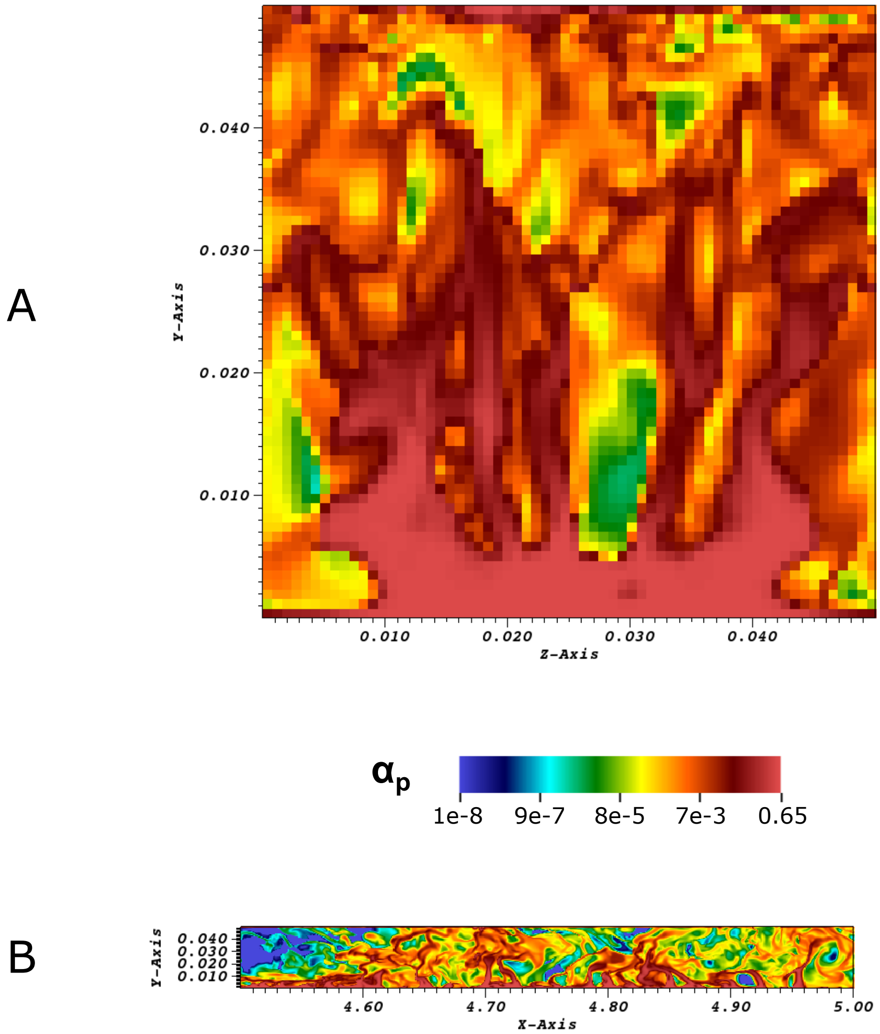

Figure 7-9. Slice plots of particle volume fraction for the 5-m long channel 3-D case with the 2-step reaction mechanism at t $\sim$ 30 ms. A) The y-z plane at x = 4.6 m. B) The x-y plane at z = 2.5 cm. This gives us an idea of what the particle streamers look like in 3-D.

of the particles, and thus the flame is also able to propagate closer to the right boundary. Furthermore, impulse and gauge pressure plots suggest that the destructive power of the dust explosions is underestimated by the 2-D simulations.

We are currently performing 3-D non-radiative simulations of the same test scenario and are awaiting the results. In the future, we would like to investigate the effects of particle size, reaction mechanism, and spectrally accurate radiation models, along with the full 3-D simulations, though such simulations would require an immense amount of computational power.

CHAPTER 8
OVERALL CONCLUSIONS AND FUTURE WORK

8.1 Conclusions

In this research work, we ran several multidimensional unsteady simulations of coal-dust explosions. For this purpose, different chemical reaction mechanisms for both the gas and solid phases were implemented, along with a variable specific heat fluid model, as well as transport and thermodynamic properties for the gas phase were added. For the three-dimensional test cases, we also implemented the filtered spherical harmonics approximation (FP_n) to the radiative transport equation (RTE) in 3-D. Radiation heat transfer is often neglected when simulating dust explosions, and thus no previous work has carried out simulations on coal-dust explosions including the effects of radiation on such a large scale.

To perform these simulations, we solved the reactive, compressible, Navier-Stokes equations, coupled to an Eulerian kinetic-theory-based granular multiphase model. We make the continuum assumption (Eulerian-Eulerian) for both the gas and the solid phases. Radiation was assumed to be gray and the boundary conditions for radiation were all assumed to be cold (300 K) and black. Both the gas and granular phase reaction mechanisms are based on global reactions for each physical process such as devolatilization, char combustion, moisture evaporation, as well as methane combustion. We used high-order Godunov methods to solve the resulting governing equations. Different test configurations were chosen to explore the effects of channel length, reaction mechanism, particle size, and dimensionality (2-D or 3-D). For most of the simulations, a layer volume fraction of 47% was used, although we also performed a few simulations with a volume fraction of 1%. For each of these cases, we performed two simulations - one with radiation and the other with radiation turned off.

The effect of radiation on coal-dust explosions is difficult to generalize. Radiation is a highly non-linear phenomenon and the coupling of radiation to the hydrodynamic solver makes things much more complicated. Thus, the observations made in this research are varied. In many cases, radiation is seen to enhance flame propagation and increase explosion severity. In some cases, however, radiation heat losses dominate, and therefore radiation has the exact opposite effect on flame propagation and explosion severity. After looking at numerous cases, we observed a trend. When the particles are easily combustible (both due to their size, dispersibility into the core flow, and the type of reaction mechanism being used), radiation almost always accelerates the flame and shock and causes higher gauge pressures and impulse than their non-radiative counterparts. Conversely, when particles are difficult to ignite, radiation losses can be more severe than the particle's ability to absorb the radiation, which reduces the flame temperature, propagation speed, and thus the impact of the explosion is lesser than when radiation is included. However, how much the particles can get lifted into the channel during mixing caused by the leading shock, can also have a major impact on the amount of radiation the particles can absorb (as seen in the case of the 150 μm particles). Due to this complex interaction of radiation with the other fluid-dynamic phenomena, more work is needed to fully understand how radiation will affect the dust explosion.

It is undeniable that the differences between the radiative and non-radiative cases are significant. Irrespective of whether radiation increases or reduces the explosion severity, not accounting for radiation heat transfer has been shown to produce quite different results. In nature, there is practically no scenario where radiation can be turned off like in our simulations. Radiation is always present and will always play a role in dust explosions, it is just a matter of significance. In the past, it has been often debated that the effect of radiation is not important enough to justify the huge computational costs it comes with. In this research, however, it was observed that radiation indeed has a substantial impact on important bulk parameters such as the flame temperature, flame speed, overall structure of the flame, overpressures caused by the explosions, etc. As an extreme example, it is evident that the reflected shock interacting with the flame for the radiative case with 150 μm particles enhanced combustion by a substantial amount, whereas for the non-radiative case, the flames were highly feeble and unstable even after the shock reflection. The gauge pressures and impulse values were off by a factor of more than four. Thus, neglecting radiation severely underestimates the destructive nature of this explosion. Though some cases showed less of a difference than such extreme cases, the differences are still large enough to conclude the need to account for radiation in dust explosion simulations. In explosion safety, it is often assumed that dust explosions behave in a similar way to gas explosions. However, as seen in this research, unlike gas explosions, radiation has a serious impact on dust explosions since dispersed dust particles can promote or inhibit the explosion severity by enhanced heat exchange due to thermal radiation. Consequently, methods of mitigating dust explosions may need to be revised.

8.2 Recommendations for Future Work

This work assumed gray radiatio. Spectrally accurate radiation models (k-distribution) need to be developed and tested to understand the validity of this assumption. It was also observed that the choice of chemical reaction mechanism can have a major impact on the overall results. The differences between results from the single-step and the two-step reaction mechanisms necessitate the need to study such coal-dust explosion scenarios using detailed reaction mechanisms.

In our simulations, we have used only monodisperse particles. The ability to include polydisperse particles can open up a world of possibilities where simulations that are closer to the actual coal mine explosion scenarios can be studied. It was also observed that three-dimensional simulations account for turbulence and particle streaming effects that two-dimensional simulations are unable to do. Thus, in an ideal scenario, the possibility to perform simulations in 3-D, with detailed chemistry, spectrally accurate radiation model, and polydisperse particles would be the ultimate achievement in this field of research. Practically though, such simulations would likely require more than a hundred thousand processors and would have to be run for a very long time to be able to extract any useful data.

REFERENCES

"Cantera users guide - methane/air combustion." 2017a.

URL https://www.cerfacs.fr/cantera/mechanisms/meth.php

"Single-step Methane-air Reaction Mechanism." http://www.cerfacs.fr/cantera/docs/mechanisms/methane-air/GLOB/CANTERA/1S_CH4_MP1.cti, 2017b.

Agrawal, Kapil, Loezos, Peter N., Syamlal, M., and Sundaresan, S. "The role of meso-scale structures in rapid gas–solid flows." *Journal of Fluid Mechanics* 445 (2001): 151 – 185.

Amyotte, Paul R. and Eckhoff, Rolf K. "Dust explosion causation, prevention and mitigation: An overview." *Journal of Chemical Health and Safety* 17 (2010).1: 15 – 28.

URL http://www.sciencedirect.com/science/article/pii/S1871553209000577

Anthony, Donald B. and Howard, Jack B. "Coal devolatilization and hydrogastification." *AIChE Journal* 22 (1976).4: 625–656.

URL https://aiche.onlinelibrary.wiley.com/doi/abs/10.1002/aic.690220403

Badzioch, Stanley and Hawksley, Peter G. W. "Kinetics of Thermal Decomposition of Pulverized Coal Particles." *Industrial & Engineering Chemistry Process Design and Development* 9 (1970).4: 521–530.

URL https://doi.org/10.1021/i260036a005

Baek, S.W., Sichel, M., and Kauffman, C.W. "Asymptotic analysis of the shock wave ignition of dust particles." *Combustion and Flame* 81 (1990).3: 219 – 228.

URL http://www.sciencedirect.com/science/article/pii/001021809090020R

Bakke, JR, van Wingerden, Kees, et al. "Guidance for designing offshore modules evolving from gas explosion research." *SPE Annual Technical Conference and Exhibition*. Society of Petroleum Engineers, 1992.

Bell, George I and Glasstone, Samuel. "Nuclear reactor theory." Tech. rep., US Atomic Energy Commission, Washington, DC (United States), 1970.

Bidabadi, Mehdi and Azad, Abazar Vahdat. "Effects of radiation on propagating spherical flames of dust–air mixtures." *Powder Technology* 276 (2015): 45 – 59.

URL http://www.sciencedirect.com/science/article/pii/S0032591014010262

Bielert, U and Sichel, M. "Numerische Simulation von Staubexplosionen in pneumatischen Saug-Flug-Forderanlagen." *VDI BERICHTE* 1601 (2001): 449–472.

Blokh, A. "The problem of flame as a disperse system." *Heat Transfer in Flames* 2 (1974): 111.

Blokh, AG and Burak, LD. “PRIMARY RADIATION CHARACTERISTICS OF CHIEF TYPES OF SOLID FUEL.” *Thermal Engineering* 20 (1973).8: 65–70.

Boiko, VM, Papyrin, AN, Wolinski, H, and Wolanski, P. “Dynamics of dispersion and ignition of dust layers by a shock wave.” *Dynamics of Shock Waves, Explosions, and Detonations,(Bowen, JR, Hanson, N., Oppenheim, AK and Soloukhin, RI, Eds.), Progress in Astronautics and Aeronautics, AIAA, New York* 94 (1984): 293–301.

Bradley, D., Chen, Z., El-Sherif, S., Habik, S. El-Din, John, G., and Dixon-Lewis, G. “Structure of laminar premixed carbon methane-air flames and ultrafine coal combustion.” *Combustion and Flame* 96 (1994).1: 80 – 96.

URL http://www.sciencedirect.com/science/article/pii/0010218094901600

Bradley, D., Lawes, M., Park, Ho-Young, and Usta, N. “Modeling of laminar pulverized coal flames with speciated devolatilization and comparisons with experiments.” *Combustion and Flame* 144 (2006).1: 190 – 204.

URL http://www.sciencedirect.com/science/article/pii/S001021800500194X

Breipohl, G, Lester, TW, and Merklin, JF. “Shock tube studies of the mechanism of grain dust ignition.” *Proceedings Symposium (International) on Grain Dust*. 1979, 191–211.

Brewster, B. Scott, Baxter, Larry L., and Smoot, L. Douglas. “Treatment of coal devolatilization in comprehensive combustion modeling.” *Energy & Fuels* 2 (1988).4: 362–370.

URL https://doi.org/10.1021/ef00010a001

Brilliantov, Nikolai V and Pöschel, Thorsten. *Kinetic theory of granular gases*. Oxford University Press, 2010.

Brunner], Thomas [A. and Holloway], James [Paul. “One-dimensional Riemann solvers and the maximum entropy closure.” *Journal of Quantitative Spectroscopy and Radiative Transfer* 69 (2001).5: 543 – 566.

URL http://www.sciencedirect.com/science/article/pii/S0022407300000996

Brunner, Thomas A. and Holloway, James Paul. “Two-dimensional time dependent Riemann solvers for neutron transport.” *Journal of Computational Physics* 210 (2005).1: 386 – 399.

URL http://www.sciencedirect.com/science/article/pii/S0021999105002275

Brunner, Thomas Andrew. *Riemann solvers for time-dependent transport based on the maximum entropy and spherical harmonics closures*. Ph.D. thesis, University of Michigan, 2000.

Brzustowski, Thomas A. and Glassman, Irvin. “Spectroscopic Investigation of Metal Combustion.” *Heterogeneous Combustion*. eds. Hans G. Wolfhard, Irvin Glassman, and Leon Green, vol. 15 of *Progress in Astronautics and Rocketry*. Elsevier, 1964. 41 – 73.

URL http://www.sciencedirect.com/science/article/pii/B9781483227306500087

Buckius, R. O. and Hwang, D. C. "Radiation Properties for Polydispersions: Application to Coal." *Journal of Heat Transfer* 102 (1980).1: 99–103.

URL https://doi.org/10.1115/1.3244256

Cao, Weiguo, Gao, Wei, Liang, Jiyuan, Xu, Sen, and Pan, Feng. "Flame-propagation behavior and a dynamic model for the thermal-radiation effects in coal-dust explosions." *Journal of Loss Prevention in the Process Industries* 29 (2014a): 65 – 71.

URL http://www.sciencedirect.com/science/article/pii/S0950423014000254

Cao, Weiguo, Gao, Wei, Peng, Yuhuai, Liang, Jiyuan, Pan, Feng, and Xu, Sen. "Experimental and numerical study on flame propagation behaviors in coal dust explosions." *Powder Technology* 266 (2014b): 456 – 462.

URL http://www.sciencedirect.com/science/article/pii/S003259101400607X

Cashdollar, Kenneth L. "Overview of dust explosibility characteristics." *Journal of Loss Prevention in the Process Industries* 13 (2000).3: 183 – 199.

URL http://www.sciencedirect.com/science/article/pii/S095042309900039X

Chang, Chih-Hao and Liou, Meng-Sing. "A robust and accurate approach to computing compressible multiphase flow: Stratified flow model and AUSM+-up scheme." *Journal of Computational Physics* 225 (2007).1: 840 – 873.

URL http://www.sciencedirect.com/science/article/pii/S0021999107000071

Cloney, Chris T., Ripley, Robert C., Pegg, Michael J., and Amyotte, Paul R. "Laminar burning velocity and structure of coal dust flames using a unity Lewis number CFD model." *Combustion and Flame* 190 (2018): 87 – 102.

URL http://www.sciencedirect.com/science/article/pii/S0010218017304492

Collins, JP, Ferguson, RE, Chien, K, Kuhl, AL, Krispin, J, and Glaz, HM. "Simulation of shock-induced dusty gas flows using various models." *AIAA, Fluid Dynamics Conference, 25 th, Colorado Springs, CO*. 1994.

Dahoe, A.E., Hanjalic, K., and Scarlett, B. "Determination of the laminar burning velocity and the Markstein length of powder–air flames." *Powder Technology* 122 (2002).2: 222 – 238. Special issue i in Honour of Prof Jimbo.

URL http://www.sciencedirect.com/science/article/pii/S0032591001004193

Droujko, J, Julien, P, Soo, M, Goroshin, S, Bergthorson, JM, Frost, DL, and Glumac, N. "The role of radiative preheating on flame propagation in aluminum dust clouds." *Proceedings of the 11th International Symposium on Hazards, Prevention, and Mitigation of Industrial Explosions*. 2016, 435–448.

Edwards, J.C. and Ford, K.M. “Model of coal-dust explosion suppression by rock dust entrainment. Report of Investigations/1988.” (1988).

Einfeldt, B, Munz, C.D, Roe, P.L, and Sjögreen, B. “On Godunov-type methods near low densities.” *Journal of Computational Physics* 92 (1991).2: 273 – 295.

URL http://www.sciencedirect.com/science/article/pii/0021999191902113

Ern, Alexandre and Giovangigli, Vincent. *Multicomponent transport algorithms*, vol. 24. Springer Science & Business Media, 1994.

Fedorov, AV, Kharlamova, Yu V, et al. “Reflection of a shock wave in a dusty cloud.” *Combustion, Explosion, and Shock Waves* 43 (2007).1: 104–113.

Foster, P.J. and Howarth, C.R. “Optical constants of carbons and coals in the infrared.” *Carbon* 6 (1968).5: 719 – 729.

URL http://www.sciencedirect.com/science/article/pii/000862236890016X

Frank, Martin, Hauck, Cory, and Kuepper, Kerstin. “Convergence of filtered spherical harmonic equations for radiation transport.” *Communications in Mathematical Sciences* 14 (2016).5: 1443–1465.

Franzelli, Benedetta, Riber, Eleonore, Gicquel, Laurent Y.M., and Poinsot, Thierry. “Large Eddy Simulation of combustion instabilities in a lean partially premixed swirled flame.” *Combustion and Flame* 159 (2012).2: 621 – 637.

URL http://www.sciencedirect.com/science/article/pii/S0010218011002525

Friedman, Raymond and Burke, Edward. “Measurement of Temperature Distribution in a Low-Pressure Flat Flame.” *The Journal of Chemical Physics* 22 (1954).5: 824–830.

URL https://doi.org/10.1063/1.1740197

Gamezo, Vadim N, Khokhlov, Alexei M, and Oran, Elaine S. “The influence of shock bifurcations on shock-flame interactions and DDT.” *Combustion and Flame* 126 (2001).4: 1810 – 1826.

URL http://www.sciencedirect.com/science/article/pii/S0010218001002917

Gamezo, Vadim N., Ogawa, Takanobu, and Oran, Elaine S. “Flame acceleration and DDT in channels with obstacles: Effect of obstacle spacing.” *Combustion and Flame* 155 (2008).1: 302 – 315.

URL http://www.sciencedirect.com/science/article/pii/S0010218008001934

Gavalas, George R., Cheong, Paul How-Kei, and Jain, Ravi. “Model of coal pyrolysis. 1. Qualitative development.” *Industrial & Engineering Chemistry Fundamentals* 20 (1981).2: 113–122.

URL https://doi.org/10.1021/i100002a001

Gidaspow, Dimitri. *Multiphase flow and fluidization: continuum and kinetic theory descriptions*. Academic press, 1994.

Goodwin, David G., Moffat, Harry K., and Speth, Raymond L. “Cantera: An Object-oriented Software Toolkit for Chemical Kinetics, Thermodynamics, and Transport Processes.” http://www.cantera.org, 2017. Version 2.3.0.

Goshayeshi, Babak and Sutherland, James C. “A comparison of various models in predicting ignition delay in single-particle coal combustion.” *Combustion and Flame* 161 (2014).7: 1900 – 1910.

URL http://www.sciencedirect.com/science/article/pii/S0010218014000157

Grant, David M., Pugmire, Ronald J., Fletcher, Thomas H., and Kerstein, Alan R. “Chemical model of coal devolatilization using percolation lattice statistics.” *Energy & Fuels* 3 (1989).2: 175–186.

URL https://doi.org/10.1021/ef00014a011

Grosshandler, William L. “RADCAL: a Narrow-band Model for Radiation.” *Calculations in a Combustion Environment, NIST Technical Note* 1402 (1993).

Gunn, D.J. “Transfer of heat or mass to particles in fixed and fluidised beds.” *International Journal of Heat and Mass Transfer* 21 (1978).4: 467 – 476.

URL http://www.sciencedirect.com/science/article/pii/0017931078900807

Haff, P. K. “Grain flow as a fluid-mechanical phenomenon.” *Journal of Fluid Mechanics* 134 (1983): 401–430.

Haghiri, Ali and Bidabadi, Mehdi. “Modeling of laminar flame propagation through organic dust cloud with thermal radiation effect.” *International Journal of Thermal Sciences* 49 (2010).8: 1446 – 1456.

URL http://www.sciencedirect.com/science/article/pii/S1290072910000852

Helland, Eivind, Occelli, René, and Tadrist, Lounès. “Numerical study of cluster formation in a gas–particle circulating fluidized bed.” *Powder Technology* 110 (2000).3: 210–221.

URL https://www.sciencedirect.com/science/article/pii/S0032591099002600

Hesthaven, Jan and Kirby, Robert. “Filtering in Legendre spectral methods.” *Mathematics of Computation* 77 (2008).263: 1425–1452.

Hjertager, B.H., Fuhre, K., and Bjørkhaug, M. “Gas explosion experiments in 1:33 and 1:5 scale offshore separator and compressor modules using stoichiometric homogeneous fuel/air clouds.” *Journal of Loss Prevention in the Process Industries* 1 (1988).4: 197 – 205.

URL http://www.sciencedirect.com/science/article/pii/0950423088850046

Horio, Masayuki and Kuroki, Hiroaki. "Three-dimensional flow visualization of dilutely dispersed solids in bubbling and circulating fluidized beds." *Chemical Engineering Science* 49 (1994).15: 2413–2421.

URL https://www.sciencedirect.com/science/article/pii/0009250994E0071W

Houim, Ryan W. and Kuo, Kenneth K. "A low-dissipation and time-accurate method for compressible multi-component flow with variable specific heat ratios." *Journal of Computational Physics* 230 (2011).23: 8527 – 8553.

URL http://www.sciencedirect.com/science/article/pii/S0021999111004621

Houim, Ryan W and Oran, Elaine S. "Effect of Radiation on the Propagation of Planar Coal Dust Flames in Air." 2015a.

Houim, Ryan W. and Oran, Elaine S. "Numerical simulation of dilute and dense layered coal-dust explosions." *Proceedings of the Combustion Institute* 35 (2015b).2: 2083 – 2090.

URL http://www.sciencedirect.com/science/article/pii/S1540748914001904

———. "Structure and flame speed of dilute and dense layered coal-dust explosions." *Journal of Loss Prevention in the Process Industries* 36 (2015c): 214 – 222.

URL http://www.sciencedirect.com/science/article/pii/S0950423015000169

———. "A multiphase model for compressible granular–gaseous flows: formulation and initial tests." *Journal of Fluid Mechanics* 789 (2016): 166–220.

Igci, Yesim, Andrews IV, Arthur T., Sundaresan, Sankaran, Pannala, Sreekanth, and O'Brien, Thomas. "Filtered two-fluid models for fluidized gas-particle suspensions." *AIChE Journal* 54 (2008).6: 1431–1448.

URL https://aiche.onlinelibrary.wiley.com/doi/abs/10.1002/aic.11481

Johnson, P. C. and Jackson, R. "Frictional–collisional constitutive relations for granular materials, with application to plane shearing." *Journal of Fluid Mechanics* 176 (1987): 67–93.

Julien, Philippe, Vickery, James, Goroshin, Samuel, Frost, David L., and Bergthorson, Jeffrey M. "Freely-propagating flames in aluminum dust clouds." *Combustion and Flame* 162 (2015a).11: 4241–4253.

URL https://www.sciencedirect.com/science/article/pii/S0010218015002540

Julien, Philippe, Vickery, James, Whiteley, Sam, Wright, Alex, Goroshin, Sam, Bergthorson, Jeffrey M., and Frost, David L. "Effect of scale on freely propagating flames in aluminum dust clouds." *Journal of Loss Prevention in the Process Industries* 36 (2015b): 230 – 236.

URL http://www.sciencedirect.com/science/article/pii/S0950423014002381

Kamenetsky, V., Goldshtein, A., Shapiro, M., and Degani, D. "Evolution of a shock wave in a granular gas." *Physics of Fluids* 12 (2000).11: 3036–3049.

URL https://aip.scitation.org/doi/abs/10.1063/1.1287514

Kauffman, C.W., Sichel, M., and Wolanski, P. "Research on dust explosions at the University of Michigan." *Powder Technology* 71 (1992).2: 119–134.

URL https://www.sciencedirect.com/science/article/pii/003259109280002E

Kauffman, CW, Wolanski, P, Ural, E, Nicholls, JA, and Van Dyk, R. "Shock wave initiated combustion of grain dust." *Proceedings Symposium (International) on Grain Dust*. 1979, 164–190.

Kazakov, Andrei and Frenklach, Michael. "Reduced reaction sets based on GRI-Mech 1.2." 1994.

URL http://combustion.berkeley.edu/drm/

Kee, Robert J, Coltrin, Michael E, and Glarborg, Peter. *Chemically reacting flow: theory and practice*. John Wiley & Sons, 2005.

Khmel', T. A. and Fedorov, A. V. "Description of dynamic processes in two-phase colliding media with the use of molecular-kinetic approaches." *Combustion, Explosion, and Shock Waves* 50 (2014a).2: 196–207.

URL https://doi.org/10.1134/S0010508214020117

———. "Modeling of propagation of shock and detonation waves in dusty media with allowance for particle collisions." *Combustion, Explosion, and Shock Waves* 50 (2014b).5: 547–555.

URL https://doi.org/10.1134/S0010508214050104

Khokhlov, A, Domínguez, I, Bacon, C, Clifford, B, Baron, E, Hoeflich, P, Krisciunas, K, Suntzeff, N, and Wang, L. "Three-dimensional Simulations of Thermonuclear Detonation with alpha-Network: Numerical Method and Preliminary Results." *Advances in Computational Astrophysics: Methods, Tools, and Outcome*. vol. 453. 2012, 107.

Kim, Kyu Hong and Kim, Chongam. "Accurate, efficient and monotonic numerical methods for multi-dimensional compressible flows: Part II: Multi-dimensional limiting process." *Journal of Computational Physics* 208 (2005).2: 570 – 615.

URL http://www.sciencedirect.com/science/article/pii/S002199910500121X

Kjäldman, L. "Numerical flow simulation of dust deflagrations." *Powder Technology* 71 (1992).2: 163 – 169.

URL http://www.sciencedirect.com/science/article/pii/003259109280005H

Kobayashi, H., Howard, J.B., and Sarofim, A.F. "Coal devolatilization at high temperatures." *Symposium (International) on Combustion* 16 (1977).1: 411 – 425.

URL http://www.sciencedirect.com/science/article/pii/S008207847780341X

Krazinski, John L., Buckius, Richard O., and Krier, Herman. "Coal dust flames: A review and development of a model for flame propagation." *Progress in Energy and Combustion Science* 5 (1979).1: 31 – 71.

URL http://www.sciencedirect.com/science/article/pii/0360128579900182

Lee, J.H.S., Zhang, F., and Knystautas, R. "Propagation mechanisms of combustion waves in dust-air mixtures." *Powder Technology* 71 (1992).2: 153 – 162.

URL http://www.sciencedirect.com/science/article/pii/003259109280004G

Liberman, M.A., Ivanov, M.F., and Kiverin, A.D. "Effects of thermal radiation heat transfer on flame acceleration and transition to detonation in particle-cloud hydrogen flames." *Journal of Loss Prevention in the Process Industries* 38 (2015): 176 – 186.

URL http://www.sciencedirect.com/science/article/pii/S0950423015300310

Liou, Meng-Sing. "A sequel to AUSM, Part II: AUSM+-up for all speeds." *Journal of Computational Physics* 214 (2006).1: 137 – 170.

URL http://www.sciencedirect.com/science/article/pii/S0021999105004274

McClarren, Ryan G. and Hauck, Cory D. "Robust and accurate filtered spherical harmonics expansions for radiative transfer." *Journal of Computational Physics* 229 (2010).16: 5597 – 5614.

URL http://www.sciencedirect.com/science/article/pii/S0021999110001622

McClarren, Ryan G., Holloway, James Paul, and Brunner, Thomas A. "On solutions to the Pn equations for thermal radiative transfer." *Journal of Computational Physics* 227 (2008).5: 2864 – 2885.

URL http://www.sciencedirect.com/science/article/pii/S0021999107005153

McMahon, GW, Britt, JR, O'Daniel, JL, Davis, LK, and Walker, RE. "CFD study and structural analysis of the Sago mine accident." *US Army Corps of Engineers, Engineer Research and Development Center, Geotechnical and Structures Laboratory, ERDC/GSL TR-06-X* (2007).

Meister, A, Ortleb, S, and Sonar, Th. "On spectral filtering for discontinuous Galerkin methods on unstructured triangular grids." *Preprint: Mathematische Schriften Kassel* (2009): 115–135.

Mitgau, P, Wagner, H Gg, and Klemens, R. "Einfluss der Turbulenzlänge und der Schwankungsgeschwindichkeit auf die Flammengeschwindigkeit von Stäuben." *Feuerungstechnik, Kaleidoskop aus aktueller Forschung und Entwicklung. Geburtstag* (1997): 17–45.

Mitgau, Peter. *Einfluss de Turbulenzlänge und der Schwankungsgeschwindigkeit auf die Verbrennungsgeschwindigkeit von Aerosolen*. Ph.D. thesis, Max-Planck-Institut für Strömungsforschung, 1996.

Modest, Michael F. *Radiative heat transfer*. Academic press, 2013.

Moen, I.O., Lee, J.H.S., Hjertager, B.H., Fuhre, K., and Eckhoff, R.K. "Pressure development due to turbulent flame propagation in large-scale methane air explosions." *Combustion and Flame* 47 (1982): 31 – 52.

URL http://www.sciencedirect.com/science/article/pii/0010218082900876

Nettleton, MA and Stirling, R. "The ignition of clouds of particles in shock-heated oxygen." *Proceedings of the Royal Society of London. Series A. Mathematical and Physical Sciences* 300 (1967).1460: 62–77.

P. Kosinski, R. Klemens, and P. Wolanski. "Potential of mathematical modelling in large-scale dust explosions." *J. Phys. IV France* 12 (2002).7: 125–132.

URL https://doi.org/10.1051/jp4:20020275

Please, C.P., McGuinness, M.J., and McElwain, D.L.S. "Approximations to the distributed activation energy model for the pyrolysis of coal." *Combustion and Flame* 133 (2003).1: 107 – 117.

URL http://www.sciencedirect.com/science/article/pii/S0010218002005540

Radice, David, Abdikamalov, Ernazar, Rezzolla, Luciano, and Ott, Christian D. "A new spherical harmonics scheme for multi-dimensional radiation transport I. Static matter configurations." *Journal of Computational Physics* 242 (2013): 648 – 669.

URL http://www.sciencedirect.com/science/article/pii/S0021999113001125

Roe, P L. "Characteristic-Based Schemes for the Euler Equations." *Annual Review of Fluid Mechanics* 18 (1986).1: 337–365.

URL https://doi.org/10.1146/annurev.fl.18.010186.002005

ROSE, M., ROTH, P., FROLOV, S.M., and NEUHAUS, M.G. "Modelling of Turbulent Gas/Particle Combustion by a Lagrangian PDF Method." *Combustion Science and Technology* 149 (1999).1-6: 95–113.

URL https://doi.org/10.1080/00102209908952101

Rusanov, Viktor Vladimirovich. "The calculation of the interaction of non-stationary shock waves with barriers." *Zhurnal Vychislitel'noi Matematiki i Matematicheskoi Fiziki* 1 (1961).2: 267–279.

Rzal-Rebière, F and Veyssière, B. "Propagation mechanisms of starch particles-air flames." *Proceedings of the 6th International Colloquium on Dust Explosions*. 1994, 186–200.

S. Zhong, A. Teodorczyk, X. Deng, and J. Dang. "Modeling and simulation of coal dust explosions." *J. Phys. IV France* 12 (2002).7: 141–147.

URL https://doi.org/10.1051/jp4:20020277

Saito, T, Marumoto, M, and Takayama, K. "Numerical investigations of shock waves in gas-particle mixtures." *Shock Waves* 13 (2003).4: 299–322.

Sapko, Michael J., Weiss, Eric S., Cashdollar, Kenneth L., and Zlochower, Isaac A. "Experimental mine and laboratory dust explosion research at NIOSH." *Journal of Loss Prevention in the Process Industries* 13 (2000).3: 229 – 242.

URL http://www.sciencedirect.com/science/article/pii/S0950423099000388

Semenov, I., Utkin, P., and Markov, V. "Numerical modelling of dust-layered detonation structure in a narrow tube." *Journal of Loss Prevention in the Process Industries* 26 (2013).2: 380 – 386. Selected Papers from the Eighth International Symposium on Hazards, Prevention, and Mitigation of Industrial Explosions (Yokohama, Japan, 5–10 September 2010).

URL http://www.sciencedirect.com/science/article/pii/S0950423012000605

Shimura, Kei and Matsuo, Akiko. "Using an extended CFD–DEM for the two-dimensional simulation of shock-induced layered coal-dust combustion in a narrow channel." *Proceedings of the Combustion Institute* 37 (2019).3: 3677 – 3684.

URL http://www.sciencedirect.com/science/article/pii/S154074891830484X

Shu, Chi-Wang. "High order ENO and WENO schemes for computational fluid dynamics." *High-order methods for computational physics*. Springer, 1999. 439–582.

Sichel, M, Baek, Seung-Wook, Kauffman, CW, Maker, B, Nicholls, JA, and Wolanski, P. "The shock wave ignition of dusts." *AIAA journal* 23 (1985).9: 1374–1380.

Smirnov, N.N., Nikitin, V.F., and Legros, J.C. "Ignition and combustion of turbulized dust–air mixtures." *Combustion and Flame* 123 (2000).1: 46 – 67.

URL http://www.sciencedirect.com/science/article/pii/S0010218000001474

Smith, G.P., Golden, D.M., Frenklach, M., Moriarty, N.W., Eiteneer, B., Goldenberg, M., Bowman, C.T., Hanson, R.K., Song, S., Gardiner, W.C., Lissianski, V.V., and Qin, Z. "GRI-Mech 3.0." 1999.

URL http://combustion.berkeley.edu/gri-mech/

Smith, K Lee, Smoot, L Douglas, Fletcher, Thomas H, and Pugmire, Ronald J. *The structure and reaction processes of coal*. Springer Science & Business Media, 2013.

Smoot, L. Douglas and Horton, M. Duane. "Propagation of laminar pulverized coal-air flames." *Progress in Energy and Combustion Science* 3 (1977).4: 235 – 258.

URL http://www.sciencedirect.com/science/article/pii/0360128577900144

Solomon, P. R., Hamblen, D. G., Carangelo, R. M., Serio, M. A., and Deshpande, G. V. "General model of coal devolatilization." *Energy & Fuels* 2 (1988).4: 405–422.

URL https://doi.org/10.1021/ef00010a006

Speight, J.G. "9 - Coal gasification processes for synthetic liquid fuel production." *Gasification for Synthetic Fuel Production*. eds. Rafael Luque and James G. Speight, Woodhead Publishing Series in Energy. Woodhead Publishing, 2015. 201 – 220.

URL http://www.sciencedirect.com/science/article/pii/B9780857098023000096

Toro, Eleuterio F. *Riemann solvers and numerical methods for fluid dynamics: a practical introduction*. Springer Science & Business Media, 2013.

Turns, Stephen R et al. *Introduction to combustion*, vol. 287. McGraw-Hill Companies, 1996.

Ugarte, O. J., Houim, R. W., and Oran, E. S. "Examination of the forces controlling dust dispersion by shock waves." *Phys. Rev. Fluids* 2 (2017a): 074304.

URL https://link.aps.org/doi/10.1103/PhysRevFluids.2.074304

Ugarte, Orlando J, Houim, Ryan W, and Oran, Elaine S. "Effect of Particle Size on the Dispersion of Dust Produced by a Shock Wave." 2017b.

van Leer, Bram. "Towards the ultimate conservative difference scheme. V. A second-order sequel to Godunov's method." *Journal of Computational Physics* 32 (1979).1: 101 – 136.

URL http://www.sciencedirect.com/science/article/pii/0021999179901451

Vandeven, Hervé. "Family of spectral filters for discontinuous problems." *Journal of Scientific Computing* 6 (1991).2: 159–192.

URL https://doi.org/10.1007/BF01062118

V.P. Korobeinikov, I.V. Semenov, I.S. Menshov, R. Klemens, P. Wolanski, and P. Kosinski. "Modelling of flow and combustion behind shock waves propagating along dust layers in long ducts." *J. Phys. IV France* 12 (2002).7: 113–119.

URL https://doi.org/10.1051/jp4:20020273

Wall, T. F., Lowe, A., Wibberley, L J., Mai-Viet, T., and Gupta, R. P. “Fly Ash Characteristics and Radiative Heat Transfer in Pulverized-Coal-Fired Furnaces.” *Combustion Science and Technology* 26 (1981).3-4: 107–121.

URL https://doi.org/10.1080/00102208108946951

Wolanski, P. “Problems of dust explosions.” *Proceedings 1st Specialists Meeting (International) of the Combustion Institute*. 1981, 497–502.

———. “Detonation in dust mixtures.” *Proceedings of Shenyang international symposium on dust explosions, Shenyang, China*. 1987, 568–598.

Worsdorfer, K, Sippel, M, Fuisting, J, and Kneer, A. “Moglichkeiten des Einsatzes numerischer Methoden im Explosionsschutz.” *VDI BERICHTE* 1601 (2001): 437–448.

Zhang, Weiqun, Almgren, Ann, Beckner, Vince, Bell, John, Blaschke, Johannes, Chan, Cy, Day, Marcus, Friesen, Brian, Gott, Kevin, Graves, Daniel, Katz, Max, Myers, Andrew, Nguyen, Tan, Nonaka, Andrew, Rosso, Michele, Williams, Samuel, and Zingale, Michael. “AMReX: a framework for block-structured adaptive mesh refinement.” *Journal of Open Source Software* 4 (2019).37.

Zydak, Przemyslaw and Klemens, Rudolf. “Modelling of dust lifting process behind propagating shock wave.” *Journal of Loss Prevention in the Process Industries* 20 (2007).4: 417 – 426. Selected Papers Presented at the Sixth International Symposium on Hazards, Prevention and Mitigation of Industrial Explosions.

URL http://www.sciencedirect.com/science/article/pii/S0950423007000691

BIOGRAPHICAL SKETCH

Swagnik Guhathakurta was born in Kolkata, West Bengal, India, and grew up in various parts of the country. After finishing school, he studied physics at Fergusson College, Pune, India, where he got his Bachelor of Science in physics and then did a Master of Science in physics at the Indian Institute of Technology, Delhi, India (IIT-D). With physics as his background, he then decided to change fields and study aerospace engineering at the University of Florida (UF), Gainesville, U.S.A and graduated with a Master of Science. He then decided to pursue a career in the industry and started work at Mentor Graphics Corporation in Wilsonville, Oregon, U.S.A. After a year of working, he realized that his passion lies in research and thus applied for a Ph.D. at his old alma mater, the University of Florida. He has been working at the Multiphase Reactive Flow Research group at UF under the guidance of Dr. Ryan W. Houim since August 2017. The primary topic of his research has been granular coal-dust explosions but has also worked on other projects including aluminum particle burning and programmed burn. In addition to this, he has also been a Graduate Teaching Assistant for a variety of undergraduate courses such as Fluid Mechanics, Heat Transfer, Aerospace Propulsion, Heat Transfer Laboratory, etc. for which he has assisted a large number of students with their coursework, graded assignments, and examinations, and has given lectures for many of the courses.